# Einzelmolekül-Mechanoenzymatik

**Dissertation**

an der

Ludwig-Maximilians-Universität München

Fakultät für Physik

von

**Elias M. Puchner**
aus Nürnberg

München, Oktober 2008

Erstgutachter: Prof. Dr. Hermann E. Gaub
Zweitgutachter: Prof. Dr. Joachim Rädler
Datum der mündlichen Prüfung: 19.12.2008

# Inhalt

1. Zusammenfassung.......................................................... 5

2. Einleitung.......................................................... 6

3. Mechanoenzymatik .......................................................... 8

3.1 Enzyme: Konformation und Funktion.......................................................... 8

3.2 Das Muskelenzym Titinkinase.......................................................... 10
- Muskelaufbau
- Autoinhibierung der Titinkinase

3.3 Fluktuierende Enzyme.......................................................... 13
- Modellsystem Candida Antarctica Lipase B
- Antikörper-Peptid basierte Sollbruchstelle für mechanische Manipulation

4. Beobachtung und 3D-Kontolle einzelner Biomoleküle .......................... 17

4.1 Rasterkraft- und TIRF-Mikroskopie .......................................................... 17

4.2 Nanoassemblierung durch molekulare Erkennung.......................................................... 18
- DNA als programmierbarer Baustein
- Hierarchische Trennkräfte von DNA für gezielte Nanoassemblierung

5. Ergebnisse.......................................................... 21

5.1 Der molekulare Kraftsensor Titinkinase.......................................................... 21
- Kraftinduzierte Entfaltungscharakteristik einzelner Titinkinase-Proteinkonstrukte
- Mechanisch aktivierte ATP-Bindung
- Lokalisierung des aktiven Zustandes durch mechanisches „pump-and-probe“
- Strukturelle Untersuchung des molekularen Aktivierungsmechanismus
- Titinkinase-Mechanismus im physiologischen Zusammenhang

5.2 Mechanische Manipulation von CalB.......................................................... 28
- Antikörper-funktionalisierte Agarosekugeln als Manipulator
- Mechanische Charakterisierung der Antikörper-Sollbruchstelle
- Enzymatische Aktivität unter Kraft

5.3 Funktionelle Nanoassemblierung.......................................................... 32
- Mechanische und optische Charakterisierung einzelner SMCP-Zyklen
- Selbstorganisation an nanoassemblierten Bindungsstellen

6. Ausblick.......................................................... 35

7. Anhang ........ 38

7.1 Kraftspektroskopie ........ 38

7.2 Kombination von AFM mit TIRF-Mikroskopie ........ 42

7.3 Publikationen ........ 44

P1 „Mechanoenzymatics of Titin Kinase“
P2 „Force-based Analysis of Multidimensional Energy Landscapes:...“
P3 „Comparing Proteiny by their Unfolding Pattern“
P4 „Single-Molecule Cut-and-Paste Surface Assembly“
P5 „Nanoparticle Self-Assembly to a DNA-Scaffold Written by Single-Molecule Cut-and-Paste“
P6 „Optically Monitoring the Mechanical Assembly of Single Molecules“

7.4 Manuskripte für Publikationen ........ 130

M1 „Triggering enzymatic activity with force“
M2 „A combined AFM-TIRF microscope for simultaneous single molecule Experiments“

8. Referenzen ........ 156

9. Lebenslauf ........ 161

10. Danksagung ........ 163

# 1. Zusammenfassung

Enzyme zählen zu den wichtigsten funktionellen Einheiten von Organismen. Sie produzieren Biomoleküle oder bauen diese ab, wirken als molekulare Motoren oder regulieren biologische Prozesse in Antwort auf beispielsweise mechanische Reize. Für die Medizin und Nano-Biotechnologie ist das Verständnis der zugrundeliegenden molekularen Mechanismen und ihres Zusammenspiels von großer Bedeutung.

Das autoinhibierte Muskelenzym Titinkinase befindet sich im langen Sarkomer-Protein Titin an idealer Position, um im Muskel Ungleichgewichte der Krafterzeugung zu detektieren. In dieser Arbeit wurde die Funktion und der molekulare Aktivierungsmechanismus der Titinkinase in der natürlichen biomolekularen Umgebung mit Einzelmolekül-Kraftspektroskopie entschlüsselt. Durch das Dehnen einzelner Proteinkonstrukte konnte gezeigt werden, dass die Titinkinase über fünf Energiebarrieren und mit Kräften unter 50 pN vor den strukturell wirkenden Titindomänen (Ig/Fn) entfaltet. In Anwesenheit des Cosubstrates ATP, das nicht an die autoinhibierte Konformation bindet, wurde im Entfaltungsmuster eine zusätzliche Energiebarriere beobachtet. Die präzise Lokalisierung der Energiebarrieren bis auf wenige Aminosäuren genau erlaubte durch den Vergleich mit Molekulardynamik-Simulationen die Bestimmung aller strukturellen Veränderungen während der Entfaltung. Die zusätzliche Barriere beim mechanisch induzierten Binden von ATP wurde durch Wechselwirkung von ATP mit den Aminosäuren Methionin-34 und Lysin-36 erklärt. Neu entwickelte mechanische „pump-and-probe“-Protokolle, mit denen die Konformation des Enzyms kontrolliert wurde, erlaubten die detaillierte Vermessung der ATP-Bindungskinetik, die Lokalisierung der mechanischen Aktivierung nach der zweiten Energiebarriere und wiesen die essenzielle Rolle der Aminosäure Lysin-36 für die ATP-Bindung nach. Durch Binden von ATP wird die Blockierung der katalytischen Aminosäure Aspartat-127 durch Autophosphorylierung von Tyrosin-170 aufgehoben. Die Titinkinase ist somit katalytisch aktiv und startet über Phosphorylierung von Substraten die Signalkaskade zur Regulation von Muskel-Genexpression und Proteinumsatz. Die Position der Titinkinase im Titin, sowie die Aktivierungskräfte und Längen im physiologischen Bereich lassen den Schluss zu, dass die Titinkinase als natürlicher Kraftsensor wirkt, um den Muskelaufbau zu steuern.

Das Konzept der mechanisch induzierten Konformationsänderung wurde in dieser Arbeit auch auf die Lipase CalB übertragen, die keine mechanisch kontrollierte Funktion besitzt. Die Aktivität einzelner kovalent immobilisierter Enzyme wurde mit TIRF-Mikroskopie und einem Substrat beobachtet, das nach enzymatischer Spaltung fluoreszierte. Dabei wurde ein charakteristisch fluktuierendes Blinkverhalten mit An- und Auszeiten im Sekundenbereich festgestellt. Durch gleichzeitige mechanische Manipulation von CalB über eine gut charakterisierte molekulare Sollbruchstelle wurde das Enzym in höherenergetische und katalytisch inaktive Zustände gebracht, von wo aus eine Relaxation über den aktiven Zustand ins Gleichgewicht stattfand und eine erhöhte Aktivität nach 1,7 Sekunden festgestellt wurde.

Die Kenntnis der Mechanismen einzelner Enzyme ist die Voraussetzung für das Verständnis ihres Zusammenspiels, bei dem ihre räumliche Anordnung essenziell ist. Um solche funktionelle Einheiten kontrolliert auf Oberflächen zu assemblieren, wurde in dieser Arbeit das natürliche Prinzip der Selbstorganisation, basierend auf molekularer Erkennung, mit der Präzision des *Atomic Force Microscope* (AFM) kombiniert. Bei dieser *„Single-Molecule Cut-and-Paste*“-Technik wurden mit der Spitze eines AFM kleine DNA-Oligomere nacheinander von einem Depot aufgenommen und im Ziel bis auf 10 nm genau an vordefinierten Positionen abgesetzt. Durch diesen Prozess, der optisch und mechanisch kontrolliert wurde, konnten Strukturen verschiedener Form und Größe bis zu beugungslimitierten Arrangements von 5 Molekülen mit Abständen von 50 nm erzeugt und optisch rekonstruiert werden. In einer Weiterentwicklung wurde diese Technik mit Selbstorganisation kombiniert. Durch das Anheften von Biotin an die DNA konnten Strukturen aus Bindungsstellen erzeugt werden. Verschiedene fluoreszierende Nanokristalle mit dem Gegenstück Streptavidin an der Oberfläche lagerten sich so von selbst zu Superstrukturen zusammen. Die entwickelte Basistechnologie erlaubt die Nanoassemblierung verschiedenster funktioneller Einheiten und könnte die Konstruktion von synergetischen Enzymkaskaden, oder das Imitieren biologischer Signalwege ermöglichen.

# 2. Einleitung

Ein Ziel der Nano-Biotechnologie ist, biologische Prozesse auf grundlegendster molekularer Ebene zu verstehen und zu nutzen. Die Größe der einzelnen molekularen Bausteine im Nanometer-Bereich, sowie deren Komplexität und Interaktion miteinander stellen dabei eine Herausforderung dar. Allein die Anzahl der unterschiedlichen menschlichen Proteine im *International Protein Index* [3] beträgt ca. 40.000, Schätzungen belaufen sich sogar auf ca. 84.0000 [4]. Proteine erfüllen die unterschiedlichsten Funktionen und wirken beispielsweise als Motoren, Filter, Sensoren oder Gerüst, und regulieren sich gegenseitig über chemische oder mechanische Signale. Die räumliche Anordnung der interagierenden Biomoleküle ist dabei essenziell. Sie wird durch das fundamentale Prinzip der Natur erreicht: die Selbstassemblierung durch molekulare Erkennung. Durch die Brownsche Molekularbewegung erkunden die funktionellen Einheiten das ihnen zugängliche Volumen und suchen ihre Andockstellen, binden aber nur an ihr spezifisches Gegenstück. Mit diesem Prinzip erzeugt die Natur nicht nur komplexe Nanostrukturen innerhalb von Zellen, sondern auch die Wechselwirkung ganzer Zellen wird auf diese Weise gesteuert und lässt sie in Organen oder ganzen Organismen zusammenarbeiten. Diese Selbstassemblierungsprozesse, die von der Natur in Milliarden von Evolutionsjahren entwickelt und optimiert wurden, stellen deshalb die wichtigste Grundlage bei der künstlichen Erzeugung von Nanostrukturen dar.

Kraft ist essenziell im Prozess der Selbstassemblierung und des dynamischen Zusammenspiels biologischer Einheiten. Sie bestimmt nicht nur wie stark einzelne Moleküle oder Zellen aneinander haften, sondern sie wird auch aktiv erzeugt und manchmal sogar in biochemische Signale übersetzt, um biologische Prozesse zu regulieren. Auf der Ebene von Organen wird sie von Muskeln generiert, wodurch diese selbst der erzeugten Kraft ausgesetzt sind. Auf zellulärer Ebene ist besonders das Zytoskelett Kräften ausgesetzt, und schließlich wird auf molekularer Ebene Kraft durch molekulare Motoren erzeugt und auf assoziierte Proteine übertragen. Für biologische Reaktionen auf diese mechanischen Reize bedarf es molekularer Kraftsensoren, die mechanische in biochemische Signale übersetzen. Die Kraft stellt deshalb eine wichtige biologische Größe dar, um die Mechanismen dieser Prozesse zu erforschen und die Natur bei der künstlichen Erzeugung von Nanostrukturen zu imitieren, wie sich in dieser Arbeit zeigen wird.

Kraft ist jedoch nicht nur eine Größe, um Proteine mit mechanischer Funktion zu untersuchen. Sie erlaubt vielmehr einen tiefen Einblick in die Organisation und Architektur von Biomolekülen. Denn die Funktion von Proteinen wird durch die selbstorganisierte dreidimensionale Faltung der Aminosäurenkette in einer ganz bestimmten Anordnung, der Tertiärstruktur, erlangt. Durch die verschiedenen physikalischen und chemischen Eigenschaften der zwanzig kanonischen Aminosäuren entsteht eine vieldimensionale Potenziallandschaft, deren Grundzustand mit niedrigster Energie von der Proteinkette in der Regel eingenommen wird und die funktionelle Konformation darstellt. Die strukturaufklärenden Methoden wie NMR oder Röntgenstrukturanalyse haben hier einen Durchbruch erwirkt, da durch sie die Positionen der einzelnen Atome kartographiert werden können. Jedoch stellen solche Messwerte einen Mittelwert dar, und die dynamische Untersuchung einzelner Proteine, die einen tiefen Einblick in molekulare Mechanismen erlaubt, ist damit nicht möglich. Die Kraftspektroskopie, bei der einzelne Moleküle gedehnt werden, wobei Kraft und Abstand als Messsignal dienen, ermöglicht die Untersuchung dieser Potenziallandschaft und der dynamischen Wechselwirkungskräfte.

Für die Erforschung der molekularen Mechanismen biologischer Einheiten und ihres Zusammenspieles ist die Kontrolle der einzelnen Bausteine sowie die Beobachtung ihrer Reaktion von größter Wichtigkeit. Das „Atomic Force Microscope“ (AFM) und seine weiterentwickelte

Form für AFM-basierte Kraftspektroskopie sind hierfür wichtige Messinstrumente. Mit einer Präzision im Nanometerbereich in allen drei Raumrichtungen können einzelne Moleküle kontrolliert, manipuliert und ihre Reaktion mechanisch oder in Kombination mit Mikroskopiertechniken optisch detektiert werden. Entscheidend ist hier die Schnittstelle zwischen der makroskopisch kontrollierten Spitze des AFM-Cantilevers, der als mechanischer Detektor und Manipulator wirkt, und der molekularen Welt, in die makroskopische Techniken nicht übertragbar sind.

Richard Feynman hat 1959 in seinem legendären und visionären Vortrag „There is plenty of room at the bottom“ veranschaulicht, dass die Herstellung miniaturisierter Versionen unserer makroskopischen Werkzeuge und Maschinen, und ihre Anwendung auf molekularer Größenordnung fehlschlägt. Zudem treten auf molekularer Ebene folgende physikalischen Effekte in den Vordergrund: Die Reibungskräfte nehmen überhand und die thermische Energie stößt Moleküle umher und hält alles in ständiger Bewegung, sodass die Gravitation keine essenzielle Rolle mehr spielt. Übertrüge man diese Welt, in der die Newtonschen Bewegungsgleichungen in die Langevin-Gleichung übergehen, in unsere makroskopische Welt, so würde dies dem Leben in einer honigartigen Flüssigkeit inmitten eines Hurrikans entsprechen. Würde es gelingen, einen Greifarm nanoskopisch nachzubauen, so könnte man damit trotzdem nicht ein einzelnes Molekül greifen und an einer bestimmten Position einfach absetzten. Um es zu ergreifen, müsste das Molekül zuerst nanometergenau lokalisiert und dann innerhalb einer millionstel Sekunde gepackt werden[1], da sich der Ort aufgrund der Brownschen Molekularbewegung ständig ändert. Selbst wenn das Molekül mit einer ausreichenden Kontaktfläche der Greifzange festhalten werden könnte, wäre es nicht aufzunehmen, da es aufgrund der laminaren Strömung beim Schließen der Zange ausweichen würde[2]. Beim Absetzten des Moleküls würde man außerdem mit dem von Smalley und Drexler debattierten Problem der „sticky fingers“ konfrontiert werden: Der für das Molekül „klebrige“ Greifarm müsste das Objekt wieder loslassen.

Für die Kontrolle und gezielte Assemblierung von Molekülen ist also nicht eine Miniaturisierung makroskopischer Hilfsmittel die Lösung, sondern die gezielte Anwendung makroskopisch präzise gesteuerter Messsonden in Kombination mit dem Prinzip der molekularen Erkennung, das die Evolution in Milliarden von Jahren entwickelt hat, um die komplexe und vielseitige Nano-Biotechnologie der Natur zu ermöglichen.

Zentrales Thema dieser Dissertation ist die Kontrolle, Manipulation und Erforschung der molekularen Mechanismen einzelner Enzyme und anderer Biomoleküle, sowie deren Nanoassemblierung zu beliebigen Strukturen. Neben dem Muskelenzym Titinkinase, dessen Funktion und molekularer Mechanismus diese Arbeit entschlüsselt, wird das ebenfalls mechanisch manipulierte, aber optisch beobachtete Enzym CalB vorgestellt. Außerdem werden Biomoleküle eingeführt, deren Fähigkeit der molekularen Erkennung die Kontrolle, Manipulation und gezielte Assemblierung funktioneller Einheiten zu komplexen Strukturen erlaubt. Für die detaillierte Beschreibung, Analyse sowie für technische Details dieser kumulativen Dissertation wird an den entsprechenden Stellen auf die zugehörigen Publikationen im Anhang verwiesen.

---

[1] Für den Wert von 1 µs wurde eine mittlere Diffusionslänge von 10 nm und ein Diffusionskoeffizient von $10^7$ $nm^2/s$ vorausgesetzt.

[2] Bakterien gelingt es durch eine kurzzeitige hohe Geschwindigkeit, zum Reißen von Beute in turbulente Bereiche zu gelangen.

# 3. Mechanoenzymatik

Enzyme zählen zu den aktiven Einheiten von Zellen. In diesem Kapitel werden ihr Aufbau und ihre Funktion dargestellt. Neben dem möglichen Einfluss externer Kräfte auf ihre Aktivität werden das in dieser Arbeit untersuchte Muskelenzym Titinkinase und die Lipase CalB vorgestellt.

## 3.1 Enzyme: Konformation und Funktion

Enzyme bilden die katalytisch aktive Klasse unter den Proteinen. Sie erfüllen in Organismen eine enorme Vielfalt spezifischer Funktionen und sind für den Stoffwechsel, für Signalkaskaden und gerichtete Bewegung in Form molekularer Motoren verantwortlich. Aufgebaut sind Enzyme aus den 20 kanonischen Aminosäuren, die kovalent zu einer Aminosäurenkette verknüpft sind. Durch die Eigenschaften der Aminosäuren einsteht eine Potenziallandschaft im Konformationsraum, die die Faltung des Proteins in den funktionellen Zustand und seine Dynamik bestimmt. Während die Abfolge der Aminosäuren als *Primärstruktur* bezeichnet wird, nennt man die verschiedenen Strukturelemente wie α-Helix, β-Faltblatt oder „random coil" *Sekundärstruktur* (siehe Abb. 1).

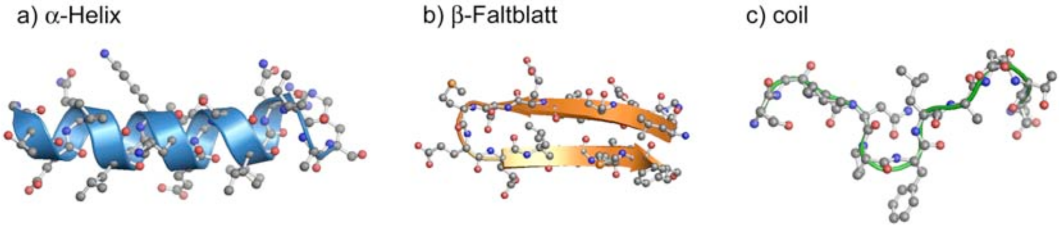

Abbildung 1: Strukturelemente von Proteinen. Je nach Eigenschaft der Aminosäuren und der lokalen Umgebung falten sich Teile der Aminosäurekette zu den stabilen Strukturelementen α-Helix (a) und β-Faltblatt (b), oder bilden flexiblere Schlaufen, auch „coil" genannt (c). In den gezeigten Kristallstrukturen sind die Atome der Aminosäuren sowie die Schemata der Peptidrückgrate dargestellt.

Aus diesen Elementen ist die gesamte Struktur eines Enzyms, die *Tertiärstruktur*, aufgebaut. Während ein großer Teil der Elemente nur strukturelle Beiträge liefert, besitzen Enzyme, je nach Art, eine oder mehrere spezifische Bindungstaschen für die molekulare Erkennung von Substraten oder Cofaktoren, sowie ein katalytisches Zentrum mit meist nur wenigen katalytischen Aminosäuren.

Für viele biologische Prozesse ist eine Steuerung von enzymatischer Aktivität wesentlich. Die Regulation geschieht meist durch Konformationsänderungen des Enzyms, die durch kovalente Modifikationen, das Binden von Liganden oder, wie bei der Titinkinase, durch Kraft induziert werden. Durch diese Modifikationen wird die Energielandschaft des Enzyms so verändert, dass Teile der Aminosäurenkette in einen neuen Zustand übergehen. Diese Konformationsänderungen können nur Teile des Enzyms, beispielsweise nahe einer Substratbindungsstelle, betreffen, oder im Fall von kovalenten Modifikationen, wie der Phosphorylierung, sogar nur einzelne Aminosäuren. Biologische Prozesse wie die Regulation von Proteinfunktionen, sind angepasst an die thermische Energie $k_B T$ ($k_B$ bezeichnet die Boltzmann-Konstante und $T$ die Temperatur). Für Funktionen, die gezielt gesteuert werden, müssen einerseits die Barrieren zwischen zwei funktionellen Zuständen hoch genug sein, um nicht zufällig eingenommen zu werden, und andererseits sollte der reversible Prozess nicht viel an wertvoller Energie verbrauchen.

Aufgrund der thermischen Energie und ihrer Flexibilität sind Enzyme hoch dynamische Einheiten [5]. Es wurde von Frauenfelder erkannt, dass sie eine Vielzahl von Konformationen in dem kleinen, durch die thermische Energie erkundbaren Bereich durchlaufen [6-9]. Außerdem konnte durch eine Reihe von Einzelmolekülmessungen gezeigt werden, dass verschiedene Enzyme auch ohne externe Einflüsse zwischen aktiven und inaktiven Zuständen wechseln, und Perioden von An- und Auszeiten zeigen [10-12]. Dieses Verhalten wurde auch in dieser Arbeit bei der Lipase CalB beobachtet, wie in folgenden Kapiteln beschrieben wird.

Da eine externe Kraft die Energielandschaft beeinflusst, ist Einzelmolekül-Kraftspektroskopie eine ideale Messmethode, um die Konformation von Enzymen zu kontrollieren und eine mögliche konformationsinduzierte Funktionsänderung zu beobachten.

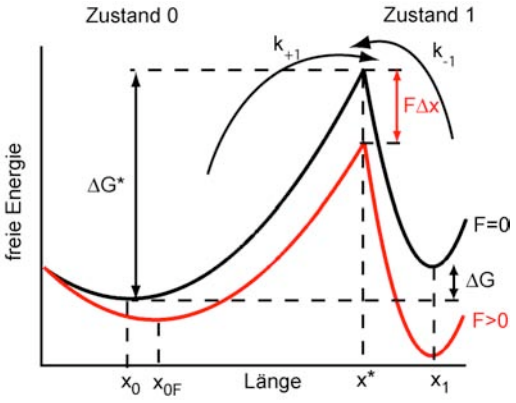

Abbildung 2: Schematische Darstellung zweier Zustände, die durch eine Energiebarriere getrennt sind. Durch eine externe Kraft wird die Potenziallandschaft verkippt, sodass sich die Energiebarriere bei x* erniedrigt und die Besetzung von Zustand 1 wahrscheinlicher wird. Konformationsänderungen können so durch Kraft induziert werden.

Wie in Abbildung 2 schematisch dargestellt, verkippt eine externe Kraft F die Energielandschaft, sodass die Energiebarriere $\Delta G^*$ bei $x^*$ für kleine Änderungen des Grundzustandes $x_{0F} - x_0 << x_1 - x_0$ verringert wird zu: $\Delta G^* = \Delta G^*(0) - F\Delta x^*, \quad \Delta x^* = x^* - x_0$.
In gleicher Weise ändert sich die freie Energie zwischen Zustand 0 und Zustand 1, sodass für die Rate $k_{+1}$ in Zustand 1 und die Gleichgewichtskonstante $K_{eq}$ unter Kraft gilt

$$k_{+1}(F) = a \cdot e^{-\frac{\Delta G^*(0) - F\Delta x^*}{k_B T}} = k_{+1}^0 e^{\frac{F\Delta x^*}{k_B T}} \quad \text{bzw.} \quad K_{eq}(F) = e^{-\frac{\Delta G - F\Delta x}{k_B T}} = K_{eq}^0 e^{\frac{F\Delta x}{k_B T}}$$

wobei $a$ den Frequenzfaktor bezeichnet. Es ist offensichtlich, dass durch die externe Kraft die Raten und das Gleichgewicht zugunsten von Zustand 1 verändert werden. Da eine weiterreichende Beschreibung der Theorie zur Dissoziation molekularer Bindungen unter Kraft zu weit führen würde, sei hier auf die Fachliteratur verwiesen [13-16].

## 3.2 Das Muskelenzym Titinkinase

Biologische Gewebe sind ständig Kräften ausgesetzt. Überall dort, wo Bewegung erzeugt wird – sei es auf makroskopischer Ebene, zum Beispiel im Muskel, oder auf mikroskopischer Ebene durch molekulare Motoren –, entstehen mechanische Spannungen, auf die die Zelle reagieren muss. Für mechanisch gesteuerte Signalkaskaden bedarf es molekularer Kraftsensoren, die Kräfte detektieren und in Form chemischer Signale weiterleiten. In dieser Arbeit konnte gezeigt werden, dass die katalytische Domäne des Titin, die Titinkinase, mechanisch aktiviert wird und so als Kraftsensor im Muskel den Proteinumsatz und die Muskel-Genexpression steuert. Die physiologische Bedeutung dieses Enzyms sowie der Mechanismus, der die enzymatische Aktivität inhibiert, werden im Folgenden dargestellt.

### Muskelaufbau

Der quergestreifte Muskel, zu dem Skelett- und Herzmuskel zählen, ist aus Muskelfasern aufgebaut, die viele Zentimeter lang und einige 100 µm dick sein können. Sie bilden sich in der embryonalen Phase durch Fusion vieler Myoblasten und enthalten deshalb viele Zellkerne und Mitochondrien. Muskelfasern bestehen wiederum aus vielen faserartigen Myofibrillen, die aus mehreren hunderttausend hintereinander gereihten Sarkomeren, den krafterzeugenden Einheiten des Muskel, aufgebaut sind. Wie in Abbildung 3 schematisch dargestellt, sind die Aktinfilamente fest mit den Enden des Sarkomers verankert, sodass die Myosinfilamente, die aus den molekularen Myosin-Motoren aufgebaut sind, Kraft auf die Aktinfilamente ausüben können. Wegen der Spiegelsymmetrie des Sarkomers ziehen die Myosinfilamente auf beiden Seiten in entgegengesetzte Richtungen, wodurch das Sarkomer kontrahiert.

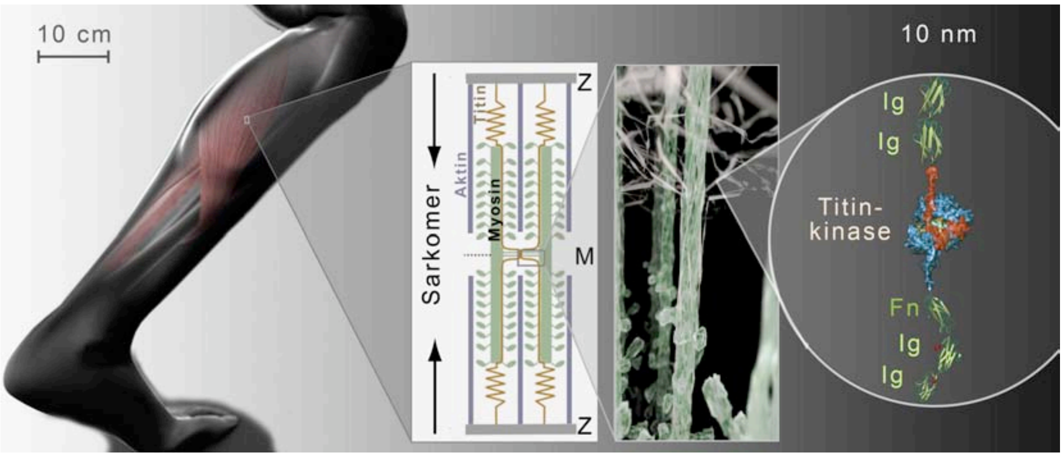

Abbildung 3: Schematische Darstellung des Muskels. Die krafterzeugende Einheit des Muskels ist das Sarkomer. Die Myosinfilamente (grün) sind über das Titin (gelb) elastisch mit der Z-Bande verbunden und bestehen aus den molekularen Motoren Myosin. Sie üben in den zwei Hälften des Sarkomers auf die fest verankerten Aktinfilamente Kräfte in entgegengesetzte Richtung aus, wodurch die Kontraktion entsteht. An der M-Bande verzweigen sich die Titine vom Mysinfilament. In dieser quervernetzten Struktur treten bei Ungleichgewichten der Krafterzeugung Scherkräfte auf. In dieser Region des Titins befindet sich die Titinkinase, umgeben von globulären Ig- und Fn- Domänen, als einzige katalytische Domäne des Titins.

In Position gehalten werden die Myosinfilamente durch das sehr lange Protein Titin, das sich von der Z-Bande bis zu M-Bande erstreckt. Neben seiner entscheidenden biochemischen Funktion bei der Selbstassemblierung des Sarkomers gibt es dem Muskel wichtige mechanische Eigenschaften. Denn der Bereich zwischen Z-Bande und Myosinfilament enthält „PEVK-Regionen“, die nach der Zusammensetzung der Aminosäuren benannt sind und strukturlose entropische Knäule bilden. Durch die entropische Kraft beim Dehnen [17, 18] erhält der Muskel seine passive Elastizität [19]. Die übrigen Teile des Titins bestehen zum größten Teil aus globulär gefalteten Immunoglobulin (Ig) - und Fibronectin-Domänen (Fn), die unter Kraft schlagartig aufbrechen, und so den Muskel bei zu hohen Kräften vor Zerstörung schützen können. Diese Teile des Titins sind mit kraftspektroskopischen Messmethoden intensiv untersucht worden [20-24].

Der hexagonalen Querschnittsstruktur des Sarkomers entsprechend, winden sich sechs Titine an einem Myosinfilament entlang bis zur M-Bande, wo sie sich vom Myosinfilament ablösen und in der netzartigen Struktur der M-Bande über Myomesin und Obscurin quervernetzt sind [25, 26]. Genau in diesem Bereich des Titins, der die ideale Position zur Detektion von mechanischen Spannungen zwischen Myosinfilamenten darstellt, befindet sich die Titinkinase.

## Autoinhibierung der Titinkinase

Proteinkinasen sind wichtige regulatorische Enzyme und steuern viele zelluläre Signalwege. Sie verändern den funktionellen Zustand ihrer Substrate durch Phosphorylierung, d.h. durch Anheften einer Phosphatgruppe (siehe Abbildung 4). Dadurch wird die Aktivität eines Enzyms entweder direkt beeinflusst oder ein Substrat erhält durch die Phosphorylierung eine veränderte Affinität zu weiteren Bindungspartnern im Signalweg. Resultat eines durch Kinasen initiierten Signalweges kann z. B. die Regulation der Genexpression oder des Proteinumsatzes sein.

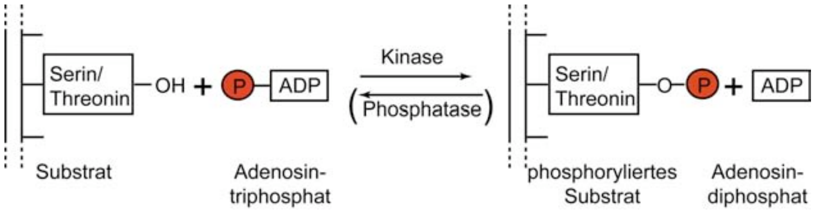

Abbildung 4: Schematische Darstellung der von Kinasen katalysierten Reaktion. Im Fall von Serin/Threonin-Kinasen wird das Gamma-Phosphat eines ATP- oder GTP-Moleküls auf die Aminosäuren Serin oder Threonin des Substrates übertragen, wodurch eine Veränderung des funktionellen Zustandes erreicht wird.

Die Titinkinase zählt zu den Serin/ Threonin spezifischen Kinasen. Obwohl sie eine Bindungsstelle für Calcium/ Calmodulin besitzt, wird sie durch Binden von Calcium/ Calmodulin im Gegensatz zu verwandten Kinasen nicht aktiviert. Es konnte vielmehr gezeigt werden, dass die Titinkinase zwei autoinhibierende Elemente enthält. Zum Einen ist die Bindungstasche für ATP in der nativen Konformation durch eine $\alpha$-Helix verschlossen, zum Anderen wird die katalytische Base Aspartat-127 (ASP127) durch Tyrosin-170 (TYR170) blockiert [27]. Die Kristallstruktur der Titinkinase ist in Abbildung 5 dargestellt, wobei die inhibitorischen Elemente rot hervorgehoben sind.

Zur Untersuchung der möglichen Signalwege aktivierter Titinkinasen wurden die inhibierenden Elemente biochemisch entfernt [2]. Dazu wurde zum Einen TYR170 zu Glutaminsäure mutiert, um die inhibierende Wirkung zu beseitigen und den phosphorylierten Zustand von TYR170 zu imitieren. Zum Anderen wurde der C-terminale regulatorische Teil, der die ATP-Bindungstasche verschließt, trunkiert. Auf diese Weise konnten aktive Titinkinasen gewonnen und Substrate wie nbr1 oder p62 identifiziert werden (siehe Abbildung 6). Die ausgelöste Signalkaskade steuert letztlich den Proteinumsatz im Muskel und reguliert im Zellkern die Expression von Muskelproteinen.

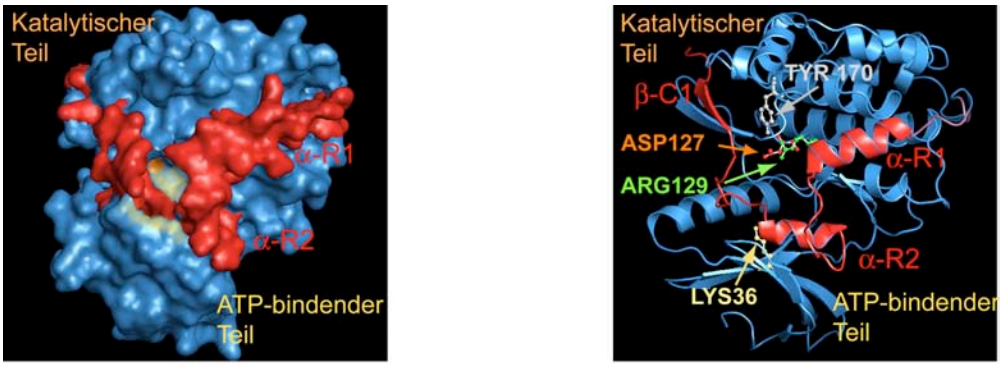
Katalytischer Teil
α-R1
α-R2
ATP-bindender Teil
Katalytischer Teil
TYR 170
β-C1
ASP127
ARG129
α-R1
α-R2
LYS36
ATP-bindender Teil

Abbildung 5: Kristallstruktur der Titinkinase pdb:1TKI. Die Titinkinase besteht aus einem größeren Teil, der für die Katalyse verantwortlich ist, und einem kleineren Teil, der die ATP-Bindungstasche enthält. Die Bindungstasche ist jedoch von der α-Helix αR2 des in rot markierten C-terminalen regulatorischen Teils blockiert, wodurch ATP nicht bindet. Der zweite inhibitorische Mechanismus besteht in der Blockierung der katalytischen Base ASP127 durch TYR170. Ebenfalls markiert sind die für die Katalyse wichtigen Aminosäuren ARG129 und LYS36, das in den meisten Kinasen konserviert ist und mit ATP interagiert.

Die ausgesprochen wichtige Funktion der Titinkinase bei der Bildung und Erhaltung des Muskels zeigt sich auch bei einer erblichen Myopathie, bei der das Arginin-279 der Helix αR1 zu Tryptophan mutiert ist [2, 28]. Die Patienten leiden schon in jungen Jahren an Muskelschwäche, die bei Versagen der Atemmuskulatur tödlich ist [29]. Auf mikroskopischer Ebene zeigen sich die Auswirkungen vor allem in einer verwaschenen, schwammigen Sarkomerstruktur, bei der die M- und Z-Banden nicht mehr klar definiert sind. Ganze Myofibrillen brechen zusammen und können keine Kraft mehr erzeugen. Dass der regulatorische Signalweg der Titinkinase auch im Herzmuskel essenziell ist, konnte an KO-Mäusen gezeigt werden, bei denen die Titinkinase deletiert wurde [30]. Auch hier löst sich die Sarkomerstruktur auf, sodass keine Kraft mehr erzeugt werden kann, was letztlich zum Herzstillstand führt.

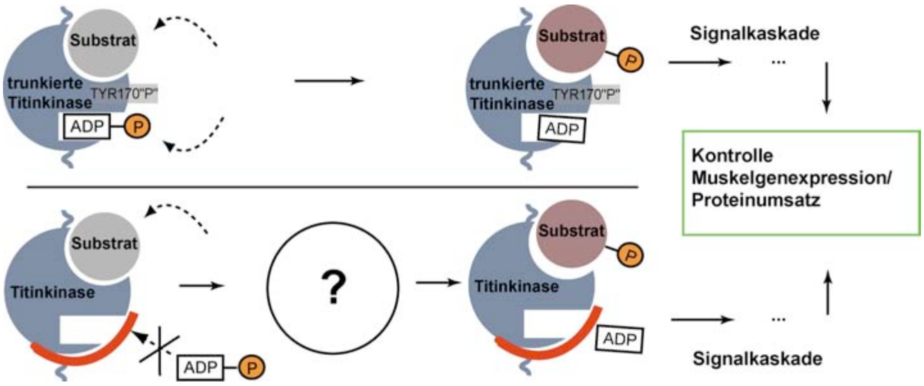
Substrat
trunkierte Titinkinase
TYR170"P"
ADP
P
Substrat
P
trunkierte Titinkinase
TYR170"P"
ADP
Signalkaskade
...
Kontrolle Muskelgenexpression/ Proteinumsatz
Substrat
Titinkinase
ADP
P
?
Substrat
P
Titinkinase
ADP
...
Signalkaskade

Abbildung 6: Schematische Darstellung der enzymatischen Aktivität der Titinkinase. Durch Trunkation des regulatorischen Teils, der die ATP-Bindungstasche verschließt, und durch Imitation des phosphorylierten TYR170 wurden in Referenz [2] aktive Kinasen gewonnen. Der untersuchte Signalweg, der über mehrere Zwischenschritte führt, steuert Proteinumsatz und Muskel-Genexpression. Der erste Schritt der ATP-Bindung, der für die Phosphorylierung von Substraten notwendig ist, findet jedoch in der ursprünglichen Konformation der natürlichen kompletten Titinkinase nicht statt.

Es ist also für die Grundlagenforschung und die Medizin von Interesse, den molekularen Aktivierungsmechanismus der kompletten Titinkinase in ihrer natürlichen Proteinumgebung zu entschlüsseln (Abbildung 6). Die Ergebnisse der Erforschung des molekularen Aktivierungsmechanismus finden sich im Kapitel 5 und in der Publikation P1 im Anhang.

## 3.3 Fluktuierende Enzyme

In gleicher Weise wie die Energielandschaft die Konformation und Funktion des mechanisch aktivierten Muskelenzyms Titinkinase bestimmt, erhalten auch andere Enzyme, die keine mechanische Aufgabe erfüllen, durch sie ihre Funktion. Neuere Untersuchungen zeigen, dass die Energielandschaft ein ganzes Ensemble an Konformationen zulassen kann, das durch die thermische Energie höchst dynamisch ist [9, 31, 32]. Diese Umwandlung zwischen verschiedenen Konformationen kann direkt mit der enzymatischen Funktion verbunden [8, 9, 33, 34] und, wie aktuelle Studien zeigen, für die Regulation von Enzymen von Bedeutung sein [31, 32].

In Ensemble-Experimenten sind Enzyme nicht synchronisiert, wodurch ihre zeitlich variierende Aktivität nicht zugänglich ist. Um das Wechseln eines Enzyms zwischen unterschiedlichen funktionellen Zuständen beobachten zu können, muss deshalb die Aktivität einzelner Enzyme beobachtet werden. Dazu wurde in mehreren Studien die Aktivität einzelner Enzyme mit Fluoreszenztechniken wie TIRF oder Konfokaler Mikroskopie beobachtet, indem ein Substrat verwendet wurde, dass als Produkt umgewandelt zu fluoreszieren beginnt. [10, 35, 36]. Diese zeigen, dass die untersuchten Enzyme verschiedene Reaktionsraten aufweisen, was im Extremfall zu An- und Auszeiten im Sekundenbereich führt. Erklärt wird dieses als „dynamische Unordnung“ bezeichnete Phänomen durch die Konversion der Enzyme in unterschiedlich aktive Zustände der Energielandschaft, wie in Abbildung 7 schematisch dargestellt ist.

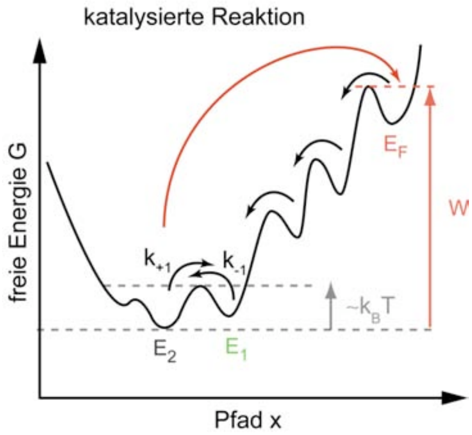

Abbildung 7: Schematische Darstellung der Energielandschaft eines Enzyms. Durch die thermische Energie ist ein Ensemble von enzymatisch aktiven ($E_1$) oder inaktiven ($E_2$) Zuständen erreichbar, was zur „dynamischen Unordnung“ führt. Durch eine externe Kraft wird die Energielandschaft verkippt, und das Enzym nimm durch die geleistete Arbeit W höherenergetische Zustände ein ($E_F$). Wirkt die Kraft nicht mehr, so kann das Enzym von dort ins ursprüngliche Gleichgewicht relaxieren.

Für eine weitergehende Untersuchung der Energielandschaft einzelner Enzyme biete sich auch hier die Kraft als externer Parameter an. Durch sie wird die Energielandschaft verkippt, wodurch sich das Gleichgewicht der Zustandsbesetzungen verschiebt. Bei gleichzeitiger Beobachtung der Enzymaktivität kann das mechanische Protokoll mit der Aktivität korreliert werden, wodurch sich verfolgen lässt, wann sich das Enzym wieder im aktiven Zustand befindet. Dieser Ansatz wurde in der vorliegenden Arbeit gewählt, um die Reaktion des Enzyms Candida Antarctica Lipase B (CalB) auf externe Kräfte zu untersuchen und Einblick in die Konformationsdynamik zu erlangen.

## Modellsystem Candida Antarctica Lipase B

Als Modellsystem wurde in dieser Arbeit die Lipase B des arktischen Hefepilzes Candida Antarctica gewählt. Sie zeichnet sich durch hohe Thermostabilität und Stabilität in organischen Lösungsmitteln aus, weshalb sie auch in der industriellen Katalyse Anwendung findet. Triacylglycerollipasen, zu denen CalB zählt, katalysieren die Hydrolyse von Carboxylesterbindungen in Alkohol und Carbonsäure (Abbildung 8). In der Natur erfüllen sie die Aufgabe, vor allem in Fettzellen gespeicherte Energie durch den Abbau von Triglyceriden nutzbar zu machen.

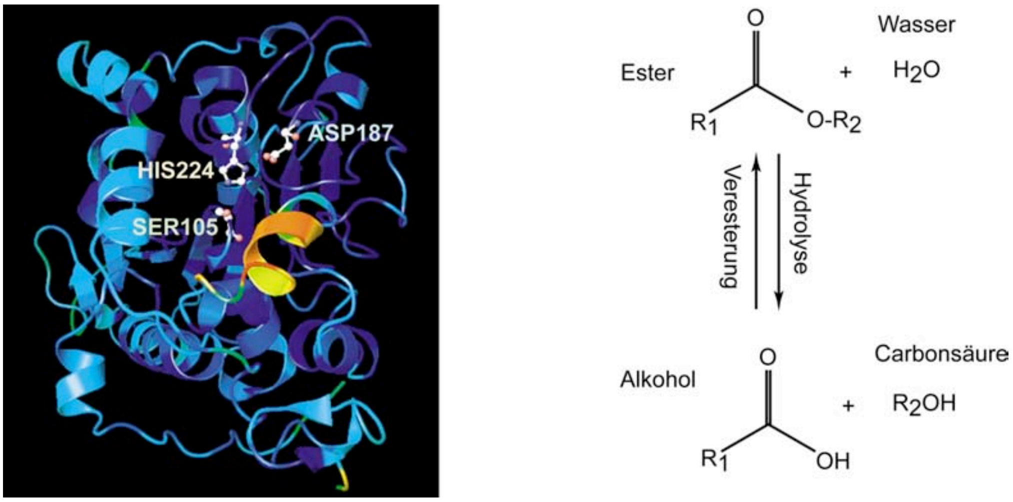

Abbildung 8: Struktur und Katalyse von CalB. Die Röntgenstruktur pdb 1LBS mit farblich codiertem b-Faktor zeigt die katalytische Triade bestehend aus Serin, Histidin und Aspartat. Vor dem katalytischen Zentrum befindet sich eine kleine $\alpha$-Helix, die durch eine hohe Mobilität auffällt (b-Faktor 95). CalB katalysiert je nach Gleichgewicht die Hydrolyse oder Veresterung.

Triacylglycerollipasen besitzen neben dem konservierten katalytischen Zentrum eine als „lid“ bezeichnete $\alpha$-Helix. Sie verschließt meist die Substratbindungstasche, wodurch in Lösung keine enzymatische Aktivität möglich ist. An einer Wasser-Lipid Grenzschicht öffnet sich die Bindungstasche durch eine Konformationsänderung des „lid“, die durch hydrophobe Wechselwirkung induziert wird und die Aktivierung verursacht [37]. In CalB ist diese Struktur jedoch so schwach ausgebildet, dass das Enzym auch in wässriger Lösung aktiv ist. Die Röntgenstruktur von CalB zeigt, dass der „lid“ einen hohen b-Faktor[3] besitzt, was auf eine hohe

---

[3] Der b-Faktor einer Kristallstruktur ist linear abhängig von der Standardabweichung der Atomposition und gilt als Maß für die Flexibilität von Strukturelementen [38]. Nach einer Faustregel sind Strukturen ab einem b-Faktor von 60 stark beweglich.

Mobilität und Fluktuation dieser Struktur schließen lässt [39]. Die Kristallstruktur von CalB mit farblich codiertem b-Faktor sowie die katalysierte Reaktion sind in Abbildung 8 dargestellt.
Aktivitätsmessungen an einzelnen immobilisierten Enzymen enthüllten, dass CalB An- und Auszeiten zeigt und dass die Aktivität nicht durch einen einfachen Poisson-Prozess beschreibbar ist [40, 41]. Der gestreckt-exponentielle Verlauf der Wahrscheinlichkeitsdichte von Auszeiten lässt vielmehr auf ein ganzes dynamisches Ensemble von Zuständen schließen, deren unterschiedliche Katalyseraten den multiexponentiellen Verlauf verursachen [42-44].

Für tiefere Einblicke in die Energielandschaft von CalB und die interne Dynamik wurden im Rahmen dieser Arbeit Techniken entwickelt, um auf immobilisierte CalB Enzyme Kräfte auszuüben und gleichzeitig ihre Aktivität zu beobachten. Dadurch wird das Enzym aus dem Gleichgewicht gebracht und besetzt Stellen in der Energielandschaft, die bei Raumtemperatur allein durch die thermische Energie nicht zugänglich sind. Durch den Einbau einer Antikörper-Peptid basierten Sollbruchstelle, die im nächsten Abschnitt vorgestellt wird, konnte in dem Kraftsprung-Experiment gewährleistet werden, dass das Enzym nicht voll entfaltet und nach dem Bindungsbruch relaxieren kann. Das simultane optische Signal erlaubt die gleichzeitige Beobachtung der Aktivität und gibt somit Auskunft, mit welchen Zeiten die Gleichgewichtsverteilung der Zustände wieder erreicht wird. Die gewonnenen Ergebnisse sowie eine Beschreibung der Experimente finden sich im Kapitel 5 und im Manuskript M1 im Anhang.

## Antikörper-Peptid basierte Sollbruchstellen für mechanische Manipulation

Für die mechanische Manipulation von Enzymen bedarf es molekularer Sollbruchstellen, die durch molekulare Erkennung eine mechanische Verbindung zwischen dem Enzym und z.B. der Spitze eines AFM-Cantilevers herstellen. Durch die vordefinierte Abrisskraft und Kontaktposition der Sollbruchstelle wird gewährleistet, dass das Enzym nicht komplett entfaltet wird und die Kraft immer in der gleichen Geometrie wirkt. Nach dem Abriss ist die Sollbruchstelle im Ausgangszustand und steht für einen weiteren Messzyklus zur Verfügung. Zwar eignet sich DNA für diesen Zweck hervorragend, da sie frei programmierbar ist und spezifisch bindet, aufgrund der Schwierigkeit, sie an definierten Stellen von Proteinen anzukoppeln, wurde jedoch in dieser Arbeit eine Antikörper-Peptid basierte Sollbruchstelle charakterisiert und für die mechanische Manipulation von CalB eingesetzt.

Die häufigste Form von Antikörpern sind die IgG Proteine (Abbildung 9). Sie bestehen aus zwei gleichen schweren Ketten und zwei gleichen leichten Ketten, die über Disulfide miteinander verbunden sind und so die typische Y-Form ergeben. Die leichte und die schwere Kette besitzen jeweils einen variablen Bereich $V_L$ und $V_H$, die für die spezifische Erkennung des Antigens verantwortlich sind. Dieses als scFv abgekürzte Fragment ist somit der kleinste spezifische Teil eines Antikörpers, der rekombinant z. B. im Bakterium *e.coli* hergestellt werden kann [45]. Ein großer Vorteil gegenüber direkt aus Tierserum gewonnenen Antikörpern ist, dass sie aus Gendatenbanken auswählbar sind und ihre Bindungseigenschaften durch Mutationen verändert werden können [46].

Besonders geeignet als Sollbruchstelle sind Antikörperfragmente, die eine kurze Peptidsequenz binden. Denn das Peptid kann als Fusionsprotein an Enzyme oder andere Proteine angehängt exprimiert werden. Zudem ist die Peptidsequenz mutierbar, um unterschiedliche Sollbruchkräfte zu erhalten. Die Bindungsaffinität der in dieser Arbeit verwendeten Antikörperfragment-Peptid-Wechselwirkung wurde in Referenz [47] bestimmt und verschiede Varianten von scFv Fragmenten wurden auf ihre mechanischen Eigenschaften mit AFM basierter Kraftspektroskopie untersucht [1].

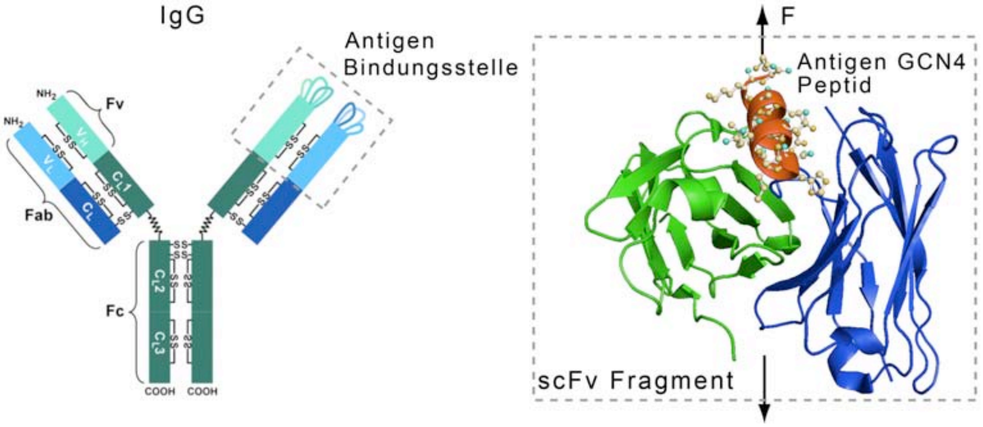
IgG
Antigen
Bindungsstelle
NH2
NH2
Fv
VH
VL
CL1
CL
Fab
Fc
CL2
CL3
COOH
COOH
F
Antigen GCN4
Peptid
scFv Fragment

Abbildung 9: Darstellung eines IgG Antikörpers und der Kristallstruktur eines scFv Fragmentes mit gebundenem Peptid. Die jeweils zwei identischen leichten und schweren Ketten sind durch Disulfidbindungen miteinander verbunden. Der variable Bereich der leichten Kette $V_L$ und der schweren Kette $V_H$ binden spezifisch das Antigen durch molekulare Erkennung. Sie können isoliert und rekombinant als scFv Fragment gewonnen werden. Die Kristallstruktur pdb 1P4B zeigt solch ein Fragment, welches das Peptid GCN4 bindet und in dieser Arbeit als Sollbruchstelle charakterisiert und eingesetzt wurde.

Für diese Arbeit wurde die Bindung dieser Antikörper-Peptid-Wechselwirkung kraftspektroskopisch weiter charakterisiert und für die mechanische Manipulation an CalB eingesetzt. Die Ergebnisse finden sich im Kapitel 5, in Publikation P2 und im Manuskript M1 im Anhang.

# 4. Beobachtung und 3D-Kontrolle einzelner Biomoleküle

Um einzelne Biomoleküle zu kontrollieren und zu beobachten, bedarf es einerseits präziser und sensibler Positionier- und Messmethoden, und andererseits der Spezifität der molekularen Erkennung. In diesem Kapitel werden die in dieser Arbeit weiterentwickelten experimentellen Einzelmolekültechniken kurz vorgestellt und eine Einführung zur molekularen Erkennung von DNA gegeben. Die darauf basierende „*Single-Molecule Cut-and-Paste*“-Technik erweitert die kraftspektroskopische vertikale Kontrolle von Biomolekülen um ihre gezielte laterale Positionierung.

## 4.1 Rasterkraft- und TIRF Mikroskopie

Die mechanische Kontrolle und Positionierung von einzelnen Biomolekülen in allen drei Raumrichtungen erfolgt mit einem Rasterkraftmikroskop, das auf der Erfindung des „Atomic Force Microscope“ von Binnig, Quate und Gerber basiert [48]. Das Prinzip des Rasterkraftmikroskops beruht auf einer sehr sensiblen Blattfeder, an deren Ende sich eine feine Spitze mit einem Krümmungsradius im 10 nm-Bereich befindet. Diese Spitze kann mit Piezos in allen drei Raumrichtungen mit Nanometer-Präzision bewegt werden, um Moleküle zu kontaktieren, Kräfte auf sie auszuüben oder sie zu positionieren. Die Kraft wird dabei über die Verbiegung der Blattfeder mit einem Lichtzeiger so genau bestimmt, dass molekulare Wechselwirkungskräfte im pN-Bereich detektierbar sind. Mit den aufgezeichneten Kraft-Abstandskurven können Wechselwirkungskräfte bestimmt, die Position von Energiebarrieren in charakteristischen Entfaltungsmustern vermessen und sogar das Binden von Liganden an Proteine beobachtet werden.

Die Kombination mit TIRF-Mikroskopie (Total Internal Reflection Fluorescence) ermöglicht die gleichzeitige Beobachtung von Einzelmolekülfluoreszenz. Der Anregungslaser wird dabei über das Objektiv so eingekoppelt, dass er vom Mikroskopdeckglas an der Glas-Wasser-Grenzfläche total reflektiert wird. Dadurch entsteht im Probenvolumen ein exponentiell abklingendes Anregungsfeld mit einer Eindringtiefe im 100 nm-Bereich. Die Unterdrückung der Hintergrundfluoreszenz des restlichen Volumens erlaubt die Beobachtung von Einzelmolekülfluoreszenz auf der Oberfläche. So wurde in dieser Arbeit die Assemblierung von Nanostrukturen und die Aktivität des Enzyms CalB beobachtet. Die Konstruktion und Weiterentwicklung dieses kombinierten AFM-TIRF-Hybrids ist zwar Teil dieser Arbeit, aufgrund des technischen Charakters ist jedoch die ausführlichere Beschreibung im Anhang, in der Publikationen P3 und im Manuskript M2 zu finden.

## 4.2 Nanoassemblierung durch molekulare Erkennung

### DNA als programmierbarer Baustein

Die Desoxyribonucleinsäure (DNA) ist Träger der genetischen Erbinformation und somit eines der wichtigsten Moleküle, auf dem das Leben basiert. Es ist deshalb nicht verwunderlich, dass sich die DNA durch besondere Eigenschaften wie Robustheit, Spezifität und Einfachheit auszeichnet. Aufgrund der sequenzspezifischen molekularen Erkennung wurde DNA in der Nano-Biotechnologie als Baustein entdeckt und wird auch in dieser Arbeit für die gezielte Nanoassemblierung verwendet.

Ein DNA Einzelstrang setzt sich aus den vier verschiedenen Basen Adenin (A), Thymin (T), Guanin (G) und Cytosin (C) zusammen, die über ein Zucker-Phosphat-Rückgrat miteinander kovalent verbunden sind. Watson und Crick konnten durch Röntgenstrukturanalyse zeigen, dass sich jeweils zwei DNA-Stränge zu einer Doppelhelix zusammenlagern [49], wobei sich jeweils zwischen den gegenüberliegenden Basen A-T und G-C Wasserstoffbrücken ausbilden und so zur sequenzspezifischen Stabilisierung führen[4] . Die beiden Stränge sind dabei antiparallel zueinander ausgerichtet, sodass jeweils das 5'-Ende dem 3'-Ende gegenüberliegt und umgekehrt (siehe Abbildung 10).

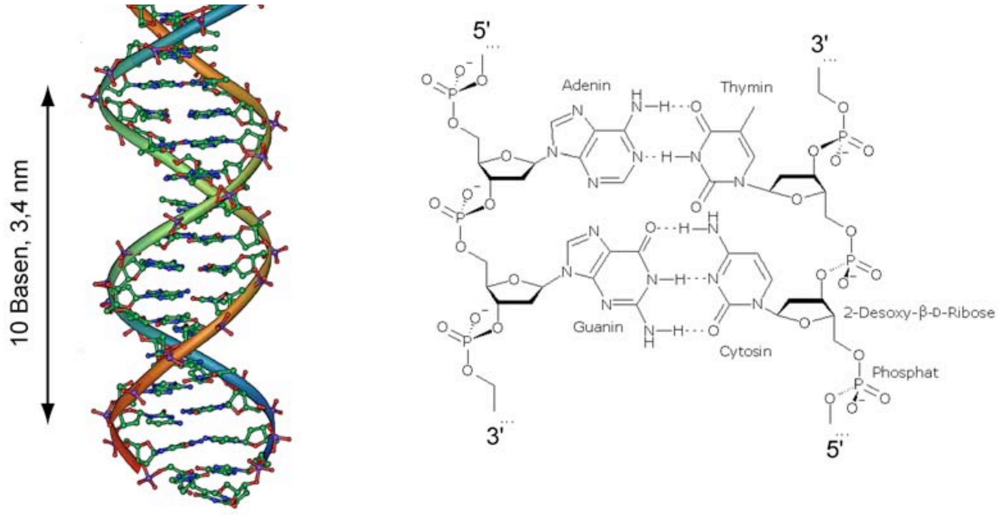

Abbildung 10: Struktur von DNA. Zwei komplementäre DNA-Stränge lagern sich über die spezifischen Basenpaarungen zu einer Doppelhelix zusammen. Dabei bilden jeweils Adenin und Thymin zwei Wasserstoffbrücken miteinander aus und Guanin und Cytosin jeweils drei. Abbildung nach: http://de.wikipedia.org/wiki/Desoxyribonukleinsäure

Diese Fähigkeit komplementärer DNA-Stränge miteinander zu hybridisieren, wird für die spezifische Anbindung von Bausteinen oder zur Selbstassemblierung komplexer Strukturen aus DNA ausgenützt. Wichtig für die schnelle Entwicklung auf diesem Gebiet sind industriell verwendete biotechnologische Methoden, mit denen bis zu 200 Basen lange DNA-Stränge mit beliebiger Sequenz künstlich synthetisiert werden können. Auch interne Modifikationen wie Farbstoffmarkierungen oder spezifische Bindungsstellen können so per Katalog bestellt werden.

---

[4] Misspaarungen destabilisieren die Doppelhelix zwar, führen aber, ja nach ihrer Anzahl, nicht unbedingt zur Dissoziation.

Die Vielseitigkeit auf dem Gebiet der DNA-basierten Selbstassemblierung zeigt die Erzeugung von Würfeln [50], Oktaedern [51], Röhren [52] oder zweidimensionalen Gittern [53]. Dabei hybridisieren DNA-Stücke mit speziell programmierter Sequenz so, dass überlappende, „klebrige“ Enden entstehen, an die wiederum weitere Stränge binden können. In einem darauf aufbauenden und mit *DNA-Origami* neu benannten Gebiet wird ein langer DNA-Strang durch viele kleine DNA-Stränge in eine bestimmte Form gefaltet und stabilisiert. Die DNA-Sequenzen für bestimmte Strukturen wie Smilies oder Kontinente können mit Computerprogrammen vorher bestimmt und dann über Selbstassemblierung erzeugt werden [54].

DNA kann aber auch für die Selbstorganisation von anderen Bausteinen, wie beispielsweise Nanopartikeln, verwendet werden [55]. Die Bausteine werden mit den entsprechenden DNA-Strängen funktionalisiert, und je nach Anbindungsdichte können sich Dimeren oder ganze Kristallstrukturen bilden [56-58].

## Hierarchische Trennkräfte von DNA für gezielte Nanoassemblierung

Die im Rahmen dieser Arbeit entwickelte Strategie zur AFM-basierten Assemblierung einzelner funktioneller Einheiten, auch *Single Molecule Cut-and-Paste* (SMCP) genannt, kombiniert die molekulare Erkennung von DNA mit der Präzision des AFM. Die spezifische Hybridisierung von DNA dient dabei zur Verankerung, zum Aufgreifen und zum Absetzen der Transport-DNA. Entscheidend für den Transport sind dabei die verschiedenen Trennkräfte, die durch unterschiedliche Belastungsgeometrien und die Sequenzlänge der DNA bestimmt werden.

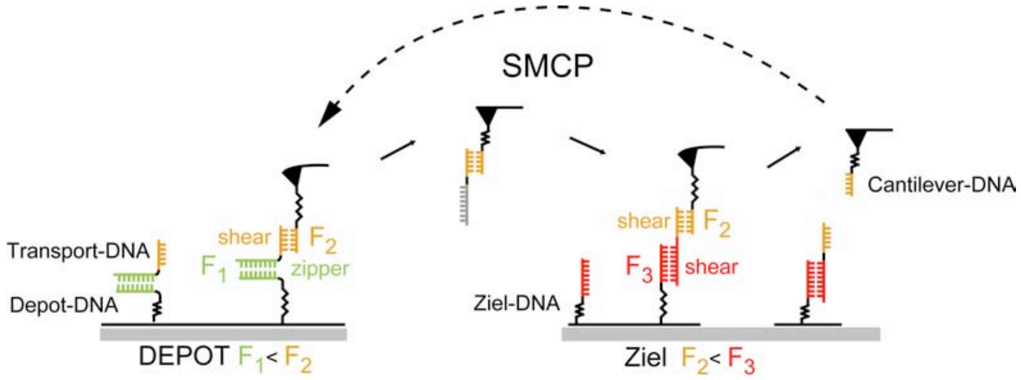

Abbildung 11: Hierarchische Trennkräfte von DNA für SMCP. Im Depot ist die 30 Basen lange Depot-DNA über PEG kovalent an der Oberfläche befestigt, um mit der Ankersequenz der Transport-DNA in der „zipper“-Geometrie zu hybridisieren (Trennkraftkraft $F_1$). Die so gespeicherte Transport-DNA kann mit ihrer Transportsequenz an die 20 Basen lange Cantilever-DNA in der „shear“-Geometrie, die höhere Trennkräfte aufweist ($F_2$), hybridisieren. Nach dem Zurückziehen des Cantilevers wird die Transport-DNA an eine definierte Stelle im Ziel transportiert, wo sie über die 30 Basen lange Ankersequenz mit der Depot-DNA hybridisiert – diesmal jedoch ebenfalls in der „shear“-Geometrie und mit der größten Trennkraft $F_3$. Dadurch bleibt sie beim Zurückziehen das Cantilevers im Ziel verankert.

Wie in Abbildung 11 schematisch dargestellt, sind in einem Depotbereich 30 Basen lange DNA-Oligomere kovalent über einen Polyethylenglycol-Spacer (PEG) an der Oberfläche verankert. Sie hybridisieren an die 30 Basen lange Ankersequenz der Transport-DNA und dienen so ihrer

Speicherung. Die Transport-DNA besitzt zudem einen überlappenden Teil mit den 20 Basen der Transportsequenz, die komplementär zur ebenfalls kovalent angebundenen Cantilever-DNA ist. Wird die Spitze nun in Kontakt mit dem Depotbereich gebracht, hybridisiert der Teil der Transportsequenz mit der Cantilever-DNA in der „shear"-Geometrie [1, 59]. In dieser Geometrie wirkt die Kraft auf die gegenüberliegenden Enden des Duplexes. Obwohl der Duplex mit der Ankersequenz mehr Basen besitzt, ist er unter der aufgebauten Kraft beim Zurückziehen des Cantilevers instabiler als der Duplex mit der Cantilever-DNA, da er in der sogenannten „unzipper"-Geometrie belastet wird [60-62]. Der anschauliche Grund liegt darin, dass beim „unzippen" der DNA die Kraft am gleichen Ende des Duplexes angreift und somit ein Basenpaar nach dem anderen getrennt wird. Die Arbeit zum Trennen wird deshalb über eine wesentlich längere Strecke als bei der „shear"-Geometrie verrichtet, weshalb die resultierende Kraft ein Plateau bei ca. 17 pN[5] zeigt. Die Transport-DNA bleibt so mit fast 100 prozentiger Wahrscheinlichkeit an der Cantilever-DNA verankert und kann zur vorbestimmten Position in der Zielregion transportiert werden[6]. Die Ziel-DNA ist, wie im Depotbereich, kovalent an die Oberfläche angebunden und besitzt die gleiche Ankersequenz, jedoch ist sie mit dem anderen Ende angebunden. Wird der Transportstrang in Kontakt gebracht, hybridisiert die freie Ankersequenz mit den 30 Basen der Ziel-DNA, diesmal jedoch aufgrund der anderen Orientierung in der „shear"-Geometrie. Beim Zurückziehen des Cantilevers ist nun der 10 Basen längere Anker-Duplex mit der Ziel-DNA stärker, sodass der Transport-Duplex mit wesentlich höherer Wahrscheinlichkeit reißt, die Transport-DNA im Ziel verankert bleibt und die Cantilever-DNA wieder frei für den nächsten Zyklus ist.

Auf diese Weise wurden verschiedenste Strukturen aus einzelnen DNA-Strängen erzeugt, wobei als funktionelle Einheiten Farbstoffe oder spezifische Bindungsstellen an die Transport-DNA gebunden wurden. Die gleichzeitige optische Beobachtung der so erzeugten Strukturen mit TIRF-Mikroskopie lieferte zusätzlich eine optische Kontrolle und weitere Untersuchungsmöglichkeiten der erzeugten Strukturen. Die Charakterisierung und die Ergebnisse finden sich im Kapitel 5 und in den Publikationen P4-P6.

---

[5] Die Kräfte für A-T liegen wegen der zwei ausgebildeten Wasserstoffbrücken etwas niedriger bei ca. 10 pN, die Kräfte für G-C dementsprechend etwas höher bei ca. 20 pN

[6] Aufgrund des statistischen Prozesses muss prinzipiell mit Wahrscheinlichkeiten gerechnet werden. Die Dissoziationsrate der 20 Basen langen DNA ist laut Referenz [1] $k_0=6\cdot10^{-13}$ 1/s und die Potentialweite $\Delta x=2{,}7$ nm. Die Rate unter dem 17 pN-Kraftplateau ist nach der Gleichung aus Kapitel 3.1 $k(17pN)=4.4\cdot10^{-8}$ $s^{-1}$, was viele Größenordungen von der ziehgeschwindigkeitsbestimmten Dissoziationsrate der zipper-Geometrie von ca. 33 $s^{-1}$ entfernt ist.

# 5. Ergebnisse

Nachdem in den vorigen Kapiteln eine Einführung in die biologischen und biophysikalischen Fragestellungen sowie in die dafür verwendeten und weiterentwickelten Techniken gegeben wurde, werden nun die Ergebnisse dieser Arbeit zusammengefasst.

## 5.1 Der molekulare Kraftsensor Titinkinase

Im einführenden Kapitel 3 wurde dargestellt, dass sich die Titinkinase im Titin an idealer Position befindet, um Kräfte zu detektieren. Jedoch ist sie durch einen dualen Mechanismus autoinhibiert: Die $\alpha$-Helix $\alpha$R2 blockiert die ATP Bindungstasche und TYR170 blockiert in nicht-phosphoryliertem Zustand die katalytische Base ASP127. Um die Funktion und den molekularen Mechanismus der Titinkinase zu erforschen, wurden einzelne Titinkinasen mit ihren natürlichen Nachbardomänen, den Immunoglobulin (Ig)- und Fibronectin-Domänen (Fn), kraftspektroskopisch untersucht. Das untersuchte Proteinkonstrukt stammt aus dem Labor von Prof. Mathias Gautel am King's College London.

### Kraftinduzierte Entfaltungscharakteristik einzelner Titinkinase-Proteinkonstrukte

Im Zyklus eines kraftspektroskopischen Experimentes wird die Spitze eines AFM-Cantilevers in Kontakt mit dem Protein gebracht, das vorher auf einer Goldoberfläche unspezifisch angebunden wurde. Beim Zurückziehen des Cantilevers wird das Protein gedehnt, wobei als Messsignal Kraft-Abstandskurven aufgezeichnet werden (Abbildung 12). Am Anfang der Kraft-Abstandskurve wird das Proteinkonstrukt gestreckt, bis die schwächsten Wechselwirkungen brechen und Kraftpeaks bei ca. 50 pN verursachen (orange). Im weiteren Verlauf ist das charakteristische Sägezahnmuster erkennbar (blau), das fünf gleichmäßige Konturlängeninkremente $\Delta L$ aufweist und durch das Entfalten der fünf Ig/Fn-Domänen verursacht wird, die die Titinkinase umrahmen. Somit wird der in orange eingefärbte Teil am Anfang der Kraftkurve durch das Entfalten der Titinkinase verursacht. Zwar wird das Proteinkonstrukt an willkürlichen Stellen kontaktiert, sodass in vielen Messkurven nicht das komplette Entfaltungsprofil erkennbar ist. Der Fingerabdruck der Ig/Fn-Domänen erlaubt jedoch die Selektion der Kurven, in denen die Entfaltung der kompletten Titinkinase enthalten ist. In all diesen Kraftkurven entfaltet die Titinkinase vor den strukturellen Ig/Fn-Domänen, was Voraussetzung für den molekularen Kraftsensor ist. Im Gegensatz zu den unabhängig entfaltenden Ig/Fn-Domänen, ist die Reihenfolge der Entfaltungsereignisse innerhalb der Titinkinase trotz vergleichbarer Kräfte immer gleich und somit topologisch vorgegeben.

### Mechanisch aktivierte ATP-Bindung

Das komplette Entfaltungsmuster der Titinkinase ist durch Überlagerung von 66 Kraft-Abstandskurven in Abbildung 13 dargestellt. Es zeigt die insgesamt fünf Energiebarrieren, die in jeder Kurve mit der gleichen Reihenfolge auftreten. In Anwesenheit von 2 mM ATP weist jedoch ein bestimmter Anteil an Kraftkurven eine zusätzliche Energiebarriere auf, die ohne ATP nicht beobachtet wird. Da die native Konformation der Titinkinase kein ATP bindet, ist dies ein erster

Hinweis, dass ATP mechanisch induziert in die geöffnete Titinkinase bindet und durch die Wechselwirkung mit der Bindungstasche eine zusätzliche Energiebarriere verursacht.

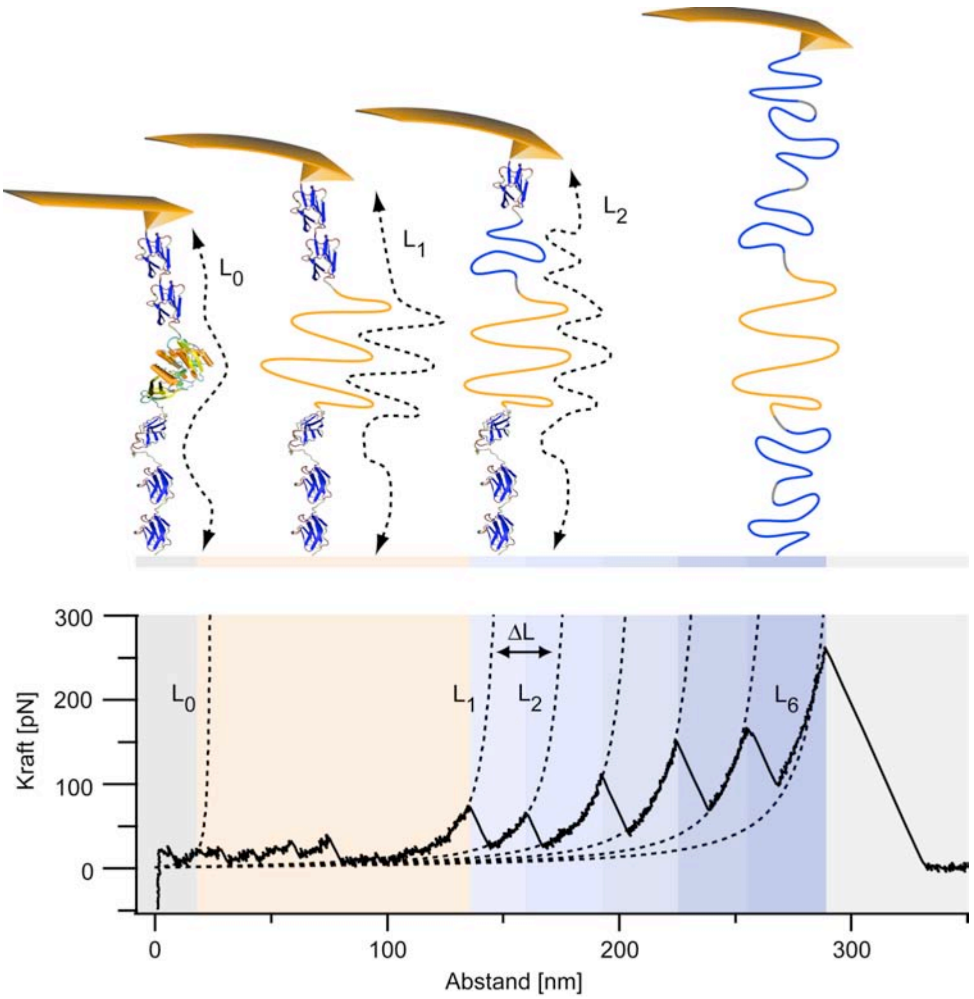

Abbildung 12: Kraftspektroskopisches Experiment mit dem Titinkinase-Proteinkonstrukt. Am Anfang der Kraft-Abstandskurve wird das Protein mit freier Konturlänge $L_0$ gedehnt, bis die Titinkinase bei Kräften unter 50 pN sequenziell entfaltet (orange) und insgesamt eine freie Konturlänge $L_1$-$L_0$ von 121 ±2 nm aufweist. Danach entfalten die fünf umliegenden Ig/Fn-Domänen mit einem mittleren Konturlängeninkrement ΔL von 30.5±0.6 nm (blau).

Der molekulare Mechanismus der ATP-Bindung kann durch den Zugang zur Bindungskinetik geklärt werden. Falls die Bindungstasche mechanisch geöffnet wird, sollte die relative Häufigkeit des ATP-Bindens einer Nichtgleichgewichtskinetik folgen und von der Zeit abhängen, in der die Bindungstasche geöffnet, aber noch nicht entfaltet ist. Wird die Hin- und Rückrate mit $k_{hin}$ bzw. $k_{rück}$ und die ATP-Konzentration mit [ATP] bezeichnet, dann folgt die zeitabhängige Wahrscheinlichkeit der ATP-Bindung $P_{ATP}(t)$ nach Öffnen der Bindungstasche der Gleichung:

$$\frac{dP_{ATP}(t)}{dt} = k_{on}[ATP] - k_{off}P_{ATP}(t) \qquad \text{mit der Lösung:} \qquad P_{ATP}(t) = \frac{k_{on}}{k_{on} + k_{off}}\left(1 - e^{-(k_{on}+k_{off})\cdot t}\right)$$

Ist jedoch ATP von Anfang an und nicht mechanisch induziert gebunden, sollte die relative Häufigkeit der Bindung nicht von der Öffnungszeit der Bindungstasche abhängen. Da die

Konformation der Titinkinase durch den Abstand des Cantilevers von der Oberfläche kontrolliert wird, kann diese Öffnungszeit über die Ziehgeschwindigkeit reguliert werden.

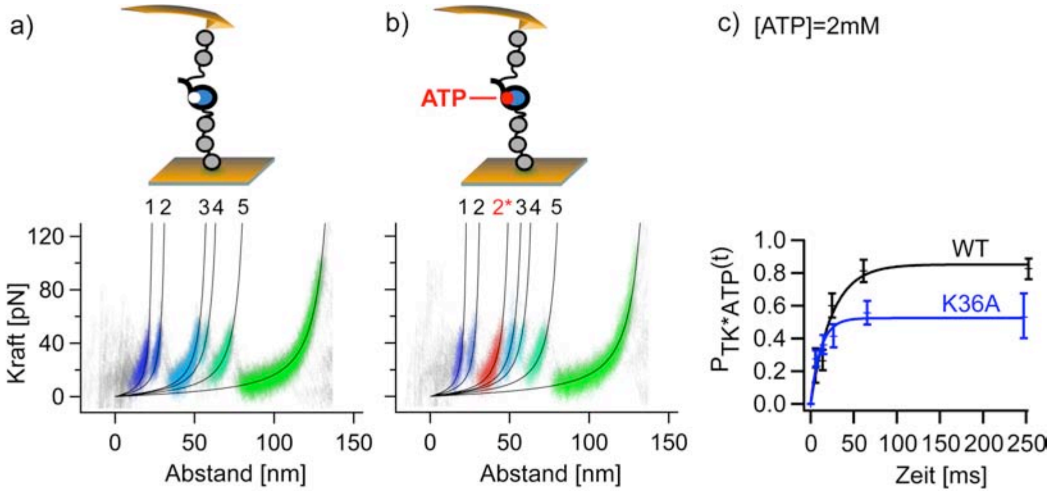

Abbildung 13: Mechanisch aktivierte ATP-Bindung. In Anwesenheit von ATP sind in der Überlagerung der Kraft-Abstandskurven zwei Entfaltungsmuster erkennbar. In a) (66 Kurven) werden die gleichen 5 Energiebarrieren wie in Abwesenheit von ATP beobachtet. Jedoch zeigt ein bestimmter Teil an Kraftkurven in b) eine zusätzliche Energiebarriere (44 Kurven), die durch das Binden von ATP und die Stabilisierung der Bindungstasche verursacht wird. c) zeigt die Bindungskinetik von ATP an die Wildtyp Titinkinase (WT) und an die Mutante K36A. Die relative Häufigkeit der Bindung hängt stark von der Öffnungszeit der Bindungstasche ab, die durch die Entfaltungsgeschwindigkeit kontrolliert wird. Für die Kinetik wurden über 1700 einzelne Messkurven verwendet, und die Fehler geben das 95% Konfidenzintervall der jeweiligen Stichprobe an.

Tatsächlich wurde eine starke Abhängigkeit der ATP-Bindung von der Öffnungszeit der Bindungstasche[7] beobachtet, die dem Verlauf der Nichtgleichgewichtskinetik folgt. Dieses Ergebnis zeigt, dass dieser erste und notwendige Schritt zur katalytischen Aktivität der Titinkinase durch eine kraftinduzierte Konformationsänderung erfolgt. Darüber hinaus konnten durch Fitten der Daten die Hin- und Rückraten der ATP-Bindung, und daraus die Gleichgewichtskonstante bestimmt werden. Experimente mit einer Mutante, bei der Lysin-36 (LYS36) zu Alanin mutiert wurde, zeigen eine mehr als sechsfach höhere Rückrate der ATP-Bindung und eine Dissoziationskonstante im millimolaren Bereich (siehe Abbildung 13). Das konservierte LYS36 ist somit auch bei der Titinkinase eine für die ATP Bindung essenzielle Aminosäure.

---

[7] Die Öffnungszeit der Bindungstasche wurde aus der Ziehgeschwindigkeit und der Längenänderung bestimmt, in der die Bindungstasche geöffnet, aber noch nicht zerstört ist. Molekulardynamik-Simulationen zeigen, dass diese Längenänderung etwa 18 nm entspricht.

## Lokalisierung des aktiven Zustandes durch mechanisches „pump-and-probe“

Die Bindungskinetik von ATP zeigt, dass die Bindungstasche der Titinkinase mechanisch geöffnet wird, und dass LYS36 eine wichtige Aminosäure für das Binden von ATP ist. Aber nach welcher der Energiebarrieren wird die aktive Konformation erreicht? Um dies herauszufinden wurde ein kraftspektroskopisches Messprotokoll entwickelt, das sowohl die Nichtgleichgewichtskinetik als auch die Konformationskontrolle der Titinkinase durch den AFM-Cantilever ausnützt. Wegen der Analogie der Herangehensweise zu optischen „pump-and-probe“-Experimenten wird die entsprechende Nomenklatur verwendet: ein bestimmter Zustand der Titinkinase wird mechanisch für die Zeit $\Delta t$ präpariert, und die daraus folgende Reaktion durch die ATP-Bindung wird mechanisch anhand der Barriere 2* ausgelesen.

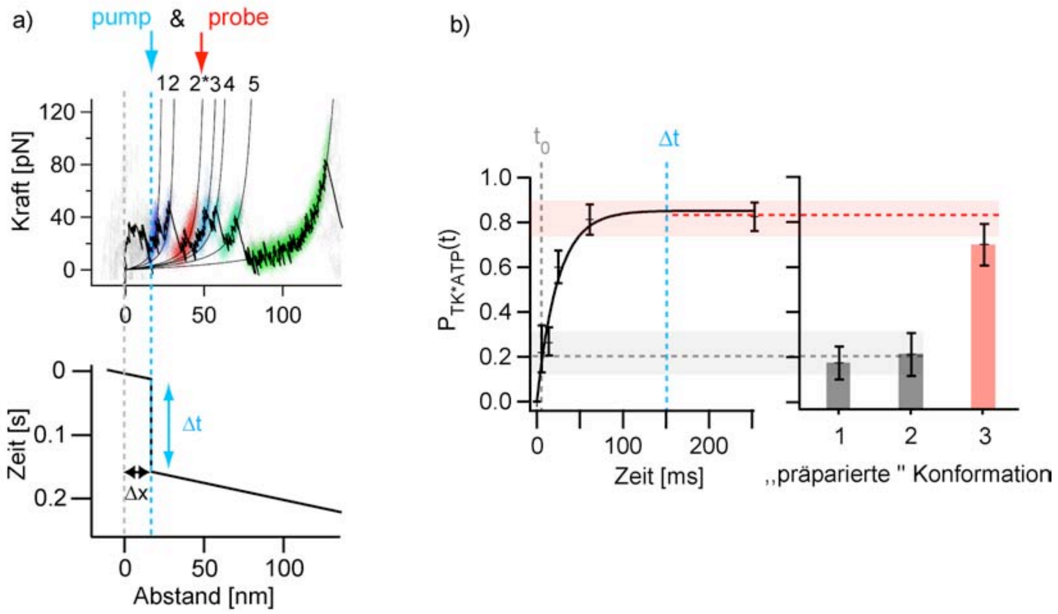

Abbildung 14: Mechanisches „pump-and-probe“. a) Die Titinkinase wird bis vor eine bestimmte Energiebarriere entfaltet, wo sie für die Zeit $\Delta t$ die Möglichkeit hat ATP zu binden. Bei weiterer Entfaltung wird mit Barriere 2* ausgelesen, ob ATP gebunden hat. Die präparierte Konformation kann durch Vorgabe von $\Delta x$ variiert werden. b) Anhand der Nichtgleichgewichtskinetik der ATP-Bindung können die verschiedenen Konformationen auf Aktivität untersucht werden. Konformation 1 (vor der 1. Barriere) und 2 (zwischen der 1. und 2. Barriere) weisen lediglich die relative Grundhäufigkeit der ATP-Bindung auf, die durch die endliche Ziehgeschwindigkeit, und somit durch die Grundöffnungszeit $t_0$, verursacht wird. Konformation 3 (nach der 2. Barriere) zeigt im Rahmen des Fehlers die dem Zeitpuls $\Delta t$ entsprechende relative Häufigkeit der ATP-Bindung. Die ATP-Bindungstasche wird somit nach der 2. Energiebarriere geöffnet.

In Abbildung 14 ist dargestellt, wie bei diesem mechanischen „pump-and-probe“-Experiment die Titinkinase bis vor eine bestimmte Energiebarriere entfaltet und die entsprechende Konformation für eine bestimmte Zeit $\Delta t$ präpariert wird. Während dieser Zeit hat das ATP die Möglichkeit zu Binden. Danach wird die Titinkinase weiter entfaltet, um mit der Energiebarriere 2* auszulesen, ob ATP gebunden hat oder nicht. Falls der Zeitpuls $\Delta t$ in der inaktiven Konformation gesetzt wurde, wird aufgrund der endlichen Ziehgeschwindigkeit von 2 µm/s nur eine geringe relative Häufigkeit für die ATP-Bindung erwartet. Denn 2 µm/s entsprechen einer Grund-Öffnungszeit $t_0$ von 10 ms, was in einer relativen Grundhäufigkeit von ca. 0.2 resultiert. Wird jedoch die aktive Konformation präpariert, so sollte die relative Häufigkeit stark zunehmen und entsprechend dem Zeitpuls von 150 ms einen Wert von ca. 0.8 erreichen. Die Variation des präparierten Zustandes erfolgt durch die Position $\Delta x$, wodurch jede Konformation vor der Barriere 2* auf Aktivität überprüft werden kann.

In Abbildung 14 b) sind die Ergebnisse dieser Experimente dargestellt. Wird vor Barriere 1 und zwischen Barriere 1 und 2 präpariert, so beträgt die relative Häufigkeit der ATP-Bindung wegen der Grundöffnungszeit $t_0$ 0.19 ± 0.07 bzw. 0.2 ± 0.1. Diese Konformationen sind somit nicht aktiv, und die Bindungstasche der Titinkinase ist verschlossen. Wird jedoch zwischen Position 2 und 3 präpariert, so erhöht sich die relative Häufigkeit der ATP-Bindung drastisch auf 0.7 ± 0.1. Dieser Wert stimmt im Rahmen des Fehlers mit dem erwarteten Wert bei einem Zeitpuls von 150 ms überein. Somit wird die Bindungstasche der Titinkinase erst nach der zweiten Energiebarriere geöffnet.

## Strukturelle Untersuchung des molekularen Aktivierungsmechanismus

Um die verschiedenen Entfaltungs- und Aktivitätszustände strukturell zuordnen zu können, müssen die während der Entfaltung überwundenen Energiebarrieren mit hoher Präzision vermessen werden. Dazu wurden die Kraft-Abstandskurven mit der in dieser Arbeit entwickelten Methode in Histogramme transformiert, die direkt die Positionen der Energiebarrieren entlang der Konturlänge zeigen (siehe Abbildung 15, Anhang und Publikation P3). Mit Berücksichtigung des Proteindurchmessers [22], der aus der Kristallstruktur bekannt ist, konnte so die Anzahl gefalteter Aminosäuren der Titinkinase und der Ig/Fn-Domänen bestimmt werden. Für die Titinkinase, die einen Durchmesser von 5.5 nm besitzt, ergibt sich bei einer Aminosäurenlänge von 0.365 nm die experimentelle Anzahl von Aminosäuren zu (5.5 nm + (121± 2) nm) / 0.365 nm = 346 ± 6. Dieses Ergebnis stimmt mit der tatsächlichen Anzahl von 344 Aminosäuren gut überein.

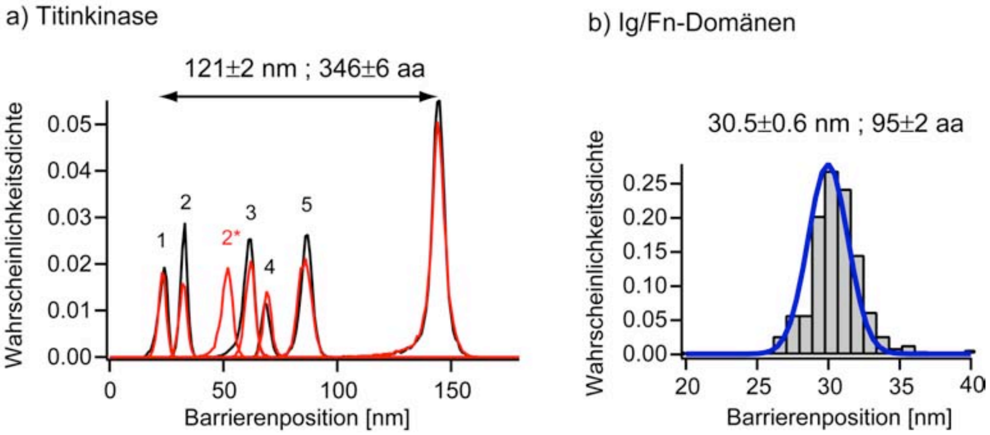

Abbildung 15: Histogramme der Barrierenpositionen, gemessen als freie Konturlänge. a) Die Konturlängeninkremente der Titinkinase betragen ohne ATP (schwarz) 9.1, 28.6, 7.3, 18.0 und 57.9 nm, und mit ATP (rot) 9.1, 19.4, 10.1, 7.5, 16.4 und 58.3 nm, wobei der relative Fehler 2% beträgt. Die experimentell bestimmte Anzahl an gefalteten Aminosäuren beträgt 346±6 , was mit dem tatsächlichen Wert von 344 gut übereinstimmt. b) Das mittlere Konturlängeninkrement der Ig/Fn-Domänen beträgt 30.5±0.6 nm, was 95 ±2 Aminosäuren entspricht und ebenfalls mit dem tatsächlichen Wert von 96 gut übereinstimmt. Für die Transformation wurde das QM-WLC-Modell mit einer Persistenzlänge von 0,8 nm verwendet. Die Konturlängenhistogramme in a) wurden durch Transformationen von 66 Kraftkurven (ATP) bzw. 44 Kraftkurven (kein ATP) erzeugt, und das Histogram in b) durch Fitten von 250 Ig/Fn-Domänen.

Die gleiche Rechnung führt bei einem mittleren Durchmesser der Ig/Fn-Domänen von 4.3 nm zu 95 ± 2 Aminosäuren, was mit dem Mittelwert von 96 gefalteten Aminosäuren ebenfalls gut übereinstimmt. Somit wurde gezeigt, dass die Energiebarrieren entlang der freien Konturlänge mit einer Genauigkeit bis auf 2% bestimmt werden können, was, je nach betrachteter Länge, in der Größenordnung einiger Aminosäuren liegt.

Für die strukturelle Untersuchung der Titinkinase wurden am Max-Planck Institut Göttingen unter der Leitung von Helmut Grubmüller Molekulardynamik-Simulationen durchgeführt. Durch Entfalten der Titinkinase mit einer virtuellen Feder wurden dabei die Bewegungen aller Atome von der Kristallstruktur ausgehend simuliert. Die auftretenden Energiebarrieren, die ebenfalls in Kraft-Abstandskurven sichtbar werden, konnten erfolgreich mit den experimentellen Barrierepositionen korreliert werden. Dadurch sind die strukturellen Veränderungen während der Entfaltung und die strukturellen Ursachen der Energiebarrieren mit atomarer Auflösung bekannt. Auch die zusätzliche Energiebarriere 2*, die beim Binden von ATP beobachtet wird, konnte erfolgreich simuliert werden. Die Hauptwechselwirkungen liegen dabei zwischen ATP und LYS36 (wie auch im Experiment gezeigt wurde) und zwischen ATP und MET34.

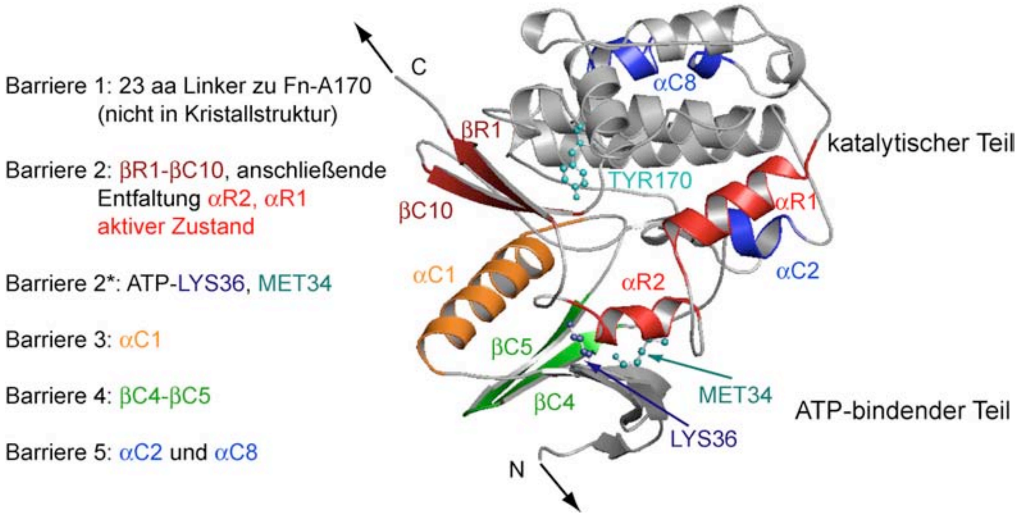

Abbildung 16: Strukturelle Zuordnung der experimentell beobachteten Energiebarrieren nach MD-Simulationen (PDB 1TKI). Bei Barriere 1 wird der 23 Aminosäuren lange Linker zur Domäne Fn-A170 entfaltet (nicht in Kristallstruktur vorhanden). Barriere 2 wird durch βR1-βC10 verursacht – danach wird αR2 und αR1 entfaltet, wodurch der aktive Zustand erreicht wird. Die ATP-Barriere 2* entsteht vor allem durch Wechselwirkung mit LYS36 und MET34, und Barriere 3 wird durch die Helix αC1 verursacht. Barriere 4 ist βC4-βC5 zugewiesen und Barriere 5 entsteht letztlich durch den kombinierten Effekt von αC2 und αC8

Auf diese Weise konnte der komplette experimentell beobachtete Entfaltungsweg der Titinkinase strukturell rekonstruiert werden. Details dazu finden sich in der Publikation P1, hier soll nur eine Zusammenfassung gegeben werden: Bis Barriere 1 wird das komplett gefaltete Proteinkonstrukt gedehnt, wobei die addierten Durchmesser aller Domänen eine Länge von 26.8 nm beitragen. Bei Barriere 1 wird der 23 Aminosäuren lange N-terminale Linker zur Domäne Fn-A170 entfaltet. Bei Barriere 2 wird der regulatorische Teil, der die Bindungstasche verschließt, entfaltet. Dabei bricht zuerst das β-Faltblatt βR1-βC10, woraufhin die α-Helices αR2 und αR1 entfalten und die Bindungstasche freigeben. Bindet ATP, so verursacht seine Wechselwirkung vor allem mit LYS36 und MET34 die Barriere 2*. Barriere 3 und 4 werden von der Entfaltung von αC1 und βC4-βC5 verursacht, und αC2 und αC8 resultieren gemeinsam in Barriere 5. Die Aminosäureketten der entfalteten Strukturelemente werden bei weiterem Strecken gedehnt und weisen ein gesamtes Konturlängeninkrement von 121± 2nm auf, was, wie bereits gezeigt wurde, 346 ± 6 Aminosäuren entspricht und mit der tatsächliche Anzahl von 344 gut übereinstimmt.

## Titinkinase-Mechanismus im physiologischen Zusammenhang

Die Entschlüsselung des molekularen Mechanismus der Titinkinase führt zu dem wichtigsten Ergebnis, dass die Bindungstasche durch eine kraftinduzierte Konformationsänderung geöffnet wird und ATP nur an diesen Zustand bindet. Wie in Publikation P1 ausführlicher dargestellt, konnten die Kollaborationspartner dieses Projektes von der Gruppe um Mathias Gautel am King's College London mit Phosphorylierungsversuchen zeigen, dass durch Binden von ATP an trunkierte Kinasen mit offener Bindungstasche das inhibierende TYR170 autophosphoryliert. Überträgt man diese Ergebnisse auf die mechanisch geöffnete Bindungstasche der natürlichen Titinkinase, so bedeutet dies, dass das mechanisch induzierte Binden von ATP zur Autophosphorylierung von TYR170 führt und das Enzym so komplett aktiviert ist. Die dadurch initiierte Signalkaskade, die im Kapitel 3 zusammengefasst wurde, steuert Proteinumsatz und Muskel-Genexpression.

Die Position der Titinkinase im Netzwerk der M-Bande sorgt dafür, dass nur an den Stellen Kräfte wirken und zur Aktivierung führen, an denen Verzerrungen der M-Banden auftreten. Diese Verzerrungen werden auch in elektronenmikroskopischen Aufnahmen beobachtet und treten bei Ungleichgewichten der Krafterzeugung durch die Myosinfilamente auf. Die Aktivierungskräfte der Titinkinase bei 37 °C betragen lediglich 20-30 pN (siehe Supplement Publikation P1), was einem Ungleichgewicht von ca. 6 Myosinmotoren oder 3% der Motoren pro Filament entspricht [63, 64] und somit im physiologischen Bereich liegt [65]. Auch die Längenänderung bei Aktivierung von 9.1 nm zwischen Barriere 1 und Barriere 2 liegen im physiologischen Bereich von 10 nm, der mit Röntgenstreuung am kontrahierenden Sarkomer beobachtet wurde [66-68]. Die Ig/Fn-Domänen, von denen die Titinkinase umrahmt wird, besitzen jedoch ausreichende Stabilität, weshalb ihre Entfaltung unter physiologischen Bedingungen unwahrscheinlich ist [68] und strukturelle Integrität gewahrt wird.

Eine 3D-Animation der Muskelfunktion und der mechanischen Aktivierung der Titinkinase, die auf den Ergebnissen dieser Arbeit basiert, steht auf der Institutshomepage http://www.biophysik.physik.uni-muenchen.de/projects/ zum Download bereit.

## 5.2 Mechanische Manipulation von CalB

Nachdem im Vorigen Kapitel der molekulare Mechanismus des natürlichen Kraftsensors Titinkinase entschlüsselt wurde, soll nun die Reaktion der Lipase CalB, die keine natürliche mechanische Funktion besitzt, auf eine externe Kraft untersucht werden. Die enzymatische Aktivität konnte dabei über ein fluoreszierendes Produkt nachgewiesen werden, während mit dem AFM gleichzeitig Kräfte ausgeübt wurden. Um möglichst viele Enzyme gleichzeitig zu manipulieren, wurden Agarosekugeln mit Antikörpern funktionalisiert, die an CalB durch molekulare Erkennung binden. Gleichzeitig wirkt die Antikörper-Peptid-Wechselwirkung als Sollbruchstelle.

### Antikörperfunktionalisierte Agarosekugeln als Manipulator

Das verwendete CalB Konstrukt wurde auf genetischer Ebene so verändert, dass es mit einem C-terminalen Cystein kovalent über Polyethylenglycol (PEG) an die Oberfläche eines Mikroskopdeckglases angebunden werden kann [69]. N-terminal befindet sich das Peptid GCN4, das von dem Antikörperfragment anti-GCN4-scFv durch molekulare Erkennung gebunden wird [70]. Da die Dichte aktiver Enzyme auf der Oberfläche nur ca. 1/20 $\mu m^2$ beträgt, musste eine Strategie entwickelt werden, um möglichst viele Enzyme auf der Oberfläche gleichzeitig zu kontaktieren und Kräfte auf sie auszuüben. Dazu wurden Agarosekugeln, auch Agarosebeads genannt, mit Epoxidharzkleber auf Cantilevern befestigt (Abbildung 17 a). Im nächsten Schritt wurde das anti-GCN4-scFv Antikörperfragment über Cystein an die Iodoacetylgruppen des Agarosebeads angebunden, was im Fluoreszenzsignal durch Zugabe von GFP-GCN4 bestätigt werden konnte (Abbildung 17 b und c). Der so erzeugte Manipulator kann über molekulare Erkennung gleichzeitig an eine Vielzahl von CalBs binden und Kräfte auf sie ausüben.

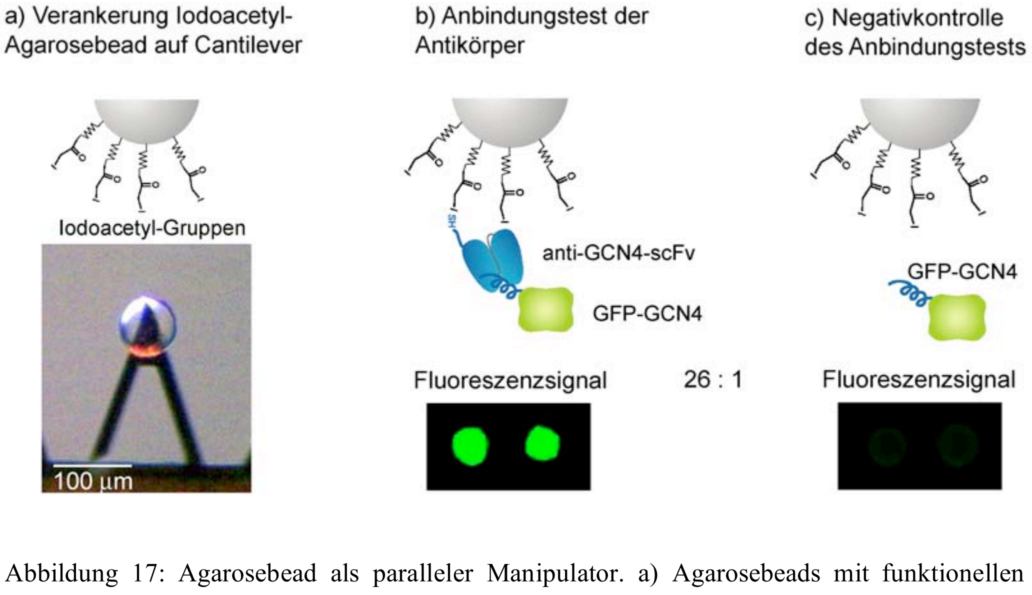
a) Verankerung Iodoacetyl-Agarosebead auf Cantilever
b) Anbindungstest der Antikörper
c) Negativkontrolle des Anbindungstests
Iodoacetyl-Gruppen
100 µm
HS
anti-GCN4-scFv
GFP-GCN4
GFP-GCN4
Fluoreszenzsignal
26 : 1
Fluoreszenzsignal

Abbildung 17: Agarosebead als paralleler Manipulator. a) Agarosebeads mit funktionellen Iodoacetylgruppen wurden in trockenem Zustand mit Epoxidharzkleber am Cantilever befestigt. b) An die Iodoacetylgruppen wurde in Lösung das Antikörperfragment über Cystein angebunden, was durch Zugabe des Peptids GCN4 mit angekoppeltem grün fluoreszierendem Protein (GFP) im Fluoreszenzsignal nachgewiesen werden konnte. c) ohne Antikörperfragment wird ein 26-fach schwächeres Signal beobachtet, was die Spezifität der Bindung zeigt.

## Mechanische Charakterisierung der Antikörper-Sollbruchstelle

Um die mechanischen Eigenschaften der Antikörperfragmente zu untersuchen, wurde das Peptid GCN4 an einen Cantilever über PEG angebunden. Details zur Immobilisierung können der Publikation P3 und Referenz [71] entnommen werden. Mit dem Cantilever wurden nun auf antikörperfunktionalisierten Agarosebeads Kraft-Abstandskurven aufgenommen (Abbildung 18 a). Die Krafthistogramme, die aus den charakteristischen Kraftkurven erzeugt wurden, weisen eine wahrscheinlichste Kraft von $F_{max}$=80±8 pN auf (Abbildung 18 b). Zusätzlich wurde auch die Ladungsrate dF/dt bestimmt, da die Abrisskraft davon abhängt und bei Auftragung gegen die Ladungsrate in logarithmischer Skalierung eine Gerade ergibt [14]. Der so ermittelte Punkt stimmt mit dem Verlauf von Referenz [1] im Rahmen der Streuung überein (Abbildung 18 c).

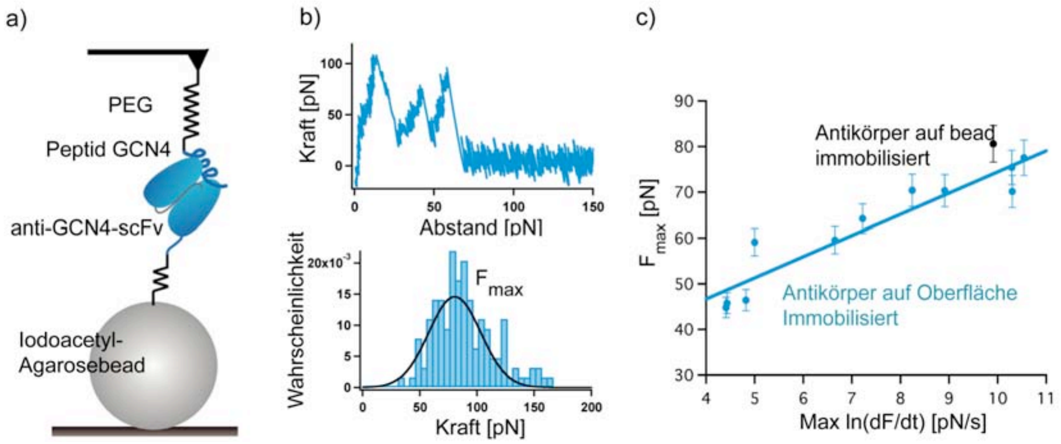

Abbildung 18: Mechanische Charakterisierung der Antikörper-Peptid-Wechselwirkung. a) Auf den Antikörper-modifizierten Agarosebeads wurden Kraftkurven mit einem Peptid-funktionalisierten Cantilever aufgenommen. b) Aus den charakteristischen Kraft-Abstandskurven, in denen oft multiple Abrisse erkennbar sind, wurden mit den letzten Abrissen Krafthistogramme erzeugt. Die Maximalkraft liegt bei 80 ±8 pN. c) Die bestimmte Maximalkraft stimmt mit zugehöriger Ladungsrate im Rahmen der Streuung mit den Werten aus Referenz [1] überein.

Diese Ergebnisse zeigen, dass die molekulare Erkennung des Peptids durch das Antikörperfragment während des Kontaktes stattfindet. Die häufige Beobachtung multipler Wechselwirkungen deutet auf eine hohe Dichte an Antikörperfragmenten hin. Somit eignet sich der charakterisierte molekulare Aufbau als reversible Sollbruchstelle mit bekannter Bruchkraft.

## Enzymatische Aktivität unter Kraft

Mit dem Antikörper-modifizierten Agarosebead wurde nun ein periodisches Kraftsprung-Experiment an den kovalent immobilisierten CalB-Enzymen durchgeführt. Bei Kontakt mit der Oberfläche binden die Antikörper an das Peptid von CalB, wodurch bei Zurückziehen des Cantilevers eine Kraft aufgebaut wird (Abbildung 19 a) und CalB in einen höherenergetischen Zustand der Energielandschaft gebracht wird. Brechen die Bindungen der Sollbruchstelle, so können die Enzyme wieder relaxieren. Während diesem periodischen Kraftprotokoll wurde die Aktivität der einzelnen Enzyme mit TIRF-Mikroskopie über das fluoreszierende Produkt gemessen, das durch die Spaltung des Substrates 5-(und-6)-Carboxyfluorescein Diacetat (CFDA) entsteht. Abbildung 19 a zeigt das Bild eines integrierten Films, auf dem neben Hintergrundfluoreszenz die immer wiederkehrende Fluoreszenz der Enzyme als helle Flecken zu erkennen ist. In Abbildung 19 b ist sowohl das aufgezeichnete Kraft- und Abstandssignal des Agarosebeads als auch das gleichzeitige Fluoreszenzsignal eines einzelnen Enzyms dargestellt. Die Aktivität zeigt das charakteristische Blinkverhalten mit An- und Auszeiten im Sekundenbereich, das auch von anderen Forschergruppen beobachtet wurde.

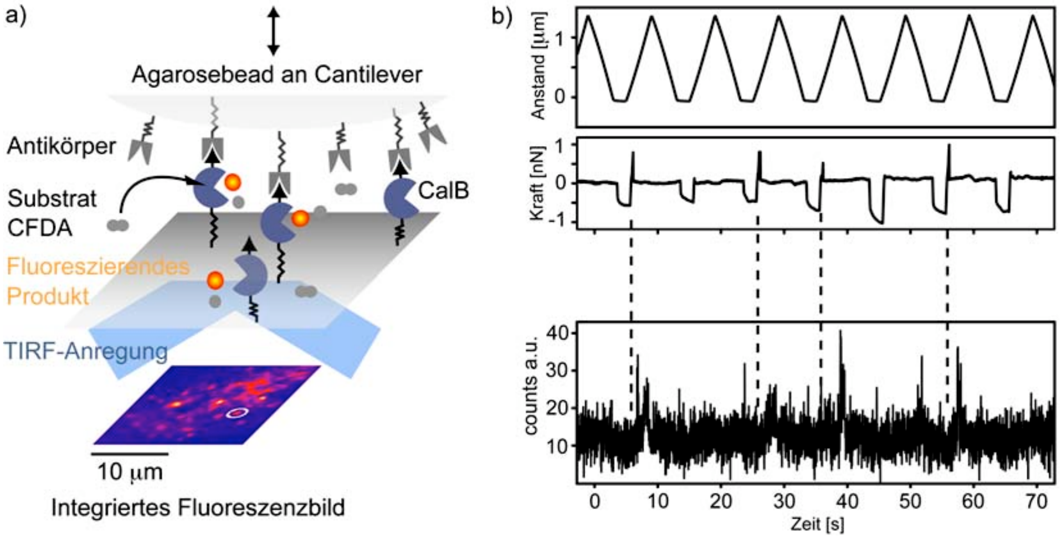

Abbildung 19: Mechanische Manipulation mit gleichzeitiger Beobachtung von Einzelenzymaktivität. a) Die Aktivität einzelner immoblisierter CalB Enzyme wird über das fluoreszierende Produkt mit TIRF-Mikroskopie beobachtet. Gleichzeitig übt der mit Antikörpern modifizierte Agarosebead Kräfte auf die Enzyme aus. b) Neben dem Abstands- und Kraftsignal des am Cantilever befestigen Agarosebead kann zu jedem Enzym die zeitliche Aktivität im Form des Fluoreszenzsignals aufgezeichnet werden.

Auffällig ist neben diesem Blinkverhalten, dass nach Perioden starker Wechselwirkung die Aktivität nach einem gewissen Zeitversatz verstärkt aufzutreten scheint. Um dies genauer zu untersuchen, wurden die Zeitkurven von insgesamt 11 Enzymen in die 10 sekündigen Zyklen der mechanischen Manipulation aufgeteilt. Der Zeitnullpunkt wurde jeweils beim Abriss der Antikörper-Peptid-Wechselwirkung gewählt. Durch Mitteln der Zeitkurven wurde ein Histogramm erzeugt, das zu den Zeitpunkten nach dem Abriss die jeweilige Fluoreszentintensitäten zeigt (Abbildung 20).

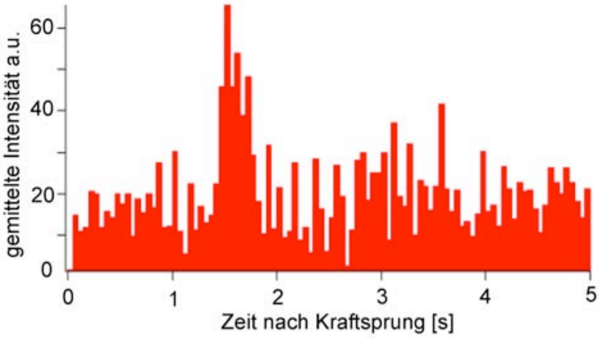

Abbildung 20: Gemitteltes Fluoreszenzhistogramm. Die Zeitverläufe der Fluoreszenz verschiedener Enzyme wurden in Bereiche mit der Länge der Manipulationsperiode eingeteilt. Nullpunkt ist jeweils beim Abriss der Antikörper-Peptidwechselwirkungen. Das gezeigte Histogramm enthält 10 Zyklen von insgesamt 11 Enzymen und zeigt eine Zunahme der

Zu erkennen ist eine Zunahme der enzymatischen Aktivität bei ca. 1.7 Sekunden nach dem Abriss. Diese Zunahme könnte durch folgendes Modell erklärt werden: Durch die Kraft wird CalB in einen höherenergetischen Zustand der Energielandschaft gehoben. Nach dem abrupten Sprung der Kraft beim Abriss kann das Enzym wieder relaxieren. Sein Weg zum Gleichgewicht zwischen Aktivität und Inaktivität führt dabei durch die komplexe und raue Energielandschaft mit mehreren Energiebarrieren in der Größenordnung $k_BT$, und über den aktiven Zustand. Details zu den experimentellen Methoden, zur Auswertung und zum Modell können dem Manuskript M1 entnommen werden.

## 5.3 Funktionelle Nanoassemblierung

In den vorherigen Abschnitten wurden die Funktionen und Mechanismen einzelner Enzyme untersucht. Im natürlichen Netzwerk der Zelle entsteht jedoch durch die Interaktion der einzelnen funktionellen Einheiten untereinander eine neue Dimension an Komplexität und Funktion. Erst durch das räumlich meist wohldefinierte Arrangement entsteht ein Zusammenspiel, das Signale verarbeitet oder biologische Prozesse reguliert. Um solche Netzwerke künstlich aus funktionellen Einheiten zu schaffen oder Signalkaskaden nachstellen zu können, wurde in dieser Arbeit die „Single-Molecule Cut-and-Paste"-Technik (SMCP) entwickelt. Sie kombiniert die Präzision des AFM mit der Selektivität von DNA, um mit der Kontrolle über einzelne Moleküle gezielt Strukturen oder räumlich definierte Bindungsstellen für die Selbstassemblierung weiterer Einheiten zu schaffen.

### Mechanische und optische Charakterisierung einzelner SMCP-Zyklen

Wie im einleitenden Kapitel 4 beschrieben, basiert der Assemblierungsprozess auf molekularer Erkennung und einem System hierarchischer Bindungskräfte von DNA. Im ersten Schritt wird die Cantilever-DNA in Kontakt mit der Transport-DNA gebracht, deren Ankersequenz (grün in Abbildung 21) in der „zipper"-Geometrie an die Depot-DNA hybridisiert. Im Kontakt hybridisiert die Transportsequenz (orange) an die Cantilever-DNA in der „shear"-Geometrie, sodass sich beim Zurückziehen des Cantilevers Kraft aufbaut. Die zugehörige Kraft-Abstandskurve zeigt, dass der Kraftanstieg, der auf die Elastizität des PEG-spacer zurückzuführen ist, in einem Plateau bei 17 ± 2 pN endet, bis die Bindung bricht. In diesem Plateau wird zwischen Transport- und Depot-DNA ein Basenpaar nach dem anderen getrennt, weshalb diese Kräfte kleiner sind als jene, mit denen die parallele Belastungsgeometrie zur Cantilever-DNA getrennt wird. Nach dem Transfer zum Ziel wird die Transport-DNA wieder in Kontakt mit der Oberfläche gebracht, wo die Ankersequenz an die Ziel-DNA in der „shear"-Geometrie hybridisiert. Beim Zurückziehen des Cantilever baut sich wieder eine Kraft auf, die die Basenpaare beider Teilsequenzen der Transport-DNA parallel belastet. Da die Bindung zur Ziel-DNA 10 Basen mehr enthält, ist das Brechen der Bindung zur Cantilever-DNA wesentlich wahrscheinlicher, was auch optisch verifiziert wurde. In der Kraft-Abstandskurve ist dies als charakteristischer Kraftanstieg der kombinierten PEG-DNA-Elastizität bis zum Bindungsbruch bei 50 ± 5 pN zu erkennen. Somit wurde im gezeigten Fall eine DNA transportiert, wonach der Cantilever für den nächsten Zyklus bereit war.

Um den Transport und die assemblierten Strukturen gleichzeitig optisch mit TIRF-Mikroskopie beobachten und kontrollieren zu können, war die Transport-DNA mit einem Farbstoff modifiziert, dessen Fluoreszenz im grünen Kanal des Mikroskops aufgezeichnet wurde. Gleichzeitig war im roten Kanal die Eigenfluoreszenz der Cantileverspitze sichtbar, sobald sie in das evaneszente Anregungsfeld eindrang. Die optische Beobachtung eines SMCP-Zyklus ist in Abbildung 21 b dargestellt. Nachdem im Depot eine DNA aufgenommen und über die Zielregion gebracht wurde, war noch kein optisches Signal detektierbar, da sich sowohl die Spitze als auch die farbstoffmarkierte DNA außerhalb des Anregungsfeldes befanden. Bei Kontakt mit der Oberfläche war im roten Kanal die Eigenfluoreszenz der Cantileverspitze und im grünen Kanal der Farbstoff sichtbar. Nach Zurückziehen des Cantilevers und Bruch der Bindung zwischen Cantilever- und Transport-DNA blieb die farbstoffmarkierte Transport-DNA im Ziel zurück. Nach einigen Sekunden bleichte der Farbstoff.

Wie in Publikation P4 im Anhang gezeigt, kann dieser Zyklus bis zu 5000 mal bei einem Effizienzverlust von ca. 10% wiederholt werden. Die Anzahl der pro Zyklus transportierten DNA-

Stränge hängt vom Krümmungsradius der Spitze und der Funktionalisierungsdichte ab. Sie kann so eingestellt werden, dass der Transport eines einzelnen Stranges am wahrscheinlichsten ist. Die tatsächliche Anzahl der aufgenommenen und abgesetzten DNA-Stränge, die dem Zufall unterworfen ist, kann man jedoch bei nicht zu hohen Funktionalisierungsdichten anhand der Kraft-Abstandskurven zählen, wodurch ein Korrekturmechanismus möglich ist.

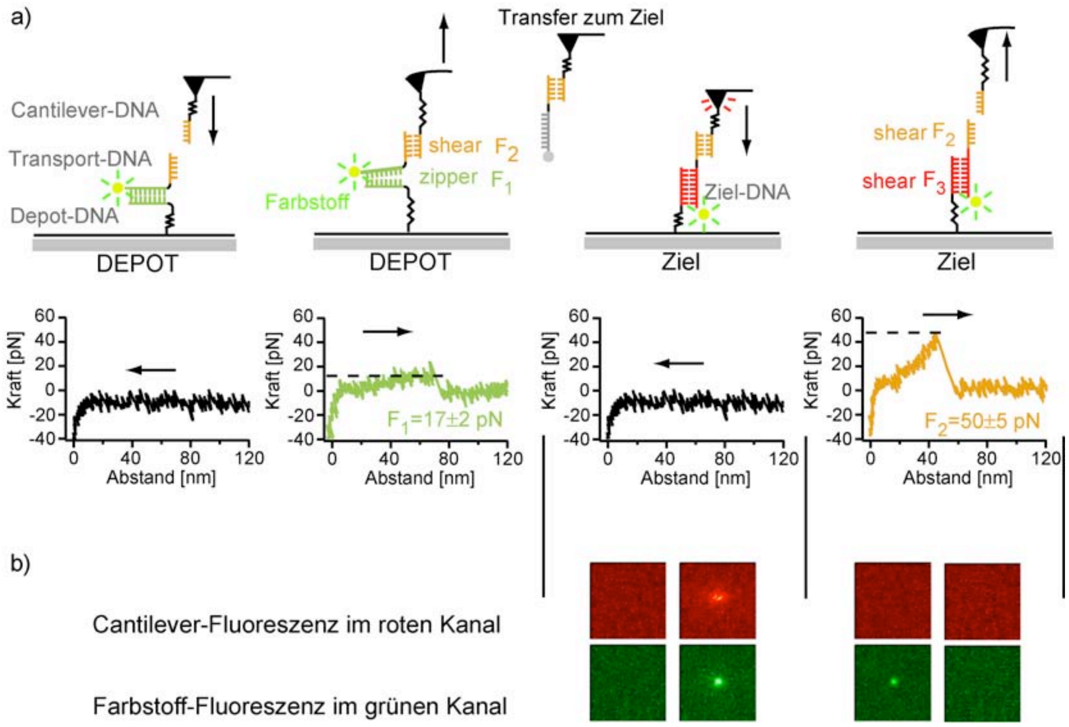

Abbildung 21: Mechanische und optische Charakterisierung von SMCP. a) Die Kraftkurven zeigen den Kontakt mit der Oberfläche und das Aufnehmen der Transport-DNA im Depot, wie auch das Absetzen im Ziel. Deutlich erkennbar ist der Kraftunterschied zwischen Depot (17 pN) und Ziel (50 pN) aufgrund der unterschiedlichen Belastungsgeometrien. b) Gleichzeitig kann das Positionieren und Absetzten einzelner farbstoffmarkierter Transport-DNAs mit TIRF-Mikroskopie beobachtet werden. Der rote Kanal zeigt den Kontakt des Cantilevers mit der Oberfläche, wobei in grün auch eine aufgenommene DNA erkennbar ist. Beim Zurückziehen des Cantilevers bricht die Bindung, die Transport-DNA bleibt jedoch verankert. Nach einigen Sekunden bleicht der Farbstoff.

Auf diese Weise konnten sowohl große Strukturen im 10 µm-Bereich (siehe Publikation P4) als auch Muster unterhalb der optischen Auflösungsgrenze mit Punktabständen von 50 nm erzeugt werden (siehe Publikation P5). Die Positionen dieser einzelnen Farbstoffe wurden über die Bleichstufen mit Nanometer-Präzision rekonstruiert. Die Analyse der Experimente ergibt eine untere Schranke der SMCP-Präzision von 10 nm, die vor allem auf die Länge der DNA und der verwendeten PEG-Spacer zurückzuführen ist.

## Selbstorganisation an nanoassemblierten Bindungsstellen

Der universelle Ansatz, einen DNA-Strang als „Transporter“ zu nutzen, erlaubt im Prinzip die Assemblierung verschiedenster Nanoobjekte organischer oder anorganischer Natur. Einzige Voraussetzung für ihre direkte Assemblierung ist, dass sie an die Transport-DNA angebunden werden können und den Transportprozess nicht stören. Um diese mögliche Einschränkung zu umgehen, wurde die SMCP-Technik erweitert, indem die Transport-DNA mit zusätzlichen spezifischen Bindungsstellen modifiziert wurde. Dadurch kann eine beliebige Struktur von Bindungsstellen erzeugt werden, an die sich im nächsten Schritt die funktionellen Einheiten mit dem entsprechenden Gegenstück durch molekulare Erkennung von selbst anlagern.

Als Rezeptor-Ligand-Paar wurde dazu Biotin-Streptavidin gewählt. Einerseits ist Biotin ein kleines Molekül, das den Hybridisierungsprozess während des Transports nicht behindert, andererseits ist seine Bindung zum tetramerischen Protein Streptavidin mit einer Affinität von $10^{15}$ $M^{-1}$ eine der stärksten biologischen nichtkovalenten Bindungen. Darüber hinaus ist die Verwendung dieser Bindung so weit verbreitet, dass viele Enzyme oder Nanopartikel als Konjugat mit Streptavidin kommerziell erhältlich sind.

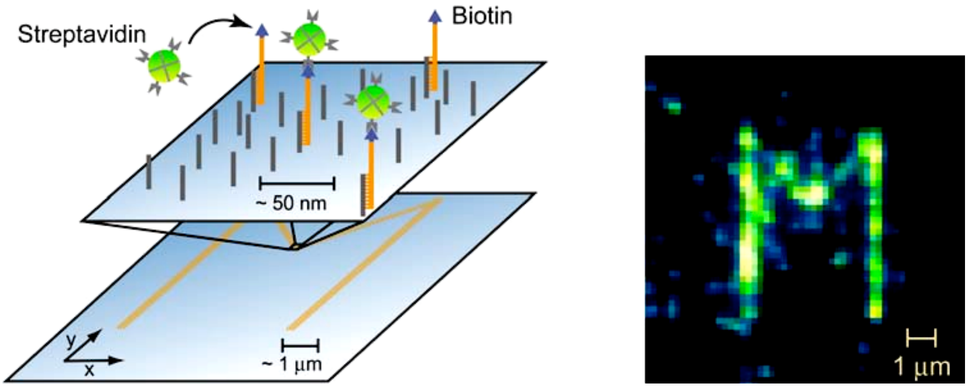

Abbildung 22: Assemblierung von Bindungsstellen für Selbstorganisation. Die Transport-DNA wurde mit Biotin modifiziert, wodurch im Zielbereich eine frei programmierbare Struktur von Bindungsstellen, in diesem Fall ein „M“, erzeugt werden kann. Nach der SMCP Assemblierung wurde 1 nM fluoreszenzmarkiertes Streptavidin in Lösung dazugegeben, dass sich spezifisch an die vordefinierten Bindungsstellen anlagerte. Das gezeigte Fluoreszenzbild wurde nach einer Minute Inkubationszeit und Waschen der Oberfläche mit 1x SSC Puffer mit TIRF-Mikroskopie aufgenommen

Ein Experiment dieser Art ist in Abbildung 22 dargestellt. Zuerst wurde mit SMCP und Biotin-modifizierter Transport-DNA ein Muster aus Bindungsstellen in der Form eines „M“ geschrieben. Nach Zugabe von fluoreszenzmarkiertem Streptavidin konnte die spezifische Selbstassemblierung mit dem TIRF-Mikroskop beobachtet und dokumentiert werden.

Die Vielseitigkeit dieser Strategie wurde demonstriert, indem aus unterschiedlichen Streptavidin-modifizierten und fluoreszierenden Nanokristallen verschiedene Superstrukturen erzeugt wurden. Die zeitliche Verfolgung des Selbstassemblierunsprozesses zeigt, dass selbst bei Konzentrationen im pM-Bereich die Struktur nach 100 Sekunden komplett und spezifisch ausgebildet ist. Details und Ergebnisse dieser Experimente finden sich in der Publikation P6.

# 6. Ausblick

Die neuen Erkenntnisse dieser Arbeit in dem Gebiet der Mechanoenzymatik und Assemblierung funktioneller Einheiten schafft direkte Anknüpfungspunkte und eine neue Basis für synthetische Einzelmolekülbiologie. In diesem abschließenden Teil der Arbeit werden konkrete, bereits geplante Forschungsvorhaben und generelle Ansätze zur Weiterführung dieses Gebietes vorgestellt.

Der experimentell neu entdeckte Mechanismus der mechanischen Aktivierung der Titinkinase ist nicht nur aus Sicht der Grundlagenforschung von Interesse, sondern auch für die Medizin von Bedeutung. Mutationen in der Titinkinase führen zur Muskelschwäche, die bei Versagen der Atemmuskulatur tödlich ist (Edström-Krankheit) [29]. Unterbrechungen des Signalweges verursachen pathogene Hypertrophie des Herzmuskels. Durch kraftspektroskopische Experimente an einzelnen Titinkinasen und in Anwesenheit weiterer Interaktionspartner könnten auch Fehlfunktionen in molekularem Detail verstanden werden. Dies könnte einen Ansatz zum gezielten Design von Wirkstoffen eröffnen, die es erlauben könnten, Fehlfunktionen zu beheben und in das Muskelwachstum regulatorisch einzugreifen.

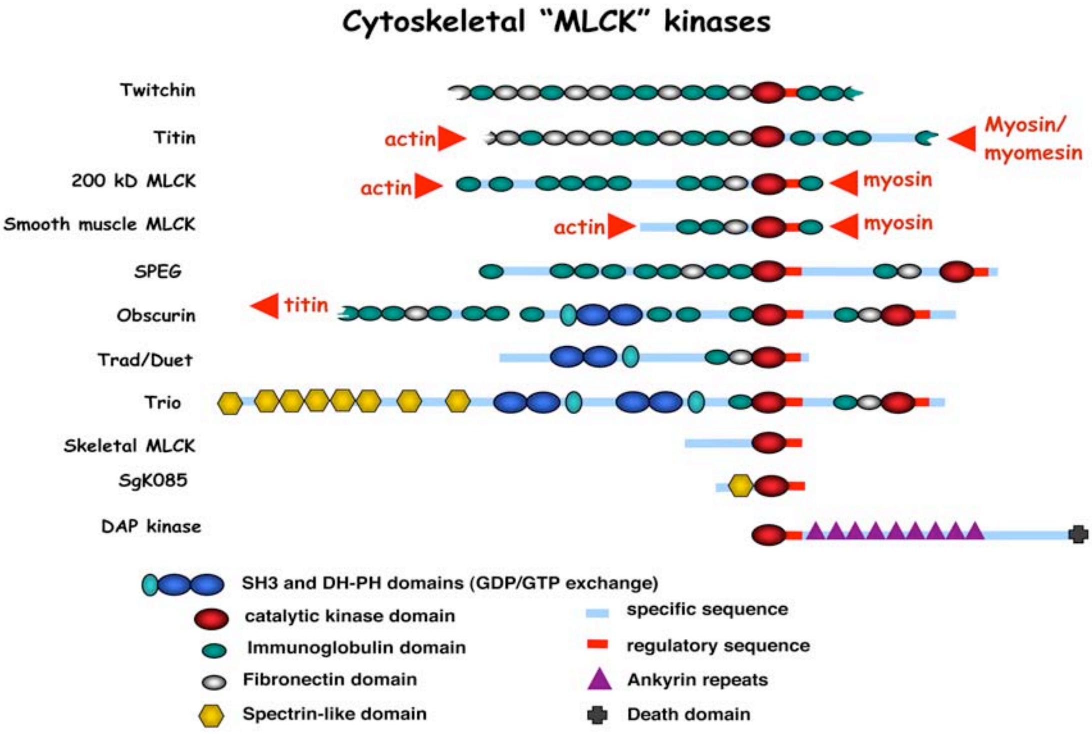
Cytoskeletal "MLCK" kinases
Twitchin
Titin
actin
Myosin/
myomesin
200 kD MLCK
actin
myosin
Smooth muscle MLCK
actin
myosin
SPEG
Obscurin
titin
Trad/Duet
Trio
Skeletal MLCK
SgK085
DAP kinase
SH3 and DH-PH domains (GDP/GTP exchange)
catalytic kinase domain
Immunoglobulin domain
Fibronectin domain
Spectrin-like domain
specific sequence
regulatory sequence
Ankyrin repeats
Death domain

Abbildung 23: Strukturelle Proteine im Zytoskelett mit „MLCK“-ähnlichen Kinasen. Durch die biomolekulare Umgebung sind sie so positioniert, dass, wie im Titin, Kräfte auf sie wirken. Aufgrund der Verwandtschaft mit der Titinkinase könnten auch diese Mitglieder des Kinoms mechanisch aktiviert werden. Die Abbildung wurde freundlicherweise von Mathias Gautel zur Verfügung gestellt.

Neben dem Titin gibt es eine Vielzahl weiterer struktureller Proteine, die vor allem im Zytoskelett der Zelle mechanischen Reizen ausgesetzt sind. Auch hier müssen Kräfte in biochemische Signale übersetzt werden, um biologische Reaktionen auszulösen. Einige dieser Proteine, die in

Abbildung 23 schematisch dargestellt sind, beinhalten Kinasen aus dem Zweig des menschlichen Kinoms, dem auch die Titinkinase zugeordnet wird. Die in dieser Arbeit entwickelte Automatisierung der Datenanalyse ermöglicht ein effektives Screening und eine große Messdatenstatistik. Es wurde bereits begonnen, Mitglieder dieser Spezies des Kinoms auf Mechanoenzymatik zu untersuchen. Mechanische „pump-and-probe“-Protokolle helfen vor allem, strukturelle Einsicht in die Mechanismen jener Kinasen zu gewinnen, deren Struktur noch nicht bekannt ist.

Um das Binden von Substraten und weitere enzymatische Schritte gleichzeitig über Fluoreszenz beobachten zu können, muss das Anregungsvolumen drastisch verringert werden. Denn hierfür sind oft millimolare Konzentrationen von farbstoffmarkierten Molekülen notwendig. Das Volumen einzelner Moleküle liegt dadurch im Zeptoliter-Bereich. Möglich ist dies z.B. mit „zero-mode waveguides“, die die Feldverstärkung in Löchern von Metallfilmen und eine laterale Einschränkung im 50 nm Bereich ausnützen [72] (Abbildung 24).

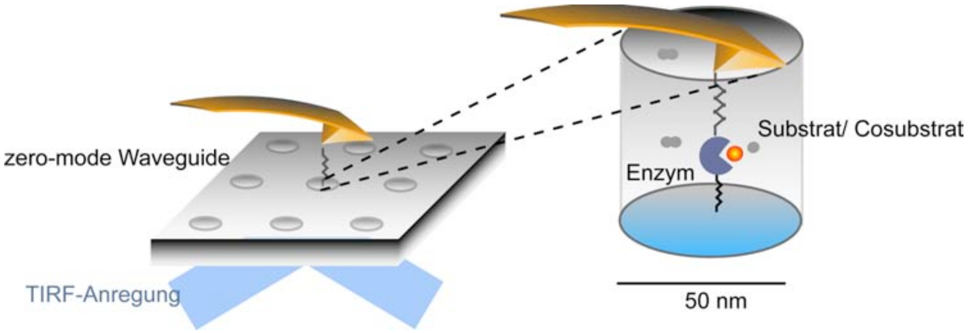

Abbildung 24: Untersuchung der Titinkinase oder anderer Enzyme in „zero-mode waveguides“. Durch die Einschränkung des Anregungsvolumens in den Zeptoliter-Bereich können einzelne farbstoffmarkierte Substrate mit einer Konzentration im millimolaren Bereich optisch aufgelöst werden. Die Positionierungspräzision und Kontrolle der Anzahl an Enzymen kann mit SMCP erreicht werden.

Von größter Wichtigkeit ist insbesondere für die Untersuchung von Enzymen, die nicht mechanisch aktiviert werden, dass sowohl ihre Position als auch ihre Anzahl auf Einzelmolekülebene kontrolliert und gesteuert werden kann. Die in dieser Arbeit entwickelte SCMP Technik stellt eine Basistechnologie mit der erforderliche Präzision und Spezifität dar, um einzelne Moleküle für diesen Zweck zu positionieren (Abbildung 24).

Ein visionärer Ansatz für das Verständnis, wie einzelne Enzyme im komplexen Zusammenspiel zellulärer Regelkreise agieren und reagieren, ist die gezielte Erzeugung und Untersuchung von wohldefinierten Netzwerken. In diesem Ansatz synthetischer Einzelmolekülbiologie ließen sich dadurch Signalwege oder synergetische Enzymkaskaden nachbauen. SMCP liefert hierzu den Beitrag die aktiven Einheiten an vordefinierten Netzwerkpositionen präzise zu platzieren (Abbildung 25 a). Die Aktivität der einzelnen Einheiten im Netzwerk könnte wie bei der Lipase CalB über ein fluoreszierendes Substrat ausgelesen und analysiert werden. Ein mögliches Modellsystem könnte z. B. auch die alkalische Phosphatase darstellen, die auch im Rahmen dieser Arbeit untersucht wurde. Die Verfügbarkeit dieses Enzyms mit spezifischer Streptavidin-Bindungsstelle und fluoreszierendem Substrat macht es für die Anbindung an Biotin-Strukturen, die mit SMCP erzeugt werden, direkt einsetzbar.

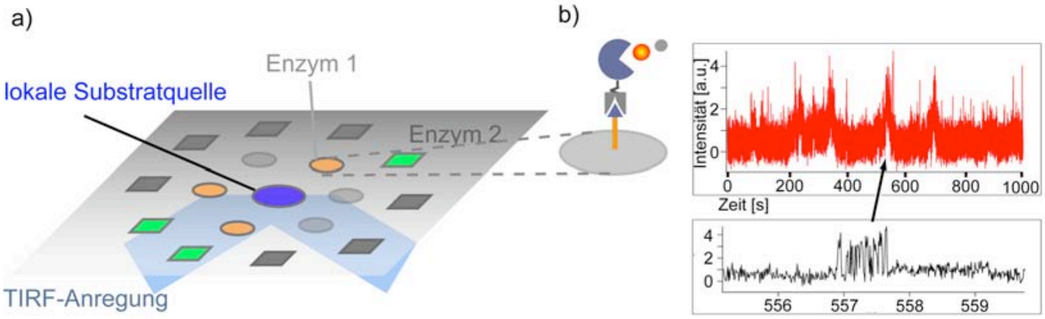

Abbildung 25: Erzeugung enzymatischer Netzwerke oder Kaskaden mit SMCP. a) Durch die Platzierung synergetischer Enzyme um eine lokale Substratquelle könnten Enzymnetzwerke oder Signalkaskaden über fluoreszierende Produkte untersucht werden. b) Die Assemblierung könnte über Streptavidin-modifizierte Enzyme erfolgen, wie im gezeigten Fall der über Streptavidin immobilisierten alkalischen Phosphatase. Die enzymatische Aktivität wurde über das fluoreszierende Produkt durch Umsetzung von 3-O-Methyl-Fluoreszein-Phosphat beobachtet und zeigt das charakteristische Blinkverhalten.

Abbildung 25 b zeigt das zeitliche Fluoreszenzsignal der immobilisierten alkalischen Phosphatase. Deutlich zu erkennen ist das fluktuierende Verhalten, das auch bei CalB beobachtet wurde. Für die Untersuchung eines breiteren Spektrums an Enzymen könnten aber auch FRET-Paare als Markierung von unterschiedlichsten Substraten wie DNA oder Proteinen dienen. Durch die Assemblierung synergetischer Einheiten könnten in Zukunft auch Signalkaskaden nachgestellt und neue oder effektivere katalytische Funktionen erzeugt werden.

# 7. Anhang

## 7.1. Kraftspektroskopie

Das grundlegende Prinzip der Kraftspektroskopie besteht darin, ein Molekül zwischen einer Unterlage und einer Feder einzuspannen und zu dehnen. Als Messsignal wird die Ausdehnung des Moleküls *x* und die anliegende Kraft *F* aufgezeichnet, die über die Ausdehnung der Feder bestimmt wird (Abbildung 26).

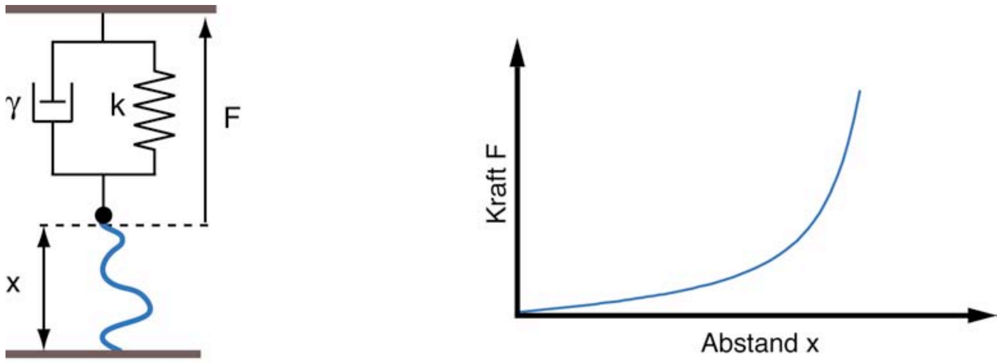

Abbildung 26: Kraftspektroskopisches Messverfahren. Das Molekül wird zwischen Unterlage und Feder eingespannt. Die Feder besitzt eine Federkonstante k und aufgrund der Viskosität der Flüssigkeit eine Dämpfung γ. Wird die Feder von der Oberfläche entfernt, so baut sich eine Kraft F auf, wodurch das Molekül auf einen End-zu-Endabstand x gedehnt wird. Das Messergebnis ist eine Kraft-Abstandskurve.

Die verschiedenen kraftspektroskopischen Techniken unterscheiden sich durch die Art der Federn und des Messverfahrens von Kraft und Abstand. Die Hauptvertreter sind in Tabelle 1 zusammengefasst.

Bei der optischen Falle werden mikrometergroße Kügelchen mit einem zum Medium unterschiedlichen Brechungsindex im Fokus eines Laserstrahls eingefangen [73, 74]. Der stetige Impulsübertrag der Photonen des gebrochenen, des reflektierten und des gestreuten Lichtes übt auf das Kügelchen eine Kraft aus. Senkrecht zur Einfallsrichtung tritt die Kraft $F_{grad}$ auf, die durch die Brechung verursacht wird und ins Zentrum des Strahles mit höchster Intensität wirkt. In Einfallsrichtung entsteht eine stabile Falle, wenn sich die Kräfte des gestreuten und reflektierten Lichtes $F_{r,s}$ mit der in entgegengesetzter Richtung wirkenden Komponente der gebrochenen Strahlen $F_{br}$ kompensieren. Durch Verschieben des Strahlzentrums kann das Kügelchen bewegt werden, wobei die Kraft aus seinem Abstand zum Strahlmittelpunkt Δz und dem effektiven Fallenpotenzial $k_{eff}$ bestimmt wird. Wichtige Anwendungsbeispiele können in den Referenzen [75-81] gefunden werden.

Bei magnetischen Fallen [82, 83] ist die Messsonde ein paramagnetisches Kügelchen, das in einem Magnetfeld magnetisiert wird. Herrscht zudem ein Magnetfeldgradient, so wird auf die Sonde eine Kraft $\vec{F}_{mag} = \vec{m} \cdot grad(\vec{B})$ ausgeübt.

Die „biomembrane-forceprobe“-Technik wurde ursprünglich entwickelt, um Trennkräfte zwischen einzelnen Rezeptor-Ligand-Paaren zu untersuchen [84]. Hierbei wurde eine rote Blutzelle mit einer Glaskapillare angesaugt. Ein mit Liganden funktionalisiertes Kügelchen, das fest an die Blutzelle angebunden ist, wurde in Kontakt mit Rezeptoren gebracht und die Kraft beim Trennen über die Deformation der Blutzelle bestimmt.

| Technik | Prinzip | Kraftbereich | Vorteil |
|---|---|---|---|
| Optische Falle<br>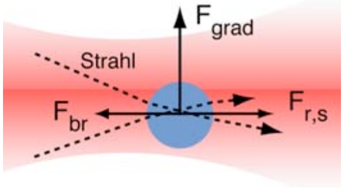<br> | Mikrometer große Kügelchen werden durch Impulsübertrag im Zentrum eines fokussierten Lasers gefangen. Auslenkungen resultieren in Kraft | 0.1 – 150 pN | Hohe Kraftauflösung |
| Magnetische Falle<br>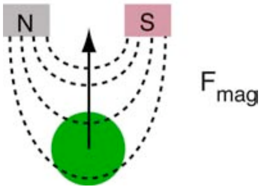<br> | Im Gradienten eines Magnetfeldes wirkt auf paramagnetische Partikel eine Kraft. | 10 fN-10 pN | Parallelität |
| Biomembran forceprobe<br>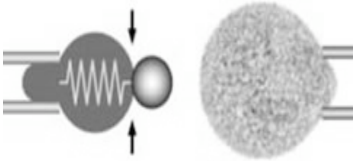 | Vesikel oder Zellen werden mit Mikropipetten angesaugt und in Kontakt gebracht. Die Kraft wird über die Deformation bestimmt. | 0.5 pN-1nN | Direkt biokompatible Grenzschicht |
| AFM<br> <br> | Die Verbiegung einer mikrofabrizierten Blattfeder wird über einen Lichtzeiger detektiert. | > 1pN | - Automatisierung<br>- Kontrolle in 3D<br>- Abrastern von Oberflächen |

## AFM basierte Kraftspektroskopie

Das „Atomic Force Microscope“ wurde von Binng, Quate und Gerber ursprünglich entwickelt, um Festkörperoberflächen abzurastern und so topografische Aufnahmen zu gewinnen und atomare Kräfte zu messen [48]. Dabei wird die Spitze einer Blattfeder mit Hilfe von Piezos über die Oberfläche gerastert und ihre Verbiegung gemessen. In der ursprünglichen Variante geschah dies über den Tunnelstrom zwischen der Blattfeder und einer darüber montierten Spitze. Am häufigsten wird mittlerweile jedoch die Methode eines von der Blattfeder reflektierten Laserstrahles verwendet, der von einer geteilten Photodiode detektiert wird (siehe Tabelle 1 und Abbildung 2).

Schon bald wurde das Potenzial des AFM erkannt, um biologische Proben in wässriger Umgebung mit einer Auflösung im nm-Bereich abzubilden [85-88].

Durch die Weiterentwicklung der Technik zur Kraftspektroskopie wurde es möglich, Bindungskräfte von Rezeptor-Ligand-Paaren und die Entfaltung von Proteinen zu messen. Die AFM-basierte Kraftspektroskopie hat den entscheidenden Vorteil gegenüber den anderen erwähnten Techniken, dass sie zusätzlich zur vertikalen Beobachtung und Kontrolle einzelner Biomoleküle eine präzise laterale Kontrolle erlaubt. Zudem ermöglicht ein spezielles Design die Kombination mit Mikroskopiermethoden.

## Auflösungsvermögen

Die frequenzabhängige Oszillationsamplitude *A(ν)* eines Cantilevers in Flüssigkeit lässt sich gut durch einen gedämpften harmonischen Oszillator beschreiben:

$$A(\nu) = A_{dc} G(\nu), \quad G(\nu) = \frac{\nu_0^2}{\sqrt{(\nu_0^2 - \nu^2)^2 + \frac{\nu_0^2 \nu^2}{Q}}}$$

wobei $A_{dc}$ die Amplitude bei Frequenz gleich Null, $\nu_0$ die Resonanzfrequenz und $Q$ den Qualitätsfaktor bezeichnet. Zur Eichung der Federkonstante $k$ von Cantilevern wird ausgenützt, dass die Auslenkung x nach dem Equipartitionstheorem den energetischen Beitrag der thermischen Energie $k_B$T zur Verfügung hat. Somit gilt: $k\langle x^2 \rangle = k_B T$, wobei $k_B$ die Boltzmann-Konstante und $T$ die Temperatur bezeichnet [89, 90]. Typische Werte z. B. für einen Olympus Biolever A mit einer Federkonstanten von k=7 pN/nm sind für die Standardabweichung des Ortsrauschens $\sqrt{< x^2 >} = 0.7\text{nm}$ und für die Standardabweichung des Kraftrauschens entsprechend $\sqrt{< F^2 >} = 5\text{pN}$. Limitiert wird das Auflösungsvermögen durch die vom Cantilever dissipierte Energie. In Referenz [91] wurde gezeigt, dass die minimal auflösbare Kraft $F_{\min}$ bei einer Bandbreite B und einem Dämpfungskoeffizienten γ gegeben ist durch $F_{\min} = \sqrt{4 k_B T \gamma B}$. Deshalb ist bei gleichbleibender Temperatur eine Erhöhung der Auflösung nur durch eine Verkleinerung der Dämpfung γ erreichbar. Ansätze hierzu sind neben der Verkleinerung der üblichen „Balken-Geometrie" die Aufhängung kleiner Cantilever im Torsionsmodus [92]. Für die Auflösung muss jedoch auch das gerätespezifische Detektorrauschen (*DR*) berücksichtigt werden. Denn bei einem periodischen Kraftsignal F(*ν*) gilt für das Signal-Rausch-Verhältnis [91]:

$$S/R = \frac{F(\nu) \cdot G(\nu)}{\sqrt{4 k_B T \gamma B G^2(\nu) + \left(k \cdot DR\right)^2}}$$

Es ist offensichtlich, dass das Signal-Rausch-Verhältnis durch eine höhere Federkonstante verschlechtert wird weshalb in der Praxis, je nach Detektor, längere, aber dafür weichere Cantilever vorteilhafter sind.

## Modelle für Polymerelastizität und Transformation in molekulare Koordinaten

Im Zyklus eines Kraftspektroskopieexperimentes wird die Spitze eines AFM-Cantilevers mit Hilfe eines Piezos in Kontakt mit der Oberfläche gebracht, wobei das zu untersuchende Molekül entweder gerichtet oder unspezifisch kontaktiert wird. Durch Zurückziehen des Cantilevers wird das Molekül gedehnt, was in den aufgenommenen Kraft-Abstandskurven zu einem charakteristischen Muster führt, das durch Modelle für Polymerelastizität erklärt werden kann. Die

Analyse dieser Kraft-Abstandskurven erlaubt die Bestimmung molekularer Abstände und Rückschlüsse auf inter- und intramolekulare Wechselwirkungskräfte.

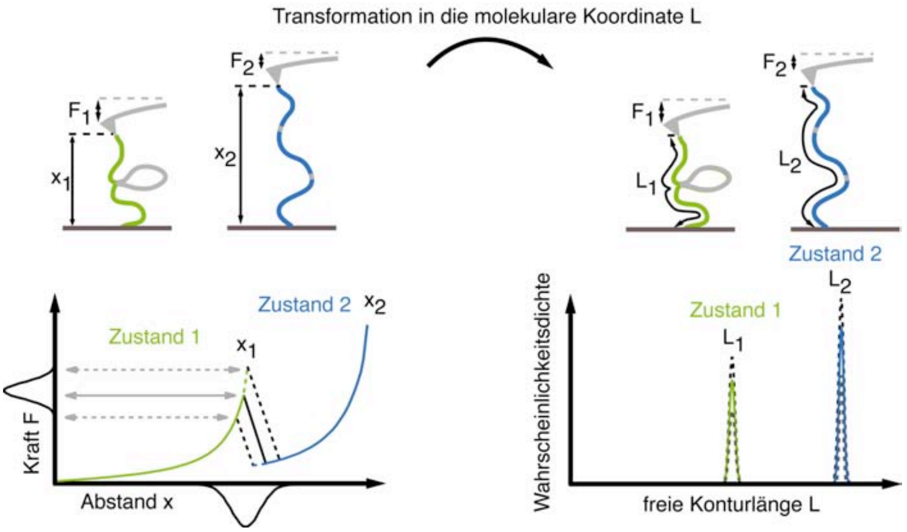

Abbildung 26: Kraft-Abstandskurve eines Polymers mit internem Bindungsbruch und zugehöriges Konturlängenhistogram. Sowohl der Abrissort als auch die Kraft sind Fluktuationen unterworfen und ändern sich mit variierenden experimentellen Parametern. Im Gegensatz dazu werden die Positionen von Energiebarrieren entlang der molekularen Konturlänge im erzeugten Konturlängenhistogramm direkt sichtbar und stellen einen festen und charakteristischen Fingerabdruck dar.

Wie in Abbildung 26 schematisch dargestellt, führt das Dehnen eines Polymers mit interner Verknüpfung zu einem Anstieg der Kraft, bis die interne Bindung bricht. Da nun wieder mehr freie Polymerlänge zu Verfügung steht, sinkt die Kraft abrupt. Bei weiterer Dehnung entsteht erneut der charakteristische Anstieg der Kraft. Der Abstand des Bindungsbruches ist jedoch keine charakteristische Größe, da er Fluktuationen unterworfen ist und stark von experimentellen Bedingungen wie z. B. Zuggeschwindigkeit [14], Temperatur [93] [94] und Eigenschaften des Lösungsmittels abhängt. Die relevante und charakteristische Länge ist die Konturlänge $L$, mit der die Position von Bindungen entlang des Polymerrückgrates gemessen wird und die in die Anzahl dazwischen liegender Monomereinheiten umgerechnet werden kann. Deshalb wurde in dieser Arbeit eine Methode entwickelt, um kraftspektroskopische Messdaten mit Hilfe der geeigneten Modelle für Polymerelastizität $F(x,L)$ vom Kraft-Abstandsraum in den Kraft-Konturlängenraum zu transformieren (siehe Abbildung 26 und Publikation P4). Dabei wird jeder Messpunkt $(F_i, x_i)$ mit dem inversen Modell $L(F,x)$ auf den Punkt $(F_i,L_i)$ abgebildet. Die dann erzeugten Konturlängenhistogramme zeigen die Barrierenpositionen bezüglich der Konturlänge an, die unabhängig von Fluktuationen und variierenden experimentellen Parametern sind. Mit diesem charakteristischen Fingerabdruck können kraftspektroskopische Daten nun automatisiert selektiert und Proteine miteinander verglichen werden. Um das Potenzial für ein automatisiertes *Screening* zu zeigen, wurde in dieser Arbeit zudem ein Experiment mit rohem Zellextrakt durchgeführt, in dem ein spezielles Proteinkonstrukt aus Tausenden anderer Moleküle automatisch erkannt wurde.

Das gebräuchlichste Modell für Polymerelastizität ist das *Worm-like Chain Modell* (WLC), das ein Polymer als flexiblen Stab beschreibt, der sich aufgrund der thermischen Energie $k_BT$ verbiegt. Betrachtet man die Korrelation der Einheitstangentenvektoren $\vec{t}$ mit Konturlängenabstand $s$, so stellt man fest, dass diese exponentiell abklingt:

$$\left\langle \vec{t}(0)\cdot\vec{t}(s)\right\rangle = e^{-\frac{s}{p}}$$

Die Persistenzlänge *p* ist also ein Maß für die Länge, ab der eine Verbiegung durch die thermische Energie stattfindet. Um Kraft-Abstandskurven mit einer analytischen Funktion anpassen zu können, wurde eine Näherungsformel entwickelt [95, 96], die das Verhalten von Polymeren unter Kraft gut beschreibt:

$$F_{WLC}(x) = \frac{k_B T}{p} \cdot \left( \frac{1}{4 \cdot (1 - x/L)^2} - \frac{1}{4} - \frac{x}{L} \right)$$

Durch das Fitten von Kraft-Abstandskurven mit fester Persistenzlänge kann so die freie Konturlänge bestimmt werden. Sie stellt im Gegensatz zum End-zu-End-Abstand die charakteristische Größe dar, die z. B. die Position von Energiebarrieren entlang des Polymerrückgrates misst und in die Anzahl dazwischen liegender Monomere umgerechnet werden kann.

Soll beispielsweise die Elastizität einer entfalteten Aminosäurekette über einen größeren Kraftbereich (>100 pN) beschrieben werden, muss eine Kraftabhängigkeit der Persistenzlänge berücksichtigt werden [22], die von 0.8 nm bei ca. 50 pN bis 0.4 nm bei ca. 300 pN reicht. Für noch höhere Kräfte müssen enthalpische Anteile einberechnet werden, die aus der Rotation und Dehnung von chemischen Bindungen des Peptidrückgrates verursacht werden und zu modifizierten Modellen wie dem QM-WLC-Modell führen [97]. Neben dem WLC-Modell sind noch das *Freely-Jointed-Chain-Modell* [82, 98] und das *Freely-Rotating-Chain-Modell* [99] gebräuchlich, sowie Modifikationen, die die Rückgratelastizität berücksichtigen [100].

## 7.2 Kombination vom AFM- mit TIRF-Mikroskopie

Neben der mechanischen Beobachtung und Kontrolle einzelner Biomoleküle hat sich auch die optische Beobachtung von Einzelmolekülfluoreszenz zu einer der wichtigsten biophysikalischen Techniken entwickelt. Das für diese Arbeit konstruierte AFM ermöglicht die Kombination mit Einzelmolekül-*Total Internal Reflection Fluorescence* Mikroskopie (TIRF), wodurch gleichzeitig unabhängige Messsignale detektiert und die Vorteile beider Techniken vereint werden.

### TIRF-Mikroskopie

Anders als beim Konfokalen Mikroskop, bei dem der Fokus des Anregungslasers über die Probe gerastert wird, ist bei der TIRF-Mikroskopie [101, 102] das ganze Gesichtsfeld ausgeleuchtet. Der Anregungslaser mit der Wellenlänge $\lambda_0$ trifft dabei oberhalb des kritischen Winkels $\theta > \theta_c = \arcsin(n_1/n_2)$ auf das Probendeckglas mit Brechungsindex $n_1$. An der Grenzschicht zum Medium mit Brechungsindex $n_2$ tritt totale Reflexion auf, sodass sich ein evaneszentes Anregungsfeld mit einer Eindringtiefe *d* im 100 nm-Bereich ausbildet (Abbildung 27)

$$I(z) = I(0) \cdot e^{-\frac{z}{d}} \quad \text{mit} \quad d = \frac{\lambda_0}{4\pi\sqrt{n_1^2 \sin^2(\theta) - n_2^2}}$$

Der große Vorteil dieser Technik im Vergleich zur Epi-Fluoreszenz ist, dass nur eine dünne Schicht an der Probenoberfläche angeregt wird, was die Hintergrundfluoreszenz unterdrückt und die Beobachtung einzelner Moleküle ermöglicht. Moderne Objektive besitzen eine ausreichende numerische Apertur (NA > 1,4), um den Laser durch das Objektiv einzukoppeln [103] [104].

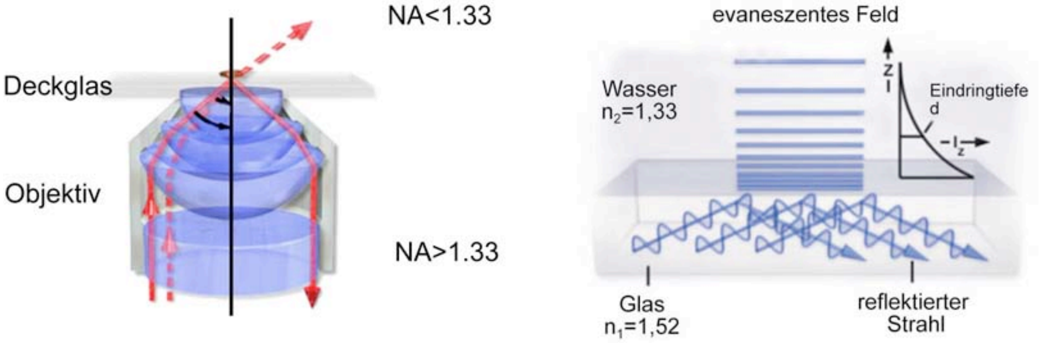

Abbildung 27: Schematik der Objektiv-basierten TIRF-Mikroskopie. Der Anregungslaser wird über das Objektiv mit einer hohen numerischen Apertur so eingekoppelt, dass er vom Deckglas total reflektiert wird. Auf der Probenseite entsteht so ein exponentiell abklingendes evaneszentes Feld, das nur ein kleines Probenvolumen anregt. Abbildung übernommen aus: http://www.olympusmicro.com/primer/techniques/fluorescence/tirf/tirfintro.html

## Optisches Auflösungslimit und Farbstofflokalisation

Die beugungslimitierte Auflösungsgrenze optischer Mikroskope wird durch das Rayleigh-Kriterium beschrieben. Nach ihm sind zwei Punktlichtquellen trennbar, wenn ihr Abstand *a* größer ist als der Radius ihrer zentralen Beugungsscheibchen.

$$a_{\min} \approx 0.61 \frac{\lambda}{NA}$$

Bei einer numerischen Apertur von 1.45 und einer Lichtwellenlänge von 488 nm liegt die theoretische laterale Auflösungsgrenze somit bei ca. 200 nm.

Wird das Intensitätsprofil eines einzelnen Farbstoffes auf mehr als vier Pixel einer CCD Kamera abgebildet, kann sein Ort mit wesentlich höherer Präzision durch Anfitten einer Gauß-Kurve bestimmt werden [105]. Abhängig vom Signal-Rausch-Verhältnis kann so eine Lokalisationsgenauigkeit im Nanometer-Bereich erreicht werden [106-109]. Aus diesem Prinzip wurden einige hochauflösende Mikroskopiermethoden entwickelt, bei denen ein Bild der fluoreszenzmarkierten Probe jenseits des Rayleigh-Kriteriums rekonstruiert werden kann. Entscheidend ist, dass pro Bildes des aufgenommenen Films nur so wenige Farbstoffe aktiv sind, dass sie optisch trennbar und somit präzise zu lokalisieren sind. Da auf verschiedenen Bildern unterschiedliche Farbstoffe aktiv und inaktiv sind, kann so die Position aller Farbstoffe rekonstruiert werden. Bei der *Stochastic Optical Reconstruction Mikroskopie* (STORM) [110-113] und der *Photoactivated Localization Mikroskopie*, (PALM) [114] wird dies z. B. durch die stochastische Aktivierung lichtschaltbarer Farbstoffe erreicht. Aber auch das Bleichen kann ausgenützt werden, um mehrere Farbstoffe in einer beugungslimitierten Fläche zu trennen [115]: Da ein Farbstoff nach dem anderen bleicht, kann der letzte aktive Farbstoff lokalisiert und sein Intensitätsprofil von dem Bild abgezogen werden, auf dem der Beitrag des letzten und vorletzten Farbstoffes enthalten ist. Dadurch kann wiederum der vorletzte aktive Farbstoff lokalisiert werden. Auf diese Art und Weise können die Positionen aller Farbstoffe rückwärts rekonstruiert werden. Diese Methode wurde im Rahmen dieser Arbeit verwendet, um ein mit dem AFM nanoassembliertes DNA-Muster zu rekonstruieren (siehe Kapitel 5 und Publikation P5).

Details zum experimentellen Aufbau finden sich im Manuskript M2.

## 7.3 Publikationen

P1:

Puchner, E.M., A. Alexandrovich, A.L. Kho, U. Hensen, L.V. Schafer, B. Brandmeier, F. Grater, H. Grubmuller, H.E. Gaub, and M. Gautel. 2008. *Mechanoenzymatics of titin kinase.* **PNAS** 105(36):13385-13390.

P2:

Morfill, J., J. Neumann, K. Blank, U. Steinbach, E.M. Puchner, K.E. Gottschalk, and H.E. Gaub. 2008.*Force-based analysis of multidimensional energy landscapes: application of dynamic force spectroscopy and steered molecular dynamics simulations to an antibody fragment-peptide complex.* **J Mol Biol** 381(5):1253-1266.

P3:

Puchner, E.M., G. Franzen, M. Gautel, and H.E. Gaub. 2008. *Comparing proteins by their unfolding pattern*. **Biophys J** 95(1):426-434.

P4:

Kufer, S.K., E.M. Puchner, H. Gumpp, T. Liedl, and H.E. Gaub. 2008. *Single-molecule cut-and-paste surface assembly.* **Science** 319(5863):594-596.

P5:

Kufer, S.K., M. Strackharn, S.W. Stahl, H. Gumpp, E.M. Puchner, and H.E. Gaub. 2008. *Mechanical Single Molecule Assembly Optically Monitored.* **Nature Nanotechnology** accepted.

P6:

Puchner, E.M., S.K. Kufer, M. Strackharn, S.W. Stahl, and H.E. Gaub. 2008. *Nanoparticle Self-Assembly on a DNA-Scaffold Written by Single-Molecule Cut-and-Paste.*
**Nano Letters.**

# Mechanoenzymatics of titin kinase

**Elias M. Puchner[†], Alexander Alexandrovich[‡], Ay Lin Kho[‡], Ulf Hensen[§], Lars V. Schäfer[§], Birgit Brandmeier[‡], Frauke Gräter[§¶], Helmut Grubmüller[§], Hermann E. Gaub[†], and Mathias Gautel[‡‖]**

[†]Chair for Applied Physics, Center for Integrated Protein Science Munich and Center for Nanoscience, Ludwig-Maximilians-Universität München, 80799 Munich, Germany; [‡]Cardiovascular Division and Randall Division for Cell and Molecular Biophysics. King's College London, London SE1 1UL, United Kingdom; and [§]Department of Theoretical and Computational Biophysics, Max Planck Institute for Biophysical Chemistry, 37077 Göttingen, Germany

Edited by Gregory A. Petsko, Brandeis University, Waltham, MA, and approved July 14, 2008 (received for review May 23, 2008)

**Biological responses to mechanical stress require strain-sensing molecules, whose mechanically induced conformational changes are relayed to signaling cascades mediating changes in cell and tissue properties. In vertebrate muscle, the giant elastic protein titin is involved in strain sensing via its C-terminal kinase domain (TK) at the sarcomeric M-band and contributes to the adaptation of muscle in response to changes in mechanical strain. TK is regulated in a unique dual autoinhibition mechanism by a C-terminal regulatory tail, blocking the ATP binding site, and tyrosine autoinhibition of the catalytic base. For access to the ATP binding site and phosphorylation of the autoinhibitory tyrosine, the C-terminal autoinhibitory tail needs to be removed. Here, we use AFM-based single-molecule force spectroscopy, molecular dynamics simulations, and enzymatics to study the conformational changes during strain-induced activation of human TK. We show that mechanical strain activates ATP binding before unfolding of the structural titin domains, and that TK can thus act as a biological force sensor. Furthermore, we identify the steps in which the autoinhibition of TK is mechanically relieved at low forces, leading to binding of the cosubstrate ATP and priming the enzyme for subsequent autophosphorylation and substrate turnover.**

atomic force microscopy | force–probe molecular dynamics simulation | muscle signaling | protein kinase regulation | single-molecular force spectroscopy

Mechanical activity and adaptive responses to changes in work load in muscle are tightly linked, but the mechanosensors triggering the sweeping adaptive changes seen *in vivo* are as yet poorly understood on the molecular level. In the vertebrate muscle sarcomere, titin serves as a molecular ruler for sarcomere assembly and is responsible for resting elasticity of muscle (1, 2) (Fig. 1*A*). At the M-band, titin contains a serine/threonine protein kinase domain (TK) (Fig. 1*B*) (3, 4). TK is regulated in a dual autoinhibition mechanism by a C-terminal regulatory tail, blocking the ATP binding site, and tyrosine autoinhibition of the catalytic base by tyrosine-170 (5). For access to the ATP binding site and the autoinhibitory tyrosine, the C-terminal autoinhibitory tail must be removed.

In most autoinhibited kinases, the relief of intramolecular autoinhibition is essentially a partial unfolding event of the autoinhibited conformation, driven by ligand binding or post-translational modification. Although TK activity can be moderately stimulated by calmodulin when tyrosine phosphorylation is mimicked, calmodulin or other calcium binding proteins are unable on their own to activate it (5). Because titin is firmly embedded in the contractile machinery (Fig. 1*A*), its conformation and function can readily be affected by mechanical forces (1, 6). The M-band, being much more compliant than the Z-disk (7, 8), is ideally placed as a strain sensor (9, 10). Because the M-band lattice is deformed only during active contraction, it is optimal for detecting the actual workload on the myofibril (10). Force–probe molecular dynamics simulations of the mechanical properties of TK suggested that kinase activation might be possible by mechanical forces (11). Indeed, a mechanosensitive signaling complex (signalosome) was identified that interacts with an open conformation of TK, and by controlling protein turnover and muscle gene transcription (12) seems to contribute to the adaptation of muscle in response to changes in mechanical strain. The importance of TK in maintaining the turnover of muscle proteins is highlighted by a point mutation in the human kinase domain that causes a myopathy with failure of load-dependent protein turnover (12).

Two recent reports on single-molecule force spectroscopy of titin kinase and *C. elegans* giant muscle protein kinase (13, 14) showed that these giant muscle protein kinases can unfold in a stepwise fashion, as predicted (11). To be strain regulated, association of the cytoskeletal lattice with the N- and C-terminal ends of the kinase domain is required. Titin is firmly integrated into the M-band lattice by interactions with obscurin, obscurin-like 1, and myomesin, which form a ternary complex at its C terminus (15). Because of their I-band (16) or broad A-band localization (17), the nematode giant muscle protein kinases have been implicated in contraction regulation. It is therefore as yet unclear whether the invertebrate giant protein kinases are similarly integrated into the cytoskeleton, follow the same activation pathways, and serve analogous functions as the M-band-associated TK.

However, experimental proof of direct mechanical activation, rather than simply partial unfolding, is lacking not only for titin kinase, but for all biological force sensors in muscle (2). Can mechanical force really induce a catalytically competent kinase conformation that will be able to bind substrates? The complex protein composition of the sarcomere M-band precludes an unequivocal experimental answer. Studying single molecules in isolation, however, can unravel their intrinsic properties in molecular detail and allow these to be compared with the known properties of intact sarcomeres and measurable enzymatic properties. We therefore used atomic force microscope (AFM)-based single-molecule force spectroscopy, molecular dynamics simulations, and enzymatics to investigate the molecular details of mechanical TK activation.

## Results

**Sequential Unfolding of TK at Low Forces.** We expressed a TK construct A168-M2, encompassing the human kinase domain flanked by its naturally surrounding Ig/Fn domains [Fig. 1 *B* and *C*; see details in supporting information (SI) *SI Text* (section 1), Fig. S1, and Table S1]. The TK construct was attached to an

BIOPHYSICS

---

Author contributions: H.G., H.E.G., and M.G. designed research; E.M.P., A.A., A.L.K., U.H., L.V.S., B.B., and F.G. performed research; M.G. contributed new reagents/analytic tools; E.M.P. analyzed data; and H.G., H.E.G., and M.G. wrote the paper.

The authors declare no conflict of interest.

This article is a PNAS Direct Submission.

Freely available online through the PNAS open access option.

[¶]Present address: Protein Mechanics and Evolution Group, Max Planck Society–Chinese Academy of Sciences Partner Institute for Computational Biology, Shanghai 200031, China.

[‖]To whom correspondence should be addressed. E-mail: mathias.gautel@kcl.ac.uk.

This article contains supporting information online at www.pnas.org/cgi/content/full/0805034105/DCSupplemental.

© 2008 by The National Academy of Sciences of the USA

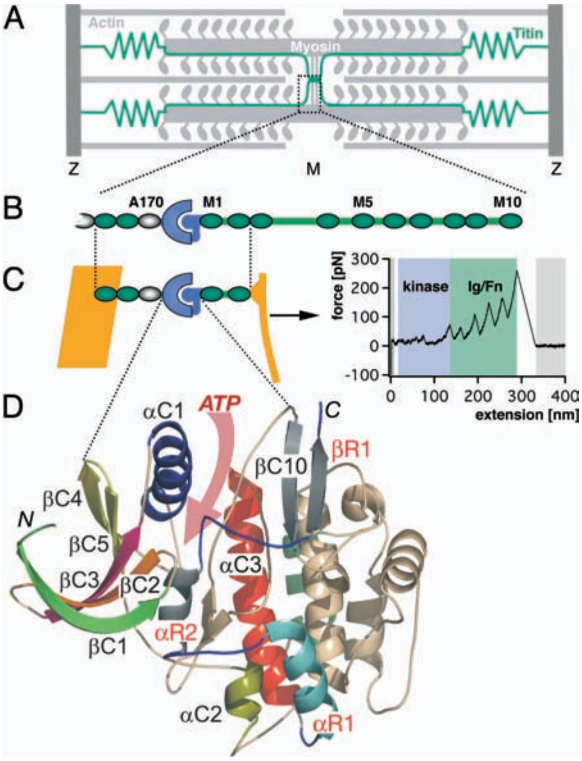

**Fig. 1.** Sarcomeric location and structure of the investigated TK protein construct. (*A*) Schematic diagram of the sarcomere showing the transverse Z- and M-bands and actin and myosin filaments, linked by the elastic titin filament. M-bands cross-link myosin filaments by a complex of titin (green), obscurin, and myomesin (15). (*B*) Domain structure of M-band titin showing the array of structural Ig (green), Fn3 domains (white), and unique sequences (green lines) surrounding titin kinase domain (TK) (blue). (*C*) The titin construct A168-M2 contains the kinase domain surrounded by Fn3 and Ig domains. ATP binding requires relief of the C-terminal autoinhibitory tail (blue) from the active site, which can be achieved by external force. In mechanical single-molecule experiments, A168-M2 is pulled off the gold support (yellow line) by a cantilever, resulting in a unique force spectrum when the protein is stretched and domains sequentially unfold. Analysis of the unfolding force spectrum (see *SI Text*) identifies the peaks shaded in blue as kinase unfolding peaks; the five unfolding peaks shaded in green correspond to sequential Ig and Fn domain unfolding. (*D*) Kinase domain structure, with the ATP binding site highlighted by the pink arrow and individual secondary structure elements color-coded. Numbering is from N to C terminus, where C1 to C10 refer to catalytic core structures, and R1 to R3 (in red) refer to the regulatory tail (5). The N and C termini are marked.

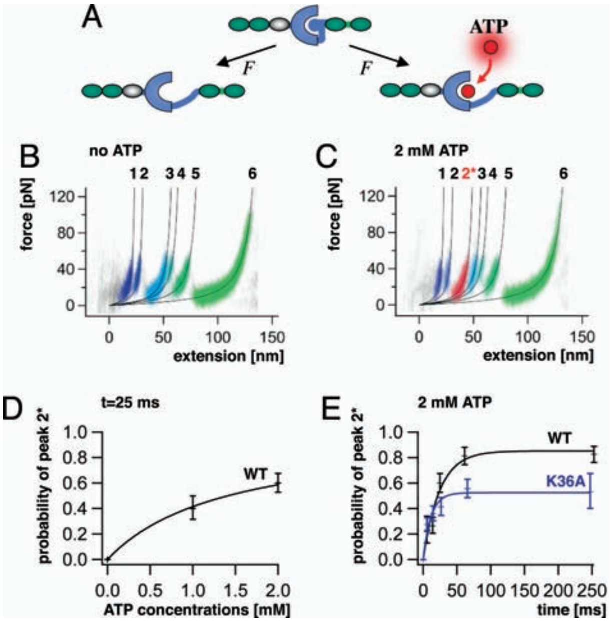

**Fig. 2.** Unfolding profile of TK and kinetics of mechanically induced ATP binding. (*A*) External force can open the ATP binding site of TK by unfolding of the autoinhibitory domain (blue ball). (*B*) Superimposed traces of 66 single-molecule unfolding events in TK show a fixed sequence of local unfolding events, numbered 1–5. (*C*) Mechanically induced ATP binding leads to a distinctly altered force profile with the appearance of an extra force peak, 2*, absent in unfolding events in the absence of ATP (44 traces). (*D*) ATP binding probability (i.e., the occurrence of peak 2*) depends on ATP concentrations, giving access to virtual direct kinetics though the system is not in equilibrium (ATP peaks detected at pulling rates of 720 nm/s, or after 25 ms). (*E*) Probability of ATP binding depends on pulling rates, decreasing at faster speeds because of reduced opening time of the ATP binding site. ATP binding is strongly reduced by mutation of lysine-36 to alanine (K36A).

AFM cantilever [see *SI Text* (sections 4 and 5) and Fig. S2] and stretched with nanometer accuracy. The resulting force, recorded with piconewton precision (Fig. 1*D*), showed a characteristic saw-tooth appearance as TK was gradually stretched and unfolded, mimicking the mechanical stress in muscle. (In a very simple comparison, the slowest experimental pulling speed per folded protein length amounts to 300 nm/s/25 nm = 12/s and is close to physiological rates. A rabbit sarcomere of 2 $\mu$m length can contract with 6 $\mu$m/s, yielding a contraction rate of 3/s.) Typically, a series of five initial low-force peaks below 50 pN was followed by up to five distinct saw-tooth-shaped high-force peaks that correlated exactly with the number and contour lengths of the flanking Ig/Fn-domains (18, 19) [Fig. 1; and see *SI Text* (sections 6–8) and Figs. S3–S5, and Table S2]. Therefore, the low-force peaks, occurring before Ig/Fn unfolding, derive from unfolding events within the kinase domain (see Fig. S2*b* for a schematic). These low-force unfolding events are strictly ordered, although their height is similar. In contrast to the independently unfolding Ig/Fn domains, their fixed sequence is not determined by mechanical stability but rather by topology. The forces required even for complete unfolding of the kinase do not exceed 50 pN at 23°C, or 30 pN at 37°C [see *SI Text* (section 9) and Fig. S6] and at pulling speeds of 1 $\mu$m/s. Such low forces were also predicted from force probe simulations (11). The fact that the mechanically more stable Ig/Fn domains always unfold after the kinase domain shows that the force acts on all domains in series, and that the protein construct is therefore completely stretched in the beginning of a retraction cycle.

**Mechanically Activated ATP Binding Detected by AFM.** Mechanical activation of TK must at an early stage uncover its ATP binding site while leaving the active site intact. Subsequent ATP binding alters the stability of the enzyme (Fig. 2*A*) and should therefore give rise to ATP-dependent changes in the TK unfolding profile (20). In the absence of ATP, five energy barriers separated by 9.1, 28.6, 7.3, 18.0, and 57.9 nm in contour length are observed (Fig. 2*B*). In the presence of Mg$^{2+}$-ATP at physiological concentrations (2 mM), a certain fraction of the traces shows an additional well pronounced peak (peak 2*) at 51.6 nm (Fig. 2*C*). This peak denotes an early interaction with ATP during the sequential unfolding of the kinase and thus demonstrates the initial opening of the active site.

The probability of observing the ATP-dependent peak should depend on the likelihood for ATP binding during the time span between the opening of the binding site and the moment when the ATP barrier (peak 2*) is probed and, therefore, on the ATP concentration (Fig. 2*D*). More interestingly, because this time span is controlled by the pulling speed, we gain direct experimental access to the ATP binding kinetics (see *SI Text*, section 10). This

Table 1. Kinetic parameters for ATP of autoinhibited titin kinase (WT and K36A) and the constitutively activated WT-kin3 measured by AFM or in solution

| Construct | $K_{\mathrm{on}}$, 1/M (AFM) | $K_{\mathrm{off}}$, 1/s (AFM) | $K_{\mathrm{d}}$, $\mu$M (AFM) | $K_{\mathrm{M}}$, $\mu$M (solution) | Autophosphorylation |
|---|---|---|---|---|---|
| WT | $1.8 \pm 0.3 \times 10^4$ | $6 \pm 3$ | 347 | No activity | − |
| K36A | $2.3 \pm 0.5 \times 10^4$ | $41 \pm 11$ | 1,810 | No activity | − |
| WT-kin3 | | | | 270 | + |

experiment can be seen as a mechanical pump–probe experiment: first the binding pocket of the TK is "pumped" open, and after a certain time ATP binding is probed. Variation of this time window provides the kinetic constants. The calibration of the time axis was estimated by the ratio of the MD-determined extension, during which the binding pocked is open but not deformed, and by the pulling speed. This mechanical pump–probe experiment showed saturation after ≈100 ms (Fig. 2*E*). Toward higher pulling rates, the probability of ATP binding decreased strongly and approached zero (Fig. 2*E*). This time dependence demonstrates that ATP binding is mechanically induced and perfectly agrees with the absence of catalytic activity of autoinhibited TK in solution (Table 1). Furthermore, this experiment allows estimates of the apparent on and off rates and resulting dissociation constant, which compare with affinity values observed for titin (Table 1) and other kinases in solution (21).

Following a suggestion from our MD simulations, we mutated lysine-36 to alanine (K36A), a highly conserved residue equivalent to lysine-72 interacting with the $\alpha/\beta$ phosphates of ATP in cAMP-dependent protein kinase (22, 23). This mutation abolishes kinase activity in TK (5). Now the ATP affinity of TK was dramatically reduced, with a >6-fold increase of $k_{\mathrm{off}}$ and a concomitant increase of $K_{\mathrm{d}}$ to millimolar values (Fig. 2*D*, *SI Text,* section 10 and Table 1). These results localize mechanically induced ATP binding to the canonical site in TK and confirm that the conserved lysine residue, known to play a crucial part in ATP binding of homologous protein kinases, is also a key residue in the TK binding pocket.

**Molecular Mechanism of TK Activation by Force.** We used force–probe MD simulations (24, 25) to characterize the force-induced unfolding of TK at the atomic level and to correlate the structural states with the energy barriers observed by the single-molecule force spectroscopy experiments. Force–probe molecular dynamics simulations (24, 25) used the TK x-ray structure [Protein Data Bank entry 1TKI (5)] as the starting structure, with the autoinhibitory tail partly removed [see *SI Text* (sections 11–16) and Tables S3 and S4]. Two sets of simulations (five each) were carried out for this truncated TK: one set with an empty binding pocket, and one set with an ATP molecule and magnesium ions inserted into the (closed) binding pocket. As a control, the autoinhibited complete TK was also subjected to force–probe MD simulations (see *SI Text*, section 17). As in the experiment, the two force profiles obtained from the simulations of the truncated TK (Fig. 3*B Top* and *Middle*) are largely similar. A notable exception is the more pronounced force peak seen in the presence of ATP (see Fig. 3*B Inset*) at the position of the measured force peak 2*. To allow direct comparison of the unfolding pathways between experiment and simulation, we transformed the force extension traces of Fig. 2 into barrier position histograms (14) and derived the same from our simulations (see *SI Text*, section 18). The two histograms agree well both in the presence and absence of ATP [Fig. 4 (dashed lines) and Fig. S7], allowing the conclusion that the main unfolding events are correctly described by the simulations.

Next, we investigated which molecular interactions determine the observed force peaks. For the ATP peak 2*, two strong interactions are seen, a salt bridge from lysine-36 to the $\alpha$-phosphate group of ATP, and a contact between methionine-34 and the adenine moiety of ATP (Fig. 3*C*). Both interactions break irreversibly upon $\beta$C3-$\beta$C4 rupture, giving rise to the significantly larger force peak of 270 ± 39 pN in the simulations with bound ATP as compared with 188 ± 13 pN without ATP (Fig. 3*B Inset* and Movie S1). Notably, in the AFM experiment, the contour length of 51.6 nm for the ATP peak position (Fig. 4, peak 2*) also points to a residue close to lysine-36. An additional peak is seen at 18 nm for the simulation with ATP present (plus sign in Fig. 3*B Top*). Here, a force-induced deformation of the N-terminal domain triggers the transient rupture and reformation of the methionine-34–ATP and lysine-36–ATP interactions.

Closer structural analysis of our simulations suggests the following sequence of events (colors in Fig. 3 *A* and *B*, and Fig. 4). Peak 1 (Fig. 4) is caused by unfolding of the 23-residue linker at the N terminus of TK, which is not present in the simulations (see *SI Text* for details). At peak 2, the autoinhibitory tail is unfolded and removed, rendering the ATP binding site accessible (region shaded in gray in Fig. 3*B Bottom*). Subsequently, N-terminal $\beta$-sheets $\beta$C1-$\beta$C2 and $\beta$C2-$\beta$C3 rupture (regions B and C). For these events, no force peak is seen in the experiment, because it would fall into the lag time after force peak 2. Peak 2* described above is dominated by interactions of ATP with the binding pocket. The truncated construct necessarily lacks part of the autoinhibitory tail stabilizing the adjacent C-terminal $\alpha$-helix $\alpha$R1 in the full-length TK. Accordingly, $\alpha$R1 unfolds first in the truncated kinase (Fig. 3*B Top* and *Middle*, region A) but after $\beta$R1 and $\alpha$R2 in the autoinhibited kinase (Fig. 3*B Bottom*). Hence, and in agreement with the complete TK unfolding simulations (Fig. 3*B Bottom*), peaks 3 and 4 are assigned to unfolding of $\alpha$C1 and $\beta$C4-$\beta$C5, respectively (regions D and E). Finally, peak 5 arises from the combined effect of $\alpha$C2 and $\alpha$C8 rupture (Fig. 3*B Bottom*). At peak 6, the complete TK is unfolded and stretched. Taking the diameter of the folded TK into account (5.5 nm), the contour length increment to peak 1 (121 nm) corresponds to (5.5 + 121 ± 2) nm/0.365 nm = 346 ± 5 residues, in agreement with the 344 aa of TK including its N-terminal linker (see *SI Text*, section 7).

**Autophosphorylation of TK.** Our simulations show that the open ATP binding site does not relieve autoinhibition of the catalytic base aspartate-127 by tyrosine-170. However, our model of the ATP-bound state of TK suggests that this semi-opened state might autophosphorylate, in agreement with previous predictions of the open apo-enzyme (11). We tested this notion by assaying recombinant TK with its ATP binding site released (TK-kin3, mimicking the mechanically induced open state after peak 2), and found that the release of ATP binding not only activates kinase activity toward substrates like telethonin, but also allows tyrosine autophosphorylation (see *SI Text*, sections 1 and 2, for experimental details). As shown in Fig. 5, although low levels of phosphotyrosine are detected by the 4G10 antibody before incubation with ATP, tyrosine phosphorylation is strongly stimulated by ATP, with a preference toward Mn$^{2+}$, similar to other enzymes (26, 27).

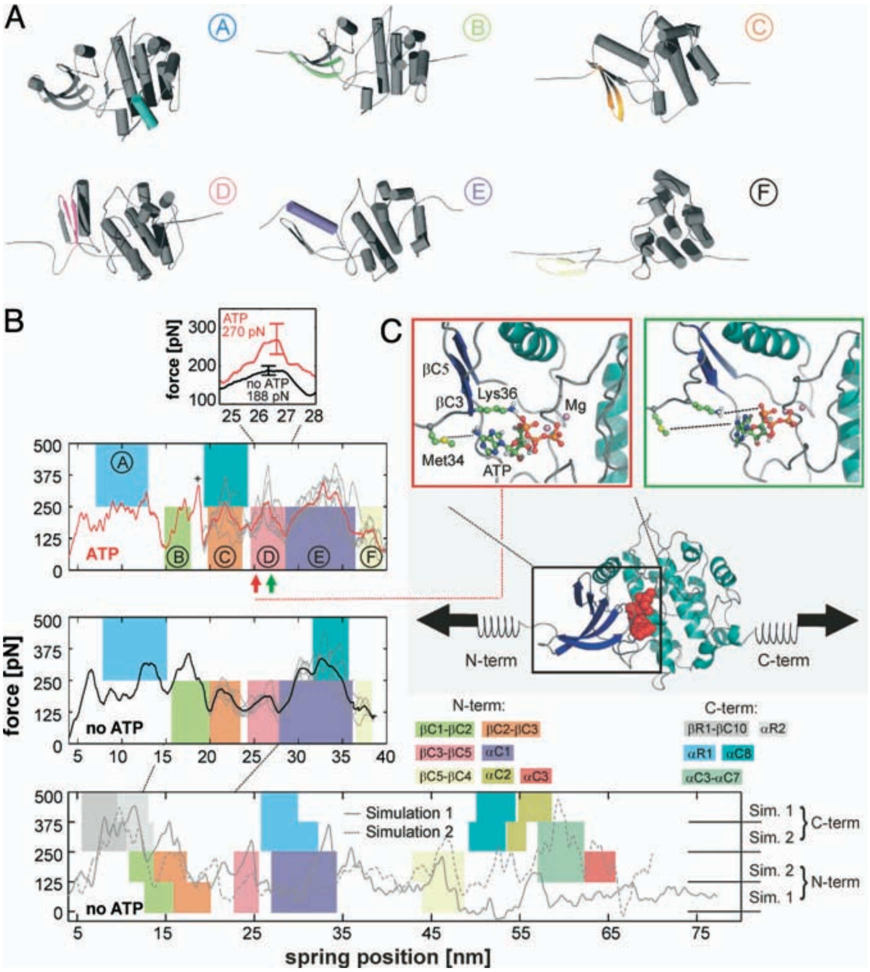

**Fig. 3.** Molecular dynamics (MD) simulations of the force-induced unfolding of titin kinase (TK). (*A*) Representative unfolding intermediates with the unfolding secondary structure elements colored according to the scheme in Fig. 1*D*; the β-strands unfold pairwise, and colors refer to the respective N-terminal strand of each pair. (*B*) Unfolding forces of truncated TK with ATP (*Top*), without ATP (*Middle*), and of the complete TK (*Bottom*). For the complete TK, two independent 90-ns simulations were carried out (solid and dashed lines). Starting from a partially unfolded structure at ≈19 nm, five 26-ns trajectories (thin gray lines) were averaged for both sets of simulations (thick lines in *Top* and *Middle*). Color-shaded areas indicate main unfolding events, which correspond to the colors used in *A* and in Fig. 1*D*. An additional force peak in the presence of ATP is predicted (plus sign and pink-shaded area in *Top*). This force peak (*Inset*) is higher for bound ATP (270 pN) than for an empty binding pocket (188 pN). Because of the necessarily much faster pulling rates of 0.8 m/s used for the simulations, larger unfolding forces are seen, which can be related to the experimental loading rates (11). (*C*) In the force–probe MD simulations, harmonic springs were attached to the protein and retracted with constant velocity (lower schematic, ATP shown as red spheres). (*C Insets*) Representative structures shortly before (*Left*) and after (*Right*) the ATP force peak. ATP and the two key residues methionine-34 and lysine-36 are shown in ball-and-stick representation, and the rupture of molecular interactions is indicated by dotted lines.

## Discussion

Our results show that mechanical stress is able to activate titin kinase by releasing the active site for ATP binding, and they unravel the first step of this mechanical signaling pathway. We also show that mechanical release of the ATP binding site allows a second step in TK activation by triggering autophosphorylation on the inhibitory tyrosine. That TK can thus indeed act as a biological force sensor is supported by the fact that the forces activating ATP binding are within the physiological range and, importantly, lower than the ones unfolding the surrounding structural titin domains. Small force imbalances of four to eight myosin motor domains, equivalent to ≈3% of the 147 myosin molecules (1) between adjacent thick filaments could thus translate into a physiologically significant signal by activation of the TK mechanosensor. Similarly, the "gating distance" between the open and closed state of the TK active site, as the distance between peaks 1 and 2, is 9 nm. The reversible increase in the width of the 14.5-nm x-ray reflection during contraction of striated muscle indicates axial displacement between adjacent myosin filaments on the order of 10 nm (28, 29), which would translate into shear strain on the M-band. Both the forces and displacements required for mechanical TK activation are therefore within the ranges observed in muscle.

Once the ATP binding site is opened by mechanical force, not only does the enzyme bind ATP, but it actually undergoes the next necessary step for full activation, the phosphorylation of the autoinhibitory tyrosine-170. Rather than leading to a dead end, mechanical activation of ATP binding thus activates the full catalytic activity of TK. This mechanism may be particularly relevant when the sarcomere is extended while generating active tension due to an opposing force greater than that generated by the muscle, also called eccentric exercise (9). Under such conditions, large changes in M-band structure are observed (30). Eccentric exercise is a strong stimulator for muscle growth and repair (31–34), and the interaction of titin kinase with ubiquitin-associated scaffold proteins with links to multiple signaling pathways controlling muscle gene expression and protein turnover (12) supports plausibly that titin kinase can act as a force sensor in the activated sarcomere. Unlike

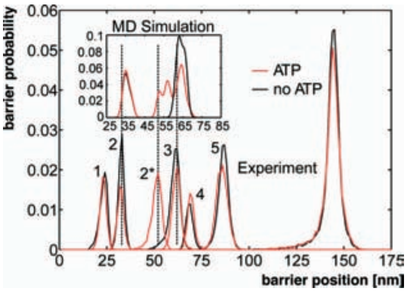

**Fig. 4.** Contour length histograms obtained from single-molecule force spectroscopy experiments (transformation with QM-WLC and $P = 0.8$ nm) and from MD simulations (*Inset*). The folded kinase construct has a length of 25 nm. The peak positions with (red) and without (black) ATP are similar in both histograms (dashed lines), except for one additional peak in the presence of ATP (red peak at ≈51.6 nm). The experimentally determined contour length increments are, in the absence of ATP, 9.1, 28.6, 7.3, 18.0, 57.9 nm; and, in the presence of ATP, 9.1, 19.4, 10.1, 7.5, 16.4, 58.3 nm—with an estimated error of ±2%. The position of the initial peak (24 nm) reflects the mean length of the TK construct with completely folded domains.

the homologous nematode kinases, which retain catalytic activity in their inhibited form (13), we show that TK is completely inactive in its autoinhibited form. Mechanical switching of its ATP-binding site thus confers a significant signal between active and inactive kinase, as expected for a signal that modulates energy-costly processes like protein breakdown and transcriptional activity (12).

Our surprising observation that a protein kinase can be activated by local protein unfolding induced by mechanical force may find analogies in the small GTPase Rab8, whose activation by the nucleotide exchange factor MSS4 also involves local protein unfolding (35). The mechanoenzymatic sensor found in titin kinase may therefore be paradigmatic also for other members of the family of cytoskeletal autoregulated protein kinases, a branch of the calcium-calmodulin-regulated enzymes of the human kinome (36), containing myosin light-chain kinase and obscurin kinases. These enzymes share with titin the N- and C-terminal cytoskeletal association (37) or specific residues involved in autoinhibition (38) and may thus bear features of mechanical modulation. Furthermore, other autoregulated cytoskeletal signaling domains, like GDP-GTP exchange factor domains, may be similarly activated. Our single-molecule approach will therefore be useful for investigating the mechanochemistry of many cellular systems that may share similar mechanosensitive regulation mechanisms.

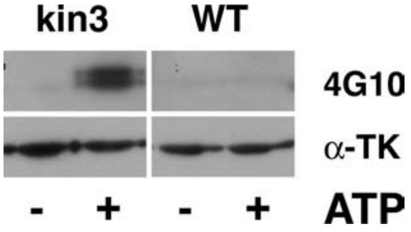

**Fig. 5.** Autophosphorylation of TK on tyrosine. Incubation of the highly purified TK-kin3 enzyme in the absence (−) and presence (+) of ATP and $Mn^{2+}$ ions leads to tyrosine phosphorylation detected by Western blot, using the phosphotyrosine antibody 4G10. The autoinhibited kinase construct A168-M2 (WT) shows no appreciable phosphotyrosine incorporation under any tested condition. Lower blot: loading control, detection with anti-titin kinase antibody (α-TK).

## Materials and Methods

Titin kinase expression was carried out in sf9 insect cells by using a recombinant baculovirus system essentially as described in ref. 5. Purification and enzymatic assays were performed essentially as described in refs. 5 and 12 (for details, see *SI Text*). Atomic force microscopy using a custom-built instrument, and analysis of the data were carried out essentially as described (14, 19); for details see the SI. Force–probe molecular dynamics simulations (24, 25) used the TK x-ray structure [Protein Data Bank entry 1TKI (5)] as the starting structure, with the autoinhibitory tail partly removed. Two sets of simulations (five each) were carried out for this truncated TK, one set with an empty binding pocket, and one with an ATP molecule and magnesium ions inserted into the (closed) binding pocket. As a control, the autoinhibited complete TK was also subjected to force–probe MD simulations. For further details, see *SI Text*.

**ACKNOWLEDGMENTS.** We thank Thorsten Kampmann for help with the ATP force field and Carsten Kutzner for help with the GROMACS force probe code. U.H. and L.V.S. were supported by the Deutsche Forschungsgemeinschaft (research training group 782 and SFB Grant 755). L.V.S. was supported by the Boehringer Ingelheim Fonds and by the European Union. This work was supported by the Center for Integrated Protein Science Munich and the Medical Research Council of the United Kingdom.

1. Tskhovrebova L, Trinick J (2003) Titin: Properties and family relationships. *Nat Rev Mol Cell Biol* 4:679–689.
2. Hoshijima M (2006) Mechanical stress-strain sensors embedded in cardiac cytoskeleton: Z disk, titin, and associated structures. *Am J Physiol* 290:H1313–H1325.
3. Labeit S, Gautel M, Lakey A, Trinick J (1992) Towards a molecular understanding of titin. *EMBO J* 11:1711–1716.
4. Obermann WMJ, *et al.* (1996) The structure of the sarcomeric M band: Localization of defined domains of myomesin, M-protein and the 250 kD carboxy-terminal region of titin by immunoelectron microscopy. *J Cell Biol* 134:1441–1453.
5. Mayans O, *et al.* (1998) Structural basis of the activation of the titin kinase domain during myofibrillogenesis. *Nature* 395:863–869.
6. Vogel V (2006) Mechanotransduction involving multimodular proteins: Converting force into biochemical signals. *Annu Rev Biophys Biomol Struct* 35:459–488.
7. Horowits R, Podolsky RJ (1987) The positional stability of thick filaments in activated skeletal muscle depends on sarcomere length: Evidence for the role of titin filaments. *J Cell Biol* 105:2217–2223.
8. Akiyama N, Ohnuki Y, Kunioka Y, Saeki Y, Yamada T (2006) Transverse stiffness of myofibrils of skeletal and cardiac muscles studied by atomic force microscopy. *J Physiol Sci* 56:145–151.
9. Agarkova I, Ehler E, Lange S, Schoenauer R, Perriard JC (2003) M-band: A safeguard for sarcomere stability? *J Muscle Res Cell Motil* 24:191–203.
10. Agarkova I, Perriard JC (2005) The M-band: An elastic web that crosslinks thick filaments in the center of the sarcomere. *Trends Cell Biol* 15:477–485.
11. Grater F, Shen J, Jiang H, Gautel M, Grubmuller H (2005) Mechanically induced titin kinase activation studied by force-probe molecular dynamics simulations. *Biophys J* 88:790–804.
12. Lange S, *et al.* (2005) The kinase domain of titin controls muscle gene Expression and protein turnover. *Science* 308:1599–1603.
13. Greene D, *et al.* (2008) Single-molecule force spectroscopy reveals a stepwise unfolding of Caenorhabditis elegans giant protein kinase domains. *Biophys J* 95:1360–1370.
14. Puchner E, Franzen G, Gautel M, Gaub H (2008) Comparing proteins by their unfolding pattern. *Biophys J* 95:426–434.
15. Fukuzawa A, *et al.* (2008) Interactions with titin and myomesin target obscurin and its small homologue, obscurin-like 1, to the sarcomeric M-band: Implications for hereditary myopathies. *J Cell Sci* 121:1841–1851.
16. Flaherty D, *et al.* (2002) Titins in C. elegans with unusual features: Coiled-coil domains, novel regulation of kinase activity and two new possible elastic regions. *J Mol Biol* 323:533–549.
17. Moerman DG, Benian GM, Barstead RJ, Schreifer LA, Waterston RH (1988) Identification and intracellular localization of the unc-22 gene product of Caenorhabditis elegans. *Genes Dev* 2:93–105.
18. Rief M, Gautel M, Schemmel A, Gaub HE (1998) The mechanical stability of immunoglobulin and fibronectin III domains in the muscle protein titin measured by atomic force microscopy. *Biophys J* 75:3008–3014.
19. Rief M, Gautel M, Oesterhelt F, Fernandez JM, Gaub HE (1997) Reversible unfolding of individual titin Ig-domains by AFM. *Science* 276:1109–1112.
20. Kedrov A, Krieg M, Ziegler C, Kuhlbrandt W, Muller DJ (2005) Locating ligand binding and activation of a single antiporter. *EMBO Rep* 6:668–674.
21. Lew J, Taylor SS, Adams JA (1997) Identification of a partially rate-determining step in the catalytic mechanism of cAMP-dependent protein kinase: A transient kinetic study using stopped-flow fluorescence spectroscopy. *Biochemistry* 36:6717–6724.
22. Knighton DR, *et al.* (1991) Crystal structure of the catalytic subunit of cyclic adenosine monophosphate-dependent protein kinase. *Science* 253:407–420.
23. Bossemeyer D, Engh R, Kinzel V, Ponstingl H, Huber R (1993) Phosphotransferase and substrate binding mechanism of the cAMP-dependent protein kinase catalytic subunit from porcine heart as deduced from the 2.0 Å structure of the complex with $Mn^{2+}$ adenylyl imidodiphosphate and inhibitor peptide PKI(5–24). *EMBO J* 12:849–859.
24. Grubmuller H, Heymann B, Tavan P (1996) Ligand binding: Molecular mechanics calculation of the streptavidin-biotin rupture force. *Science* 271:997–999.

25. Izrailev S, Stepaniants S, Balsera M, Oono Y, Schulten K (1997) Molecular dynamics study of unbinding of the avidin-biotin complex. *Biophys J* 72:1568–1581.
26. Cobb MH, Sang BC, Gonzalez R, Goldsmith E, Ellis L (1989) Autophosphorylation activates the soluble cytoplasmic domain of the insulin receptor in an intermolecular reaction. *J Biol Chem* 264:18701–18706.
27. Tennagels N, Hube-Magg C, Wirth A, Noelle V, Klein HW (1999) Expression, purification, and characterization of the cytoplasmic domain of the human IGF-1 receptor using a baculovirus expression system. *Biochem Biophys Res Commun* 260:724–728.
28. Huxley HE, Faruqi AR, Kress M, Bordas J, Koch MH (1982) Time-resolved x-ray diffraction studies of the myosin layer-line reflections during muscle contraction. *J Mol Biol* 158:637–684.
29. Linari M, *et al.* (2000) Interference fine structure and sarcomere length dependence of the axial x-ray pattern from active single muscle fibers. *Proc Natl Acad Sci USA* 97:7226–7231.
30. Suzuki S, Sugi H (1983) Extensibility of the myofilaments in vertebrate skeletal muscle as revealed by stretching rigor muscle fibers. *J Gen Physiol* 81:531–546.
31. Goldspink, G, Williams, P, Simpson, H (2002) Gene expression in response to muscle stretch. *Clin Orthop Relat Res* S146–152.
32. Barash IA, Mathew L, Ryan AF, Chen J, Lieber RL (2004) Rapid muscle-specific gene expression changes after a single bout of eccentric contractions in the mouse. *Am J Physiol* 286:C355–C364.
33. Carlsson L, Yu J-G, Moza M, Carpen O, Thornell L-E (2007) Myotilin—A prominent marker of myofibrillar remodelling. *Neuromuscular Disorders* 17:61–68.
34. Eliasson J, *et al.* (2006) Maximal lengthening contractions increase p70 S6 kinase phosphorylation in human skeletal muscle in the absence of nutritional supply. *Am J Physiol* 291:E1197–E1205.
35. Itzen A, Pylypenko O, Goody RS, Alexandrov K, Rak A (2006) Nucleotide exchange via local protein unfolding—Structure of Rab8 in complex with MSS4. *EMBO J* 25:1445–1455.
36. Manning G, Whyte DB, Martinez R, Hunter T, Sudarsanam S (2002) The protein kinase complement of the human genome. *Science* 298:1912–1934.
37. Kamm KE, Stull JT (2001) Dedicated myosin light chain kinases with diverse cellular functions. *J Biol Chem* 276:4527–4530.
38. Fukuzawa A, Idowu S, Gautel M (2005) Complete human gene structure of obscurin: Implications for isoform generation by differential splicing. *J Muscle Res Cell Motil* 26:427–434.

# Supporting Information

## Puchner *et al.* 10.1073/pnas.0805034105

### SI Text

**1. Expression and Purification of Titin Kinase.** Three titin kinase constructs were expressed for this study: A168-M2 (867 aa, from 24422 to 25288 in human cardiac N2-B titin, accession number NP_003310.3); A168-M2 K36A, where lysine 24783 is mutated to alanine; and TK-kin3 (314 aa, from 24725 to 25038 in NP_003310.3), where the autoregulatory tail is partially removed to expose the ATP binding site (2). The boundaries of TK-kin3 mimic the mechanically opened state where the autoinhibitory tail is removed apart from the mechanostable $\alpha$R1 helix (see molecular dynamics section for details). The numbering of the constructs can be converted to that of the amino acids in the titin kinase structure [Protein Data Bank (PDB) entry 1TKI] by subtracting 24747 from the amino acid numbers in N2B titin NP_003310.3, respectively, by adding 24747 to the numbers in 1TKI. A conversion table for residues discussed in the manuscript is given in Table S1. The cDNAs encoding these constructs were cloned into a modified baculovirus shuttle plasmid and N-terminally fused to a tag sequence encoding, from the N terminus, a hexa-histidine tag, HA-tag, and TEV cleavage site. Constructs were verified by DNA sequencing. After generation of recombinant virus, expression was carried out in suspension cultures of *Spodoptera frugiperda* sf9 cells essentially as described (3). Soluble protein was purified at a yield of 6 mg/liter of culture for A168-M2, and 20 $\mu$g/liter for TK-kin3 and purified by sequential nickel-affinity chromatography, ion-exchange chromatography on a Mono Q column, and size-exclusion chromatography on a Superdex 75 column (GE Healthcare). For some experiments, the His-tag sequence was cleaved off by TEV protease, but the presence or absence of the tag had no detectable influence on kinetic parameters or unfolding characteristics. Final fractions were >99.5% pure as judged from overloaded gels (Fig. S1). Protein was stored in small aliquots at a concentration of 1 mg/ml in 20 mM 2-[4-(2-hydroxyethyl)-1-piperazine]ethanesulfonic acid (Hepes)/KOH (pH 7), 2 mM $MgCl_2$, 50 mM NaCl, 2 mM DTT, and 10% glycerol in liquid nitrogen. Identity of the proteins was ascertained by gel electrophoresis, analytical gel filtration, Western blots using anti-titin kinase antibodies (4), and mass spectrometry (MS). MS confirmed not only the correct molecular weight for TK-kin3, but also detected two bound magnesium ions in this open form of the kinase, indicating that protein kinases bind $Mg^{2+}$ independently of ATP. Kinase assays with recombinant telethonin showed that only kin3, but not the long forms of the kinase, showed protein kinase activity *in vitro*.

**2. Kinase Assays.** Michaelis–Menten kinetics of TK was performed similarly as described for phosphorylase kinase (5) but using telethonin as substrate at a constant concentration of 10 $\mu$M in assay buffer [20 mM Hepes/KOH (pH 7), 5 mM $MgCl_2$, 5 mM DTT]. ATP concentrations varied from 165 nM to 800 $\mu$M for kinetic analysis with a constant 165 nM [$\gamma$-$^{33}$P]ATP label. Samples were taken from triplicate assays at regular intervals from 20-$\mu$l reaction mixtures, spotted on nitrocellulose, and immediately quenched in 5% ice-cold trichloroacetic acid (TCA). After several washes with TCA, the filters were dried and protein-incorporated radioactivity determined by liquid scintillation counting. After correction for background (label and telethonin, no enzyme), the averaged protein phosphorylation rate expressed as $\mu$mol/minute was fitted to the Michaelis–Menten equation by using Mathematica, and $K_M$ was derived. Results are summarized in Table 1.

**3. Autophosphorylation of Titin Kinase.** Highly purified TK kin3 (see above) was incubated at 30°C in assay buffer supplemented with 0.1 mM sodium orthovanadate in the absence and presence of ATP, with either 5 mM $Mg^{2+}$ or $Mn^{2+}$ as counterion (6). The reaction was stopped after 20 min by addition of Laemmli sample buffer, and the samples were electrophoresed on 14% SDS-polyacrylamide gels. After Western blotting of the gels by standard procedures, phosphotyrosine was detected by using the 4G10 monoclonal antibody (Upstate Biotechnology) and a site-specific anti-titin kinase antibody raised against the peptide APEYY($PO_4$)APE, which specifically reacts with titin kinase phosphorylated on tyrosine 170.

Both antibodies detect the formation of phosphotyrosine under these conditions, and autoradiographs of assays in the presence of [$\gamma$-$^{33}$P]ATP demonstrate label incorporation. Similar assays were performed at several enzyme concentrations (0.5, 1, 2, and 5 $\mu$M) in the presence of 165 nM [$\gamma$-$^{33}$P]ATP label and 100 $\mu$M total ATP, and TK-incorporated radiolabel was determined as above to test for concentration dependence of phosphate incorporation. The correlation of label incorporation was linear with enzyme concentration, suggesting that the phosphorylation occurred intramolecularly (7).

### Atomic Force Microscopy (AFM) Measurements

**4. AFM Sample Preparation.** Microscope slides were washed with denatured ethanol and $H_2O_{dd}$ in a supersonic bath. After drying, a layer of 4-nm Cr/Ni followed by a layer of 40-nm Au was evaporated onto the surface. Twenty microliters of the protein solution (1 mg/ml) was incubated for 20 min on the gold surface and washed three times with the measurement buffer, consisting of 40 mM Hepes/KOH, 2 mM $MgCl_2$, 2 mM DTT (pH 7.2), and, depending on the experiment, 2 mM ATP.

**5. AFM Measurements.** All force spectroscopy measurements were performed with a custom-built and completely automated AFM (Fig. S2). The instrument is controlled with an Asylum Research MFP3D controller and Igor Pro 5.0 (WaveMetrics). The software was written such that it automatically adjusts the height of the AFM and the position of the photodiode to compensate for instrument and cantilever drift. If an experiment is performed at several pulling speeds, the software periodically changes the speed after each force extension trace to allow a better comparison. In this way, force extension traces can be recorded for several days with the same sample and the same cantilever. To avoid evaporation of the buffer, a fluid cell consisting of Teflon and a latex membrane seals the probe volume during the experiment.

After calibration of the cantilevers (Olympus biolevers A) using the equipartition theorem (8), the automated measurement was started as described above. Because the surface is not homogeneously covered with the non-specifically adsorbed protein constructs, the *x*–*y* scanner of the AFM moves the sample by 20 nm after each trace. In this way, the number of traces showing unfolding of the protein construct is enhanced and in each trace a new molecule is picked up that was not unfolded before.

**6. Selection of Traces.** In single-molecule force spectroscopy experiments, the density of molecules attached to the surface has to be low enough to address individuals. Therefore, in ≈95% of measurement cycles, the approach of the cantilever to the surface does not result in a contact with a molecule. Furthermore, the protein construct is contacted at random positions resulting in traces that do not show unfolding of the complete titin kinase. Because the protein construct contains three domains at the N terminus of the titin kinase and two on its C terminus, all traces showing more than three domains must contain the unfolding of the complete enzyme. Because of the small tip radius of the AFM cantilever (30 nm), traces showing more than one protein construct in parallel are very rare. They can be identified by the higher forces and by the superposition of their unfolding patterns that are in most of the cases shifted with respect to each other. In total, ≈1% of the recorded traces show the unfolding of one individual titin kinase molecule and are therefore selected for further analysis.

Because of the large amount of traces recorded for this study, and the low efficiency of complete unfolding traces due to the reasons mentioned above, we developed a method that allows automated selection of traces and recognition of unfolding patterns (1). In a first step, force extension traces are transformed into contour length space by using the QM-WLC model (9). In the next step, contour length histograms are obtained that directly reflect the barriers of the unfolding potential. This fingerprint is independent of fluctuations and variable experimental parameters and therefore can be used to screen for characteristic patterns. In this study, we adjusted the parameters such that only traces were selected showing more than three Ig-domains with a barrier spacing of ≈30 nm.

Because the folded protein construct is contacted at random positions, the initial part of a force extension varies in length. This variable offset can be determined choosing the rupture of the first Ig-domain as the point of reference. This has to be taken into account in superpositions of force extension traces or averaged barrier position histograms (Fig. S3). Once we identified the complete unfolding pattern of the titin kinase, we also took traces into account that show less than four Ig-domains but contain the complete unfolding pattern of the enzyme. In these cases, the protein construct was either picked up at its ends but de-adsorbed before all domains were unfolded, or it was contacted at the surrounding domains so that complete unfolding of the titin kinase took place.

***Overview of the number of recorder traces. Recorded total traces, 392,000; total traces with some captured "bait," ≈30,000; total complete kinase traces, 2,100.*** Therefore, in ≈95% of measurement cycles, the approach of the cantilever to the surface does not result in a contact with a molecule. Because of the random attachment of the molecules, a substantial number of these traces are incomplete and contain mostly just some Ig/Fn domain unfolding signatures.

Traces with complete kinase signature used for analysis were as follows: kinetics with WT, 812 complete kinase traces; kinetics with K72A mutant, 962 complete kinase traces; concentration series with WT, 275 complete kinase traces; concentration series with K72A mutant, 348 complete kinase traces.

**7. Molecular Calibration by Using Ig/Fn Domains.** To confirm the proper calibration of the AFM, we compare the experimental contour length increments of Ig/Fn domain unfolding with the expected ones. The theoretical values are obtained in the following way. First, the number of folded amino acids is multiplied by 0.365 nm (corresponding to the separation of the C$\alpha$ atoms of two adjacent amino acids in the completely extended conformation), which results in the complete contour length of the protein domain. In the next step, the diameter of the folded domain is subtracted from the complete contour length to obtain the experimentally visible contour length. This can be better seen if the gedanken experiment is performed backwards: if the two ends of a completely stretched Ig/Fn domain are brought together until the domain is in its globular folded conformation, then the distance between the attachment points corresponds with the diameter of the folded domain. Because this conformation is the starting point for the length measurement, the domain diameter is missing and has therefore to be subtracted from the complete contour length if compared with the experimental one (Table S2). The theoretical mean contour length of 30.86 nm deviates from the experimental one, determined in Fig. S4 to be 30.45 nm, by only 1%.

**8. Influence of Ig Domains on the Unfolding Pattern.** The use of spacer domains that provide their fingerprint for the selection of force extension traces has become a widespread approach (10). Although the unfolding pattern of these spacer domains is well studied, we verified the interpretation of force extension traces by performing experiments with TK protein constructs containing three and five spacer domains. As can be seen in Fig. S5, the maximum number of equal intervals corresponding to a contour length increment of ≈30 nm perfectly correlates with the number of spacer domains. Although the initial part of titin kinase unfolding is not so clearly resolved with *Escherichia coli*-expressed protein constructs (most likely because of folding differences, in agreement with *E. coli*-derived protein being catalytically inactive), this experiment justifies the interpretation that allows to separate unfolding of the titin kinase from unfolding of spacer domains.

**9. Unfolding Behavior of the Titin Kinase at 37°C.** Although also the titin of cold-blooded animals contains the titin kinase domain (e.g., frogs and fish), we investigated the unfolding pattern of the TK protein construct at 37°C. For these measurements, the whole AFM setup was put into a temperature-controlled oven, where force extension traces were recorded. We found that the unfolding forces of the titin kinase are smaller (≈30 pN) than at room temperature (≈50 pN) because the energy barriers are overcome more easily due to the higher thermal energy. This observation is consistent with other studies (11, 12). However, the unfolding pattern was found to be the same as the one observed at room temperature (Fig. S6). Therefore, we conclude that the structure and function of titin kinase is the same at both temperatures, allowing its investigation under the experimentally more stable conditions.

**10. Detection of Force-Induced ATP Binding and Determination of the Reaction Kinetics.** As shown, binding of ATP to the titin kinase causes an additional energy barrier in the unfolding pathway. By counting the traces showing this barrier, the relative frequency of ATP binding can be determined. Because the activation is mechanically triggered, the binding process takes place in chemical nonequilibrium and can be described as follows. Let TK* be the activated enzyme with accessible binding pocket and TK*:ATP the titin kinase–ATP complex. Then, the probability $P_{\mathrm{TK^*:ATP}}(t)$ of finding the complex after a reaction time $t$ is given by the simple differential equation

$$\frac{dP_{\mathrm{TK^*:ATP}}(t)}{dt} = k_{\mathrm{on}}[\mathrm{ATP}] - k_{\mathrm{off}} P_{\mathrm{TK^*:ATP}}(t), \qquad [1]$$

where $k_{\mathrm{on}}$ and $k_{\mathrm{off}}$ are the association and the dissociation rates of ATP. Solving this equation yields

$$P_{\mathrm{TK^*:ATP}}(t) = \frac{k_{\mathrm{on}}}{k_{\mathrm{on}} + k_{\mathrm{off}}}\left(1 - e^{-(k_{\mathrm{on}}+k_{\mathrm{off}})t}\right). \qquad [2]$$

This model perfectly describes our experimental data and allows us to determine the kinetic parameters of ATP binding. The experimental time scale is given by the inverse ratio of the pulling speed and the extension increase, during which the ATP binding pocket is accessible and still correctly folded. This extension increase was determined with MD simulations and values 18 nm. The errors of the experimentally determined kinetic parameters are mainly due to the fact that a limited number of random samples is available. Therefore, the errors are calculated by using the beta function and assuming a 95% confidence interval to be certain.

**11. Molecular Dynamics (MD) Simulations.** All simulations were carried out with the GROMACS simulation suite (13, 14), using the OPLS all-atom force field (15) and periodic boundary conditions. NpT ensembles were simulated, with the protein and solvent coupled separately to a 300-K heat bath ($\tau_T = 0.1$ ps) (16). The systems were isotropically coupled to a pressure bath at 1 bar ($\tau_p = 1.0$ ps) (16). Application of the Lincs (17) and Settle (18) algorithms allowed for an integration time step of 2 fs. Short-range electrostatic and Lennard–Jones interactions were calculated within a cut-off of 1.0 nm, and the neighbor list was updated every 10 steps. The particle mesh Ewald (PME) method was used for the long-range electrostatic interactions (19), with a grid spacing of ≈0.12 nm.

**12. ATP Force Field.** The atomic partial charges of ATP used along with the OPLS force field were derived from quantum chemical calculations. The charges were obtained from B3LYP/6–31+G* calculations using the CHELPG electrostatic potential fitting scheme (20). The quantum chemical calculations were carried out with Gaussian 03 (21). All nonbonded parameters are given in Tables S3 and S4. Bonded parameters were taken from ref. 22.

**13. Generation of Starting Structure.** The simulations of the full-length titin kinase (TK) were set up as described in ref. 23, with the exception that, here, the OPLS force field was used (see above).

The starting structures of the truncated TK were obtained from the TK crystal structure (PDB entry 1TKI) (3) in three steps detailed below. First, 33 residues at the C terminus comprising the $\beta$R1 and $\alpha$R2 motives of the autoinhibitory tail (ai tail) were removed from the structure, because they block the ATP binding site. Second, the ATP ligand was docked into the active site. Third, the ligand-induced conformational closure of the protein structure was enforced by MD.

**14. Docking of ATP.** ATP was docked into the active site of TK by using the protein kinase A (PKA) (PDB entry 1Q24) (24) as a homology model. After aligning of the two protein structures, the ATP and one $Mg^{2+}$ ion were adopted from PKA. The second $Mg^{2+}$ ion was added by using the phosphorylase kinase structure as a template (PDB entry 2PHK) (25), because it was not resolved in the PKA structure.

**15. Energy Minimization and Equilibration of the Solvent.** Before the free MD simulations, the systems were solvated with TIP4P water within a cubic box of 8.5 nm length. Sodium and chloride ions were added ($c \approx 0.15$ mol/liter), and the systems were energy-minimized for 1,000 steps by using steepest descent. The solvent was then equilibrated for 500 ps with positional restraints on the protein heavy atoms (force constant 1,000 kJ·mol$^{-1}$·nm$^{-2}$).

**16. Closure of the Active Site.** The ligand-induced conformational closure of the protein structure was enforced by means of essential-dynamics MD (26). To this end, the closed conformation of the PKA (1Q24) was used as the target structure. First, the two protein structures (TK and PKA) were aligned. Then, the N-terminal $\beta$-hairpin (residues 13–21 in TK) was selected, and a principal component analysis (PCA) was carried out, yielding one eigenvector that describes the closing motion. Essential dynamics sampling was then performed, during which motion along the eigenvector toward the target structure was enforced [radcon option in EDsampling module (27) of GROMACS]. To allow the protein to relax along the enforced closing motion, the maximal step size along the eigenvector was restricted to a maximum of 0.05 pm per step, leading to a closed structure within ≈1 ns. Subsequently, the closed structure was simulated for 1 ns with positional restraints on the $C^\alpha$ atoms (force constant 1,000 kJ·mol$^{-1}$·nm$^{-2}$). Finally, a 1-ns free MD simulation was carried out, during which no opening motion was observed in the presence of ATP. As a control, the closed structure was simulated also in the absence of ATP. As expected, significant reopening motion was observed. The starting conformation for the force-probe MD simulations were taken from the final free MD simulations after 1 ns.

In the resulting structure with ATP bound, a salt bridge between Lys-36 and the $\alpha$-phosphate group of ATP, and interaction between Met-34 and the adenine moiety, respectively, were formed. For the latter, two types of interactions with ATP are seen, a hydrogen bond between the sulfur atom and the $NH_2$ group of adenine, and, alternatively, a stacked conformation of the S-$CH_3$ group and the adenine 6-ring. Additional hydrogen bonds were formed between the $\beta$-phosphate of ATP and the N-H backbone of Glu-17, as well as between the hydroxyl groups of the ribose and the carbonyl backbone of Arg-15.

**17. Force–Probe MD Simulations.** To mimic the AFM experiments, force–probe MD simulations (FPMD) were carried out (28, 29). In these simulations, a harmonic spring was attached to the carbon atom of the carboxyl C terminus and one to the nitrogen atom of the amino N terminus, each described by a spring potential,

$$V_{\mathrm{spring},i}(t) = \frac{k_0}{2}\left(z_i - z_{\mathrm{spring},i}(t)\right)^2, \qquad [3]$$

which was included within the force field. In Eq. **3**, $k_0 = 500$ kJ·mol$^{-1}$·nm$^2$ is the force constant of the spring, $z_i$ is the position of the pulled atom $i$, and $z_{\mathrm{spring},i}$ is the position of the spring that is attached to atom $i$. The springs were then moved with constant velocity $v = 0.4$ m/s in opposite directions, $z_{\mathrm{spring},i}(t) = z_i(0) \pm vt$. Because of the moving springs, the pulled atoms experienced an additional force

$$F_i = k_0\left(z_i - z_{\mathrm{spring},i}(t)\right). \qquad [4]$$

The average force at the two springs was monitored during the simulations, yielding the force profiles shown in Fig. 3*B*.

Before the FPMD simulations, the protein was aligned along the pulling direction ($z$ axis), and the simulation box was extended along the $z$ axis to ≈20 nm, allowing for the accommodation of an elongated conformation. Further, water, sodium, and chloride ions ($c \approx 0.15$ mol/liter) were added, and the system was energy-minimized, followed by equilibration for 200 ps with positional restraints on the protein heavy atoms (force constant 1,000 kJ·mol$^{-1}$·nm$^{-2}$).

To generate statistically independent unfolding trajectories (five trajectories with and without ATP, respectively), a partially unfolded conformation was selected after 19.2 and 20.2 ns of FPMD simulation time with and without ATP, respectively. These conformations were chosen because they correspond to minima in the force profiles. The nitrogen atom of the N terminus and the carbon atom of the C terminus, respectively, were kept fixed with a positional restraint (force constant 1,000 kJ·mol$^{-1}$·nm$^{-2}$), and the systems were equilibrated for 1 ns with free MD. From this trajectory, five equidistant frames ($\Delta t = 200$ ps) were chosen as starting structures for the additional force–probe simulations.

Simulations were interrupted before any of the springs had crossed the box boundary. Here, care was taken that, because of the applied periodic boundary conditions, the pulled termini did not interact with each other. At this point, fully unfolded residues at both termini were removed, and new termini, water, and ions were added. The FPMD simulations were then continued after equilibration of the solvent with positional restraints on the protein heavy atoms (force constant 1,000 $\mathrm{kJ \cdot mol^{-1} \cdot nm^{-2}}$) for 200 ps.

The simulated systems comprised ≈180,000 atoms. The total simulation time was ≈500 ns.

**18. Contour Length Plots.** The plotted contour lengths aim at quantitative comparison between the simulations and the experiments. Such comparison is complicated by the fact that (*i*) different pulling speeds are used and, (*ii*) in the simulations, a stiffer spring has to be used then in the AFM experiments. To account for these differences, we derived contour length plots from the force profiles obtained from the MD simulations in three steps. First, prominent force peaks were selected along the force profiles. Here, only those force peaks $j$ were included whose height $F_{\max,j}$ exceeded a certain threshold. This threshold was defined as

$$F_{\max,j} \geq F_{\max,j-1} - k_{\mathrm{AFM}}\left(\Delta z_{\mathrm{spring},j} - \Delta z_{\mathrm{spring},j-1}(t)\right), \qquad [5]$$

where $k_{\mathrm{AFM}}$ is the effective spring constant of the AFM cantilever and the attached linkers, and $\Delta z_{\mathrm{spring}}$ is the distance between the two springs attached to the C and N terminus, respectively, and $j-1$ denotes the force peak preceding peak $j$. Here, $k_{\mathrm{AFM}}$ was estimated as 10 pN/nm, which is an upper limit. This selection procedure mimics the effect of the soft AFM cantilever, which, in contrast to the force probe simulations, is insensitive to minor force peaks that immediately follow a larger peak. Second, the number of unfolded residues $N_{\mathrm{unf},j}$ and the length of the folded core $\Delta z_{\mathrm{folded},j}$ were determined for the conformations corresponding to each of these peaks. The contour length $l_{c,j}$ was then calculated as $l_{c,j} = N_{\mathrm{unf},j} \times 0.365$ nm + $\Delta z_{\mathrm{folded}}$. Third, a Gaussian function was assigned to each of the peaks, weighted by its height $F_{\max,j}$:

$$G_j(l_c) = F_{\max,j}\exp\left(\frac{(l_c - l_{cj})^2}{2\sigma^2}\right), \qquad [6]$$

with a width $\sigma = 1$ nm. The final contour length plot is obtained from the sum of all these Gaussian functions. As an exception, this procedure was not applied to the force peak marked with a plus sign in Fig. 3*B Top*. Structural analysis shows that peak arises from transient rupture and reformation of the interactions between Lys-36/Met-34 and ATP, similar to the subsequent ATP peak 2*. From the considerable scatter of heights seen for peak 2*, we expect that the peak in question is exceptionally pronounced and, therefore, that the described shadowing effect will not occur in most of the cases. No other peak showed a similar effect.

Fig. 4 compares the contour lengths from experiment and MD simulation. For direct comparison, one has to consider that the AFM measurements were conducted with a full TK that additionally includes a linker of 23 residues. No structural information was available for this 23-residue linker between A170 and the catalytic core. In the homologous twitchin kinase, this sequence wraps around the ATP binding lobe of the kinase but makes no contacts with the autoregulatory domain. We therefore expect this part to affect the relative positions of the observed unfolding peaks but not the sequence of local unfolding events at the C terminus. In fact, the contour length difference of 9 nm between peaks 1 and 2 corresponds the 23-residue linker length, which provided further support for our assignment. In the MD simulations, either a full-length TK or a truncated TK—i.e., with a part of the autoinhibitory tail removed—was used. As a reference point for comparison, peak 6 was chosen, which indicates unfolding of Ig-domain "handles" at a fully unfolded TK ($l_c$ = 144.4 nm). The 321 residues of the full TK or the 289 residues of the truncated TK would all be unfolded at this point. The simulations allow assigning the ATP peak (peak 2*) to the anchor point Lys-36. Thus, 289 − 36 = 253 residues unfold between peaks 2* and 6, which corresponds to a contour length increment of 253 × 0.365 nm = 92 nm. Including the length of the folded core of 5.5 nm, this estimate yields an $l_c$ for peak 2* of 144.4 nm − 92 nm + 5.5 nm = 57.9 nm from the simulations, in good agreement with the value of 51.6 nm from the AFM.

The above procedure rests on two assumptions. First, we assume that before peak 2*, all N-terminal residues before Lys-36 unfold. In addition, by simulating a truncated TK, we assume that unfolding of the omitted part of the autoinhibitory tail is uncoupled from the other unfolding events and precedes peak 2*. Both assumptions are corroborated by the simulations of the complete TK, where such an unfolding behavior was indeed observed (see Fig. 3).

The simulations of the complete TK also show that peak 2 can be assigned to the unfolding of the autoinhibitory tail (Fig. 3). Hence, the first part of the contour length profile shown in Fig. 4 *Inset* is based on these simulations. Here, Tyr-7 was chosen as an anchor point, a residue that lies at the beginning of βR1. Following the same argumentation as outlined above, this choice yields a barrier position for peak 2 of 35.5 nm, in good agreement with the 32.3 nm obtained from the AFM data. We note that, in contrast to peak 2*, where the anchor point can be easily assigned to the Met-34/Lys-36 motive, such a detailed assignment is more challenging for peak 2. Here, only a range of βR1 residues between Glu-5 and Asp-12 can be specified, thus leading to an uncertainty in the position of peak 2 of ≈1.5 nm.

Fig. S7 compares the barrier positions obtained from the AFM experiments and the two independent MD simulations of the complete TK in the absence of ATP (Fig. 3*B Bottom*). The MD simulations yield positions of peaks 2, 3, 4, and 5 at 35.5, 63.3, 80.1, and 86.8 nm, respectively. The corresponding peak positions obtained from the AFM experiments are 32.3, 61.3, 68.6, and 86.6 nm, respectively. For the force peaks 2, 3, and 5, the positions obtained from the simulations agree well with those obtained from the experiments, taking into account that the former are based on only two independent simulations. For peak 4, the difference between the simulations and the experiments is somewhat larger. We speculate that this difference results from the underlying free energy landscape that, at such partially unfolded conformations, is shallow and exhibits many barriers of comparable height along various unfolding directions, such that the pathways followed in the individual trajectories are different. Such heterogeneity of unfolding pathways is indeed seen from the color-coded unfolding events in Fig. 3*B Bottom*. A much larger number of trajectories would be required to thoroughly characterize this region of the energy landscape, which, however, is not the focus of this work.

1. Puchner EM, Franzen G, Gautel M, Gaub HE (2008) Comparing proteins by their unfolding pattern. *Biophys J* 95:426–434.
2. Lange S, *et al.* (2005) The kinase domain of titin controls muscle gene expression and protein turnover. *Science* 308:1599–1603.
3. Mayans O, *et al.* (1998) Structural basis of the activation of the titin kinase domain during myofibrillogenesis. *Nature* 395:863–869.
4. Obermann WMJ, *et al.* (1996) The structure of the sarcomeric M band: Localization of defined domains of myomesin, M-protein and the 250 kD carboxy-terminal region of titin by immunoelectron microscopy. *J Cell Biol* 134:1441–1453.
5. Skamnaki VT, *et al.* (1999) Catalytic mechanism of phosphorylase kinase probed by mutational studies. *Biochemistry* 38:14718–14730.
6. Wedegaertner PB, Gill GN (1989) Activation of the purified protein tyrosine kinase domain of the epidermal growth factor receptor. *J Biol Chem* 264:11346–11353.

7. Tennagels N, Hube-Magg C, Wirth A, Noelle V, Klein HW (1999) Expression, purification, and characterization of the cytoplasmic domain of the human IGF-1 receptor using a baculovirus expression system. *Biochem Biophys Res Commun* 260:724–728.
8. Butt HJ, Jaschke M (1995) Calculation of thermal noise in atomic force microscopy. *Nanotechnology* 6:1–7.
9. Hugel T, Rief M, Seitz M, Gaub HE, Netz RR (2005) Highly stretched single polymers: Atomic-force-microscope experiments versus ab-initio theory. *Phys Rev Lett* 94:048301.
10. Dietz H, Rief M (2004) Exploring the energy landscape of GFP by single-molecule mechanical experiments. *Proc Natl Acad Sci USA* 101:16192–16197.
11. Janovjak H, Kessler M, Oesterhelt D, Gaub H, Muller DJ (2003) Unfolding pathways of native bacteriorhodopsin depend on temperature. *EMBO J* 22:5220–5229.
12. Schlierf M, Rief M (2005) Temperature softening of a protein in single-molecule experiments. *J Mol Biol* 354:497–503.
13. Van Der Spoel D, *et al.* (2005) GROMACS: Fast, flexible, and free. *J Comput Chem* 26:1701–1718.
14. Hess B, Kutzner C, van der Spoel D, Lindahl E (2008) GROMACS 4: Algorithms for highly efficient, load-balanced, and scalable molecular simulation. *J Chem Theory Comput* 4:435–447.
15. Jorgensen WL, Tirado-Rives J (1988) The OPLS potential functions for proteins. Energy minimizations for crystals of cyclic peptides and crambin. *J Am Chem Soc* 110:1657–1666.
16. Berendsen HJC, Postma JPM, van Gunsteren WF, DiNola A, Haak JR (1984) Molecular-dynamics with coupling to an external bath. *J Chem Phys* 81:3684–3690.
17. Hess B, Bekker H, Berendsen HJC, Fraaije GEM (1997) A linear constraint solver for molecular simulations. *J Comput Chem* 18:1463–1472.
18. Miyamoto S, Kollmann PA (1992) An analytical version of the SHAKE and RATTLE algorithms for rigid water models. *J Comput Chem* 13:952–962.
19. Darden T, York D, Pedersen L (1993) Particle mesh Ewald—An Nlog(N) method for Ewald sums in large systems. *J Chem Phys* 98:10089–10092.
20. Breneman CM, Wiberg KB (1990) Determining atom-centered monopoles from molecular electrostatic potentials—The need for high sampling density in formamide conformational-analysis. *J Comput Chem* 11:361–373.
21. Frisch MJ (2004) (Gaussian, Inc).
22. Klahn M, Schlitter J, Gerwert K (2005) Theoretical IR spectroscopy based on QM/MM calculations provides changes in charge distribution, bond lengths, and bond angles of the GTP ligand induced by the Ras-protein. *Biophys J* 88:3829–3844.
23. Grater F, Shen J, Jiang H, Gautel M, Grubmuller H (2005) Mechanically induced titin kinase activation studied by force-probe molecular dynamics simulations. *Biophys J* 88:790–804.
24. Gassel M, *et al.* (2003) Mutants of protein kinase A that mimic the ATP-binding site of protein kinase B (AKT). *J Mol Biol* 329:1021–1034.
25. Lowe ED, *et al.* (1997) The crystal structure of a phosphorylase kinase peptide substrate complex: Kinase substrate recognition. *EMBO J* 16:6646–6658.
26. Amadei A, Linssen AB, Berendsen HJ (1993) Essential dynamics of proteins. *Proteins* 17:412–425.
27. de Groot BL, Vriend G, Berendsen HJ (1999) Conformational changes in the chaperonin GroEL: New insights into the allosteric mechanism. *J Mol Biol* 286:1241–1249.
28. Grubmuller H, Heymann B, Tavan P (1996) Ligand binding: Molecular mechanics calculation of the streptavidin-biotin rupture force. *Science* 271:997–999.
29. Israelewitz B, Izrailev S, Schulten K (1997) Binding pathway of retinal to bacterio-opsin: A prediction by molecular dynamics simulations. *Biophys J* 73:2972–2979.

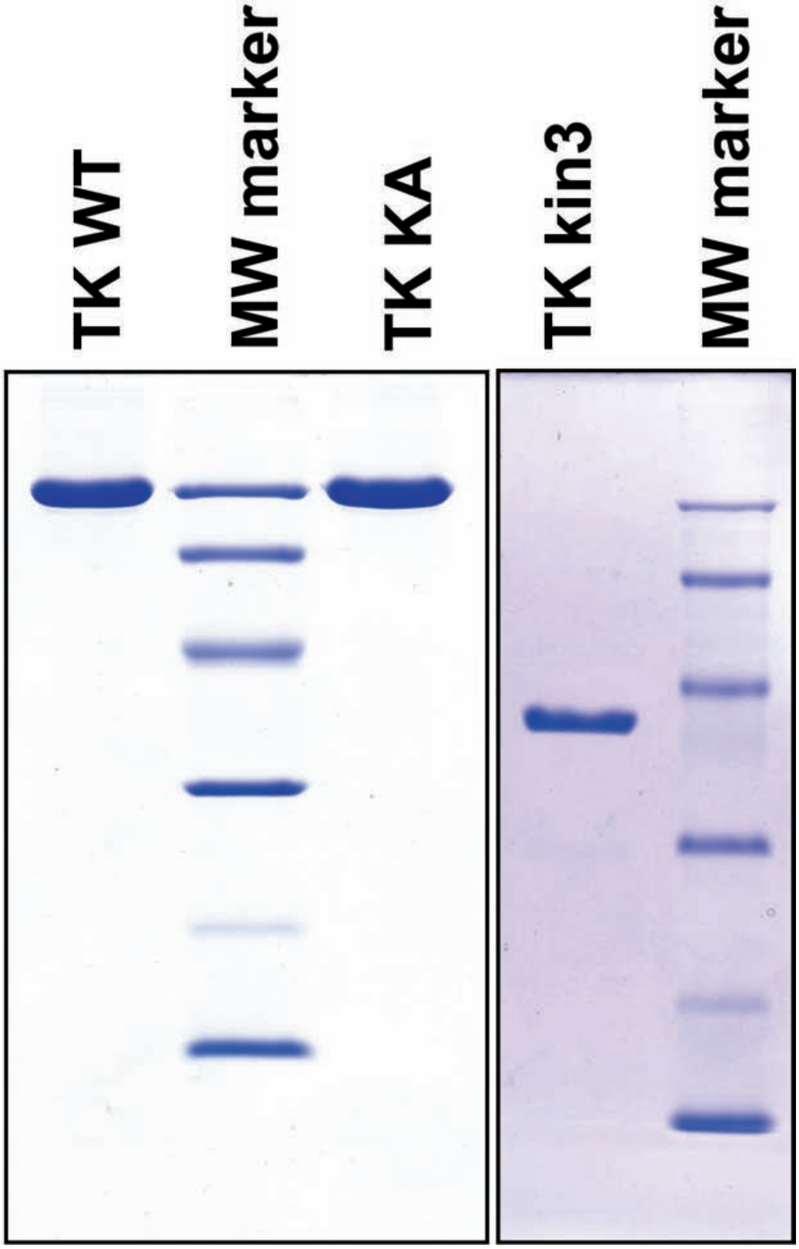

**Fig. S1.** (*Left*) Wild type (WT) and K36A mutant of the titin kinase A168-M2 construct after two-step purification; 2.5 μg of both WT and KA mutant titin kinase were loaded. (*Right*) Titin kinase domain kin3 after three-step purification; 1 μg was loaded. Molecular mass marker (in kDa), from top: 94, 64, 43, 30, 20, and 14.

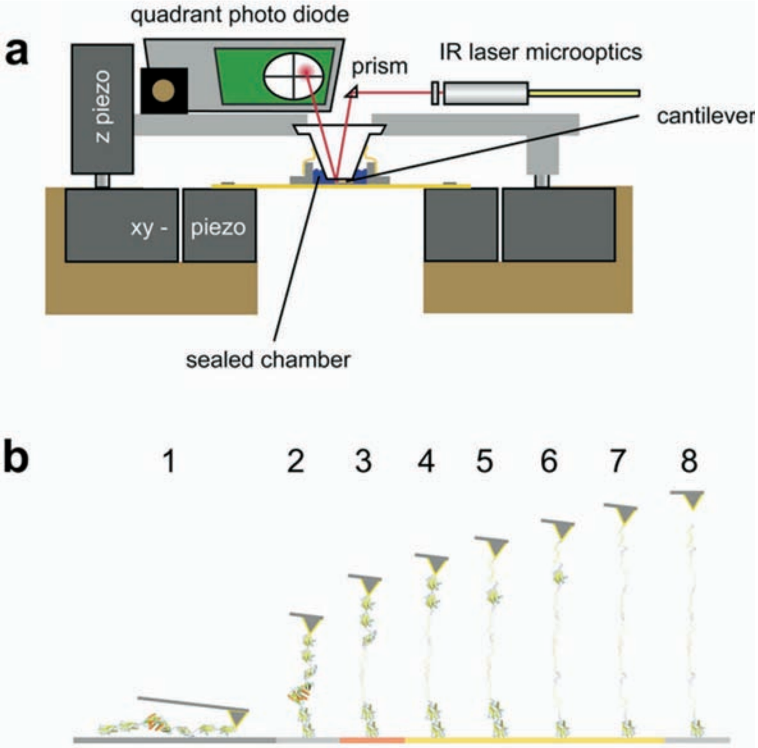
a
quadrant photo diode
prism
IR laser microoptics
cantilever
z piezo
xy - piezo
sealed chamber
b
1
2
3
4
5
6
7
8

**Fig. S2.** (*a*) Schematics of the experimental setup. An IR laser is coupled through a fiber into the AFM head where it is focused onto the cantilever with a microoptic. The reflected beam is detected by a computer adjustable four-quadrant photodiode. The AFM head is moved up and down by a Z-piezo drive, and the sample is moved after each trace by a *x*–*y* piezo stage. To avoid evaporation of the buffer, we used a sealed measurement chamber. (*b*) Schematic overview of the AFM experiment showing the initial attachment of the protein to surface and cantilever (1), straightening of the protein to its folded length of ≈25 nm (2), unfolding of the kinase at low force (3), and sequential unfolding of the independently folding Ig and Fn3 domains at high forces (4–7). A rupture peak is observed when the completely unfolded peptide chain is pulled off the cantilever or surface (8).

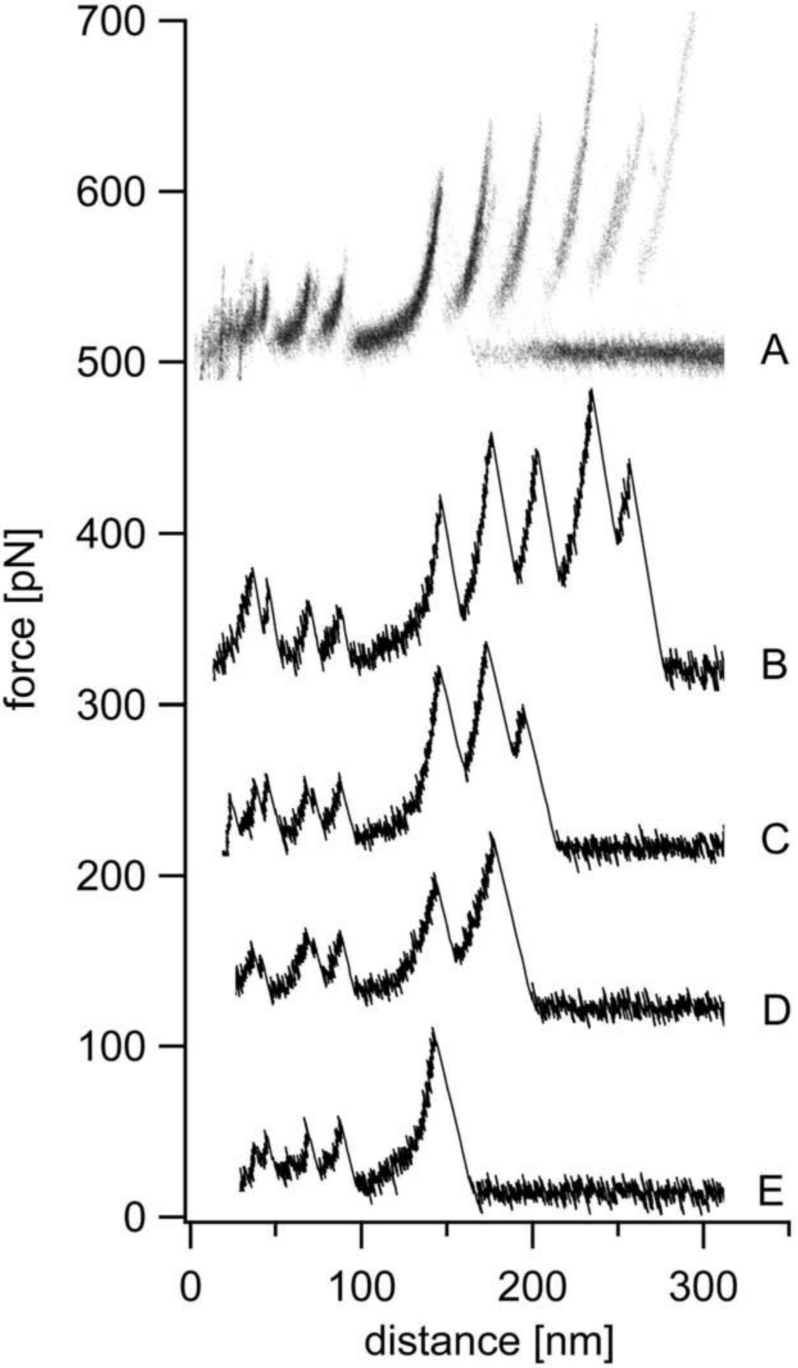

**Fig. S3.** Selection of traces and identification of the TK unfolding pattern in the absence of ATP. ''A'' is the superposition of traces showing the unfolding of one to five spacer domains and the complete unfolding pattern of the titin kinase domain. Traces are shifted with respect to each other whereas the rupture of the first Ig-domain served as the barrier of reference. In this way the different offsets in the initial part of the force extension traces, caused by rupture of spacer domain fragments and unspecific interactions, are taken into account. For clarity the points are plotted semitransparent. Once we identified the unfolding pathway of the titin kinase by means of traces showing more than three spacer domains (e.g., B), we took also traces into account exhibiting the complete unfolding pattern of the titin kinase but less spacer domains (C–E).

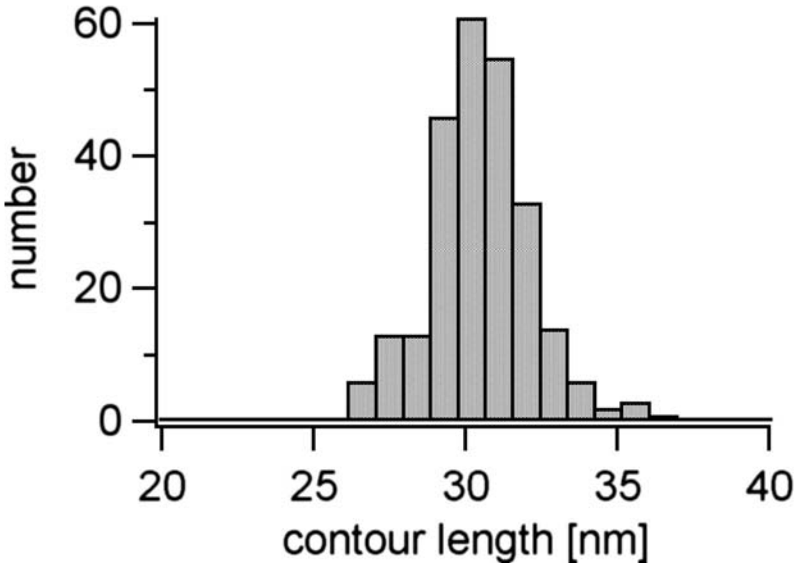

**Fig. S4.** Histogram of experimental Ig/Fn domain contour length increments. The values are obtained by transforming each trace with the QM-WLC model (persistence length $P = 0.8$ nm) into a barrier position histogram [Puchner EM, Franzen G, Gautel M, Gaub HE (2008) *Biophys J* 95:426–434] and by fitting the corresponding peaks with Gaussians. The mean value amounts to 30.45 nm, and the standard deviation values 1.68 nm.

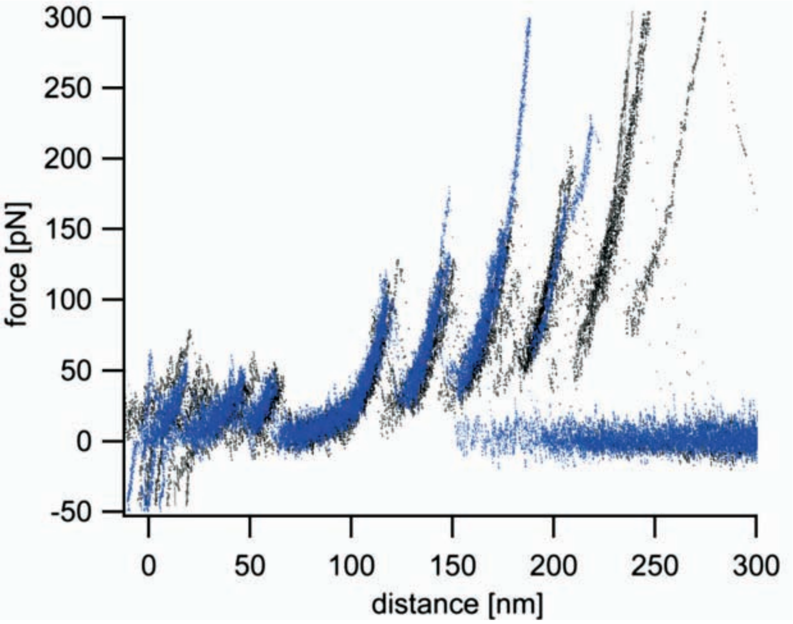

**Fig. S5.** Superposition of traces from different TK protein constructs. The traces in black show the unfolding of the *E. coli*-expressed protein construct consisting of five spacer domains whereas the other one contains only three spacer domains (blue). The maximum number of even spacings at the end of the traces ($\Delta L \approx$ 30 nm) reflects the number of spacer domains in both cases.

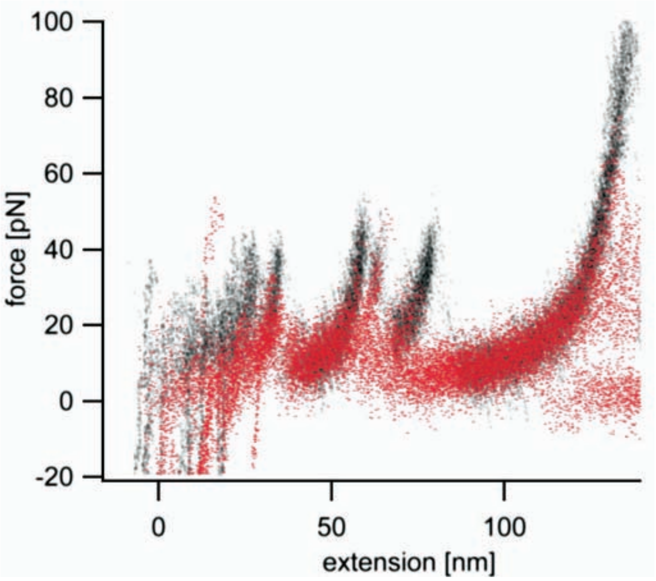

**Fig. S6.** Unfolding pattern of the titin kinase at 37°C. The black points show the superposition of traces recorded at room temperature, whereas the red traces were recorded at 37°C. Although the unfolding forces are smaller by ≈20 pN, the unfolding pattern is the same at 37°C.

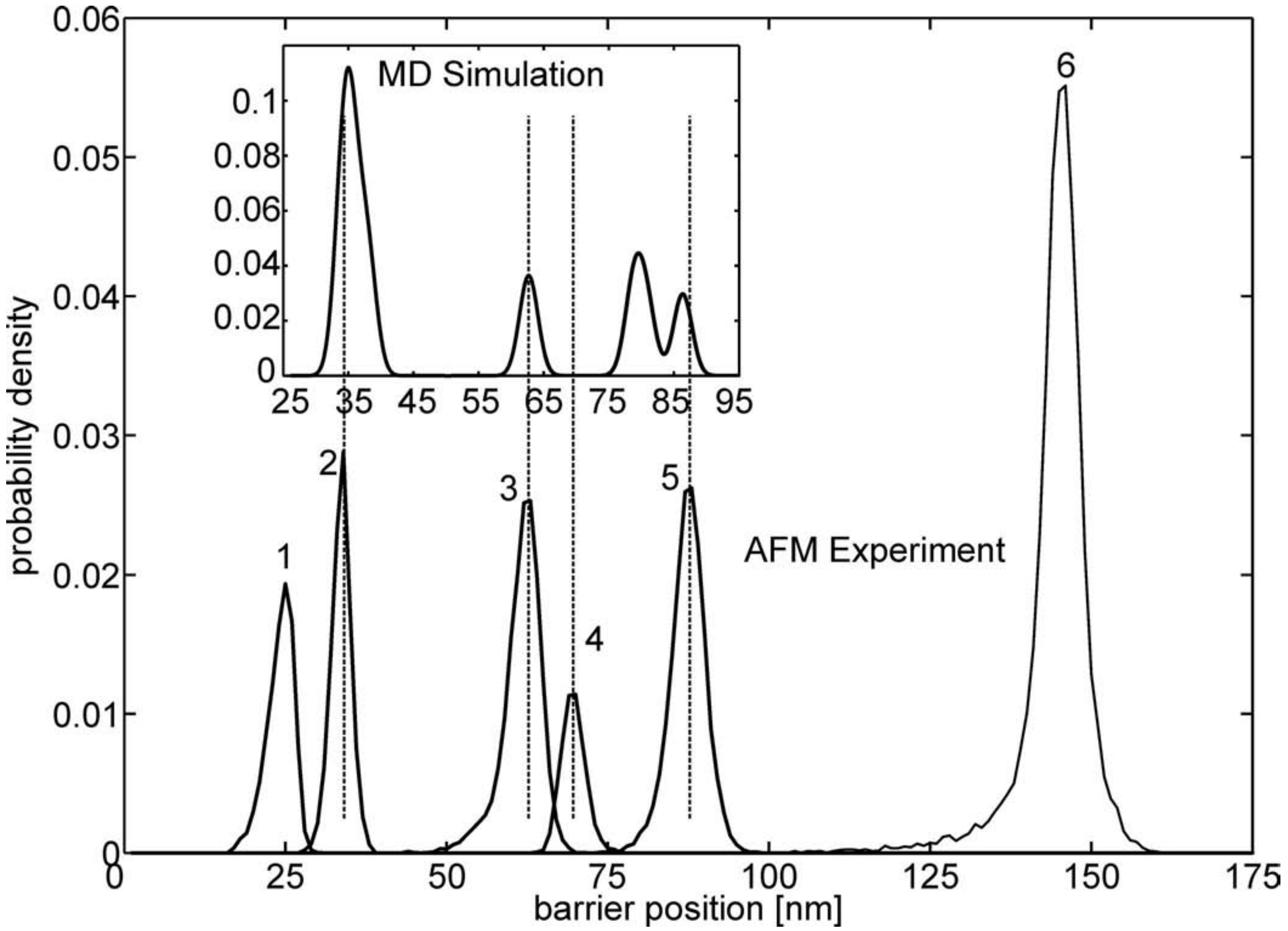

**Fig. S7.** Barrier positions from AFM experiments and MD simulations in the absence of ATP. The latter were obtained from the simulations of the complete TK (321 residues) shown in Fig. 3*B Bottom*. The positions of the force peaks obtained from the AFM experiments are indicated by the dashed lines.

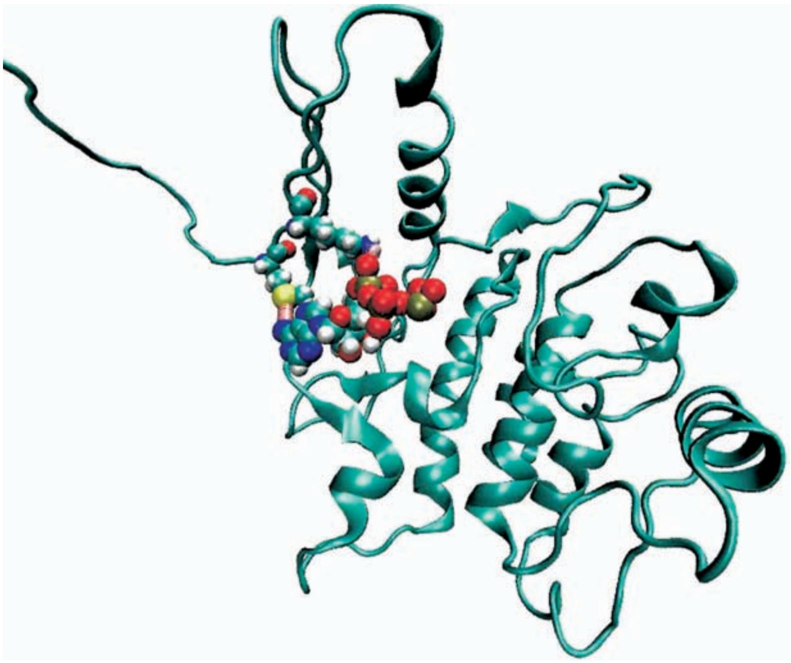

**Movie S1.** Structural changes during peak 2*: Unfolding of titin kinase (ribbon representation) upon mechanical stress, with ATP (ball-and-stick representation) bound to the active site. Interactions with ATP (dashed lines) cause an additional force peak (peak 2* in Fig. 2) in both the AFM experiment and the molecular dynamics simulations, which is not seen in the ATP-free state. Particularly strong interactions contributing to this peak are seen with Met-34 and Lys-36, which are shown in ball-and-stick representation. The bond with Met-34 with the purine base breaks before that of Lys-36 with the $\alpha$-$\beta$ phosphate groups.

Movie S1 (MPG)

**Table S1. Conversion of residues in N2B titin (NP_003310.3) to the numbering in the titin kinase crystal structure 1TKI**

| Residue in 1TKI | Residue in N2B titin |
|---|---|
| Met-34 | Met-24781 |
| Lys-36 | Lys-24783 |
| Asp-127 | Asp-24874 |
| Tyr-170 | Tyr-24917 |

**Table S2. Expected experimental contour length increments of Ig/Fn-domain unfolding**

| Domain | Folded diameter, nm | No. of folded amino acids | Contour length increment, nm |
|---|---|---|---|
| A168 (PDB entry 2NZI) | 4.3 | 95 | 30.74 |
| A169 (PDB entry 2NZI) | 4.8 | 101 | 32.07 |
| A170 (PDB entry 2NZI) | 4.0 | 95 | 30.68 |
| M1 (PDB entry 2BK8) | 4.1 | 93 | 29.95 |

The theoretical contour length increments were calculated by multiplying the number of folded amino acids with 0.365 nm and subtracting the diameter of the folded domains. The mean value amounts to 30.86 nm.

**Table S3. Schematic structure of ATP (above), defining the atom numbers used in the tables, and atomic partial charges for ATP (below)**

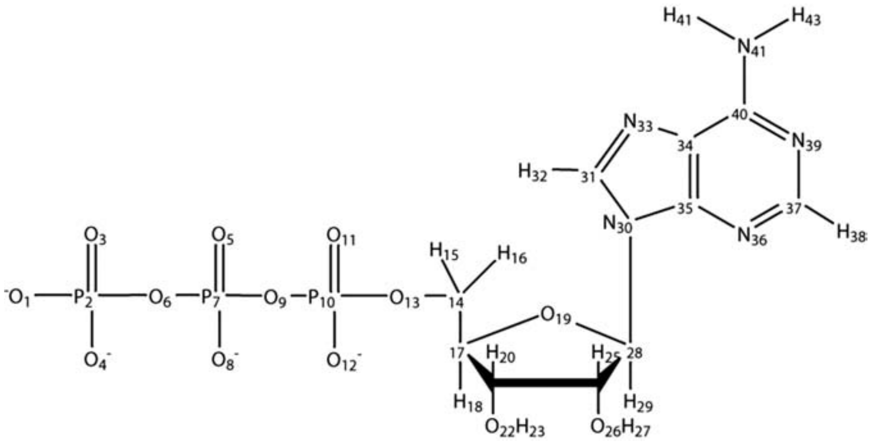
H41
H43
N41
40
N33
34
N39
H32
31
35
37
H38
N30
N36
O3
O5
O11
H15
H16
-O1
P2
O6
P7
O9
P10
O13
14
O19
O4-
O8-
O12-
17
H20
H25
28
H18
H29
O22H23
O26H27

| No. | OPLS type | Charge |
|---|---|---|
| 1 | lopls_969 | −1.1 |
| 2 | opls_966 | 1.9 |
| 3 | opls_969 | −1.1 |
| 4 | opls_969 | −1.1 |
| 5 | opls_968 | −0.6 |
| 6 | opls_969 | −1.1 |
| 7 | opls_966 | 1.9 |
| 8 | opls_969 | −1.1 |
| 9 | opls_968 | −0.7 |
| 10 | opls_966 | 1.9 |
| 11 | opls_969 | −1.1 |
| 12 | opls_969 | −1.1 |
| 13 | opls_968 | −0.7 |
| 14 | opls_183 | −0.12 |
| 15 | opls_140 | 0.06 |
| 16 | opls_140 | 0.06 |
| 17 | opls_183 | 0.17 |
| 18 | opls_140 | 0.03 |
| 19 | opls_180 | −0.6 |
| 20 | opls_158 | 0.2 |
| 21 | opls_140 | 0.06 |
| 22 | opls_171 | −0.68 |
| 23 | opls_172 | 0.42 |
| 24 | opls_158 | 0.2 |
| 25 | opls_140 | 0.06 |
| 26 | opls_171 | −0.68 |
| 27 | opls_172 | 0.42 |
| 28 | opls_183 | 0.3 |
| 29 | opls_140 | 0.06 |
| 30 | opls_354B | −0.38 |
| 31 | opls_353 | 0.2 |
| 32 | opls_359 | 0.14 |
| 33 | opls_352 | 0.2 |
| 34 | opls_350 | 0.15 |
| 35 | opls_349 | 0.38 |
| 36 | opls_348 | −0.55 |
| 37 | opls_347 | 0.35 |
| 38 | opls_355 | 0.2 |
| 39 | opls_346 | −0.53 |
| 40 | opls_351 | 0.53 |
| 41 | opls_356 | −0.74 |
| 42 | opls_357 | 0.385 |
| 43 | opls_358 | 0.355 |

**Table S4. Lennard–Jones (6, 12) parameters**

| OPLS type | *d* | *e* |
|---|---|---|
| opls_966 | 0.374 | 0.837 |
| opls_967 | 0.350 | 0.276 |
| opls_968 | 0.296 | 0.879 |
| opls_969 | 0.296 | 0.879 |

doi:10.1016/j.jmb.2008.06.065 *J. Mol. Biol.* (2008) **381**, 1253–1266

JMB

Available online at www.sciencedirect.com
ScienceDirect

ELSEVIER

# Force-based Analysis of Multidimensional Energy Landscapes: Application of Dynamic Force Spectroscopy and Steered Molecular Dynamics Simulations to an Antibody Fragment–Peptide Complex

**Julia Morfill, Jan Neumann, Kerstin Blank*, Uta Steinbach, Elias M. Puchner, Kay-E. Gottschalk and Hermann E. Gaub**

*Lehrstuhl für Angewandte Physik & Center for Nanoscience, LMU München, Amalienstrasse 54, D-80799 München, Germany*

*Received 13 March 2008; received in revised form 18 June 2008; accepted 20 June 2008*
Available online 28 June 2008

***Edited by D. Case***

Multidimensional energy landscapes are an intrinsic property of proteins and define their dynamic behavior as well as their response to external stimuli. In order to explore the energy landscape and its implications on the dynamic function of proteins dynamic force spectroscopy and steered molecular dynamics (SMD) simulations have proved to be important tools. In this study, these techniques have been employed to analyze the influence of the direction of the probing forces on the complex of an antibody fragment with its peptide antigen. Using an atomic force microscope, experiments were performed where the attachment points of the 12 amino acid long peptide antigen were varied. These measurements yielded clearly distinguishable basal dissociation rates and potential widths, proving that the direction of the applied force determines the unbinding pathway. Complementary atomistic SMD simulations were performed, which also show that the unbinding pathways of the system are dependent on the pulling direction. However, the main barrier to be crossed was independent of the pulling direction and is represented by a backbone hydrogen bond between Gly$^{H}$-H40 of the antibody fragment and Glu$^{O\varepsilon}$-6$_{peptide}$ of the peptide. For each pulling direction, the observed barriers can be correlated with the rupture of specific interactions, which stabilize the bound complex. Furthermore, although the SMD simulations were performed at loading rates exceeding the experimental rates by orders of magnitude due to computational limitations, a detailed comparison of the barriers that were overcome in the SMD simulations with the data obtained from the atomic force microscope unbinding experiments show excellent agreement.

© 2008 Elsevier Ltd. All rights reserved.

*Keywords:* single molecule force spectroscopy; atomic force microscope; molecular dynamics simulations; energy landscape; antibody–antigen interaction

## Introduction

The knowledge of protein structures has revolutionized the understanding of protein function on the atomic level. However, crystal structures provide static pictures and do not account for the fact that proteins are soft materials, which, due to thermal fluctuations sample a large ensemble of slightly different conformations around their average structure. Multidimensional energy landscapes, which define the relative probabilities of the conformational states and the energy barriers between them, are able to describe the dynamical equilibrium of

---

**Corresponding author.* E-mail address: Kerstin.Blank@chem.kuleuven.be.

Present address: K. Blank, Department of Chemistry, Katholieke Universiteit Leuven, Celestijnenlaan 200 F, B-3001 Heverlee, Belgium.

Abbreviations used: AFM, atomic force microscope; scFv, single-chain Fv fragment; SMD, steered molecular dynamics; PEG, poly(ethylene glycol); SPR, surface plasmon resonance; MD, molecular dynamics.

0022-2836/$ - see front matter © 2008 Elsevier Ltd. All rights reserved.

protein conformations.[1–3] As a result, the complexation of two proteins forming a protein–protein complex also occurs on these multidimensional energy landscapes. The corresponding complexation rates of a protein–protein interaction are determined by the barriers in the underlying energy landscape (Fig. 1a) that can be influenced by a variety of internal and external factors such as phosphorylation, mutations, or even the action of external forces. All these factors can alter the relative energy barrier height between different substates or even generate new local substates.

Since force is an ideal control parameter to explore the multidimensional energy landscape of a protein (Fig. 1b), single-molecule force spectroscopy experiments have become an important tool for studying the dynamic function of individual proteins and protein–protein complexes.[4–10] Technically, the application of forces on the single-molecule level can be realized using different experimental techniques as well as molecular dynamics simulations. The atomic force microscope (AFM) and laser tweezers have evolved into the most prominent experimental tools for the analysis of the mechanical and dissociation properties of proteins and protein–protein interactions.[11–14]

Here, the energy landscape of an antibody fragment–peptide complex was explored using single-molecule force spectroscopy and molecular dynamics simulations. We chose this system because the crystal structure of the complex is known,[15] and therefore provides the possibility of explaining the response of this complex to the externally applied force with structural data. The peptide antigen was derived from the leucine zipper domain of the yeast transcription factor GCN4. For the generation of antibodies, two proline mutations have been introduced into this 33 amino acid long peptide to prevent coiled coil formation. Using this peptide, mice have been immunized and the mouse antibody genes derived from the spleen cells have been cloned into a ribosome display system to select and improve peptide binders.[15,16] The antibody single-chain Fv fragment (scFv; clone H6) was obtained from this affinity maturation process and has been further modified by site-directed mutagenesis. In order to crystallize the complex of scFv fragment and peptide, a truncated 12 amino acid long peptide was used, which is recognized by the scFv fragment. The truncated peptide binds to the scFv fragment in an α-helical conformation facing the scFv fragment with the side that binds the complementary peptide in the leucine zipper. This region of the peptide corresponds to the so-called trigger sequence, which has been found by Kammerer *et al*.[17] The trigger region has been shown to be essential for folding and coiled coil formation of the leucine zipper and contains a high α-helical content.[18] It is considered that the interaction of the two peptides upon coiled coil formation involves assembly of these α-helical stretches by conformational selection. The similarity of the peptide conformation in the coiled-coil pep-

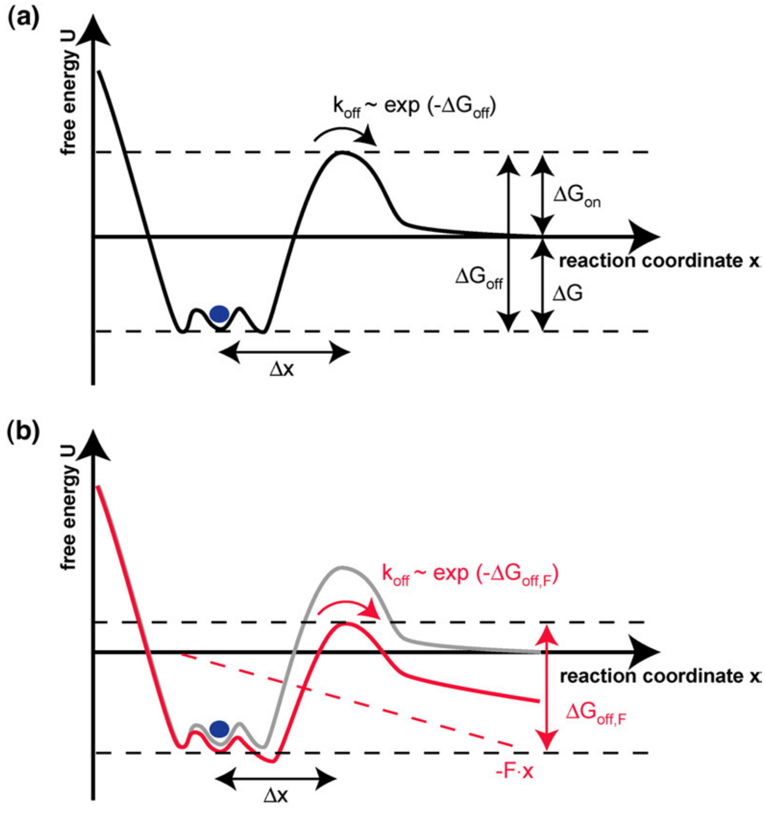

**Fig. 1.** Influence of an externally applied force on the energy landscape of a protein or a protein–protein complex. (a) Two-dimensional cross-section through the energy landscape without an externally applied force (black). In this picture the protein or the protein–protein complex (blue) is situated in one of the closely related substates at minimal energy. The free energy difference $\Delta G$ between the folded protein or the bound protein-protein complex (blue) and the unbound or unfolded state is determined by the difference between the energy barrier $\Delta G_{\mathrm{off}}$ and the activation energy $\Delta G_{\mathrm{on}}$. Therefore, the barrier between these two states ($\Delta G_{\mathrm{off}}$), which can be overcome due to thermal fluctuations, determines the rate of interconversion ($k_{\mathrm{off}}$). $k_{\mathrm{off}}$ is the basal dissociation rate; $\Delta x$ is the potential width. (b) Two-dimensional cross-section through the energy landscape with an externally applied force (red). If an external force $F$ is applied, the energy landscape is tilted (red), thereby reducing the energy barrier by $-Fx$ (broken red line). This reduction leads to an increase of the dissociation rate.

tide and in the complex with the antibody fragment implies that the binding to the antibody fragment follows a similar mechanism with helix formation being the prerequisite for binding to the antibody fragment.

For our studies, the peptide antigen provides the possibility to vary the attachment points of the peptide, since the amino acid for coupling can be introduced easily at different positions. This gives us the possibility to investigate whether the unbinding pathway of the regarded antibody fragment-peptide complex is changed by the direction of the applied force, which would point to the existence of a multidimensional energy landscape. High-resolution AFM-based single molecule force spectroscopy measurements were performed to determine the basal dissociation rate $k_{\mathrm{off}}$, which correlates with the height of the energy barrier, which has to be overcome for unbinding, and the potential width $\Delta x$, which is a rough measure of the width of the binding potential. The results for $k_{\mathrm{off}}$ were then compared with the $k_{\mathrm{off}}$ values determined under equilibrium conditions with surface plasmon resonance (SPR).

Complementary, steered molecular dynamics (SMD) simulations were performed to provide additional information about the energy landscape of the respective antibody fragment-peptide system. Furthermore, SMD simulations allow the analysis of the chosen unbinding pathway with atomic resolution.[19–22] SMD simulations enable the identification of the rupture events and the corresponding molecular interactions correlated with these ruptures. This structural information was related to the results obtained from the AFM measurements.

## Results and Discussion

### Single-molecule force spectroscopy

The antibody fragment H6 used in our studies binds the truncated 12 amino acid long peptide antigen corresponding to amino acids 17–28 of the wildtype leucine zipper GCN4-p1.[15,23] Here, the numbering of the structure file (PDB code 1P4B) is used, which numbers the amino acids of the peptide from 1 to 12. To explore the energy landscape of the antibody fragment–peptide complex in detail, force spectroscopy measurements were performed using an atomic force microscope (AFM). For this purpose, the antibody fragment H6 was covalently coupled to a surface containing covalently attached poly(ethylene glycol) (PEG) and the peptide was immobilized on the cantilever tip in the same way (Fig. 2). The use of the elastic spacer PEG minimizes nonspecific interactions and maximizes the probability of detecting specific and single rupture events. Three configurations representing different attachment points were analyzed in detail: For configuration N, a cysteine followed by three glycine residues was attached to the N terminus (Tyr-$1_{\mathrm{peptide}}$; corresponding to amino acid 17 of the full-length leucine zipper) in order to couple the peptide to the cantilever of the AFM. For configuration M, the coupling

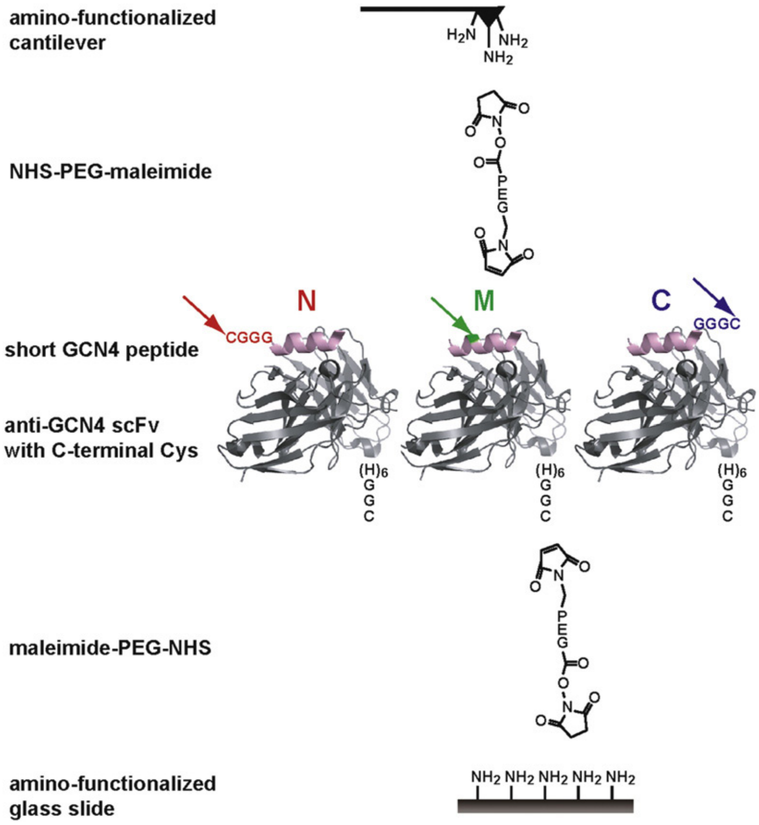

**Fig. 2.** Experimental setup. The antibody fragment H6 possessing a C-terminal cysteine was covalently immobilized onto an amino-functionalized glass slide using a heterobifunctional poly(ethylene glycol) spacer. The same coupling chemistry was used for the immobilization of the peptide to the cantilever. N, M and C show different measurement configurations. In configuration N, a cysteine and three glycine residues were attached to the N terminus of the peptide. In configuration M, alanine on position 8 of the peptide sequence was changed to a cysteine. In configuration C, three glycine residues followed by a cysteine were attached to the C terminus of the peptide.

to the cantilever was achieved via a cysteine residue, which replaced Ala-$8_{\text{peptide}}$ (corresponding to amino acid 24 of the full-length leucine zipper) in the "middle" of the peptide. It is obvious from the structure of the peptide that Ala-$8_{\text{peptide}}$ is not involved in interactions with the antibody fragment. However, this amino acid is in the region of the leucine zipper with the highest helix propensity and mutations in this region might impair helix formation.[24] For configuration C, a spacer of three glycine residues followed by a cysteine was attached to the C terminus of the truncated peptide (Lys-$12_{\text{peptide}}$; corresponding to amino acid 28 of the full-length leucine zipper). In the following, the three different attachment possibilities of the peptide are abbreviated to N, M and C. In all experiments, the surface was approached with the tip of the cantilever, allowing the antibody fragment–peptide complex to bind. Subsequently, the cantilever was retracted and the antibody fragment–peptide complex was loaded with an increasing force until the complex ruptured and the cantilever relaxed back into its equilibrium position. The force applied to this complex was recorded as a function of the distance between the cantilever tip and the surface. Fig. 3a shows three different force-extension curves, which correspond to the rupture events of the different antibody fragment–peptide complexes N (red), M (green) or C (blue) respectively. The force-extension curves measured for the three different configurations N, M and C exhibit similar rupture forces. To obtain good statistics, several hundreds of force-extension curves at different retract velocities were recorded using only one cantilever for every configuration. The use of one cantilever per configuration is crucial in these experiments to minimize errors originating from the cantilever calibration. The rupture force and the rupture length were determined from the force-extension curves. Force-time curves revealed the corresponding loading rate. Fig. 3b and c show the rupture force and loading rate distributions for configuration N, measured at a retract velocity of 800 nm/s. The rupture force histogram was fit with a Gaussian distribution (black curve) and has a most probable force of 47.3 pN. The Gaussian distribution of the loading rates (plotted logarithmically) (Fig. 3c) shows a maximum at a loading rate of 1307.8 pN $s^{-1}$. The maxima of the force and the loading rate distributions were determined for a large range of loading rates (from 40 pN $s^{-1}$ to 31,000 pN $s^{-1}$) for all three configurations, which were each measured with only one cantilever to reduce spring calibration errors within one measurement. In the following step these values were plotted in a force *versus* loading rate (plotted logarithmically) diagram (Fig. 4). Following the approach used by Evans and coworkers,[4] the basal dissociation rate $k_{\text{off}}$ and the potential width $\Delta x$ were determined from a linear fit to the data points in the force *versus* loading rate diagram (Eq. (1)). The measurements of configuration N resulted in a $k_{\text{off}}$ of $16.9(\pm 1.0) \times 10^{-3}$ $s^{-1}$ and a $\Delta x$ of $0.82 \pm 0.01$ nm. The denoted errors refer to the constant estimated error of ±0.2 pN, which includes the injected noise and oscillations as described in Materials and Methods. In order to obtain the total error of the measurement, the systematic error for the calibration of the spring constant needs to be taken into account. The resulting maximum and

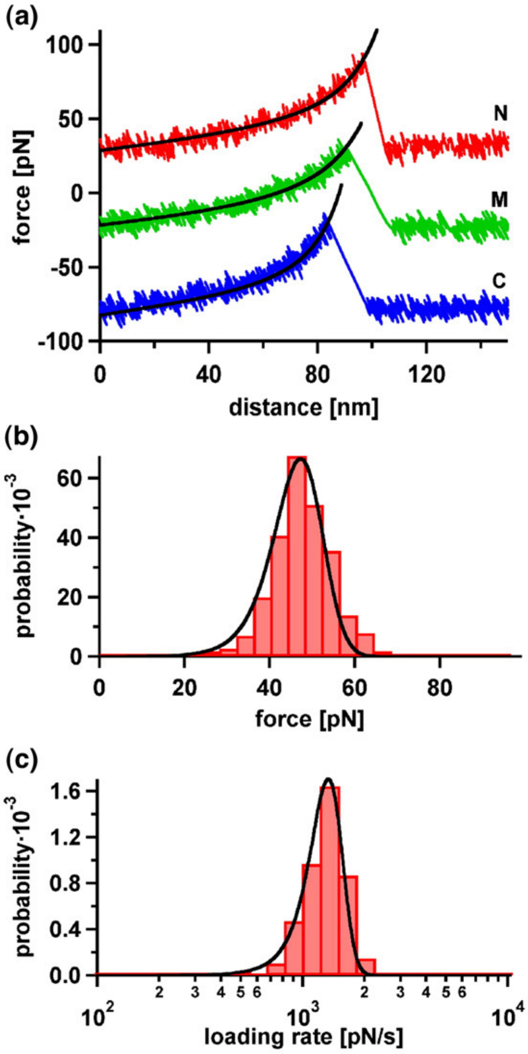

**Fig. 3.** Results from the AFM measurements. (a) Example of three typical force-extension curves measured for configurations N, M and C. The force-extension curves show the rupture event of the scFv–peptide complex, recorded at a retract velocity of 800 nm/s. The red force-extension curve corresponds to a rupture event measured for configuration N. The green and blue force-extension curves were gained for configurations M and C, respectively. All force-extension curves follow the characteristic shape of an extension curve of the poly(ethylene glycol) spacer and possess very similar rupture forces. The elastic behavior of the spacer can be described with the two-state FJC-fit (black curve). (b) Example of a rupture force distribution, obtained for configuration N. The rupture force histogram contains ~300 rupture events and was fitted with a Gaussian curve (black). (c) Example of a loading rate distribution obtained for configuration N. The histogram of the loading rates was plotted logarithmically and fit with a Gaussian curve (black).

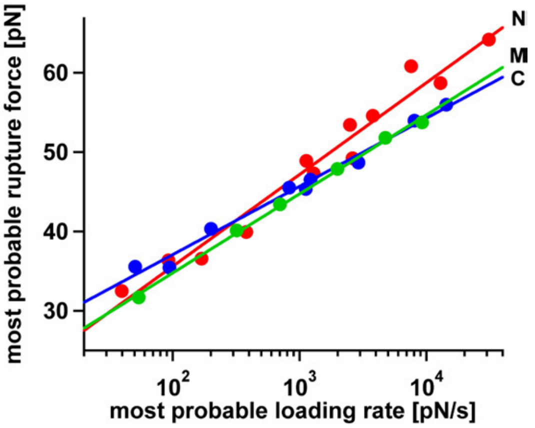

**Fig. 4.** Diagram showing the most probable rupture force plotted against the corresponding loading rate (logarithmically) for all three configurations N, M and C. The data points were gained from the Gaussian fits of the rupture force histogram and the histogram of loading rates. The red data points (configuration N) were fit to a straight line. From this linear fit, $\Delta x = 0.82 \pm 0.01$ nm and $k_{\text{off}} = 16.9(\pm 1.3) \times 10^{-3}$ $\text{s}^{-1}$ were obtained. The green data set was measured for configuration M. From the linear fit, $\Delta x = 0.95 \pm 0.01$ nm and $k_{\text{off}} = 7.6(\pm 1.0) \times 10^{-3}$ $\text{s}^{-1}$ were obtained. Finally, the measurement of configuration C yielded the blue data set. Here, the linear fit led to $\Delta x = 1.10 \pm 0.01$ nm and $k_{\text{off}} = 1.3(\pm 0.2) \times 10^{-3}$ $\text{s}^{-1}$.

minimum linear fit (see Materials and Methods) reveals the following values for $k_{\text{off}}$ and $\Delta x$: $14.5(\pm 1.0) \times 10^{-3}$ $\text{s}^{-1}$ for $k_{\text{off,max}}$ and $0.79 \pm 0.01$ nm for $\Delta x_{\text{max}}$ and $14.8(\pm 1.0) \times 10^{-3}$ $\text{s}^{-1}$ for $k_{\text{off, min}}$ and $0.87 \pm 0.01$ nm for $\Delta x_{\text{min}}$. The obtained values for $k_{\text{off}}$ and $\Delta x$, including their calculated errors, for all configurations N, M and C are given in Table 1. This detailed error analysis demonstrates that the basal dissociation rates and the potential widths of the three different configurations N, M and C can be clearly separated. A comparison of the three different configurations shows that configuration N possesses the smallest potential width and the fastest basal dissociation rate, which corresponds to the smallest energy barrier in the respective multidimensional energy landscape. In contrast, configuration C revealed the largest potential width ($\Delta x = 1.10 \pm 0.01$ nm) and the slowest basal dissociation rate ($k_{\text{off}} = 1.3(\pm 1.0) \times 10^{-3}$ $\text{s}^{-1}$), which therefore corresponds to the highest energy barrier of the three measured configurations. The values for the basal dissociation rate ($k_{\text{off}} = 7.6(\pm 1.0) \times 10^{-3}$ $\text{s}^{-1}$) and the potential width ($\Delta x = 0.95 \pm 0.01$ nm) for configuration M are between the values obtained for configurations N and C. Interestingly, the configuration with the fastest basal dissociation rate has the smallest potential width (configuration N), and the configuration with the slowest basal dissociation rate has the largest potential width (configuration C). Hence, in our system the length that the complex can be stretched before it finally ruptures is correlated with the basal dissociation rate. This correlation has been observed before for the interaction of different anti-fluorescein scFv fragments with their antigen fluorescein.[25] For the experiments performed here, this correlation can originate from a different starting conformation of the bound complexes. In this case, the number and strength of the stabilizing interactions would determine the basal dissociation rate and the potential width. Alternatively, the direction of the applied force can result in different unbinding pathways on the multidimensional energy landscape.

## Comparison of the basal dissociation rates (AFM) with surface plasmon resonance (SPR) data

In order to rule out the existence of different starting conformations, SPR measurements were done to investigate whether the attached cysteine residues (at the N terminus, the C terminus and the Ala8Cys$_{\text{peptide}}$ mutation) led to different conformations of the complex and as a result to differences in the dissociation rates and potential widths. These measurements revealed a dissociation rate of $1.5(\pm 0.6) \times 10^{-3}$ $\text{s}^{-1}$ for the peptide with the cysteine at its N terminus and $0.9(\pm 0.2) \times 10^{-3}$ $\text{s}^{-1}$ for the peptide with the cysteine at its C terminus. Furthermore, the following equilibrium binding constants were obtained: $13.4(\pm 8.7) \times 10^{-9}$ M for configuration N and $9.2(\pm 5.0) \times 10^{-9}$ M for configuration C. SPR measurements using the peptide with the Ala8Cys$_{\text{peptide}}$ mutation failed due to an insufficient signal. As indicated earlier, the mutation might reduce the helix propensity and therefore result in a lower fraction of α-helical peptides that are available for binding to the antibody fragment. On the basis of this assumption, the amount of helical peptides is considered to be too low to produce a signal in the SPR measurements. Therefore, no conclusion can be drawn about the stability of the complex itself and configuration M is not discussed further. In contrast, the values for the peptides with the cysteine attached at the N or C terminus agree within the experimental error. Concluding from

**Table 1.** Summary of the values for $k_{\text{off}}$ and $\Delta x$ for the three different configurations N, M and C (AFM and SPR measurements)

| | AFM | | | | | | |
|---|---|---|---|---|---|---|---|
| | Original linear fit | | Maximum linear fit | | Minimum linear fit | | SPR |
| Configuration | $k_{\text{off}}$ ($\times 10^{-3}\text{s}^{-1}$) | $\Delta x$ (nm) | $k_{\text{off}}$ ($\times 10^{-3}\text{s}^{-1}$) | $\Delta x$ (nm) | $k_{\text{off}}$ ($\times 10^{-3}\text{s}^{-1}$) | $\Delta x$ (nm) | $k_{\text{off}}$ ($\times 10^{-3}\text{s}^{-1}$) |
| N | 16.9±1.3 | 0.82±0.01 | 14.5±1.0 | 0.79±0.01 | 14.8±1.0 | 0.87±0.01 | 1.5±0.6 |
| M | 7.6±1.0 | 0.95±0.01 | 9.2±1.0 | 0.89±0.01 | 10.2±1.2 | 0.97±0.01 | – |
| C | 1.3±0.2 | 1.10±0.01 | 1.5±0.2 | 1.04±0.01 | 2.0±0.2 | 1.11±0.01 | 0.9±0.2 |

these data, the differences in the basal dissociation rates and potential widths, observed with the AFM, do not result from conformational changes in the peptide resulting from the cysteine residues attached either at the N or C terminus.

However, from these experiments it cannot be excluded that the different attachment points lead to a disturbance of the system when performing the AFM measurements. The structure together with the SMD simulations (see below) show that one of the main interactions between the peptide and the scFv fragment is very close to the N-terminal attachment point. Hence, the faster dissociation rate observed for the AFM in comparison to the SPR results might be caused by a partial unfolding of the peptide close to the attachment point, so that the interaction is partially weakened due to the linker used in the AFM measurements.

Although it cannot be ruled out that the immobilization on the AFM cantilever leads to slightly different conformations of the peptide, the data suggest that the different basal dissociation rates and potential widths are a consequence of the direction of the applied force. Assuming that the direction of the applied force results in different unbinding pathways, the values obtained for the basal dissociation rates and potential widths can be explained as follows. Within the experimental error, the basal dissociation rate for the peptide with the C-terminal cysteine determined with SPR agrees with the $k_{\mathrm{off}}$ value obtained for configuration C with the AFM. This leads to the conclusion, that the same barrier in the energy landscape is probed. In contrast, configuration N revealed a 13-fold higher basal dissociation rate, compared with the SPR value for the peptide with the N terminal cysteine. This difference for configuration N can be explained by considering an energy landscape with at least two barriers that need to be overcome (Fig. 5a). If no external force is applied, as is the case in the SPR measurements, the unbinding of the antibody fragment–peptide complex always follows the pathway with the lowest energy barrier. In contrast, in the AFM measurements the externally applied force is considered to define the pathway. In addition, the applied force tilts the energy landscape. The expected experimentally observed barrier heights and unbinding pathways are shown in the 2-D projection in Fig. 5b. For the SPR measurements, the second higher energy barrier is rate limiting for the unbinding of the antibody fragment–peptide complex, since this barrier has to be overcome to generate the free antibody fragment and the peptide (black curve in Fig. 5b). If an external force is applied, unbinding follows a different pathway and the energy landscape is tilted (red curve in Fig. 5b) such that the first originally lower energy barrier becomes prominent and is rate limiting. This simplified picture of the underlying energy landscape is able to explain the observed higher dissociation rate with the AFM for configuration N compared with the equilibrium measurement.

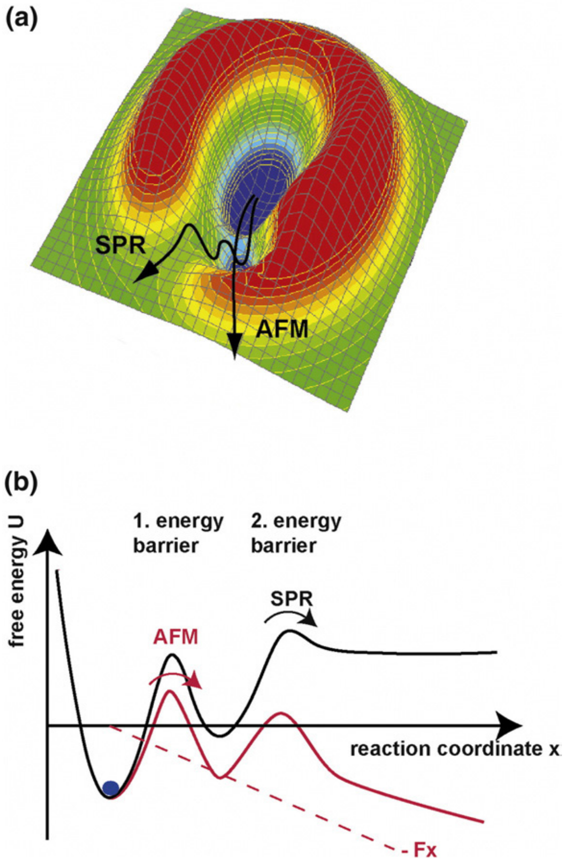

**Fig. 5.** Simplified model energy landscape explaining the AFM and SPR unbinding pathways of configuration N. (a) Three-dimensional representation of the energy landscape. In the SPR measurements, the unbinding of the antibody fragment–peptide complex always follows the pathway with the lowest energy barrier. In contrast, in the AFM measurements the pathway is determined by the direction of the applied force. (b) Two-dimensional projection of the unbinding pathway, including two energy barriers, in a defined direction. For the SPR measurements (black curve), the second higher energy barrier is rate limiting for the unbinding of the antibody fragment–peptide complex. If an external force is applied, the energy landscape is tilted (red curve). As a consequence, the first originally lower barrier becomes prominent and rate limiting for the unbinding process. Therefore, for configuration N, the AFM and SPR measurements probe different barriers of the energy landscape.

## Steered molecular dynamics (SMD) simulations

SMD simulations were done in order to explore the energy landscape in the high-velocity regime and to obtain more structure-based information about the energy barriers.[8,19–22,26] The structure PDB code 1P4B[15] of the truncated 12 amino acid long peptide bound to the antibody fragment was used for all simulations. Corresponding to the AFM experiments, three different attachment points on the peptide were defined (see Fig. 6). A pulling potential was attached to the N terminus of the peptide (configuration N; Ala-$1_{\mathrm{peptide}}$), its C-terminus (configuration C; Lys-$12_{\mathrm{peptide}}$) and Ala-$8_{\mathrm{peptide}}$

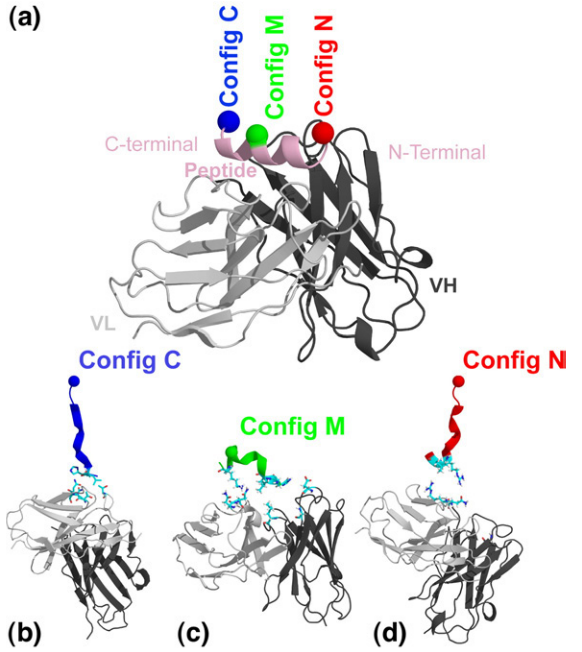

**Fig. 6.** Steered molecular dynamics simulations setup. All molecular dynamics simulations were started using the same initial structure. The center of mass (COM) of the heavy chain $V_H$ was fixed in space during the whole simulation time, whereas the light chain $V_L$ was not constricted. (a) For the simulation of the unbinding forces the pulling potential was attached to different $C^\alpha$ atoms of the peptide to yield the configurations N, M and C. (b–d) Last contacts between the scFv fragment and the peptide revealed by the SMD simulations. The last contacts between the peptide and the antibody fragment are shown for the respective configurations. The amino acids are identified in the main text.

(configuration M). In contrast to the AFM measurements, no additional amino acid was attached to the N or C terminus of the peptide and the alanine at position 8 was not replaced with a cysteine, which was necessary for the AFM-based analysis. The pulling potential steered the attached amino acid directly away from the antibody fragment at a speed of $v_{\text{pull}} = 2$ nm/ns. The all-atom trajectories and the pulling forces for every time-step were recorded for every simulation.

An average force-time curve out of 20 trajectories was generated for every configuration. A characteristic force-time curve with minimal root-mean-square deviation from the average force-time curve is shown in Figs 7–9. At least 65% of all 20 trajectories show the main pathway of the average force-time curve and were used for further analysis. For each configuration, the average times $t_i^j$ and average forces $F_i^j$ ($i = 1, 2$, corresponding to the number of the force peak; $j = $ N, M, C) were determined by analyzing the force peaks, which indicate the positions of the major rupture events in the unbindning pathways, and the errors were calculated as Gaussian errors.

In configuration N, the peptide is zipped off the antibody fragment starting from its N terminus. Here, two main barriers have been identified (Fig. 7; Table 2). The first barrier is crossed after $t_1^{\text{N}} = 440 \pm 25$ ps with a mean force of $F_1^{\text{N}} = 567 \pm 25$ pN and corresponds to the rupture of a hydrophobic contact between the amino acids Tyr-L40 and Leu-$3_{\text{peptide}}$. For the first rupture event, a rupture length of $r_1^{\text{N}} = 0.88 \pm 0.05$ nm was detected. The pathway that involves this interaction is taken in 75% of all trajectories. The second rupture event occurs after $t_2^{\text{N}} = 860 \pm 28$ ps with a mean force of $F_2^{\text{N}} = 716 \pm 23$ pN. For this second rupture event, the rupture length equaled $r_2^{\text{N}} = 1.72 \pm 0.06$ nm. The force peak, which corresponds to the second main barrier crossing and appears in 65% of all trajectories, results from the rupture of the H-bond between $\text{Glu}^{\text{O}\varepsilon}$-$6_{\text{peptide}}$ and the backbone hydrogen $\text{Gly}^{\text{H}}$-H40. The last contact for the unbinding process is formed by Asn-L69, Arg-L70, Arg-$9_{\text{peptide}}$ and Leu-$10_{\text{peptide}}$.

In configuration M, the peptide is separated from the antibody fragment in a double zipper mode, which leads to breakage of two stabilizing interactions next to the steered amino acid (Fig. 8).

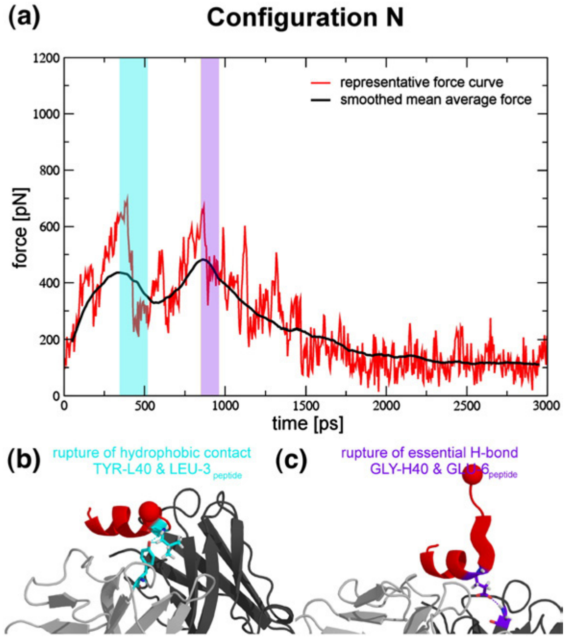

**Fig. 7.** Unbinding process of configuration N. (a) Force-time curves. The mean average force-time curve (black) and a representative force-time graph (red) were plotted. The unbinding process shows two important events, which correspond to the highlighted force peaks. The colors of the highlighted force peaks were chosen according to the colors in the molecular structures (cyan for the first rupture event and purple for the second rupture event). (b) Structural origin of the first unbinding event. The first unbinding event (cyan) corresponds to the rupture of the hydrophobic contact between Tyr-L40 and Leu-$3_{\text{peptide}}$. The picture shows the molecular structure shortly before the event is observed. c. Structural origin of the second unbinding event. The second unbinding event (purple) corresponds to the rupture of the important H-bond between $\text{GLY}^{\text{H}}$-H40 and $\text{GLU}^{\text{O}\varepsilon}$-$6_{\text{peptide}}$. The picture shows the molecular structure shortly before the event is observed. This second rupture event has also been found in the two other configurations M and C.

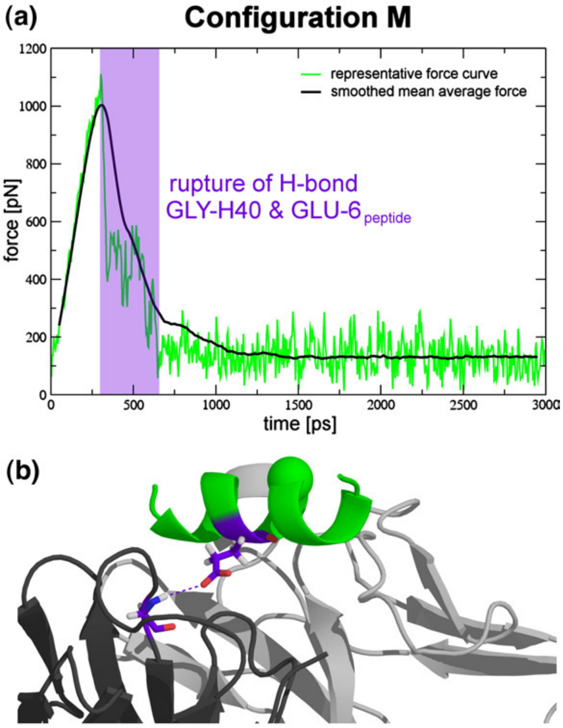

**Fig. 8.** Unbinding process of configuration M. (a) Force-time curves. The mean average force curve (black) and a representative force-time graph (green) were plotted. The force-time curve shows one major peak highlighted in purple. (b) Structural origin of the observed unbinding event. The unbinding event (purple) corresponds to the rupture of the important H-bond between Gly$^{H}$-H40 and Glu$^{O\varepsilon}$-6$_{peptide}$. The picture shows the molecular structure shortly before the event is observed. This rupture event has also been found in configurations N and C.

Nevertheless, only one major force peak can be identified after an average pulling time of $t_1^{M}=319\pm 9$ ps (corresponding to a rupture length of $r_1^{M}=0.64\pm 0.02$ nm) at an average force of $F_1^{M}=1161\pm 28$ pN (Table 2). The main barrier is identified clearly as the rupture of the H-bond between Gly$^{H}$-H40 and Glu$^{O\varepsilon}$-6$_{peptide}$ (in 95% of all trajectories). This interaction also causes the second rupture event in the majority of trajectories in configuration N (Fig. 7; Table 2). Subsequent to this H-bond rupture in configuration M, after a mean time of additional $\Delta t^{M}=40\pm 8$ ps (corresponding to $\Delta r^{M}=0.08\pm 0.02$ nm), the double H-bond between Asp$^{O\delta i}$-H137 and Arg$^{H\zeta i}$-9$_{peptide}$ ($i=1,2$) ruptures (Fig. 8) without a resolvable additional force peak. The last contact for the unbinding process in configuration M is formed via Asn-L68, Asn-L69 and Lys-11$_{peptide}$ on the C-terminal side. The last contact on the N-terminal side of the peptide ruptures shortly before the C-terminal last contact between Leu-3$_{peptide}$ and His-2$_{peptide}$ of the peptide and Asn-L68, Asp-H33 and Leu-H110 of the scFv fragment.

In configuration C, the peptide is zipped off starting from its C terminus end. Again, two main force peaks are identified. The first force peak was detected after $t_1^{C}=514\pm 20$ ps (corresponding to a rupture length of $r_1^{C}=1.03\pm 0.04$ nm) at a mean force of $F_1^{C}=775\pm 28$ pN. This force peak coincides with the opening of the stabilizing backbone H-bond of the first peptide helix loop between Val-7$_{peptide}$ and Leu-10$_{peptide}$. Hence, the first major rupture event refers to the opening of the secondary structure of the peptide and not to the breakage of a peptide–antibody fragment bond. The rupture of this interaction on the main unbinding pathway is seen in 85% of all trajectories. The second barrier crossing occurred after an average time of $t_2^{C}=750\pm 45$ ps with an average rupture length of $r_2^{C}=1.50\pm 0.09$ nm and an average force of $F_2^{C}=720\pm 21$ pN. This force peak is again determined by the rupture of the H-bond between Gly$^{H}$-H40 and Glu$^{O\varepsilon}$-6$_{peptide}$ (Fig. 9; Table 2). A total of 65% of all trajectories crossed this second barrier via the main unbinding pathway. The last contact for the unbinding process of configuration C is formed via His-2$_{peptide}$ , LEU-3$_{peptide}$, Thr-L32, Thr-L67, Asn-L68 and Asn-L69.

The three configurations underline the importance of the H-bond between the backbone of Gly$^{H}$-H40 and Glu$^{O\varepsilon}$-6$_{peptide}$. The breakage of this bond is a

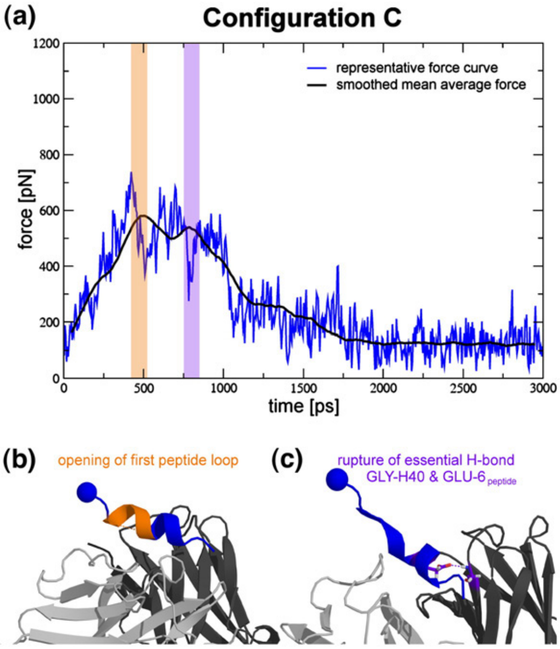

**Fig. 9.** Unbinding process of configuration C (a) Force-time curves. The mean average force-time curve (black) and a representative force-time graph (blue) were plotted. The two important rupture events represented by the force peaks of the mean curve were highlighted according to the colors in the molecular structures. (b) Structural origin of the first unbinding event. The first rupture event (orange) corresponds to the breakage of a backbone hydrogen bond stabilizing the α-helical structure of the peptide resulting in the opening of a peptide loop. The picture shows the molecular structure shortly before this event is observed. (c) Structural origin of the second unbinding event. The second unbinding event (purple) corresponds to the rupture of the important H-bond between Gly$^{H}$-H40 and Glu$^{O\varepsilon}$-6$_{peptide}$. The picture shows the molecular structure shortly before the event is observed. This rupture event has also been found in configurations N and M.

**Table 2.** Summary of the information obtained from the force curves from the three different configurations N, M and C (SMD simulations)

| | Force peak 1 | | | | Force peak 2 | | | |
|---|---|---|---|---|---|---|---|---|
| Configuration | $t_1$ (ps) | $F_1$ (pN) | $r_1$ (nm) | Interaction | $t_2$ (ps) | $F_2$ (pN) | $r_2$ (nm) | Interaction |
| N | 440±25 | 567±25 | 0.88±0.05 | Tyr-L40 and Leu-3$_{\text{peptide}}$ | 860±28 | 716±23 | 1.72±0.06 | Gly$^{\text{H}}$-H40 and Glu$^{\text{O}\varepsilon}$-6$_{\text{peptide}}$ |
| M | 319±9 | 1161±28 | 0.64±0.02 | Gly$^{\text{H}}$-H40 and Glu$^{\text{O}\varepsilon}$-6$_{\text{peptide}}$ | 359±8 | n. d. | 0.72±0.02 | Asp$^{\text{O}\delta i}$-H137 and Arg$^{\text{H}\zeta i}$-9$_{\text{peptide}}$ ($i=1$, 2) |
| C | 514±20 | 775±28 | 1.03±0.04 | Loop opening | 750±45 | 720±21 | 1.50±0.09 | Gly$^{\text{H}}$-H40 and Glu$^{\text{O}\varepsilon}$-6$_{\text{peptide}}$ |

dominant rupture event in the majority of all trajectories independent of the pulling vector. The configurations N and C, where the peptide unbinds in a single zipper mode, show two main rupture events. In configuration N, the first force peaks occurs earlier ($t_1^{\text{N}} < t_1^{\text{C}}$) and at lower forces ($F_1^{\text{N}} < F_1^{\text{C}}$) with respect to configuration C. The respective first force peak in configurations N and C results from different molecular interactions. Therefore, different force vectors probe different pathways through the landscape. However, the second force peak corresponds to the same molecular interaction of Gly$^{\text{H}}$-H40 and Glu$^{\text{O}\varepsilon}$-6$_{\text{peptide}}$ in both configurations. The rupture forces of this interaction, indicative of the slope of the energy surface, are comparable in both configurations. And yet, in configuration C, the second force peak occurs earlier ($t_2^{\text{N}} > t_2^{\text{C}}$). The rupture length for this second force peak of configuration C ($r_2^{\text{C}} = 1.50 \pm 0.09$ nm) is hence shorter than in configuration N ($r_2^{\text{N}} = 1.72 \pm 0.06$ nm), despite probing the identical interaction. This is due to the different intramolecular distances between force attachment points and the Glu$^{\text{O}\varepsilon}$-6$_{\text{peptide}}$, demonstrating that, depending on the configuration, the same barrier can have different characteristics (here, the barrier width). Furthermore, this interaction between Gly$^{\text{H}}$-H40 with Glu$^{\text{O}\varepsilon}$-6$_{\text{peptide}}$ is also probed in configuration M, showing a very different fingerprint of the force curve than in the other two configurations. The shorter rupture length and higher rupture forces compared with configurations N and C result from the very direct force attachment point, again underlining the fact that the molecular nature of the interaction and the geometry of the force probing crucially determine the characteristics of the probed interaction.

## Comparison of the SMD and AFM results

Both simulation and experiment probe the respective antibody fragment–peptide complex at the same positions on the peptide, thereby exerting forces in the same directions. SMD simulations, due to computational limitations, probe the system at much higher loading rates.[22,27] Hence, thermal relaxation occurs only partially. The system lacks the time to relax orthogonally to the pulling direction and resulting from this, lacks the time to explore the energy landscape locally to find the optimal pathway to cross the barrier.[27] This might lead to a steeper pathway on the energy landscape potentially crossing higher barriers and finally resulting in higher rupture forces. Whereas higher rupture forces have been observed for all configurations, this effect is most dominant for configuration M, which unbinds in a double zipper mode (nearly simultaneous rupture of two bonds). In the simulations, as soon as the first important interaction breaks (H-bond Gly$^{\text{H}}$-H40, which binds Glu$^{\text{O}\varepsilon}$-6$_{\text{peptide}}$), the more stable double H-bond of the interaction between Asp$^{\text{O}\delta i}$-H137 and Arg$^{\text{H}\zeta i}$-9$_{\text{peptide}}$ ($i = 1$, 2) experiences the full load and ruptures within 40 ps (Fig. 8). In contrast, in the AFM experiments, the system can relax orthogonally to the applied force and can re-arrange after the first breakage. As a result, after the first breakage the complex might become so unstable that dissociation occurs on a timescale too fast to be observed with the AFM.

Furthermore, the Ala8Cys mutation in the peptide used in the AFM experiments may lead to additional disturbances of the peptide structure, which may result in a lower stability of the complex. The mutation lies in that region of the peptide with the highest probability for α-helix formation and mutations at this position have been shown to have an influence on the stability of the leucine zipper.[24,28] Although, as described previously, this mutation is considered to influence the binding process more than the stability of the bound complex, a destabilizing contribution of the mutation on the complex cannot be fully excluded.

A more detailed comparison of the values obtained from the AFM experiments and the SMD simulations provides an explanation of the energy barriers on the unbinding pathways for the respective configurations. The comparison of the potential widths obtained with the AFM and the rupture lengths obtained from the SMD simulations shows that the rupture lengths for configurations N and C for the first barrier crossing of the main unbinding pathway ($r_1^{\text{N}}$, $r_1^{\text{C}}$) are in good agreement with the potential widths obtained with the AFM ($\Delta x^{\text{N}}$, $\Delta x^{\text{C}}$) (Tables 1 and 2). Hence, the AFM experiments probe the first barrier observed in the SMD simulations (Fig. 10). Again, for configuration M, the observed differences might result from the different relaxation due to different time regimes and from the potentially destabilizing mutation, as discussed above.

Furthermore, the SMD simulations provide further evidence for the existence of a second energy barrier,

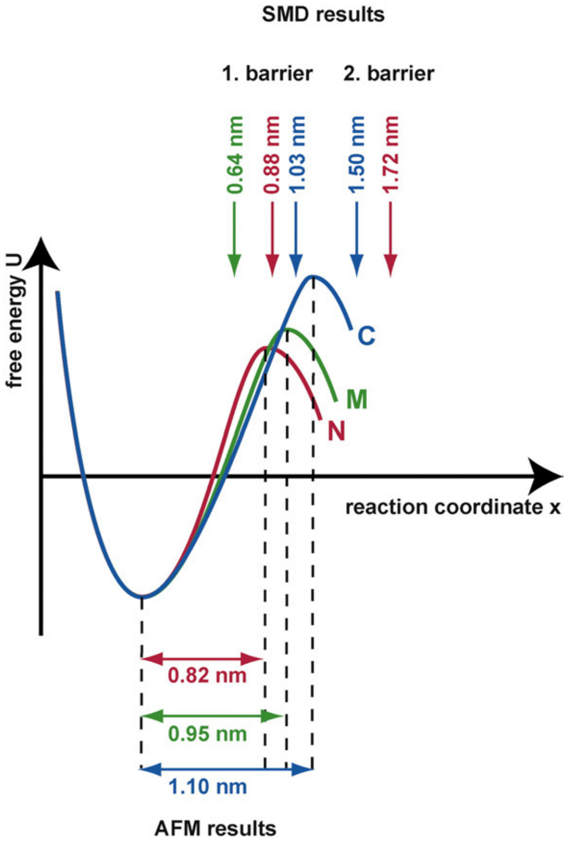

**Fig. 10.** Two-dimensional projection of the energy barriers obtained from the AFM experiments and the rupture lengths obtained from the SMD simulations. To summarize the results, the potential widths and basal dissociation rates have been taken from the AFM measurements and plotted in a 2-D energy diagram (configuration N, red; configuration M, green; and configuration C, blue) to provide an overview of the barriers that need to be crossed. Further unbinding pathways on the respective energy landscapes are not known. The arrows above the energy landscapes indicate the positions of the respective rupture lengths for the first and second barrier crossing of the main unbinding pathway, obtained from the SMD simulations.

which was not shown unambiguously by the AFM and SPR data. The forces needed to overcome the second barrier of the main unfolding pathway are of the same order of magnitude as for the first barrier crossing. Yet, the second rupture event for configurations N and C occurs at nearly twice the distance of the first rupture event (Table 2). Hence, the second energy barrier of the main unfolding pathway in the energy landscape has a large potential width. Outer barriers are much more influenced by externally applied forces than inner barriers, due to the tilted energy landscape. Because of this large potential width of the second barrier observed in the SMD simulations, it is plausible that this barrier is not probed in the AFM measurements, even at the lowest applied loading rates. Therefore, the existence of two energy barriers is not in conflict with the observation that the AFM data could be fit with a straight line in the force *versus* loading rate plot in Fig. 4.

The SMD data explain the observed potential widths in the different experimental configurations, and they provide more information about the basal dissociation rates of the first barrier crossing obtained from the AFM measurements. As stated earlier, the results from the SMD simulations show that the first barrier crossing in configuration C occurs at a longer rupture length ($r_1^C > r_1^N$) and at a greater force ($F_1^C > F_1^N$) than in configuration N. Since the forces measured with the SMD simulations correspond to the slope of the energy barrier in the energy landscape, the higher forces observed in configuration C result from a steeper energy barrier. This steeper energy barrier together with the longer rupture length indicates that the first energy barrier of the main unbinding pathway is higher in configuration C than in configuration N. A higher energy barrier corresponds to a lower dissociation rate. Hence, if — as already concluded from the comparison of AFM and SPR — the inner energy barrier is rate-determining for the AFM experiments (Fig. 5), experiment and simulation agree on a lower dissociation rate for configuration C compared with the dissociation rate for configuration N ($k_{\mathrm{off},1}(\mathrm{C}) < k_{\mathrm{off},1}(\mathrm{N})$).

## Conclusions

A well-characterized antibody–antigen interaction has been chosen to explore the underlying energy landscape with a combination of different techniques. The main focus was to investigate if different pulling directions lead to different unbinding pathways and therefore provide a more detailed insight into the unbinding process of the interaction. SMD simulations detected two rupture events for every pulling direction. One rupture event in each configuration is determined by the same molecular bond, whereas the other rupture event originates from the breakage of different bonds. These findings show clearly that the underlying energy landscape is multidimensional. This information could not be obtained from the AFM measurements alone, which show a linear dependence of the rupture forces on the logarithm of the loading rate — a feature that is characteristic for a two-state system with only one barrier. However, a comparison of AFM and SPR points to the existence of at least one more barrier. SPR always probes the lowest energy barrier in the energy landscape. When performing AFM measurements, the complex might be forced to follow a steeper unbinding pathway, which would result in a lower dissociation rate (corresponding to a higher barrier). But, as stated earlier, the basal dissociation rate for configuration N obtained with the AFM is higher than the $k_{\mathrm{off}}$ value obtained with SPR. This leads to the conclusion that the energy barrier probed with the AFM is lower than the energy barrier that has to be overcome under equilibrium conditions. Therefore, an additional energy barrier has to exist along the pulling direction of configuration N (Fig. 5), which is not detectable with the

AFM. The results from the SMD simulations further support this conclusion, since the outer (second) barrier has a very large potential width so that the inner (first) barrier is most likely rate-determining even at the smallest loading rates. For configuration C, the SMD simulations also show a second barrier, which is considered to be lower than the first barrier and which is therefore not probed experimentally.

In conclusion, the experimental set-up chosen for the AFM measurements, which allows the site-specific immobilization of the binding partners, shows clearly that the direction of the applied force defines the unbinding pathway on a multidimensional energy landscape. This finding points out clearly that non(site)-specific coupling procedures provide a simplified picture of the molecular interactions as the contributions of different unbinding pathways are averaged out.

## Materials and Methods

### Preparation of the peptides and the scFv fragment

Peptides representing a truncated version of the GCN4-p1 leucine zipper $Y_1HLENEVA_8RLKK_{12}$ were obtained from Jerini Peptide Technologies GmbH, Berlin, Germany. A cysteine has been introduced at different positions during solid-phase synthesis to provide site-specific attachment points for the immobilization on the cantilever (Fig. 2): $NH_2$-CGGGYHLENEVARLKK-amide (configuration N), $NH_2$-YHLENEVCRLKK-amide (configuration M), and $NH_2$-YHLENEVARLKKGGGC-amide (configuration C).

The expression and purification of the scFv fragment H6 was carried out as described.[29] Briefly, the scFv fragment H6 was expressed with a C-terminal His tag followed by cysteine to allow a site-specific immobilization. The plasmid for the periplasmic expression in *Escherichia coli* is based on the pAK series.[30] The gene for co-expression of the periplasmic chaperone Skp was introduced.[31] The original His tag was replaced by a $His_6$ tag followed by two glycine residues and a cysteine. For the expression and purification of H6, the protocol described by Hanes *et al*.[16] was slightly modified. In short, the bacteria with the transformed plasmid were grown at 25 °C in SB medium (20 g $l^{-1}$ Tryptone, 10 g $l^{-1}$ yeast extract, 5 g $l^{-1}$ NaCl, 50 mM $K_2HPO_4$) containing 30 μg $ml^{-1}$ chloramphenicol. Expression was induced with 1 mM isopropyl-β-d-thiogalactopyranoside (IPTG) at an $A_{600}$ between 1.0 and 1.5. The cells were harvested 3 h after induction by centrifugation. Cell disruption was achieved by French press lysis. The scFv fragment H6 was purified using two chromatography steps. After chromatography on a $Ni^{2+}$-NTA column (Qiagen, Hilden, Germany) using standard protocols the eluted fraction was loaded directly onto an affinity column with immobilized antigen. The fractions from the affinity column were dialyzed against coupling buffer (50 mM sodium phosphate, pH 7.2, 50 mM NaCl, 10 mM EDTA) and concentrated using Centricon YM-10 (Millipore, Eschborn, Germany). The actual concentration of the purified scFv fragment H6 was determined by measuring $A_{280}$. The extinction coefficient was calculated using the program Vector NTI (Invitrogen, Karlsruhe, Germany). The preparation of the purified protein was adjusted to a concentration of 0.8 mg $ml^{-1}$ and stored at −80 °C.

### Preparation of slides and cantilevers for the AFM measurements

Poly(ethylene glycol) (PEG) was used as a spacer between the biomolecules and the surfaces. PEG is an ideal spacer for force spectroscopy measurements[25,32–37], as it provides protein-resistant surfaces,[38] thereby reducing the number of non-specific binding events. In addition, PEG shows a characteristic force-extension curve, allowing the discrimination between specific and non-specific interactions during data analysis. The scFv fragment H6 possessing a C terminal cysteine was immobilized on an amino-functionalized slide using a hetero-bifunctional NHS-PEG-maleimide (mass = 5000 g/mol; Nektar, Huntsville, AL, USA). The three peptides were separately immobilized via their introduced cysteine to an amino-functionalized cantilever, again using the NHS-PEG-maleimide spacer (Fig. 2).

In detail, the cantilevers (Bio-lever, Olympus, Tokyo, Japan) were activated with a 10 min UV-ozone cleaning treatment and amino modified with 3-aminopropyl-dimethylethoxysilane (ABCR GmbH, Karlsruhe, Germany) as described.[29,35,36] Commercially available amino-functionalized slides (Slide A, Nexterion, Mainz, Germany) were used for the immobilization of the scFv fragment. For the next steps, both surfaces (slide and cantilever) were treated in parallel as described.[39] Briefly, they were incubated in 50 mM sodium borate buffer, pH 8.5, in order to increase the fraction of unprotonated amino groups for coupling to the NHS groups of the PEG. NHS-PEG-maleimide was dissolved at a concentration of 50 mM in borate buffer and incubated on the surfaces for 1 h. In parallel, one of the peptides and the scFv fragment H6 were reduced using TCEP beads (Perbio Science, Bonn, Germany) in order to generate free thiols. After washing both surfaces with ultrapure water, a solution of the peptide (200 μM) was incubated on the cantilever and a solution of the scFv fragment H6 (0.13 mg/ml) was incubated on the slide for 1 h. Finally, both surfaces were rinsed with PBS (10 mM sodium phosphate, pH 7.4, 137 mM NaCl, 2.7 mM KCl) to remove non-covalently bound material, and stored in PBS at room temperature.

### Force spectroscopy

All force measurements were performed with a MFP-1D AFM (Asylum Research, Santa Barbara, CA, USA) at room temperature in PBS. The cantilever spring constants were 8.7 pN/nm for the measurement of configuration N (see Fig. 2), 3.4 pN/nm for the measurement of configuration M, and 4.2 pN/nm for the measurement of configuration C (B-Bio-Lever) and were obtained as described.[40,41] During the experiments, the approach and retract velocity were held constant, whereas the applied force was adjusted by changing the distance between the cantilever tip and the surface to obtain single binding events. Several hundred approach–retract cycles were carried out to achieve good statistics. Each experiment was done for different retract velocities ranging from 50 nm/s to 10 μm/s to obtain measurements over a broad range of loading rates.

### Data extraction

The experimental data were converted into force-extension curves. From these, the rupture force (the force at which the antibody fragment–antigen complex ruptures), the rupture length and the loading rate were determined using the program Igor Pro 5.0 (Wavemetrics, Lake Oswego, OR, USA) and a custom-written set of procedures. The rupture force was determined as described.[4,42] The loading rate was determined using the two-state, freely jointed chain fit to the force-extension curve, according to previous studies.[43]

### Data analysis

To analyze the data set obtained from one experiment, which was recorded at a constant retract velocity, the rupture forces, the rupture lengths and the loading rates were plotted in three histograms. These histograms were analyzed with a method based on the so-called Bell-Evans model.[4,44] The rupture force and loading rate (plotted logarithmically) histograms for each data set, i.e. for each retract velocity, were fitted with a Gaussian distribution to determine the maxima. Finally, these obtained maxima were plotted in a force *versus* loading rate diagram. The maximum force (from the Gaussian distribution of the rupture force histogram) represents the most probable force F*:

$$F^* = \frac{k_B \cdot T}{\Delta x} \ln \frac{F \cdot \Delta x}{k_B \cdot T \cdot k_{\mathrm{off}}} \quad (1)$$

where $k_B$ is the Boltzmann constant, $T$ is temperature, $\Delta x$ is the potential width, $k_{\mathrm{off}}$ is the basal dissociation rate at zero force and $F^*$ ($= \mathrm{d}F/\mathrm{d}t$) is the loading rate. From a linear fit of the force *versus* loading rate (pictured logarithmically) plot and Eq. (1), $\Delta x$ and $k_{\mathrm{off}}$ of the antibody fragment–antigen complex can be determined from the slope and the intercept of the linear fit with the abscissa.

### Error estimation

To calculate the error of the dissociation rate $k_{\mathrm{off}}$ and the potential width $\Delta x$, the following assumptions were made:

(i) The error in the calibration of the spring constant constitutes 10 %.
(ii) Injected noise and oscillations lead to an error of ±0.2 pN in the measured rupture force. This value was estimated from the integration of the frequency spectrum of the cantilever in PBS to a frequency of 10 Hz.

As described above, $k_{\mathrm{off}}$ and $\Delta x$ can be calculated from the linear fit to the data points in the force *versus* loading rate diagram. Due to the use of only one cantilever for all data points, the error, originating from the calibration of the spring constant, leads to systematic higher or lower rupture forces and loading rates, and therefore to higher or lower most probable rupture forces and loading rates. We therefore determined the maximum and minimum linear fit. From these two fits, the maximum and minimum $k_{\mathrm{off}}$ and $\Delta x$ can be calculated. In addition, the estimated value of ±0.2 pN was taken into account. This error is not systematic and can be added or subtracted from the most probable rupture force. By using a random generator, a mean linear fit was calculated. From this, we gained a mean value for $k_{\mathrm{off}}$ and $\Delta x$ with the corresponding standard deviation. This procedure was applied to the original, the maximum and the minimum linear fit in the force *versus* loading rate plot to receive the maximum and minimum $k_{\mathrm{off}}$ and $\Delta x$ with their corresponding standard deviations.

### Proof of specificity

To prove the specificity of the force spectroscopy measurements, experiments were performed, either without the antibody fragment or without the peptide. By measuring the antibody fragment H6, attached to the surface, against a cantilever tip passivated with PEG, more than 1000 force-extension curves were recorded. Thereby, less than 1% non-specific interactions were detected. The measurements without the peptide led to similar results.

### SPR measurements

The measurements of the dissociation rate $k_{\mathrm{off}}$ (25 °C) and the equilibrium constants $K_d$ of the scFv fragment H6 and the peptide with cysteine at either its N or C terminus were done with a Biacore X instrument (BIAcore, Freiburg, Germany). For this purpose a CM5 sensor chip (BIAcore) was modified via amine coupling according to the manufacturer's protocol. Clone H6 was diluted in immobilization buffer (10 mM sodium acetate, pH 5.0) to a final concentration of 11.4 ng/μl and placed onto the chip. The final signal intensity on the surface was ~200 RU. A series of the respective peptide solutions in PBS buffer in the range of 1.64–400 nM for the measurement of $k_{\mathrm{off}}$ and 4–400 nM for the measurement of $K_d$ was placed onto the chip. After binding, dissociation was followed at a flow rate of 50 μl/min. The dissociation and association phase was fit globally, using the single-exponential fit function of the program BIAEvaluation 3.2. The equilibrium constants were gained from separate determination of the dissociation and association rate.

### Molecular dynamics simulations (MD)

All MD simulations were based on the 2.35 Å resolution X-ray structure 1P4B[15] of the antibody scFv fragment bound to the peptide $A_1HLENEVA_8RLKK_{12}$. Here, the amino acids of the antibody fragment are labeled with the three-letter code of the amino acid, the location in the $V_H$ or $V_L$ domain, and the position in the 1P4B PDB structure. The amino acids of the peptide are labeled as a combination of the three-letter code and the number of the amino acid in the crystal structure. To distinguish between antibody fragment and peptide amino acids, the residues of the peptide are identified by the subscript peptide.

The first amino acid of the 1P4B PDB structure differs from the experimentally used amino acid. We chose not to mutate the sequence to match the experimental one, because this would have reduced the resolution of the structure. The influence of this sequential difference will not be significant, since it is located at the non-interacting end of the peptide.

All MD simulations were performed using the software GROMACS.[45–47] We used periodic boundary conditions, the OPLS-AA force field[48] and SPC/E water[49] for all MD simulations. For all simulations first one energy-minimized, equilibrated and pre-oriented state of the proteins solved in water was generated. This initial structure was assigned to new Boltzmann-distributed velocities and again equilibrated shortly before the SMD simulations were performed.

### System preparation

The antibody fragment–peptide structure 1P4B was pre-oriented with the helical peptide axis parallel with the *z*-

axis of the system. Then the molecules were solvated in a 6.8 nm × 6 nm × 11.6 nm waterbox (16,034 $H_2O$) ionized with 45 sodium and 43 chloride atoms. The overall charge of the system was neutral.

Steepest descent energy minimization was performed with a maximum step size of 0.01 nm up to a precision of 2000 kJ/(mol·nm). No pressure or temperature coupling was used. The cut-off radius for Coulomb and van der Waals interactions was set to 1 nm.

Afterwards, a water relaxation simulation of 200 ps was preformed. On all protein atoms, a positional restraint was placed using a harmonic potential with a force constant of 2000 kJ/(mol·nm$^2$) = 3.32 nN/nm on the protein atoms. The LINCS algorithm was used on all bond constraints.[50] Protein and non-protein atoms were coupled separately to a heat-bath of 300 K using a time constant of 0.1 ps.

All further simulations were performed using fast particle-mesh Ewald electrostatics with an order of 4 and a van der Waals cut-off of 1.0 nm. A 1 ns equilibration of the whole system followed. A leapfrog algorithm with a time-step of 2 fs was used. All $C^\alpha$ atoms were restrained with a harmonic potential of 1000 kJ/(mol·nm) = 1.8 nN/nm to avoid an unwanted rotation of the system. The restraint potential was weak enough to allow small conformational changes of the backbone due to the equilibration. The side chains were not restricted and therefore freely equilibrating. The RMSD (nm) fit of the $C^\alpha$ position reached a stable plateau within this equilibration (data not shown). The temperature was restricted to 300 K analogs to the last step. The resulting structure was used as the initial structure for all configurations to allow a better comparison of the results. Before the actual SMD simulations were performed, for each simulation new random Boltzmann distributed velocities were assigned and an additional 200 ps pre-equilibration was performed.

### Simulations

In every SMD simulation the antibody fragment was fixed in space via a COM movement removal of the chain $V_H$ of the antibody fragment. In each configuration, a different $C^\alpha$ atom was steered away from the antibody fragment (in the $x$-direction) with a harmonic potential using a spring constant of $k = 1600$ kJ/(mol·nm$^2$) = 2.66 nN/nm. This steering was executed for 3 ns at a speed of $v_{\text{pull}} = 2$ nm/ns resulting in a final separation of 6 nm. The strong steering potential forces the attached atom to follow it closely. No other atom of the peptide is restricted in any way, leaving it to respond freely to the forced movement of the attached atom.

Three different configurations were tested in correspondence to the AFM experiments. In configuration N, the $C^\alpha$ atom of the N-terminal alanine Ala-$1_{\text{peptide}}$ of the antigen peptide was attached to the steering potential. In configuration C, the $C^\alpha$ atom of the C-terminal amino acid Lys-$12_{\text{peptide}}$ was attached and in the configuration M the $C^\alpha$ atom of the eighth amino acid Ala-$8_{\text{peptide}}$ was attached. In contrast to the AFM experiments, no mutation in configuration M was performed, because no cysteine for external linkage was needed in the SMD simulations.

## Acknowledgements

We thank Dr. Torsten Pirch and Professor Dr. Kirsten Jung for the SPR data, Professor Dr. Andreas Plückthun for the gift of the expression vector of the antibody fragment and Gert De Cremer for help in preparing Fig. 5. This work was supported by the Center for Integrative Protein Science Munich, the European Union, the Deutsche Forschungsgemeinschaft and the Fonds der Chemischen Industrie.

## References

1. Henzler-Wildman, K. & Kern, D. (2007). Dynamic personalities of proteins. *Nature*, **450**, 964–972.
2. Tsai, C. J., Ma, B., Sham, Y. Y., Kumar, S. & Nussinov, R. (2001). Structured disorder and conformational selection. *Proteins: Struct. Funct. Genet.* **44**, 418–427.
3. Kumar, S., Ma, B., Tsai, C. J., Sinha, N. & Nussinov, R. (2000). Folding and binding cascades: dynamic landscapes and population shifts. *Protein Sci.* **9**, 10–19.
4. Evans, E. & Ritchie, K. (1999). Strength of a weak bond connecting flexible polymer chains. *Biophys. J.* **76**, 2439–2447.
5. Merkel, R., Nassoy, P., Leung, A., Ritchie, K. & Evans, E. (1999). Energy landscapes of receptor-ligand bonds explored with dynamic force spectroscopy. *Nature*, **397**, 50–53.
6. Bustamante, C., Bryant, Z. & Smith, S. B. (2003). Ten years of tension: single-molecule DNA mechanics. *Nature*, **421**, 423–427.
7. Nevo, R., Brumfeld, V., Kapon, R., Hinterdorfer, P. & Reich, Z. (2005). Direct measurement of protein energy landscape roughness. *EMBO Rep.* **6**, 482–486.
8. Barsegov, V. & Thirumalai, D. (2005). Probing protein-protein interactions by dynamic force correlation spectroscopy. *Phys. Rev. Lett.* **95**, 168302.
9. Kessler, M., Gottschalk, K. E., Janovjak, H., Müller, D. J. & Gaub, H. E. (2006). Bacteriorhodopsin folds into the membrane against an external force. *J. Mol. Biol.* **357**, 644–654.
10. Bornschlögl, T. & Rief, M. (2006). Single molecule unzipping of coiled coils: sequence resolved stability profiles. *Phys. Rev. Lett.* **96**, 118102.
11. Evans, E., Ritchie, K. & Merkel, R. (1995). Sensitive force technique to probe molecular adhesion and structural linkages at biological interfaces. *Biophys. J.* **68**, 2580–2587.
12. Rief, M., Gautel, M., Oesterhelt, F., Fernandez, J. M. & Gaub, H. E. (1997). Reversible unfolding of individual titin immunoglobulin domains by AFM. *Science*, **276**, 1109–1112.
13. Oesterhelt, F., Oesterhelt, D., Pfeiffer, M., Engel, A., Gaub, H. E. & Müller, D. J. (2000). Unfolding pathways of individual bacteriorhodopsins. *Science*, **288**, 143–146.
14. Kessler, M. & Gaub, H. E. (2006). Unfolding barriers in bacteriorhodopsin probed from the cytoplasmic and the extracellular side by AFM. *Structure*, **14**, 521–527.
15. Zahnd, C., Spinelli, S., Luginbühl, B., Amstutz, P., Cambillau, C. & Plückthun, A. (2004). Directed *in vitro* evolution and crystallographic analysis of a peptide-binding single chain antibody fragment (scFv) with low picomolar affinity. *J. Biol. Chem.* **279**, 18870–18877.
16. Hanes, J., Jermutus, L., Weber-Bornhauser, S., Bosshard, H. R. & Plückthun, A. (1998). Ribosome display efficiently selects and evolves high-affinity antibodies *in vitro* from immune libraries. *Proc. Natl Acad. Sci. USA*, **95**, 14130–14135.
17. Kammerer, R. A., Schulthess, T., Landwehr, R., Lustig, A., Engel, J., Aebi, U. & Steinmetz, M. O. (1998). An

autonomous folding unit mediates the assembly of two-stranded coiled coils. *Proc. Natl Acad. Sci. USA*, **95**, 13419–13424.

18. Myers, J. K. & Oas, T. G. (1999). Reinterpretation of GCN4-p1 folding kinetics: partial helix formation precedes dimerization in coiled coil folding. *J. Mol. Biol.* **289**, 205–209.
19. Grubmüller, H. (1995). Predicting slow structural transitions in macromolecular systems: conformational flooding. *Phys. Rev. E*, **52**, 2893–2906.
20. Sotomayor, M. & Schulten, K. (2007). Single-molecule experiments *in vitro* and *in silico*. *Science*, **316**, 1144–1148.
21. Grubmüller, H. (2005). Force probe molecular dynamics simulations. *Methods Mol. Biol.* **305**, 493–515.
22. Rief, M. & Grubmüller, H. (2002). Force spectroscopy of single biomolecules. *ChemPhysChem*, **3**, 255–261.
23. O'Shea, E. K., Klemm, J. D., Kim, P. S. & Alber, T. (1991). X-ray structure of the GCN4 leucine zipper, a two-stranded, parallel coiled coil. *Science*, **254**, 539–544.
24. Holtzer, M. E., Lovett, E. G., d'Avignon, D. A. & Holtzer, A. (1997). Thermal unfolding in a GCN4-like leucine zipper: $^{13}$C alpha NMR chemical shifts and local unfolding curves. *Biophys. J.* **73**, 1031–1041.
25. Schwesinger, F., Ros, R., Strunz, T., Anselmetti, D., Güntherodt, H. J., Honegger, A. *et al.* (2000). Unbinding forces of single antibody-antigen complexes correlate with their thermal dissociation rates. *Proc. Natl Acad. Sci. USA*, **97**, 9972–9977.
26. Gao, M., Wilmanns, M. & Schulten, K. (2002). Steered molecular dynamics studies of titin I1 domain unfolding. *Biophys. J.* **83**, 3435–3445.
27. Evans, E. & Ritchie, K. (1997). Dynamic strength of molecular adhesion bonds. *Biophys. J.* **72**, 1541–1555.
28. Zitzewitz, J. A., Ibarra-Molero, B., Fishel, D. R., Terry, K. L. & Matthews, C. R. (2000). Preformed secondary structure drives the association reaction of GCN4-p1, a model coiled-coil system. *J. Mol. Biol.* **296**, 1105–1116.
29. Morfill, J., Blank, K., Zahnd, C., Luginbühl, B., Kühner, F., Gottschalk, K. E. *et al.* (2007). Affinity-matured recombinant antibody fragments analyzed by single molecule force spectroscopy. *Biophys. J.* **93**, 3583–3590.
30. Krebber, A., Bornhauser, S., Burmester, J., Honegger, A., Willuda, J., Bosshard, H. R. & Plückthun, A. (1997). Reliable cloning of functional antibody variable domains from hybridomas and spleen cell repertoires employing a reengineered phage display system. *J. Immunol. Methods*, **201**, 35–55.
31. Bothmann, H. & Plückthun, A. (1998). Selection for a periplasmic factor improving phage display and functional periplasmic expression. *Nature Biotechnol.* **16**, 376–380.
32. Hinterdorfer, P., Baumgartner, W., Gruber, H. J., Schilcher, K. & Schindler, H. (1996). Detection and localization of individual antibody-antigen recognition events by atomic force microscopy. *Proc. Natl Acad. Sci. USA*, **93**, 3477–3481.
33. Ros, R., Schwesinger, F., Anselmetti, D., Kubon, M., Schäfer, R., Plückthun, A. & Tiefenauer, L. (1998). Antigen binding forces of individually addressed single-chain Fv antibody molecules. *Proc. Natl Acad. Sci. USA*, **95**, 7402–7405.
34. Kienberger, F., Pastushenko, V. P., Kada, G., Gruber, H. J., Riener, C. K., Schindler, H. & Hinterdorfer, P. (2000). Static and dynamic properties of single poly (ethylene glycol) molecules investigated by force spectroscopy. *Single Mol.* **1**, 123–128.
35. Neuert, G., Albrecht, C., Pamir, E. & Gaub, H. E. (2006). Dynamic force spectroscopy of the digoxigenin-antibody complex. *FEBS Lett.* **580**, 505–509.
36. Morfill, J., Kühner, F., Blank, K., Lugmaier, R. A., Sedlmair, J. & Gaub, H. E. (2007). B-S transition in short oligonucleotides. *Biophys. J.* **93**, 2400–2409.
37. Kühner, F., Morfill, J., Neher, R. A., Blank, K. & Gaub, H. E. (2007). Force-induced DNA slippage. *J. Biophys.* **92**, 2491–2497.
38. Alcantar, N. A., Aydil, E. S. & Israelachvili, J. N. (2000). Polyethylene glycol-coated biocompatible surfaces. *J. Biomed. Mater. Res.* **51**, 343–351.
39. Blank, K., Morfill, J. & Gaub, H. E. (2006). Site-specific immobilization of genetically engineered variants of *Candida antarctica* lipase B. *ChemBioChem*, **7**, 1349–1351.
40. Butt, H. J. & Jaschke, M. (1995). Calculation of thermal noise in atomic-force microscopy. *Nanotechnology*, **6**, 1–7.
41. Hugel, T. & Seitz, M. (2001). The study of molecular interactions by AFM force spectroscopy. *Macromol. Rapid Commun.* **22**, 989–1016.
42. Friedsam, C., Wehle, A. K., Kühner, F. & Gaub, H. E. (2003). Dynamic single-molecule force spectroscopy: bond rupture analysis with variable spacer length. *J. Phys. Condens. Matter*, **15**, S1709–S1723.
43. Oesterhelt, F., Rief, M. & Gaub, H. E. (1999). Single molecule force spectroscopy by AFM indicates helical structure of poly(ethylene-glycol) in water. *New J. Phys.* **1**, 6.1–6.11.
44. Bell, G. I. (1978). Models for the specific adhesion of cells to cells. *Science*, **200**, 618–627.
45. Berendsen, H. J. C., van der Spoel, D. & van Drunen, R. (1995). GROMACS: A message-passing parallel molecular dynamics implementation. *Comput. Phys. Commun.* **91**, 43–56.
46. Lindahl, E., Hess, B. & van der Spoel, D. (2001). GROMACS 3.0: a package for molecular simulation and trajectory analysis. *J. Mol. Model.* **7**, 306–317.
47. van der Spoel, D., Lindahl, E., Hess, B., Groenhof, G., Mark, A. E. & Berendsen, H. J. C. (2005). GROMACS: fast, flexible and free. *J. Comput. Chem.* **26**, 1701–1718.
48. Jorgensen, W. L., Maxwell, D. S. & Tirado-Rives, J. (1996). Development and testing of the OPLS all-atom force field on conformational energetics and properties of organic liquids. *J. Am. Chem. Soc.* **118**, 11225–11236.
49. Berendsen, H. J. C., Grigera, J. R. & Straatsma, T. P. (1987). The missing term in effective pair potentials. *J. Phys. Chem.* **91**, 6269–6271.
50. Hess, B., Bekker, H., Berendsen, H. J. C. & Fraaije, J. G. E. M. (1997). LINCS: A linear constraint solver for molecular simulations. *J. Comput. Chem.* **18**, 1463–1472.

# Comparing Proteins by Their Unfolding Pattern

Elias M. Puchner,* Gereon Franzen,† Mathias Gautel,† and Hermann E. Gaub*
*Lehrstuhl für Angewandte Physik and Center for Nanoscience, LMU München, Munich, Germany; and †Cardiovascular Research Division and The Randall Division, King's College London, London, Great Britain

ABSTRACT Single molecule force spectroscopy has evolved into an important and extremely powerful technique for investigating the folding potentials of biomolecules. Mechanical tension is applied to individual molecules, and the subsequent, often stepwise unfolding is recorded in force extension traces. However, because the energy barriers of the folding potentials are often close to the thermal energy, both the extensions and the forces at which these barriers are overcome are subject to marked fluctuations. Therefore, force extension traces are an inadequate representation despite widespread use particularly when large populations of proteins need to be compared and analyzed. We show in this article that contour length, which is independent of fluctuations and alterable experimental parameters, is a more appropriate variable than extension. By transforming force extension traces into contour length space, histograms are obtained that directly represent the energy barriers. In contrast to force extension traces, such barrier position histograms can be averaged to investigate details of the unfolding potential. The cross-superposition of barrier position histograms allows us to detect and visualize the order of unfolding events. We show with this approach that in contrast to the sequential unfolding of bacteriorhodopsin, two main steps in the unfolding of the enzyme titin kinase are independent of each other. The potential of this new method for accurate and automated analysis of force spectroscopy data and for novel automated screening techniques is shown with bacteriorhodopsin and with protein constructs containing GFP and titin kinase.

## INTRODUCTION

Biomolecules like DNA, RNA, or proteins are polymers that self-assemble into a more or less compact form. The function of these molecules is determined by their structure and dynamics. Because the folding potential determines both structure and dynamics, it is a central research goal to investigate the energy landscape of biomolecules to understand their function. However, biomolecules are individuals. Different populations and states cannot be distinguished by ensemble experiments. The resulting average makes detailed insight into the underlying mechanisms difficult. Therefore, it is essential to investigate biomolecules on a single molecule level.

Molecular processes of biological relevance are adapted to energies close to the thermal energy $kT$. Thermal excitations drive the dynamics of processes and cause fluctuations. Therefore, it is a common goal to compare experimental data from individual biomolecules, which are subjected to large fluctuations. In this article, we describe a solution for single molecule force spectroscopy.

In mechanical single molecule experiments, the barriers of the energy landscape are determined by means of force extension traces. The force extension traces are obtained by measuring the force and the distance of a probe, which contacts the biomolecule and is retracted during one cycle of an experiment. Realizations of this technique are the atomic force microscope (AFM) (1) and optical (2,3), or magnetic tweezers (4). In the beginning of a retraction cycle, the unfolded part of the molecule is stretched. As illustrated in Fig. 1, its elastic response causes a rise in force with increasing extension. Many models have been developed to describe this force extension behavior. The most prominent ones are the worm-like chain (WLC), the freely jointed chain (FJC), the freely rotating chain (FRC), and modifications that take into account the backbone elasticity at high forces.

Several models were developed that describe how the energy barriers of the folding potential are overcome under an external force. For our purposes here we can stick to the simplest picture: because the force increases continuously with increasing extension, the energy landscape gets tilted more and more until the barrier is overcome by thermal fluctuations. Both the force and extension at which this occurs are therefore subject to fluctuations and depend on the timescale of the experiment, and specifically, on the loading rate (5,6). This is illustrated by means of the distributions on the left side of Fig. 1. The new folding state of the molecule is associated with a sudden increase in the contour length. As a consequence, the force drops and the elastic response of the completely unfolded part of the molecule is observed on further extension (Fig. 1, *dark gray*).

Because the rupture forces can be determined directly from force extension traces, we focus on the positions of energy barriers. Until now, the positions were determined by fitting such force extension traces with models for polymer elasticity. However, extension is an inappropriate variable for the characterization of molecular energy landscapes as it depends on fluctuations, external experimental parameters such as the loading rate, as temperature (7), properties of the solution and other changes that result in a different bond strength (8,9). Therefore, we perform a variable transformation from extension to contour length. The contour length is an appropriate

---

*Submitted January 22, 2008, and accepted for publication March 5, 2008.*

Address reprint requests to Elias M. Puchner, Tel.: 49-89-2180-2306; Fax: 49-89-2180-2050; E-mail: elias.puchner@physik.lmu.de.

Editor: Lukas K. Tamm.

© 2008 by the Biophysical Society

0006-3495/08/07/426/09 $2.00

doi: 10.1529/biophysj.108.129999

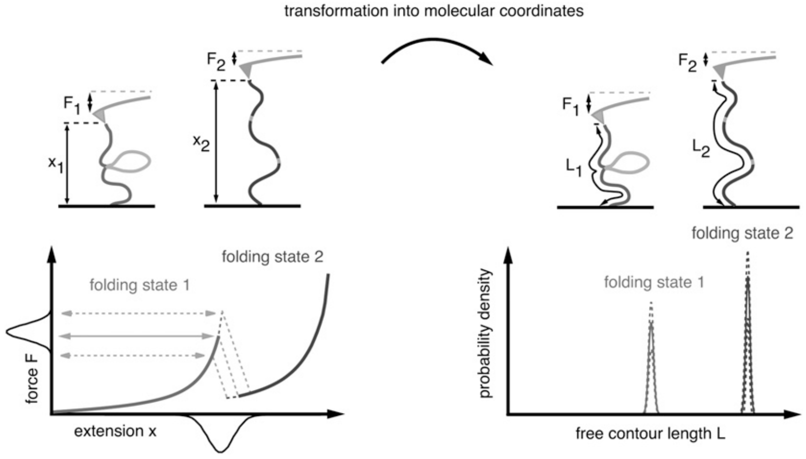

FIGURE 1 Transformation of force spectroscopy data from extension space into contour length space. The left side illustrates an AFM experiment. During retraction of the cantilever, the force and the extension are recorded. In the beginning, the unfolded part of the molecule is stretched and the force increases until the energy barrier is overcome by thermal fluctuations. Further stretching results again in a rise of force (*dark gray*). The rupture force and position differs from trace to trace due to fluctuations and may change on altered experimental conditions. The transformation of each data point from extension to contour length space and the accumulation in a histogram is shown on the right side. The representation with respect to this molecular coordinate does not exhibit the variances of the extension, but directly characterizes the energy barriers of the folding potential. Details that are lost by fitting, are still conserved with this approach.

variable, because it is independent of fluctuations and mutable external parameters and directly reflects the folding state of the molecule (right side of Fig. 1). With known monomer length, this new coordinate can be scaled to the number of polymer units to localize the energy barriers.

Besides its physical meaning, this new representation of force spectroscopy data has other advantages, as well. Although contour length histograms directly reflect energy barriers, they are also independent of fluctuations and external experimental parameters. Their height fluctuations and all of the details along the unfolding pathway are preserved with high resolution. This allows the comparison of different traces, the automated recognition of a specific molecular pattern, and a reasonable averaging of traces.

## MATERIALS AND METHODS

### Sample preparation and AFM measurements

All measurements, except the ones concerning bacteriorhodopsin (BR), were carried out with a home built AFM and with Olympus biolevers B (Bio-lever, Olympus, Tokyo, Japan), which have a spring constant ranging from 5 to 6 pN/nm. In the first example, we show unfolding traces of an Ig-GFP protein construct. It consists of four Ig-domains at the N-terminus of GFP (Ig27–Ig30) and four other Ig-domains at its C-terminus (Ig31–34) as well as a mutant of $O^6$-alkylguanine-DNA-alkyltransferase (hAGT):

Ig27-Ig28-Ig29-Ig30-GFP-Ig31-Ig32-Ig33-Ig34-hAGT.

hAGT can be used for the covalent immobilization of benzylguanine. However, the data shown in this article is recorded with unspecifically adsorbed proteins. Therefore, the unfolding of hAGT might be observed in some traces. A detailed description of the protein construct can be found in reference (10). The protein solution was incubated for 20 min on a glass substrate with freshly evaporated gold surface at a concentration of ~1 mg/ml. After washing with PBS, the cantilevers were calibrated using the equipartition theorem (11), and the automated recording of force extension traces was started with a pulling speed of 1 $\mu$m/s.

The unfolding of the enzyme titin kinase was studied through a protein construct that was expressed in *Escherichia coli* and that consists of two Ig-domains and one fibronectin domain on the N-terminus of the titin kinase followed by two Ig domains at its C-terminus (kindly provided by Gereon Franzen and Mathias Gautel, King's College London):

Ig A168-Ig A169-Fn3 A170-TK-Ig M1-Ig M2.

The protein solution was incubated for 20 min on a glass substrate with freshly evaporated gold surface and washed with PBS.

As shown in Rief et al. (12), the mechanical properties of Fn domains are very similar to the ones of Ig-domains. Because the Fn domains serve only as spacer that provide a characteristic fingerprint, these domains will not be distinguished from Ig-domains.

The third data set shows the unfolding of BR. The sample preparation, data recording, and the interpretation of force extension traces are published elsewhere (13). Membranes of purple bacteria were immobilized on mica and imaged with a multimode AFM (Nanoscope IIIa, Digital Instruments, Santa Barbara, CA) and a cantilever with a spring constant of 90 pN/nm (OMCL TR400PS,Olympus). After identification of the membrane orientation, individual BR proteins were unfolded from the cytoplasmic side of the membrane.

### Models for polymer elasticity and their transformation functions

Several models have been developed to describe the elastic response of unfolded biopolymers in force extension traces. Solving these relations for contour length, the transformation function is obtained with which the transformation from the extension space to the contour length space is carried out. In the following, we explain this principle more mathematically and give examples of models, where the transformation functions were deduced.

The function describing the force extension behavior is denoted $F(x,L,..)$. The force $F$ depends on the extension $x$, on the contour length $L$ and on other parameters that are fixed. The aim of our new method is to transform each data point from extension space $[F_i,x_i]$ into contour length space $[F_i,L_i]$. Using the correct restrictions $L,x,F > 0$, $x < L$, all models for polymer elasticity are one-to-one mappings. This means that only one defined force value $F_i$ exists for a given point $[x_i,L_i]$. Therefore the model can be solved for the desired parameter $L$. With the obtained function $L(F,x,..)$ each data point can be transformed into contour length space: $[F_i,x_i] \rightarrow [F_i,L_i(F_i,x_i)]$.

One of the most common models is the worm-like chain model (WLC) introduced by Bustamante et al. (14)

$$F(x,L) = \frac{k_B T}{p}\left(\frac{1}{4(1-x/L)^2} + \frac{x}{L} - \frac{1}{4}\right). \qquad (1)$$

In a first approximation, the persistence length $p$ is fixed. Solving this model for the contour length $L$ results in the transformation function $L_{WLC}(F,x)$.

However, it has been shown that the persistence length has to be adjusted to different force regimes (12). Therefore, modifications to this model like the

QM-WLC (15) have been developed that account for the backbone elasticity of the polymer and allow for a more accurate fit in the high force regime. The result of the quantum mechanical ab initio calculation was approximated by the polynomial representation (2)

$$F = \gamma_1\left(\frac{L}{L_0} - 1\right)^1 + \gamma_2\left(\frac{L}{L_0} - 1\right)^2, \tag{2}$$

and the elastic parameters of this expansion were determined. For peptides it was found that $\gamma_1 = 27.4$ nN and $\gamma_2 = 109.8$ nN. To take into account the force dependency of the contour length, the transformation is done in two steps. First, the data is transformed with the WLC model, $L_{\mathrm{WLC}}(F,x)$. In the second step, the force-independent contour length at zero force is determined by solving the expansion (2) for $L_0$ and inserting $L_{\mathrm{WLC}}$ and $F$: $L_0 = L_0(L_{\mathrm{WLC}}, F)$ .

Finally, the freely rotating chain model (FRC) considers bonds of length $b$, which are connected by fixed angles $\gamma$. However, the torsional angles are not restricted. A detailed discussion of the stretching behavior is given in (16), which can be summarized as follows.

In the infinite-chain limit, the Kuhn length a is given by $a = b(1+\cos\gamma)/((1-\cos\gamma)\cos(\gamma/2))$ and the persistence length $p$ of the FRC equals $p = b(\cos(\gamma/2))/(|\ln(\cos\gamma)|)$. The force extension behavior exhibits three different scaling ranges and is given by

$$\frac{x}{L} \cong \begin{cases} \dfrac{Fa}{3k_{\mathrm{B}}T} & for \quad \dfrac{Fb}{k_{\mathrm{B}}T} < \dfrac{b}{p} \\ 1 - \left(\dfrac{Fp}{4k_{\mathrm{B}}T}\right)^{-1/2} & for \quad \dfrac{b}{p} < \dfrac{Fb}{k_{\mathrm{B}}T} < \dfrac{p}{b}. \\ 1 - \left(\dfrac{Fb}{2k_{\mathrm{B}}T}\right)^{-1} & for \quad \dfrac{p}{b} < \dfrac{Fb}{k_{\mathrm{B}}T} \end{cases} \tag{3}$$

Again, the transformation function is obtained by solving for $L$.

Once a force-extension trace is transformed into a force-contour length trace, all points above the noise level are accumulated in an area-normalized contour length histogram referred to as barrier position histogram.

## RESULTS AND DISCUSSION

In this section, we apply the transformation method to several proteins. Although not all examples have a mechanical function in nature, the identification of energy barriers in the contour length histograms allows for conclusions about the energy landscape. The pathway through the folding potential (i.e., the order of unfolding events) can be determined and visualized by means of the cross-superposition of contour length histograms.

The positions of energy barriers in the contour length histograms are independent of fluctuations and external experimental parameters. Therefore, contour length histograms can be averaged, which is not the case for force extension traces. In addition, this approach makes it possible to detect characteristic unfolding patterns. The implementation in a pattern recognition algorithm could enable new force spectroscopy screening techniques.

### Transformation of Ig-GFP unfolding traces with the WLC model

In the first example, we analyze the unfolding of an Ig-GFP protein construct by means of its contour length histogram. A typical force extension trace is shown in Fig. 2 *a*. The regular saw-tooth pattern at high extensions is caused by Ig-domains (marked in *dark gray*) and serves as a fingerprint for the selection of relevant traces. Because the protein construct consists of four Ig-domains on the N-terminus of the GFP and four on its C-terminus, each unfolding trace that shows more than four Ig-domains must contain the unfolding of GFP (Fig. 2 *a*). The initial peak is presumably due to the unfolding of hAGT.

Fig. 2 *b* shows the transformation of the force extension trace with the WLC model using a persistence length of 0.4 nm. At low forces, the thermal excitation of the cantilever causes significant noise in the contour length space. Therefore, only points with forces above a threshold of 10 pN were collected in the contour length histogram (Fig. 2 *c*). The contour length coordinate does not depend on fluctuations or variable experimental parameters, but it directly reflects the molecular folding states and its energy barriers. This histogram in which the barrier position is measured along the unfolded part of the protein, will therefore be referred to as the barrier position histogram.

The first two barriers in Fig. 2 *c* presumably correspond to the unfolding of hAGT. Once the rupture of the first GFP $\beta$-sheet occurs, the protein is no longer stable, and the unfolded portion contributes to the total contour length (the intermediate steps reported in Dietz et al. (17) were not resolved in this study). Therefore, all points recorded after bond rupture appear at a new contour length position that is characteristic for the new folding state of the protein. The same holds true for the unfolding of the Ig-domains. After each

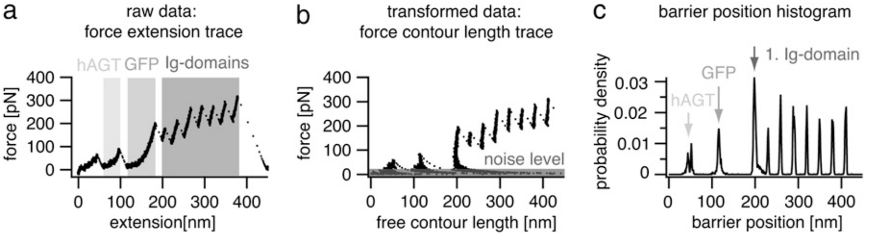

FIGURE 2 Transformation of force spectroscopy data into barrier position histograms. (*a*) Force extension trace of the Ig-GFP protein construct. Cleary visible is the sawtooth pattern caused by unfolding of hAGT, GFP, and IG-domains. (*b*) Transformed trace. The transformation of each point was done with the WLC model and a persistence length of 0.4 nm. (*c*) Barrier position histogram. All points above the noise level of 10 pN were accumulated in a area-normalized histogram with a bin width of 1 nm. The coordinate of this representation is independent of fluctuations, and the energy barriers can be directly determined.

rupture, the protein construct is in a new folding state and each point appears at the corresponding contour length. For the GFP unfolding, we measure a peak-to-peak distance of 77 ± 0.5 nm that agrees with the finding of a contour length increment of 76.6 nm in reference (17). Each Ig-domain unfolding shows an increase in contour length of 29 ± 0.5 nm, which is again in agreement with other studies (18).

## Comparison of different models: WLC, QM-WLC, and FRC

We now compare different models for polymer elasticity with respect to the quality of barrier position histograms. The standard WLC-model does not account for backbone elasticity at high forces. Therefore, an ab initio based modification (QM-WLC) was introduced in Hugel et al. (15), which describes the elasticity above 200 pN better. As a third model, we use the FRC model that treats molecules as bonds of fixed length $b$, which are connected by fixed angles $\gamma$ but at arbitrary torsional angles (16).

These three models are compared in Fig. 3. The part of a force extension trace in Fig. 3 *a* is transformed, and it is shown in Fig. 3 *b* that the peaks of the QM-WLC model are higher and slightly narrower than the ones obtained by the standard WLC ($p = 0.4$ nm in both cases). This indicates that the QM-WLC describes the data more accurately. However, the best result is achieved with the FRC model ($\gamma = 22°$, $b = 0.4$ nm). The full width at half maximum (FWHM) of the different models is compared in Table 1. Fig. 3 *c* shows the section of a trace with forces up to 600 pN. At these high forces, the WLC model is no longer able to resolve small intermediate steps. In contrast, both the QM-WLC and the FRC models resolve the two folding states, which are separated by 5 nm.

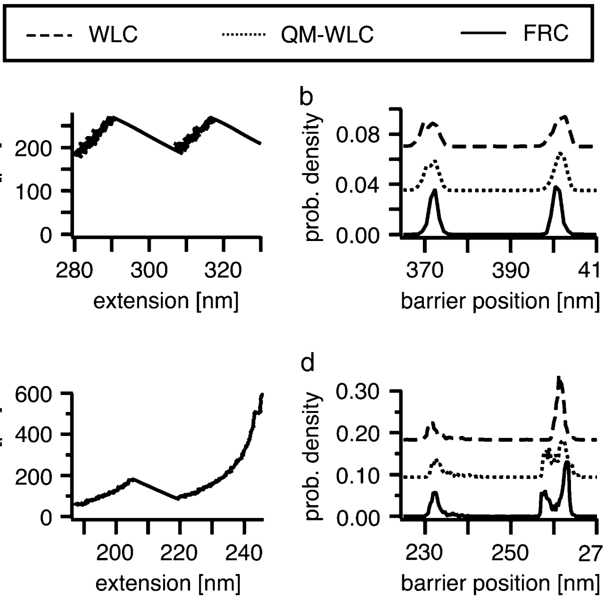

FIGURE 3 Comparison of different models for polymer elasticity. (*a*) Fraction of a force extension trace. (*b*) Three energy barrier histograms obtained by transforming trace (*a*) with the WLC model ($p = 0.4$ nm), the QM-WLC model and the FRC model ($\gamma = 22°$, $b = 0.4$ nm). The best result is achieved with the FRC, which produces the highest and sharpest peaks (compare Table 1). (*c*) Fraction of a force extension trace showing a small step at high forces. (*d*) Three energy barrier histograms of trace (*c*) with the same parameters as in (*b*). In contrast to the WLC, the QM-WLC and FRC models are able to resolve the small substep of 5 nm at 500 pN.

These results show that sharp peaks and a high resolution are achieved in barrier position histograms using an appropriate model and suitable parameters for the transformation.

## Averaging in contour length space preserves information

Small energy barriers of the unfolding potential are not resolved in each trace. To extract these details, several traces are necessary. However, the dependency of the rupture position on fluctuations prevents reasonable averaging of force extension traces. Therefore, traces were in the past usually superpositioned.

In the following, we show that barrier position histograms can be averaged due to the independence of fluctuations. The matter under investigation is the well-studied membrane protein BR. Because the data has already been published (13), it represents a suitable model system. In Fig. 4 *a*, 13 traces of BR, unfolded from the cytoplasmic side of the membrane, are superpositioned. As mentioned above, averaging is not possible in this representation because the coordinate is subjected to fluctuations.

The transformation into contour length space was done with the WLC model and a persistence length of 0.4 nm (Fig. 4 *b*). Because of the high spring constant of the cantilevers (90 pN/nm), the force threshold for the barrier position histograms was set to 60 pN. The averaged barrier position histogram shown in Fig. 4 *c* was obtained by averaging each corresponding peak of the 13 barrier position histograms. By using a Gaussian fit, the precise positions of energy barriers were determined. A comparison of these values to those obtained by the force extension traces fit with the WLC model is shown in Table 2. The mean deviation equals 0.3 nm, and the maximum deviation of 1 nm is still within the error of the WLC fit.

Other averaging methods or ensemble experiments are susceptible to fluctuations, which would obscure information about the unfolding potential. Averaging in contour length space by contrast preserves the details of the energy landscape due to the fluctuation independence of the individual traces in this representation.

**TABLE 1 Comparison of different transformation models**

| Peak number | 1 | 2 |
|---|---|---|
| FWHM: WLC | 4.7 nm | 4.0 nm |
| FWHM: QM-WLC | 3.8 nm | 3.2 nm |
| FWHM: FRC | 2.3 nm | 2.4 nm |

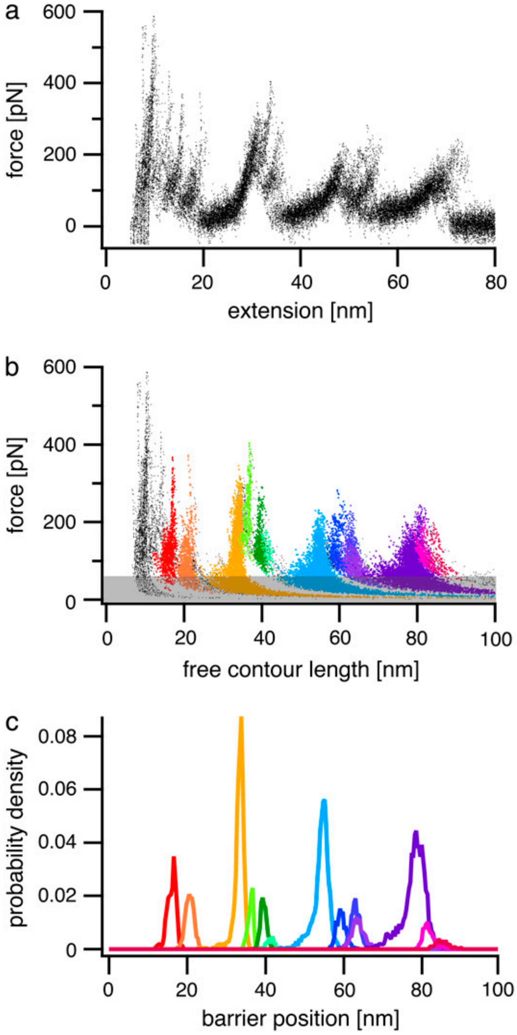

FIGURE 4 Averaging of barrier position histograms. (*a*) Superposition of 13 BR force extension traces. (*b*) The transformation into contour length space was accomplished with the WLC model and a persistence length of 0.4 nm. (*c*) The averaged barrier position histogram is obtained by averaging each peak of the 13 barrier position histograms. The threshold force was set to 60 pN and the bin width amounts to 0.36 nm.

## Comparing unfolding pathways of bacteriorhodopsin and titin kinase

Barrier position histograms show the barriers of the molecular energy landscape. Because of its high dimensionality, several pathways between two given states may exist, which allow for conclusions about the architecture of a protein.

The experimental determination and visualization of unfolding pathways can be achieved by means of the cross-superposition of 2D barrier position histograms. First, the $n$ entries $h1_i$, $i = 1\dots n$, of the first histogram $h1$ are assigned to the $n$ columns of each row of a $n \times n$ matrix $M1$: $M1_{ki} = h1_i$, $k,i = 1\dots n$. Graphically represented, the energy barriers appear as stripes. The second $n \times n$ matrix $M2$ is created by assigning the $n$ entries $h2_i$ of the second histogram $h2$ to the $n$ rows of each column of $M2$: $M2_{ki} = h2_k$, $k,i = 1\dots n$. In the graphical representation the stripes are rotated by 90°. Addition of the two matrices results in the $n \times n$ superposition matrix $S$, $S = M1 + M2$. In this pattern, each part of the first histogram interferes with each part of the second one. The reason why we use the sum of the matrices, reflecting the probability of occurrence of either of two events, in contrast to multiplication, reflecting the occurrence of both events, is ascribed to the clearer signal. As shown by the examples below, matching squares, corresponding to matching unfolding events, can be directly identified. Graphically represented, multiplication would result in points from which the same information could be reconstructed, however, it cannot be as easily seen as in the case of summation.

Fig. 5 shows two cross-superpositions of four different histograms that are obtained from BR force extension traces. The way to read the pattern is the following: first the smallest squares, formed by matching contour length increments, are determined. If subsequent squares are aligned in the diagonal with positive slope, they occur in the same order in both traces. If the diagonal has negative slope, the order is permutated. This is also the case for squares that consist of multiple small squares. In the cross-superposition of Fig. 5 *a*, the matching parts of the two histograms are colored. For a better overview, several of the smaller substeps are combined. Those unfolding events with squares that are aligned along the diagonal with positive slope occur in the same order. If not all energy barriers are resolved in each trace, the cross-superposition pattern cannot be filled with smallest squares. This case is shown in Fig. 5 *b*. The unfolding steps, which are marked in blue, fit and have the same size and sequence as in Fig. 5 *a*. But because there is a step, which is not visible in histogram 4, the two corresponding steps of histogram 3 must be combined to obtain the smallest square that fits. The smallest square is marked in green and is again aligned along the diagonal with positive slope.

The 13 traces indicate that BR always unfolds along the same pathway. This observation supports the common notion that during the unfolding process one helix after the other is pulled out of the membrane (13,19,20).

The unfolding behavior of the Ig-titin kinase protein construct (Ig-TK) is different from that of BR. To corroborate the notion that the enzyme titin kinase acts as a force sensor in muscles (21,22), it is essential to study its mechanical prop-

**TABLE 2 Barrier positions in the unfolding potential of BR determined by barrier position histograms and WLC fits to force extension traces**

| | | | | | | | | | | | | | |
|---|---|---|---|---|---|---|---|---|---|---|---|---|---|
| Histogram (±1 nm) | 16.2 | 20.6 | 33.6 | 36.3 | 39.4 | 41.3 | 54.7 | 59.2 | 62.9 | 63.5 | 78.7 | 81.3 | 84.9 |
| WLC fit (±1 nm) | 16.2 | 20.0 | 33.6 | 36.1 | 39.4 | 40.7 | 54.9 | 59.0 | 62.6 | 64.5 | 79.2 | 81.6 | 85.1 |

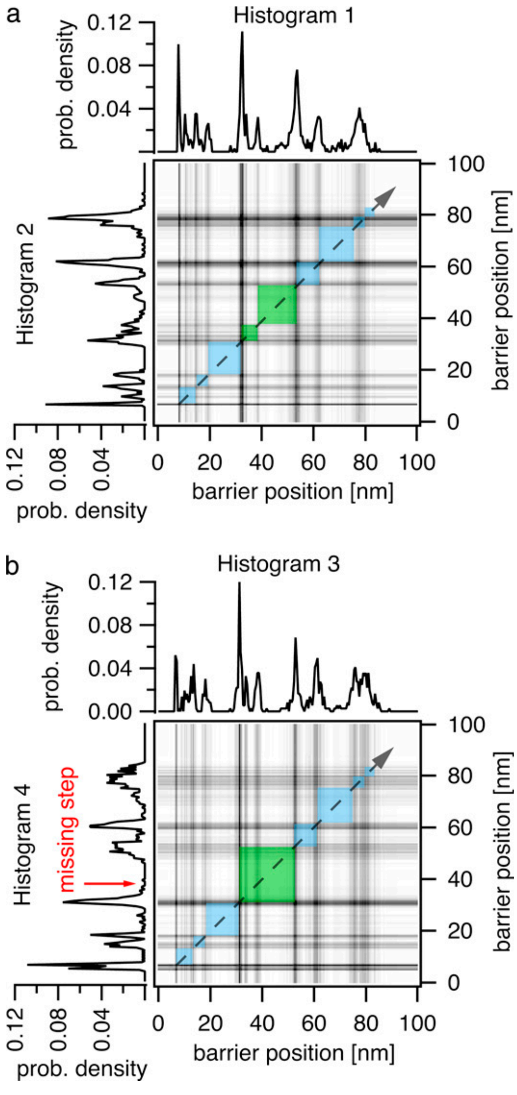

FIGURE 5 Cross-superposition of four BR barrier position histograms. (*a*) Both histograms show the same energy barriers. The smallest squares are aligned along the diagonal with positive slope indicating that the order of unfolding events is identical. The same holds true for *b*. However, histogram 4 lacks one energy barrier. Therefore the squares that are marked in green must be combined to determine the smallest matching steps.

erties. However, we will not give a detailed interpretation of the unfolding traces here, and an explanation of their physiological meaning would go beyond the scope of this article, as well. The unfolding traces from the protein construct shall only serve as an example for protein unfolding, which does not always occur in the same sequence. Because the titin kinase is flanked by three spacer domains on the N-terminus and two domains on the C-terminus, each trace showing the unfolding of more than three domains contains the unfolding of the titin kinase.

Fig. 6 shows the cross-superpositions of barrier position histograms that are obtained by transforming the force extension traces with the QM-WLC model ($p = 0.6$ nm). The four even increments of ~29 nm, which are marked in yellow, are due to the unfolding of four Ig/Fn-domains. Because the folded protein construct is contacted at random positions, the initial part of a histogram may exhibit the rupture of Ig-domain fragments in addition to unspecific interactions. This part can be separated from the TK unfolding by choosing the rupture of the first Ig-domain as the point of reference. A search backward for matching increments results in the colored squares that have a contour length of 124 ± 2 nm in total. In Fig. 6 *a*, the squares corresponding to the different unfolded segments of the titin kinase are marked in violet, red, green, and blue. Again, small substeps are combined for

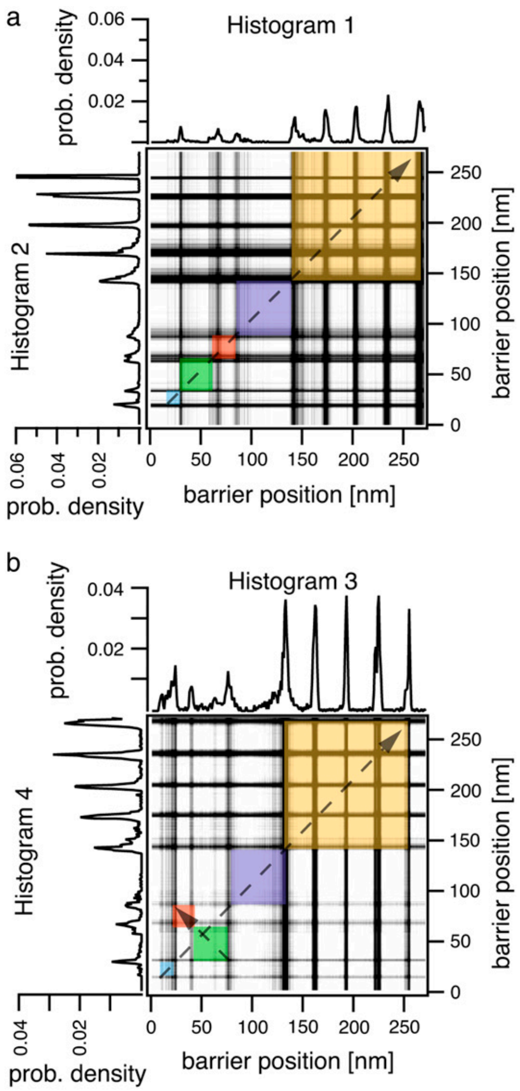

FIGURE 6 Cross-superposition of Ig-TK barrier position histograms. The even increments of ~29 nm, which are located in the upper right corner, are due to Ig/Fn domain unfolding (*yellow*). Segments between the major barriers of the titin kinase are marked in blue, green, and red. In *a* the segments are aligned along the diagonal with positive slope. This indicates that the order of unfolding events is the same in both traces. The titin kinase in contrast takes two different unfolding pathways in *b*. Because the two segments, marked in green and red, are aligned along the diagonal with negative slope, their order is changed.

clarity. Because these squares are aligned along the diagonal with positive slope, the enzyme chose the same unfolding pathway in both traces. The cross-superposition of Fig. 6 *b* shows the same increments between the titin kinase energy barriers. However, the green and red squares are aligned along the diagonal with negative slope, indicating that their order is switched. Although this is a rare case, it shows that these two unfolding events do not depend on each other completely and that different unfolding pathways exit. The combination of these two states into a larger square shows the same sequence as in Fig. 6 *a*. As this is the case in all traces, the last energy barrier depends strongly on the proceeding ones.

These examples show that by means of the cross-superposition of barrier position histograms, unfolding pathways can be determined and visualized. The special dependencies among the different energy barriers provide new and otherwise unobtainable insight into the architecture of a molecule.

In the last part of this article, we describe how the transformation into barrier position histograms can be implemented in a powerful pattern recognition algorithm.

## Pattern recognition with barrier position histograms

Single molecule force spectroscopy experiments pose the challenge of discriminating between impurities or nonspecific interactions and selecting only those traces that exclusively stem from the molecule under investigation. Although the concentration of adsorbed molecules must be low enough to observe individual molecules, each approach of the cantilever to the surface will not results in contact with the molecule of interest. This is especially true in the case where molecules are unspecifically attached to the surface and tip: the rate of yield can be in the 1/1000 range. In addition, force extension traces showing adsorption of other molecules (e.g., impurities) must be filtered out. The use of protein constructs, fusion proteins and protein polymers makes the selection easier, because their regular unfolding pattern results in better contrast. However, the automatic detection of these patterns (23,24) is difficult because both the extension and the force of an unfolding pattern differ from trace to trace due to fluctuations. Variances of experimental parameters such as pulling speed, temperature, solution properties, or changes that result in different bond strengths have even greater impact. This is not the case if the force extension traces are transformed into the contour length space with the transformation method introduced in this article. As the contour length is a molecular coordinate, which is independent of force and only reflects the folding state of the molecule, the barrier position histograms of different traces can be directly compared, even if experimental parameters are altered.

We developed force spectroscopy data analysis software (IgorPro 5.0, Wavemetrics, Lake Oswego, OR) that includes a pattern recognition algorithm based on barrier position histograms. The currently implemented models for polymer elasticity, with which the transformation is carried out, are the WLC, QM-WLC, two-state FJC, and FRC models. The software can be used to identify and filter traces showing a particular pattern. In these traces, energy barriers are automatically detected and the relevant parameters of peaks such as contour length, rupture force and loading rate can be determined and stored. It can also be used to screen traces for a specific molecule in a multi component sample.

We show the performance of this method by applying it to a data set of 1000 force extension traces of the Ig-GFP construct. In this case, the regular pattern caused by Ig-domain unfolding is detected by means of the autocorrelation function of the barrier position histogram (Fig. 7 *a*). Our algorithm attributes to each trace an evaluation value that considers the level of the autocorrelation function at a certain contour length as well as the sharpness of a possible peak at this position. To prefer traces with several Ig-domains, the process is repeated for the double contour length. We chose 29 nm for this parameter, but it can be adjusted for each regular pattern. The trace shown in Fig. 7 *a* exhibits seven contour length increments of ~29 nm and high, sharp peaks in its autocorrelation (Fig. 7 *b*). Using the formula given in the Appendix, it is evaluated with a quality factor of +8.7. In contrast to this, the trace in Fig. 7 *e*, which shows the unfolding of BR, does not exhibit increments of 29 nm and therefore it has a low autocorrelation at this value (quality factor −1.1). In this way, the algorithm can identify traces with special properties and select the relevant traces for further analysis.

Besides this very useful application, the transformation of force extension traces into barrier position histograms also allows for the comparison of different traces. By calculating the correlation function of two histograms, the maximum degree of correlation can be determined. If the two traces correspond to the same molecule, then their barrier position histograms exhibit a similar pattern, which results in a high degree of correlation. This is shown in Fig. 7 *d* by means of two Ig-TK traces. The maximum degree of correlation from these two traces is 87%. In the other case, where two traces correspond to different molecules, the correlation is expected to be lower, as shown in Fig. 7 *f*. The maximum degree of correlation between the histogram of BR and of the Ig-tk construct equals 37%.

In this manner, a data set containing different types of traces can be classified. It is even imaginable to screen a sample with unknown composition with respect to a known molecular unfolding pattern.

## CONCLUSIONS

In this article, we introduced a new method for representing and analyzing force spectroscopy data. By transforming force extension traces into contour length space, histograms can be created that reflect the folding barriers of a molecule. The

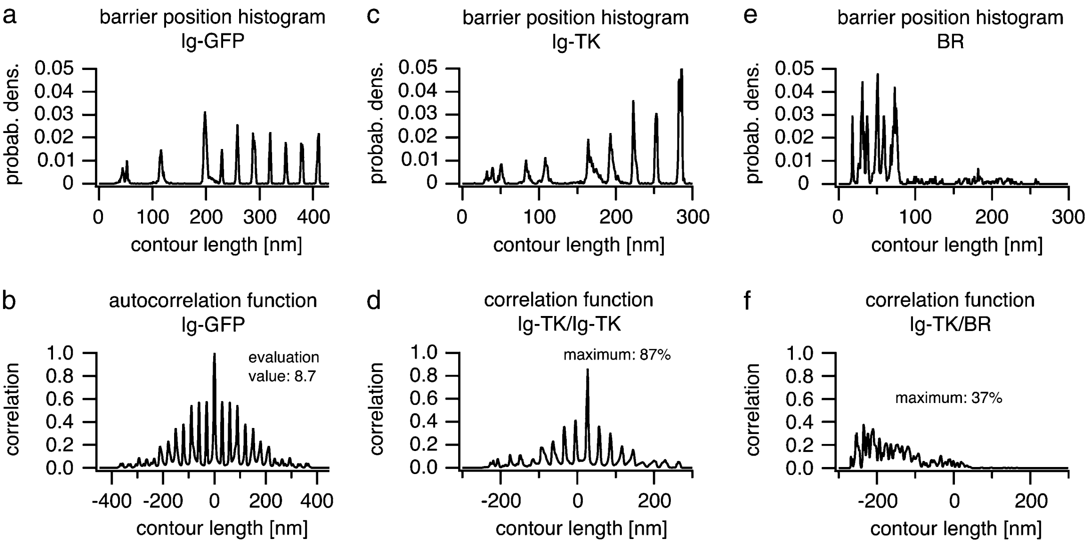

FIGURE 7 Pattern recognition and screening for different single molecule compounds based on barrier position histograms. (*a*) Barrier position histogram of Ig-GFP. The even 29 nm spacings of the Ig-domain unfolding cause peaks in the autocorrelation function (*b*) at 29 nm and at integer multiples. The evaluation procedure of a trace takes into account the correlation at 29 nm and 58 nm as well as the sharpness of the peaks and yields a value of +8.7 (for details see Appendix). In this manner, a set of data can be filtered for relevant traces. To compare two different traces, the cross correlation of the corresponding barrier position histograms can be calculated. The result with the Ig-TK trace (*c*) and another Ig-TK trace (not shown) is diagramed in *d* and exhibits a correlation of 87%. In contrast, the correlation function in *f* of the traces of the two different molecules Ig-TK (*c*) and BR (*e*) only shows a correlation of 37%. In this way, traces of a multi-component sample could be classified and attributed to the corresponding molecules.

new molecular coordinate is independent of fluctuations and varying external parameters. Energy barriers can be directly determined, and details along the unfolding pathway are conserved. Different unfolding pathways can be determined and visualized from the cross-superposition barrier position histograms. In contrast to BR, which is known to always exhibit the same order of unfolding events, we found that sequences of unfolding steps in titin kinase follow a more complex pattern.

The implementation of this method in a pattern recognition algorithm enables the automated identification of traces with characteristic features. Different traces can be compared and classified allowing for the examination of a multi component sample or a sample with unknown composition. This technique may become a very useful tool for research and enable new approaches for screening techniques.

## APPENDIX: EVALUATION OF ENERGY BARRIER HISTOGRAMS

The aim is to filter contour length histograms that exhibit several peaks with even spacing $l_{\max}$. First, the evaluation algorithm finds the maximum in the autocorrelation function $a(l)$ in the interval $[l_{\max} - w/2, l_{\max} + w/2]$ with width $w$. In the second step, the relative height of the maximum is determined by averaging on both sides of the maximum $l_{\max}$ in the interval $[l_{\max} - 3/2w, l_{\max} - 1/2w]$ and $[l_{\max} + 1/2w, l_{\max} + 3/2w]$ respectively:

$$\langle a\rangle_{\text{left}} = \int_{l_{\max}-3/2w}^{l_{\max}-1/2w} a(l)dl, \quad \langle a\rangle_{\text{right}} = \int_{l_{\max}+1/2w}^{l_{\max}+3/2w} a(l)dl.$$

The evaluation value $v$ is obtained by the following equation:

$$v = 5\cdot\left(\left|a(l_{\max}) - \langle a\rangle_{\text{left}} + a(l_{\max}) - \langle a\rangle_{\text{right}}\right| - \left|\langle a\rangle_{\text{left}} - \langle a\rangle_{\text{right}}\right|\right).$$

This procedure is done for $l$ and $2l$ and the obtained values are added.

We thank Max Kessler for providing the BR unfolding data, Jonas Eicher for programming, Ann Fornof, Julia Zimmermann, and Stefan Stahl for helpful discussions and Jens Struckmeier, nAmbition GmbH, for good collaboration.

This work was supported by the Center for Integrated Protein Science Munich and the Fonds der Chemischen Industrie.

## REFERENCES

1. Binnig, G., C. F. Quate, and C. Gerber. 1986. Atomic force microscope. *Phys. Rev. Lett.* 56:930–933.
2. Block, S. M., L. S. Goldstein, and B. J. Schnapp. 1990. Bead movement by single kinesin molecules studied with optical tweezers. *Nature.* 348:348–352.
3. Smith, S. B., Y. J. Cui, and C. Bustamante. 1996. Overstretching B-DNA: the elastic response of individual double-stranded and single-stranded DNA molecules. *Science.* 271:795–799.
4. Smith, S. B., L. Finzi, and C. Bustamante. 1992. Direct mechanical measurements of the elasticity of single DNA-molecules by using magnetic beads. *Science.* 258:1122–1126.
5. Evans, E., and K. Ritchie. 1997. Dynamic strength of molecular adhesion bonds. *Biophys. J.* 72:1541–1555.
6. Dudko, O. K., A. E. Filippov, J. Klafter, and M. Urbakh. 2003. Beyond the conventional description of dynamic force spectroscopy of adhesion bonds. *Proc. Natl. Acad. Sci. USA.* 100:11378–11381.

7. Schlierf, M., and M. Rief. 2005. Temperature softening of a protein in single-molecule experiments. *J. Mol. Biol.* 354:497–503.
8. Li, H., M. Carrion-Vazquez, A. F. Oberhauser, P. E. Marszalek, and J. M. Fernandez. 2000. Point mutations alter the mechanical stability of immunoglobulin modules. *Nat. Struct. Biol.* 7:1117–1120.
9. Nevo, R., C. Stroh, F. Kienberger, D. Kaftan, V. Brumfeld, M. Elbaum, Z. Reich, and P. Hinterdorfer. 2003. A molecular switch between alternative conformational states in the complex of Ran and importin beta1. *Nat. Struct. Biol.* 10:553–557.
10. Kufer, S. K., H. Dietz, C. Albrecht, K. Blank, A. Kardinal, M. Rief, and H. E. Gaub. 2005. Covalent immobilization of recombinant fusion proteins with hAGT for single molecule force spectroscopy. *Eur. Biophys. J.* 35:72–78.
11. Butt, H.-J., and M. Jaschke. 1995. Calculation of thermal noise in atomic force microscopy. *Nanotechnology.* 6:1–7.
12. Rief, M., M. Gautel, A. Schemmel, and H. E. Gaub. 1998. The mechanical stability of immunoglobulin and fibronectin III domains in the muscle protein titin measured by atomic force microscopy. *Biophys. J.* 75:3008–3014.
13. Kessler, M., and H. E. Gaub. 2006. Unfolding barriers in bacteriorhodopsin probed from the cytoplasmic and the extracellular side by AFM. *Structure.* 14:521–527.
14. Bustamante, C., J. F. Marko, E. D. Siggia, and S. Smith. 1994. Entropic elasticity of lambda-phage DNA. *Science.* 265:1599–1600.
15. Hugel, T., M. Rief, M. Seitz, H. E. Gaub, and R. R. Netz. 2005. Highly stretched single polymers: atomic-force-microscope experiments versus ab-initio theory. *Phys. Rev. Lett.* 94:048301.
16. Livadaru, L., R. R. Netz, and H. J. Kreuzer. 2003. Stretching response of discrete semiflexible polymers. *Macromolecules.* 36:3732–3744.
17. Dietz, H., and M. Rief. 2004. Exploring the energy landscape of GFP by single-molecule mechanical experiments. *Proc. Natl. Acad. Sci. USA.* 101:16192–16197.
18. Rief, M., M. Gautel, F. Oesterhelt, J. M. Fernandez, and H. E. Gaub. 1997. Reversible unfolding of individual titin immunoglobulin domains by AFM. *Science.* 276:1109–1112.
19. Oesterhelt, F., D. Oesterhelt, M. Pfeiffer, A. Engel, H. E. Gaub, and D. J. Muller. 2000. Unfolding pathways of individual bacteriorhodopsins. *Science.* 288:143–146.
20. Muller, D. J., M. Kessler, F. Oesterhelt, C. Moller, D. Oesterhelt, and H. Gaub. 2002. Stability of bacteriorhodopsin $\alpha$-helices and loops analyzed by single-molecule force spectroscopy. *Biophys. J.* 83: 3578–3588.
21. Lange, S., F. Xiang, A. Yakovenko, A. Vihola, P. Hackman, E. Rostkova, J. Kristensen, B. Brandmeier, G. Franzen, B. Hedberg, L. G. Gunnarsson, S. M. Hughes, S. Marchand, T. Sejersen, I. Richard, L. Edstrom, E. Ehler, B. Udd, and M. Gautel. 2005. The kinase domain of titin controls muscle gene expression and protein turnover. *Science.* 308:1599–1603.
22. Grater, F., J. Shen, H. Jiang, M. Gautel, and H. Grubmuller. 2005. Mechanically induced titin kinase activation studied by force-probe molecular dynamics simulations. *Biophys. J.* 88:790–804.
23. Kuhn, M., H. Janovjak, M. Hubain, and D. J. Muller. 2005. Automated alignment and pattern recognition of single-molecule force spectroscopy data. *J. Microsc.* 218:125–132.
24. Marsico, A., D. Labudde, T. Sapra, D. J. Muller, and M. Schroeder. 2007. A novel pattern recognition algorithm to classify membrane protein unfolding pathways with high-throughput single-molecule force spectroscopy. *Bioinformatics.* 23:e231–e236.

EXTENDED PDF FORMAT
SPONSORED BY
usb
Products from Affymetrix
www.usbweb.com

Science
AAAS

# Single-Molecule Cut-and-Paste Surface Assembly

S. K. Kufer, *et al.*

*Science* **319**, 594 (2008);
DOI: 10.1126/science.1151424

***The following resources related to this article are available online at www.sciencemag.org (this information is current as of October 29, 2008 ):***

**Updated information and services,** including high-resolution figures, can be found in the online version of this article at:
http://www.sciencemag.org/cgi/content/full/319/5863/594

**Supporting Online Material** can be found at:
http://www.sciencemag.org/cgi/content/full/319/5863/594/DC1

A list of selected additional articles on the Science Web sites **related to this article** can be found at:
http://www.sciencemag.org/cgi/content/full/319/5863/594#related-content

This article **cites 33 articles**, 16 of which can be accessed for free:
http://www.sciencemag.org/cgi/content/full/319/5863/594#otherarticles

This article has been **cited by** 3 article(s) on the ISI Web of Science.

This article appears in the following **subject collections**:
Chemistry
http://www.sciencemag.org/cgi/collection/chemistry

Information about obtaining **reprints** of this article or about obtaining **permission to reproduce this article** in whole or in part can be found at:
http://www.sciencemag.org/about/permissions.dtl

Downloaded from www.sciencemag.org on October 29, 2008

*Science* (print ISSN 0036-8075; online ISSN 1095-9203) is published weekly, except the last week in December, by the American Association for the Advancement of Science, 1200 New York Avenue NW, Washington, DC 20005. Copyright 2008 by the American Association for the Advancement of Science; all rights reserved. The title *Science* is a registered trademark of AAAS.

19. V. Reinke, I. S. Gil, S. Ward, K. Kazmer, *Development* **131**, 311 (2004).
20. H. Browning, S. Strome, *Development* **122**, 391 (1996).
21. R. W. Beeman, K. S. Friesen, R. E. Denell, *Science* **256**, 89 (1992).
22. G. D. Hurst, J. H. Werren, *Nat. Rev. Genet.* **2**, 597 (2001).
23. A. Atlan, H. Mercot, C. Landre, C. Montchamp-Moreau, *Evol. Int. J. Org. Evol.* **51**, 1886 (1997).
24. R. W. Beeman, K. S. Friesen, *Heredity* **82**, 529 (1999).
25. L. Fishman, J. H. Willis, *Genetics* **169**, 347 (2005).
26. H. A. Orr, S. Irving, *Genetics* **169**, 671 (2005).
27. F. A. Reed, R. G. Reeves, C. F. Aquadro, *Evol. Int. J. Org. Evol.* **59**, 1280 (2005).
28. E. A. Stahl, G. Dwyer, R. Mauricio, M. Kreitman, J. Bergelson, *Nature* **400**, 667 (1999).
29. D. Tian, H. Araki, E. Stahl, J. Bergelson, M. Kreitman, *Proc. Natl. Acad. Sci. U.S.A.* **99**, 11525 (2002).
30. M. Shapira *et al.*, *Proc. Natl. Acad. Sci. U.S.A.* **103**, 14086 (2006).
31. J. H. Thomas, *Genome Res.* **16**, 1017 (2006).
32. J. H. Thomas, *Genetics* **172**, 127 (2006).
33. H. A. Orr, D. C. Presgraves, *Bioessays* **22**, 1085 (2000).
34. K. A. Frazer, L. Pachter, A. Poliakov, E. M. Rubin, I. Dubchak, *Nucleic Acids Res.* **32**, W273 (2004).
35. Z. Yang, *Comput. Appl. Biosci.* **13**, 555 (1997).

36. We thank the *Caenorhabditis* Genetics Center, the National Bioresource Project of Japan, the NemaGENETAG Consortium, M.-A. Félix, A. Barrière, E. Dolgin, and H. Van Epps for strains; R. Maruyama and A. Singson for advice; S. Skrovanek for lab assistance; and H. Coller, A. Cutter, D. Gresham, R. Gosh, L. Moyle, J. Shapiro, and E. Smith for comments on the manuscript. Supported by a National Defense Science and Engineering Graduate fellowship to H.S.S., a Jane Coffin Childs Fellowship to M.V.R., NIH grants R37 MH059520 and R01 HG004321 and a James S. McDonnell Foundation Centennial Fellowship to L.K., and NIH grant GM071508 to the Lewis-Sigler Institute. GenBank sequence accession numbers are EU163897 to EU163940.

**Supporting Online Material**
www.sciencemag.org/cgi/content/full/1151107/DC1
SOM Text
Fig. S1
Tables S1 to S7
References

28 September 2007; accepted 17 December 2007
Published online 10 January 2008;
10.1126/science.1151107
Include this information when citing this paper.

# Single-Molecule Cut-and-Paste Surface Assembly

**S. K. Kufer,[1] E. M. Puchner,[1] H. Gumpp,[1] T. Liedl,[2] H. E. Gaub[1]**

**We introduce a method for the bottom-up assembly of biomolecular structures that combines the precision of the atomic force microscope (AFM) with the selectivity of DNA hybridization. Functional units coupled to DNA oligomers were picked up from a depot area by means of a complementary DNA strand bound to an AFM tip. These units were transferred to and deposited on a target area to create basic geometrical structures, assembled from units with different functions. Each of these cut-and-paste events was characterized by single-molecule force spectroscopy and single-molecule fluorescence microscopy. Transport and deposition of more than 5000 units were achieved, with less than 10% loss in transfer efficiency.**

Functional biomolecular assembly aims to create structures from a large variety of biomolecular building blocks in a geometrically well-defined manner in order to create new functions (*1*, *2*), such as artificial signaling cascades or synergetic combinations of enzymes. Hybrid devices could include quantum dots coassembled with dye molecules, or gold particles assembled as plasmon hot spots with a sample protein positioned into the focus (*3*). One way to assemble such molecular devices would be to physically pick up the different units needed with a scanning probe tip, translocate these units to a different location, and deposit them with high spatial precision (*4*–*6*). The entire process would also have to be carried out in an aqueous environment.

For the translocation of nanoscale objects, we used atomic force microscopy, which has been used in this context for mechanical single-molecule experiments (*7*–*12*) or lithography (*13*, *14*); however, previously suggested devices include the use of molecular pliers at the end of atomic force microscope (AFM) cantilevers that could grab and release the building blocks, triggered by an external signal of either electrical or optical nature (*15*). We report a simpler and robust solution based on DNA hybridization and hierarchical bonds defined by different unbinding forces.

A well-sorted "depot," with a large variety of molecular species, stably stored in well-defined loci, is a prerequisite for the assembly of a multicomponent device. DNA chips offer a freely programmable pattern of oligomers that are commercially available and have spot sizes in the submicrometer range (*16*). Niemeyer *et al.* (*17*) converted such a DNA pattern into a protein pattern by binding a DNA-labeled protein to its corresponding spot on a DNA chip. The length of the oligomers can be chosen so that after incubation and stringent washing, a thermodynamically stable pattern of proteins is obtained. Given the known sequence map of the DNA chip, different molecular species can be stored in a known position on the depot chip. Alternatively, when only a limited variety of building blocks is needed, microfluidic elastomer channels may be used to create patterns (*18*–*20*) of building blocks, which after removal of the elastomer may be manipulated with the AFM tip (fig. S3).

We used this approach to store our functional units and also extended the DNA oligomers to fulfill a second function; namely, to serve as a handle (Fig. 1). This additional stretch of DNA can hybridize to a complementary DNA covalently attached to an AFM tip. We chose the duplexes to be comparable in length and binding free energy, but we selected the sequences so that the anchor hybridizes in the so-called "unzip" geometry and the handle hybridizes in the "shear" geometry [Fig. 1 and (*21*)]. These two duplex geometries differ substantially in that, upon forced unbinding, the zipper duplex is opened up base pair by base pair, whereas in the shear geometry, all base pairs are loaded in parallel (Fig. 2 and fig. S1). Although the thermodynamic stability and the spontaneous off rate of both geometries are comparable, their rupture forces differ dramatically (*22*), as has been shown experimentally and was validated theoretically in several studies (*21*, *23*–*27*). Thus, upon retraction of the AFM tip, the anchor duplex will break open and the functional unit will be bound to the tip.

As can be seen in Fig. 2C, these force distance curves provide a characteristic fingerprint and serve as a robust criterion to decide whether a molecule was picked up from the depot. To avoid multiple transfers, we chose the density of the anchors on the tip to be low enough that in 35% of the attempts, only one unit was picked up, and in 20% of the attempts, just two units. In 20% of all attempts, we recorded traces like the lower two in Fig. 2C, which showed that we had not picked up any unit (fig. S5D). Because we recorded such a force distance curve for every pickup, we knew exactly how many units were transferred to the tip. The pickup process can be corrected online by either picking up more units or by dropping excess units in a "trash can" on the target area.

Once a unit is transferred to the tip, it can be moved to its new position on the target area. The target area had surface chemistry similar to that of the depot area, but the anchor oligomers were chosen so that when the tip was lowered, they bound to the transfer DNA in shear geometry and formed a duplex, which was longer than the handle duplex. Although the AFM tip can be positioned with subnanometer reproducibility, the precision with which the units can be

---

[1] Center for Nanoscience and Department of Physics, University of Munich, Amalienstrasse 54, 80799 Munich, Germany.
[2] Department of Biological Chemistry and Molecular Pharmacology, Harvard Medical School, and Department of Cancer Biology, Dana-Farber Cancer Institute, Boston, MA 02115, USA.

Downloaded from www.sciencemag.org on October 29, 2008

deposited is limited by the lateral density of the anchor oligomers and their spacer length (presently in the 10-nm range).

Upon retraction of the tip from the surface, the force in the two DNA duplexes in series gradually increases until the weaker of the two complexes ruptures. The upper traces in Fig. 2D show examples of this process, which differs considerably in its signature from the unzipping shown in Fig. 2C (*28*, *29*). It was shown (*21*) that a length difference of 10 base pairs (bp) is sufficient to make the rupture of the shorter handle duplex more likely by one order of magnitude than the rupture of the longer anchor duplex. As was the case during pickup, no bond rupture was detected in certain cases (Fig. 2D, lower traces). Here the hybridization with the target anchor oligomer had failed, although a functional unit was offered. In the majority of cases, a second or third attempt made a few nanometers away from the originally planned target spot was successful. Again, a protocol with a characteristic force distance curve (for brevity referred to as a transfer protocol) was recorded for each transfer event. After delivery of the functional unit to the target, the oligomer covalently attached to the AFM tip was free again to hybridize with another handle sequence in the depot area.

For simplicity, we transferred only functional units of the same species but created patterns from single units with multiple functions instead. As functional units, we used molecular constructs consisting of a fluorophore (rhodamine green), a generic small ligand (biotin), and a DNA with extra overlap (which allows further docking of other units to the assembly in a later step) (Fig. 2 shows the schematics). The units were picked up

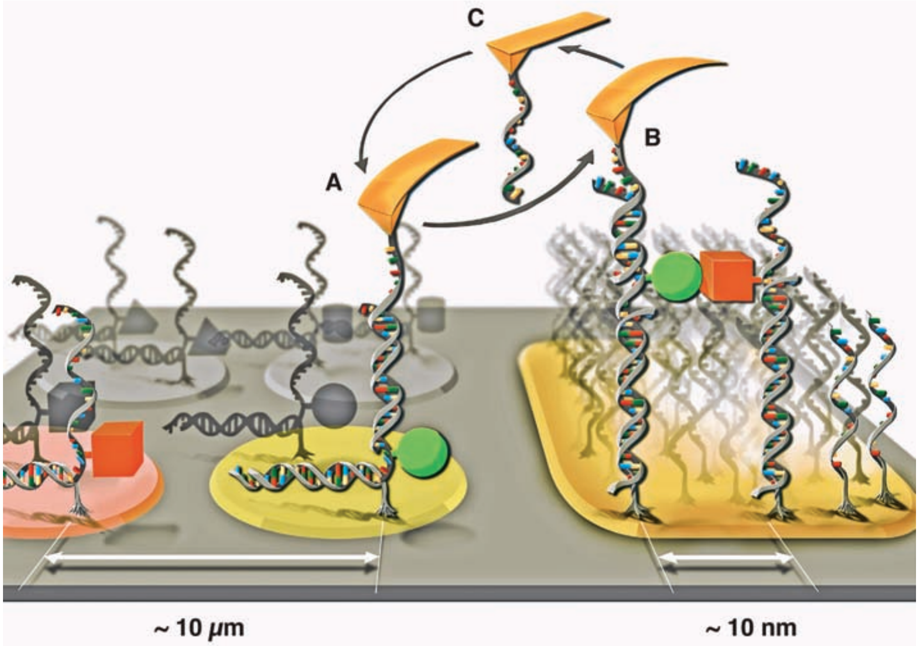

**Fig. 1.** Cartoon of the single-molecule cut-and-paste process. (**A**) Individual nanosized objects are picked up from discrete storage sites with a DNA oligomer at the tip of an AFM cantilever and transferred to a target site, where they are deposited with high spatial precision (**B**). (**C**) The length and binding geometry of the oligomers, which are used as an anchor or a handle, are chosen so that a hierarchy of unbinding forces allows the repetition of this process over and over again.

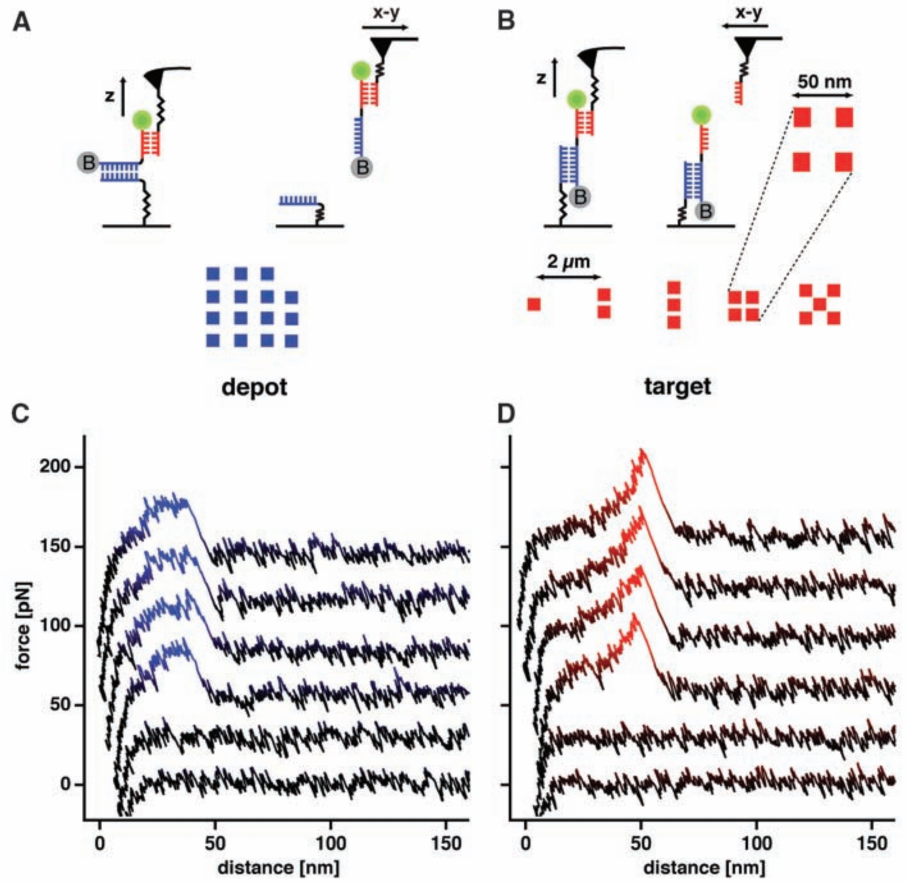

**Fig. 2.** Design of the assembled pattern with typical transfer protocols. (**A**) Individual functional units stored on the depot were picked up one at a time and transferred to the target area. The functional units consisted of a DNA oligomer with anchor and handle sequences, one fluorophore, one biotin, and an additional DNA binding site. (**B**) Five different patterns with different geometries were assembled on spots, which were 2 μm apart. In the first spot, we deposited one unit; in the second spot, two units with a lateral spacing of 50 nm; in the third spot, three units, and so forth. The lateral precision of the closed-loop feedback was ±6 nm. Force distance curves were recorded in every cycle as transfer protocols recording successful pickup and deposition. (**C**) Typical force distance curves measured during the pickup of functional units from the depot. At low extensions, the cantilever acts against the entropic force of the polyethylene glycol–DNA complex. When the force reaches about 20 pN, the anchor sequence is pulled open in a zipperlike mode, resulting in a plateau ~20 nm long. (**D**) Typical force distance curves recorded during the deposition of a single unit to the target area. The shape, with its sudden drop in force at about 50 pN, is characteristic of a rupture of a 20-bp DNA handle duplex loaded in shear geometry. The lower two force distance curves in (C) and (D) show attempts, where no transfer had occurred.

Downloaded from www.sciencemag.org on October 29, 2008

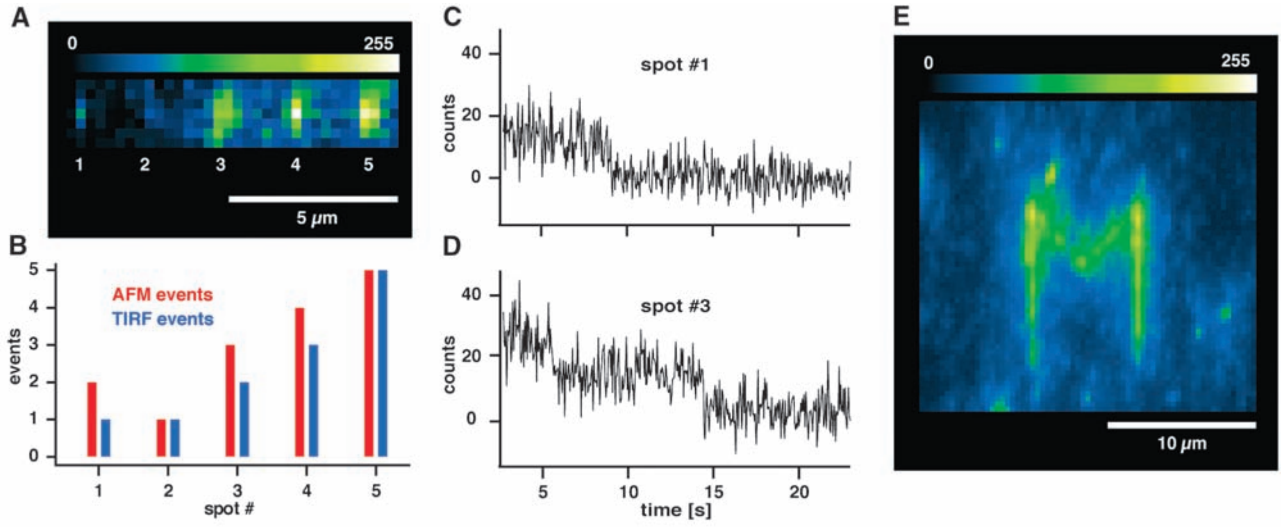

**Fig. 3.** (**A**) Fluorescence micrograph of the assembled pattern described in Fig. 2, imaged with TIRF excitation. The image was averaged over 440 frames, with 50 ms of integration time each. Because of the diffraction limit, individual fluorophores cannot be resolved spatially but can be resolved temporally. (**C**) and (**D**) show time traces of the two diffraction-limited 3 × 3–pixel–sized spots 1 and 3, exhibiting the typical stepwise bleaching of one and two single fluorophores, respectively. (**B**) Correlation analysis of the number of successfully transferred units as judged by the AFM transfer protocols and the number of bleaching steps in the fluorescence. (**E**) The capital letter M written by transporting 400 molecules from the depot area to defined positions at the target area. It was assembled with a tip that had already been used to transport more than 5000 molecules from the depot to the target area. These results demonstrate the long-term stability of the tip functionalization and the possibility of assembling extended constructs.

from a 100-nm-square pattern (Fig. 2A) and transferred to the target area. A pattern, as sketched in Fig. 2B, was assembled where we deposited a single unit in the first spot, a pair in the second spot, a triplet in the third, and so on. The transfer protocols always documented the actual number of transferred units.

After the assembly was completed, total internal reflection fluorescence (TIRF) imaging (*30*) showed discrete spots at the predicted positions (Fig. 3A). Because of the limited optical resolution, no details of the assemblies are resolved, but larger assemblies appear brighter. Time traces (Fig. 3, C and D) exhibited well-pronounced steps that were a clear indication of bleaching of individual fluorophores (*31*, *32*) (movie S1). On the spot in the first column, we recorded a single step only, and the fluorophore was bleached after 9 s. The spot in the third column exhibited only two steps, although our transfer protocol reported the deposition of three functional units. Either one of the fluorophores was inactive from the beginning or it was bleached during the first 2 s of the illumination and not recorded because of background fluorescence. A direct correlation between the number of deposited units as judged by the transfer protocol and the number of bleaching steps is given in Fig. 3B. Both independent experiments are in excellent agreement, which indicates that we lost only a minor fraction of fluorophores in the transfer process.

In order to demonstrate the formation of larger constructs, we assembled the capital letter M shown in Fig. 3E. It consists of 400 units and was written with a tip that had already been used to transport more than 5000 functional units from the depot to the target area. All of the data shown here and in the supporting online material were recorded with one cantilever. Because the pickup probability dropped by only 10% toward the end of the experiment, the lifetime of the tip functionalization was adequate. The pattern was assembled at an average rate of 7 s per transfer. This slow transfer rate was limited by the rather large distance between depot and target area of 15 μm and the closed-loop feedback of the translational stages of the instrument. The online analysis of the transfer protocols was also not optimized. The physical limits are given by the resonance frequency of the piezo stage, and so improvements of several orders of magnitude are possible (*33*). With the development of massively parallel–operating AFM cantilevers (*34*), molecule-by-molecule assembly based on hierarchical forces may evolve into a versatile technology.

### References and Notes

1. B. A. Grzybowski, H. A. Stone, G. M. Whitesides, *Nature* **405**, 1033 (2000).
2. T. Pellegrino *et al.*, *Small* **1**, 48 (2005).
3. M. Ringler *et al.*, *Nano Lett.* **7**, 2753 (2007).
4. D. M. Egler, E. K. Schweizer, *Nature* **344**, 524 (1990).
5. M. T. Cuberes, R. R. Schlittier, J. K. Gimzewski, *Appl. Phys. Lett.* **69**, 3016 (1996).
6. S. J. Greissl *et al.*, *J. Phys. Chem. B* **108**, 11556 (2004).
7. G. Binnig, H. Rohrer, C. Gerber, E. Weibel, *Phys. Rev. Lett.* **49**, 57 (1982).
8. G. Binnig, C. F. Quate, C. Gerber, *Phys. Rev. Lett.* **56**, 930 (1986).
9. P. K. Hansma, V. B. Elings, O. Marti, C. E. Bracker, *Science* **242**, 209 (1988).
10. M. Radmacher, R. W. Tillmann, M. Fritz, H. E. Gaub, *Science* **257**, 1900 (1992).
11. P. E. Marszalek *et al.*, *Nature* **402**, 100 (1999).
12. D. Fotiadis *et al.*, *Curr. Opin. Struct. Biol.* **16**, 252 (2006).
13. M. Jaschke *et al.*, *Biosens. Bioelectron.* **11**, 601 (1996).
14. R. D. Piner, J. Zhu, F. Xu, S. Hong, C. A. Mirkin, *Science* **283**, 661 (1999).
15. C. P. Collier *et al.*, *Science* **289**, 1172 (2000).
16. S. P. Fodor *et al.*, *Science* **251**, 767 (1991).
17. C. M. Niemeyer, T. Sano, C. L. Smith, C. R. Cantor, *Nucleic Acids Res.* **22**, 5530 (1994).
18. E. Delamarche, A. Bernard, H. Schmid, B. Michel, H. Biebuyck, *Science* **276**, 779 (1997).
19. S. R. Quake, A. Scherer, *Science* **290**, 1536 (2000).
20. D. C. Duffy, J. C. McDonald, O. J. A. Schueller, G. M. Whitesides, *Anal. Chem.* **70**, 4974 (1998).
21. C. Albrecht *et al.*, *Science* **301**, 367 (2003).
22. A hand-waving argument: Upon separation, the binding energy is overcome in the shear geometry within a much shorter distance than in the unzip geometry, therefore the force to overcome the energy barrier is much lower in the unzip geometry. Because the forced unbinding of the oligomer in shear geometry is a nonequilibrium process, its unbinding force is rate-dependent. In all experiments shown here, the duplexes were loaded with a rate of 3000 pN/s.
23. G. I. Bell, *Science* **200**, 618 (1978).
24. S. B. Smith, Y. J. Cui, C. Bustamante, *Science* **271**, 795 (1996).
25. B. Essevaz-Roulet, U. Bockelmann, F. Heslot, *Proc. Natl. Acad. Sci. U.S.A.* **94**, 11935 (1997).
26. M. Rief, H. Clausen-Schaumann, H. E. Gaub, *Nat. Struct. Biol.* **6**, 346 (1999).
27. G. Neuert, C. H. Albrecht, H. E. Gaub, *Biophys. J.* **93**, 1215 (2007).
28. J. Morfill *et al.*, *Biophys. J.* **93**, 2400 (2007).
29. T. Strunz, K. Oroszlan, R. Schafer, H. J. Guntherodt, *Proc. Natl. Acad. Sci. U.S.A.* **96**, 11277 (1999).
30. R. D. Vale *et al.*, *Nature* **380**, 451 (1996).
31. G. Seisenberger *et al.*, *Science* **294**, 1929 (2001).
32. P. Tinnefeld, M. Sauer, *Angew. Chem. Int. Ed.* **44**, 2642 (2005).
33. G. Schitter *et al.*, *IEEE Trans. Control Syst. Technol.* **15**, 906 (2007).
34. P. Vettiger *et al.*, *IBM J. Res. Devel.* **44**, 323 (2000).
35. Helpful discussions with P. Hansma, G. M. Whitesides, J. Fernandez, H. Heus, P. Tinnefeld, J. Morfill, C. Albrecht, and L. Whetton are gratefully acknowledged. Supported by the German Science Foundation and the Nanosystems Initiative Munich.

### Supporting Online Material

www.sciencemag.org/cgi/content/full/319/5863/594/DC1
Materials and Methods
Figs. S1 to S5
References
Movie S1

9 October 2007; accepted 18 December 2007
10.1126/science.1151424

Downloaded from www.sciencemag.org on October 29, 2008

www.sciencemag.org/cgi/content/full/319/5863/594/DC1

# Supporting Online Material for

## Single-Molecule Cut-and-Paste Surface Assembly

S. K. Kufer, E. M. Puchner, H. Gumpp, T. Liedl, H. E. Gaub

Published 1 February 2008, *Science* **319**, 594 (2008)
DOI: 10.1126/science.1151424

**This PDF file includes:**

- Materials and Methods
- Figs. S1 to S5
- References

**Other Supporting Online Material for this manuscript includes the following:** (available at www.sciencemag.org/cgi/content/full/319/5863/594/DC1)

- Movie S1

# Supporting online material

# Single-Molecule, Cut-and-Paste Surface Assembly

S. K. Kufer[1], E. M. Puchner[1], H. Gumpp[1], T. Liedl[2], H. E. Gaub[1]

## Materials and Methods

**General:**
In this report, DNA oligomers were employed as anchors and handles for pick-up and delivery of nanosized objects (e.g. fluorophores) with an AFM. The oligomers were chosen such that they form duplexes, which under load unbind at different forces. They define a hierarchical set of unbinding forces. Upon pick-up, the force at which the anchor releases the object from the depot must be smaller than the force that binds it to the tip. Upon delivery, however, the force at which the object is released from the tip must be smaller than the force that anchors the object at the target site. This is achieved by choosing both length and unbinding geometries of the duplexes accordingly. A schematic of the molecular constructs employed is shown in Fig. S1. The sequences of the oligomers are given in Fig. S2.

**Preparation of cover slips:**
Cover slips were cleaned through a 15 min supersonic treatment in a mixture (1:1 (v/v)) of ethanol and $H_2O$ (Millipore water with a conductance of 0.054 µS), rinsed with $H_2O$ and dried in a nitrogen stream. After 10 min of activation using a UV-ozone cleaning system (UVOH 150 LAB, FHR Anlagenbau GmbH, Ottendorf-Okrilla, Germany) the cover slips were functionalized with a solution of 2 % 3-aminopropyldimethylethoxysilane, 88 % ethanol and 10 % $H_2O$ for 30 min at room temperature. Cover slips were again rinsed with ethanol and $H_2O$ and dried in a nitrogen stream. After 30 min of curing at 80 °C the amino modified cover slips were immersed for 1 h in sodium borate (SB) buffer (50 mM, pH 8.5) to deprotonate the amino groups. Then NHS-PEG-maleimide was dissolved in a concentration of 50 mM in SB buffer and incubated on the amino modified cover slips for 1 h. After rinsing with $H_2O$ a PDMS flow chamber (fabrication and features are described below) was mounted on one of the cover slips. Both channels were connected to a peristaltic pump (Minipuls3, Gilson International B.V. Bad Camberg, Germany) that was operated at a flow rate of 1 µl/min. The anchor oligomers for the depot and target area (Fig. S2) were reduced using TCEP beads in order to generate free mercaptans. The left channel (depot area) was rinsed for 1 h with a 10-µM solution of depot anchor oligomers and the right one (target area) with a 10-µM solution of target anchor oligomers. Afterwards both channels were rinsed with $H_2O$ to remove all non-covalently bound oligomers. The left channel (depot area) was rinsed with a 1-µM solution of transfer-DNA

---

[1] Center for Nanoscience & Physics Department, University Munich, Amalienstr. 54, 80799 Munich
[2] Department of Biological Chemistry and Molecular Pharmacology, Harvard Medical School & Department of Cancer Biology, Dana-Farber Cancer Institute, Boston, MA 02115, USA

(dissolved in 5*saline sodium citrate buffer (SSC) buffer) for 1 h. After rinsing both channels for 5 min with 1*SSC buffer to remove all non-hybridized transfer-DNA from the depot channel, the PDMS flow chamber was removed and the cover slip was dried in a nitrogen stream. Finally the cover slip was mounted to the AFM-TIRF sample holder (Fig. S4) and immersed in 2*SSC buffer.

**Preparation of cantilevers:**

Cantilevers (Bio-lever, Olympus, Tokyo, Japan) were activated by a 10 min UV-ozone cleaning treatment and modified with 3-aminopropyldimethyl-ethoxysilane as described in (*1, 2*). Afterwards they were rinsed with SB buffer for 1 h to deprotonate the amino groups. NHS-PEG-maleimide was dissolved in a concentration of 50 mM in SB buffer and incubated for 1 h on the amino modified cantilevers. After washing with $H_2O$, the cantilevers were incubated for 1 h with a 10-µM solution of reduced cantilever oligomers. Finally, the cantilevers were rinsed with $H_2O$ to remove all non-covalently bound oligomers and stored in an argon atmosphere until use.

To prepare cantilevers with reduced functionalization densities the NHS-PEG-maleimide and therefore the binding sites for the mercaptans were diluted with NHS-PEG-methoxy. An ideally prepared cantilever has only one binding site for the handle sequence and therefore the optimal ratio between the NHS-PEG-maleimide and NHS-PEG-methoxy depends on the area of the apex and varies from cantilever to cantilever. During many cut-and-paste experiments, a ratio between the NHS-PEG-maleimide and NHS-PEG-methoxy of 1:5 (m/m) dissolved in SB buffer with a final concentration of 50 mM was determined as an optimal mixture for cantilevers with low functionalization densities.

**Fabrication of PDMS microfluidic channels:**

PDMS siloxane elastomer and curing reagent were mixed at a ratio of 10:1 (m/m) and poured onto a lithographically prepared microstructured silicon wafer (master) shown schematically in Fig. S3A. After incubation for 1 h at 60 °C, the polymer was removed from the master and a 1.5 cm x 1.5 cm piece was cut out with a scalpel. An inlet and outlet were pierced in both channels using a canula with a diameter of 0.8 mm. Then the PDMS flow chamber was placed on a NHS-PEG-maleimide activated cover slip and cured again for 10 min at 60 °C to seal the flow channels. The two resulting flow channels run parallel and were separated by a 15-µm PDMS wall. Each channel was 100 µm broad, 20 µm high and 2 cm long. Fig. S3B shows a TIRF image of the depot and target area and the 15-µm gap between them. To make not only the depot area but also the target area visible both regions were activated here with fluorescently labeled DNA. Fig. S3C shows a typical fluorescence image of a functionalized cover slip used for the experiments. The depot area is visible due to fluorescently labeled DNA. No fluorescence signal is detectable on the target area, which clearly shows that crosstalk between both channels is negligible. The fluorescence image was recorded with a confocal laser scanner (LS 300 Scanner, Tecan Deutschland GmbH, Crailsheim, Germany). The fluorescence signal is equivalent to a surface density of 15 fmol/mm$^2$ and therefore the mean distance between the anchor oligomers is roughly 10 nm.

**AFM measurements:**

All single-molecule cut-and-paste experiments were performed with a custom built AFM (*3*) at room temperature in 2* SSC (Fig. S4). The spring constant of the DNA modified cantilever was calibrated in solution using the equipartition theorem (*4, 5*). This method provides an accuracy of roughly 10% and yielded a spring constant of 4.2 pN/nm and a resonance frequency of 1.6 kHz for the cantilever used in this study.

The protocol for the single-molecule cut-and-paste as well as the data recording was programmed using Igor Pro (Wave Metrics) and an Asylum Research controller, which provides ACD and DAC channels as well as a DSP board for setting up feedback loops. Cantilever positioning for pick-up and delivery was controlled in closed-loop operation. Usually the precision was set to ±6 nm. For the letter "M" in Fig. 3E, the precision of the feedback was reduced in order to speed up the cut-and-paste protocol. In this case the experimental deviation from the given positions amounts ± 50 nm. Once this position was reached within an accuracy of 10 nm, the cantilever approached the surface with closed-loop control until the repulsion reached 50 pN within an error of 5 pN. The tip was then withdrawn from the surface at a speed of 1200 nm/s, and the force was recorded at a sampling rate of 10 kHz. The resulting force distance curve characterizes the cut-and-paste process and allows determination of the number of molecules that were picked up and delivered (Fig. S5). The timing of the process is roughly as follows: approach ~ 1 s, dwell time for pick up ~ 0.5 s, retract ~ 1 s, approach new position ~ 0.5-2 s (depending on precision of the closed-loop) approach ~ 1 s, dwell time for contact ~ 0.5 s, retract and reposition ~ 1 s, resulting in a total time of ~ 7 s for one cut-and-paste cycle.

The functionalization density on the tip was chosen in a compromise between no pick-up (Fig. S5A) and multiple pick-ups, as shown in Fig. S5C. In cases where multiple units were picked up, they were either “dropped” in the “trash can” (we deposited them in an area next to the structure to be assembled) or we deposited multiples like we did when we assembled the capital letter “M”. The traces in Fig. S5, E-G were recorded from these transfers. Under the category “others” in Fig. S5, D and H, we collected all traces, which resulted from higher multiples we were unable to quantify precisely.

**Fluorescence microscopy:**

Single-molecule fluorescence microscopy was carried out in TIRF excitation. Fluorescence excitation of the rhodamine green dyes is performed by a 472 nm, 80 mW DPSS laser (Viasho Technology Co., Ltd., Beijing, China) through a 100x/1.45 oil immersion objective lens (alpha Plan-Fluar, Zeiss, Oberkochen, Germany), where the collimated laser beam is focused in the back focal plane of the objective lens such that the beam is totally reflected at the cover slip (*6*). The focus is controlled with a piezo (Mipos 100, Piezosystemjena, Jena, Germany). The emitted light is detected by a 128 x 128 pixel back-illuminated EMCCD camera (DU-860, Andor, Belfast, Ireland). Time series where recorded in frame-transfer mode with an integration time of 50 ms per frame. The peltier-cooled CCD chip was typically operated at a temperature of -60°C and an electron multiplication gain of 200x was used.

The movie M1 of the supplement shows the step-wise bleaching of individual fluorophores, which were deposited as displayed in the first frame of this movie. The six bright spots constituting the uppermost row were written by performing 9 transfer cycles whereas all other spots were written in single approaches. The content of the tip was deposited regardless of the number of units that were picked up. As was to be expected from the statistics in Fig. S4, the single dots are predominantly single units, and some spots remained empty. As can be seen in the movie, under our experimental conditions, the average lifetime of one rhodamine green fluorophore is about 10 s. As it becomes clear in this movie, the closely spaced molecules in the first row cannot be resolved optically. However, the accurate positions of individual fluorophores can in principle be determined by taking advantage of the time domain. This, however, remains to be shown in future studies.

**Materials:**

- $H_2O$ with a conductance of 0.054 µS (Millipore, Eschborn, Germany)
- Water-for-chromatography (Merck KGaA, Darmstadt, Germany)
- Ethanol 99,8 % (Carl Roth GmbH + Co. KG, Karlsruhe, Germany)
- Argon (AIRLIQUIDE Deutschland GmbH, Düsseldorf, Germany)
- Cover slips (Marienfeld, Lauda-Königshofen, Germany)
- Sylgard184$^{TM}$ polydimethylsiloxane (PDMS), (Dow Corning, Wiesbaden, Germany)
- 3-Aminopropyldimethylethoxysilane (ABCR, Karlsruhe, Germany)
- Oligomers (IBA GmbH, Göttingen, Germany)
- N-hydroxy-succinimide-ester-polyethylenglycol-maleimide (NHS-PEG-Maleimide), MW 5000 g/mol (Nektar, Huntsville, Alabama, USA)
- N-hydroxy-succinimide-ester-polyethylenglycol-methoxy (NHS-PEG-Methoxy), MW 5000 g/mol (Rapp Polymere GmbH, Tübingen, Germany)
- 20*Saline sodium citrate buffer (SSC) (Sigma, Taufkirchen, Germany)
- 5*SSC buffer were prepared by diluting 20*SSC with $H_2O$
- 2*SSC buffer were prepared by diluting 20*SSC with water-for-chromatography
- Sodium borate buffer (SB) (50 mM, pH 8.5)
- TCEP beads (Perbio Science, Bonn, Germany)
- Canula (Sterican, 0,80 x 22 mm, Carl Roth GmbH + Co, Karlsruhe, Germany)

# Figures

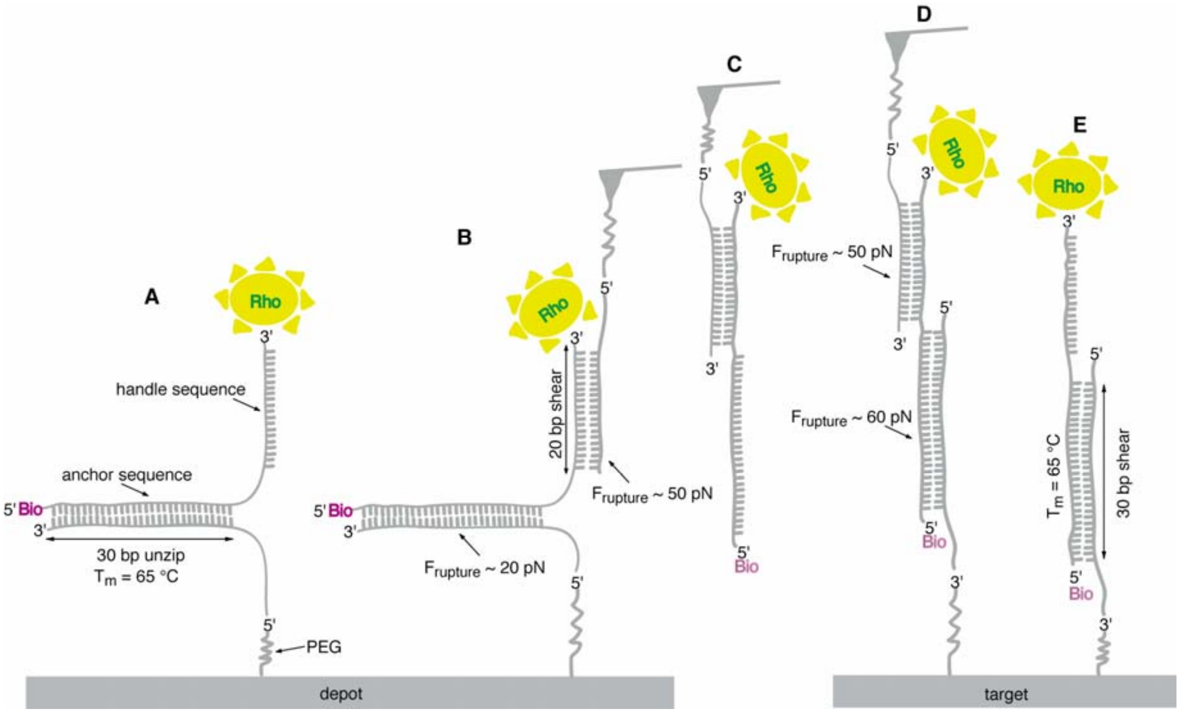
A
Rho
3'
handle sequence
anchor sequence
5' Bio
3'
30 bp unzip
$T_m$ = 65 °C
5'
PEG
depot
B
Rho
5'
3'
20 bp shear
$F_{rupture}$ ~ 50 pN
5' Bio
3'
$F_{rupture}$ ~ 20 pN
5'
C
5'
3'
Rho
3'
5'
Bio
D
5'
3'
Rho
$F_{rupture}$ ~ 50 pN
5'
3'
$F_{rupture}$ ~ 60 pN
5'
Bio
3'
E
Rho
3'
5'
$T_m$ = 65 °C
30 bp shear
5'
Bio
3'
target

**Fig. S1.** Schematic of the pick-up and delivery system based on DNA duplexes with hierarchical unbinding forces. (A) The 5' end of the depot anchor oligomer is covalently attached to a cover slip via a PEG spacer. Upon incubation, the transfer-DNA with the functional unit hybridizes to the 30-bp anchor in the depot area. The remaining 20 nucleotides long sequence was chosen to be complementary to the cantilever oligomer and serves as a molecular handle. (B) The cantilever oligomer is covalently bound via a PEG spacer with the 5' end to the AFM tip. Upon approaching the depot area, the handle sequence of the transfer-DNA and the cantilever oligomer hybridize. By retracting the tip from the substrate, both duplexes are loaded in series and thus equally, however, in different geometries. The anchor duplex is loaded in unzip geometry whereas the handle duplex is loaded in shear geometry. Despite the fact that the anchor duplex is longer than the handle duplex, it unbinds at lower forces and as a result the transfer-DNA goes along with the tip (C). It may now be transferred to the target area. The target anchor oligomer has the same sequence as the depot anchor oligomer but it is attached to the target surface with its 3' end. Therefore it hybridizes with the transfer-DNA in shear geometry (D). When the tip is withdrawn from the target surface both duplexes are loaded in shear geometry. Since the shorter of the duplexes opens first, the transfer-DNA with its functional unit remains at the target site (E). The tip is in its initial state and the cycle may start over again.

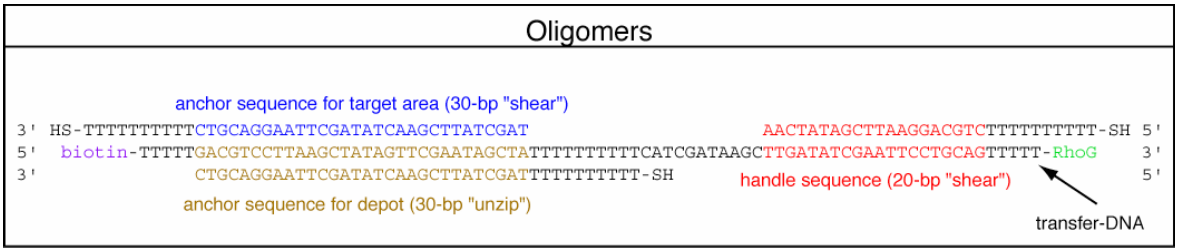
Oligomers
anchor sequence for target area (30-bp "shear")
3' HS-TTTTTTTTTTCTGCAGGAATTCGATATCAAGCTTATCGAT AACTATAGCTTAAGGACGTCTTTTTTTTTT-SH 5'
5' biotin-TTTTTGACGTCCTTAAGCTATAGTTCGAATAGCTATTTTTTTTTTCATCGATAAGCTTGATATCGAATTCCTGCAGTTTTT-RhoG 3'
3' CTGCAGGAATTCGATATCAAGCTTATCGATTTTTTTTTTT-SH 5'
handle sequence (20-bp "shear")
anchor sequence for depot (30-bp "unzip")
transfer-DNA

**Fig. S2.** Sequences of the handle, transfer and anchor oligomers. All oligomers were synthesized and purified (HPLC-grade) form IBA (IBA GmbH, Göttingen, Germany).

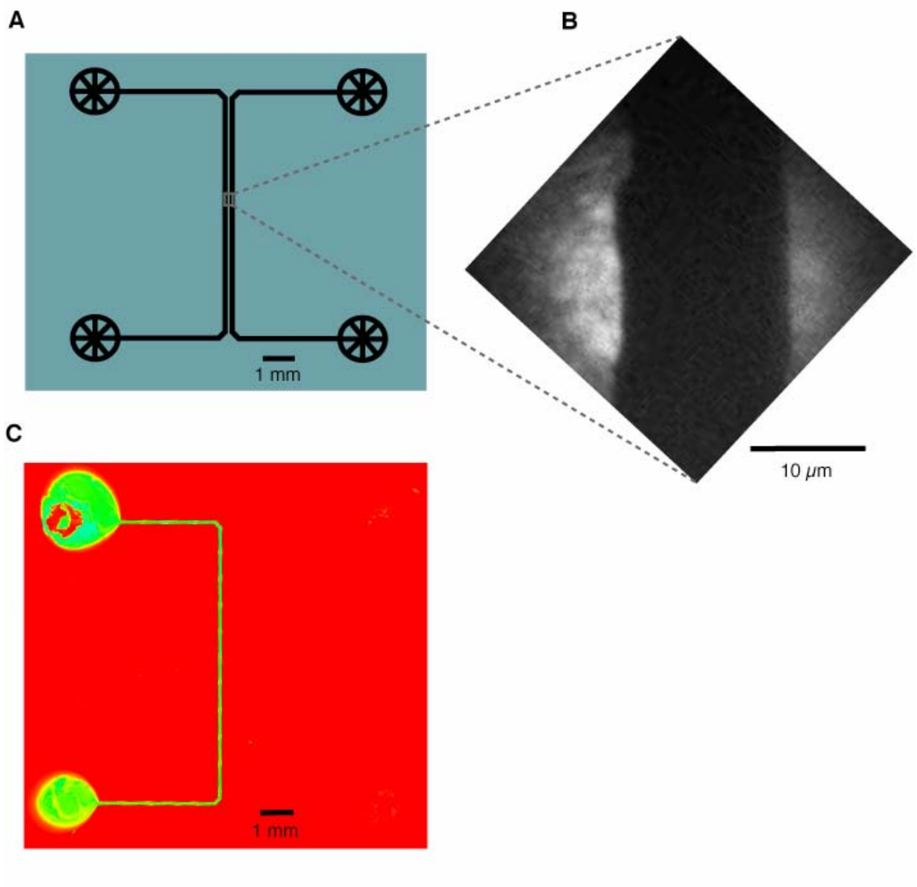

**Fig. S3.** Surface functionalization by means of PDMS flow channels. (A) Schematic illustration of the microstructured silicon wafer used as a mold for the PDMS elastomer. Each channel was 100 µm wide, 20 µm high, 2 cm long and separated by a 15-µm gap. Round microstructures were at both ends of each channel, where an inlet and outlet could be pierced into the cured PDMS flow channels. (B) TIRF image of the depot and target area and the 15-µm gap between them. The left channel serves as depot and the right as target area. For this image both areas were functionalized with fluorescently labeled DNA to make them visible. (C) Fluorescence image of a functionalized cover slip used for a typical cut-and-paste experiment.

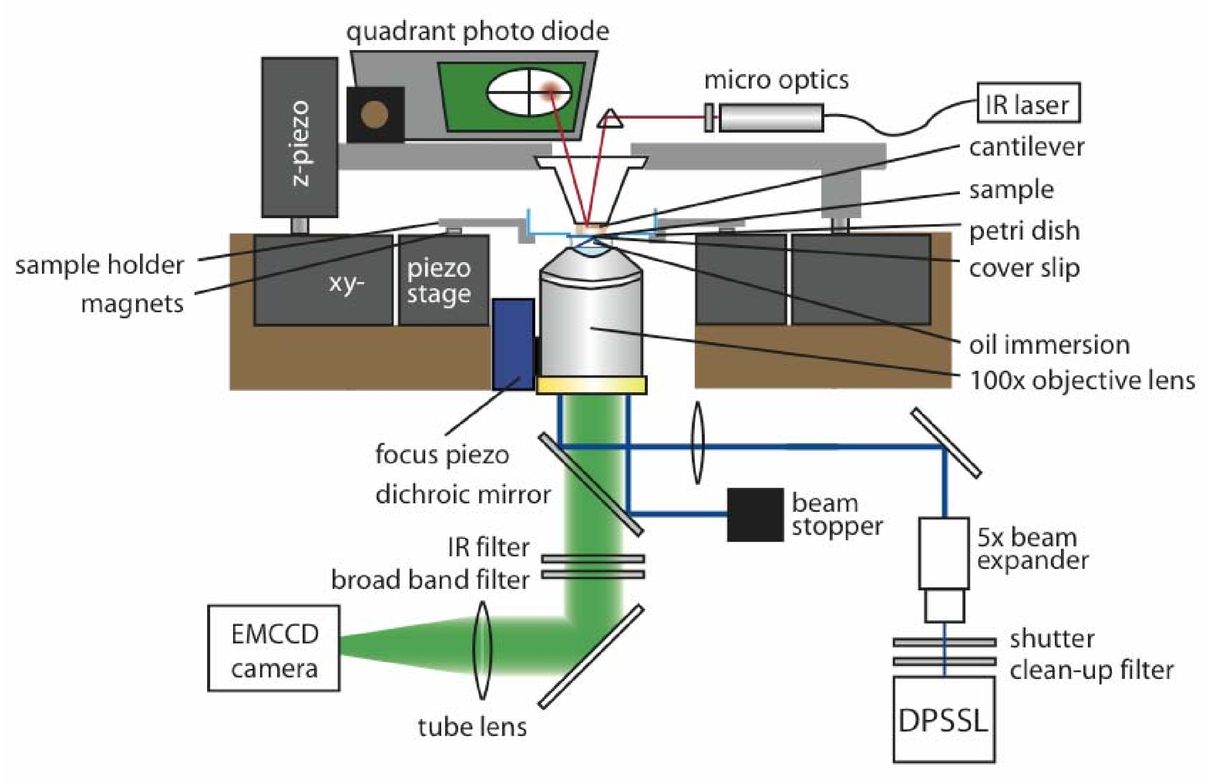
quadrant photo diode
z-piezo
micro optics
IR laser
cantilever
sample
petri dish
cover slip
sample holder
magnets
xy-
piezo stage
oil immersion
100x objective lens
focus piezo
dichroic mirror
beam stopper
5x beam expander
IR filter
broad band filter
EMCCD camera
tube lens
shutter
clean-up filter
DPSSL

**Fig. S4.** Experimental setup. The combined TIRF-AFM setup comprises an inverted microscope for objective-type wide-field TIRF excitation and a custom built AFM installed on an x-y piezo scanning stage. The sample is situated on a cover slip glued into a drilled petri dish, which is mounted into a steal vessel that can be moved by the piezo scanner.

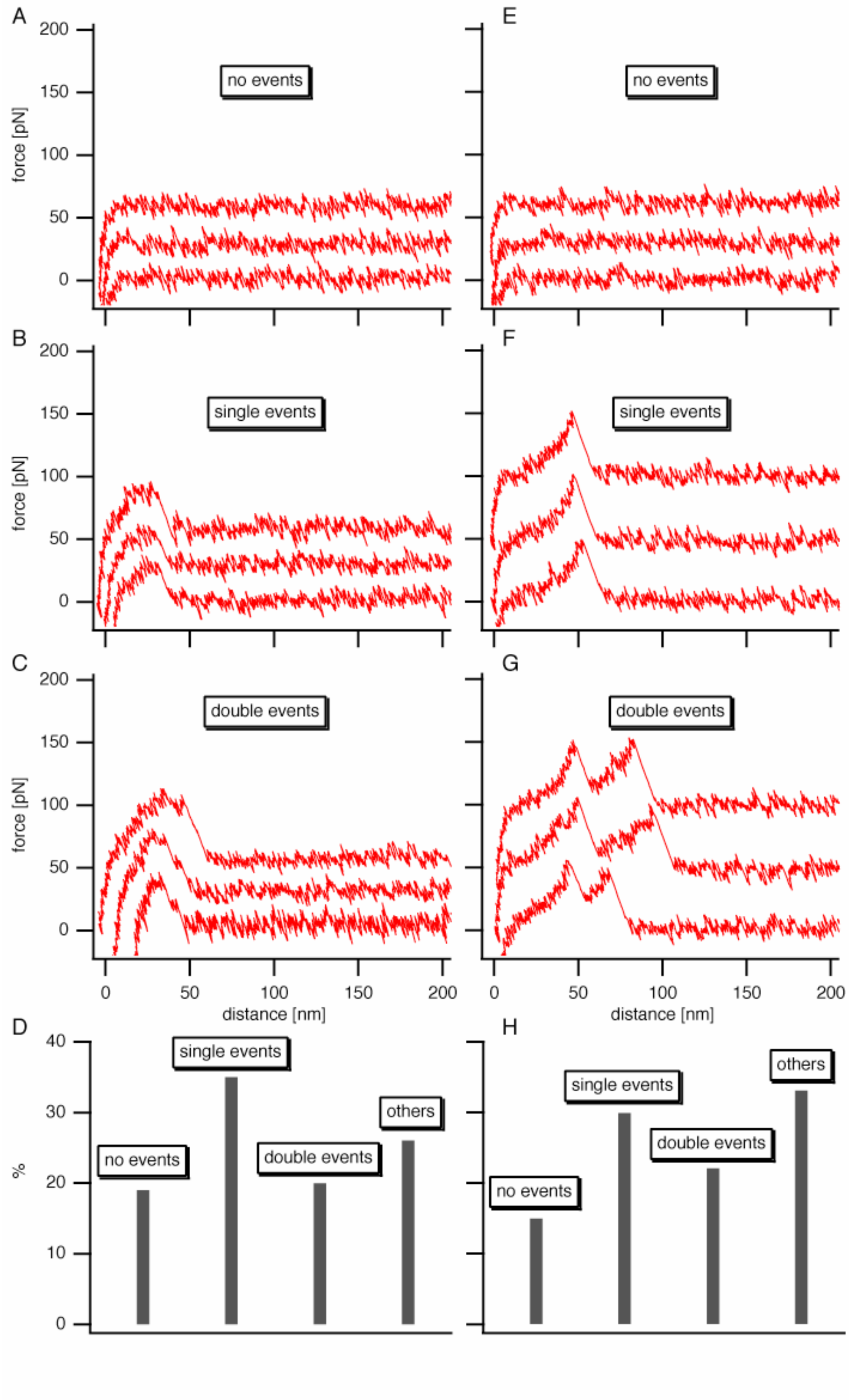

**Fig. S5.** Typical single-molecule force distance transfer protocols of the individual steps of the pick-up (A-C) and the delivery (E-G) and their statistical analysis (D) and (H). Double events are clearly distinguishable from single pick-ups or deliveries by the doubled height of the plateau or the multiple rupture peaks, respectively.

## References

1. G. Neuert, C. Albrecht, E. Pamir, H. E. Gaub, *FEBS letters* **580**, 505 (2006).
2. J. Morfill *et al.*, *Biophys. J.* (June 8, 2007).
3. F. Kühner, R. Lugmaier, S. Mihatsch, H. E. Gaub, *Rev. Sci. Instrum.* **78** (2007).
4. H. J. Butt, M. Jaschke, *Nanotechnology* **6**, 1 (1995).
5. E.-L. Florin *et al.*, *Biosensors and Bioelectronics* **10**, 895 (1995).
6. T. Funatsu, Y. Harada, M. Tokunaga, K. Saito, T. Yanagida, *Nature* **374**, 555 (1995).

# Optically monitoring the assembly of single molecules

Stefan K. Kufer[1], Mathias Strackharn[1], Stefan W. Stahl[1], Hermann Gumpp[1], Elias M. Puchner[1,2] and Hermann E. Gaub[1*]

[1]Center for Nanoscience & Physics Department, University Munich, Amalienstr. 54, 80799 Munich
[2]Center for Integrated Protein Science Munich
*E-mail: Gaub@LMU.de

accepted by Nature Nanotechnology 10/08

**Super-resolution imaging[1-10] of a diffraction limited spot consisting of multiple fluorophores was demonstrated on randomly adsorbed DNA duplexes carrying several dye molecules[6-9]. We used single-molecule cut-and-paste surface assembly[11] for the controlled deposition of individual fluorophores in well-defined nanometer sized patterns. Although the size of the pattern is far beyond the Abbe limit, the individual dyes could be identified by centroid localization combined with photobleaching. A hybrid TIRF-AFM setup allowed to monitor the deposition process of single fluorophores in real time and to determine their position with nanometer precision.**

Objects smaller than the diffraction limit of an imaging system are projected as blurry spots with the size of a Rayleigh disc. Nonetheless the center position of these spots can be determined with an accuracy far beyond the Abbe limit[12, 13], and the precision is only limited by the number of photons collected from this object[14]. This way individual fluorophores can be localized with nanometer precision[15]. Multiple emitters within a diffraction limited spot may also be localized if their individual contributions to the overall signal can be discriminated either spectrally or by other means. In recent years various techniques, subsumized under the expression super-resolution imaging (SRI), have been developed, which use different methods to extract one high-resolution image from a series of low-resolution images[6, 7, 9, 10, 16]. Such attempts may be employed to first separate the contributions of the individual molecules and then to reconstruct the ensemble. Several methods were suggested to create image sequences of single-fluorophores and to reconstruct the position of these fluorophores using different localization algorithms[13, 14].

Impressive proof of principle experiments for super-resolution imaging were reported in the literature, where samples were designed with different fluorophores on defined positions[6-9]. Predominantly DNA duplexes with modified bases were employed as molecular rulers for this purpose. This however limits the potential pattern to a linear arrangement of the dyes. We recently introduced a new means to assemble individual nanoscale functional units called single-molecule cut-and-paste (SMCP). It combines the precision of the atomic force microscope (AFM) with the selectivity of DNA hybridization. Here we employed this technique to assemble two-dimensional (2d) patterns of individual fluorophores, which we then subsequently localized by SRI.

The SMCP system used here uses a transfer DNA with an anchor and a handle sequence carrying a single Cy3 dye molecule. The anchor sequence provides a thermodynamically stable attachment of the transfer DNA in both the depot and the target area. The handle sequence allows pick up of the transfer DNA with the AFM tip and movement of the transfer DNA from the depot to the target. Binding geometry and overlap length of the oligomers were chosen such that this cut-and-paste process may be operated in cycles. Details of the underlaying hierarchical system of unbinding forces are described in the supplement.

In Fig. 1 the deposition of a single fluorophore, which had previously been picked up from the depot area, is shown step by step. When the tip is lowered towards the target site (Fig 1a black curve), the anchor sequence hybridizes with a complementary strand. When the tip is withdrawn from the surface, both sequences are loaded in shear mode but the shorter handle sequence ruptures first, and the transfer system remains at the target site (Fig. 1b). As a force distance curve of the deposition process is recorded, the paste process can be validated with this characteristic AFM fingerprint (Fig. 1a).

Advantageously the combined AFM-TIRF setup allows monitoring of the deposition process simultaneously with single-molecule fluorescence microscopy. As can be seen in Fig. 1c only a very low background signal is detected when the tip is far away from the surface. When the tip penetrates the evanescence excitation field, a strong fluorescence signal from the dye molecule is detected in the green channel of the camera. As the tip inelastically scatters light over a wide range of wavelengths[17] the tip is visible in both, the red and the green detection channels. When the tip is withdrawn, the signal from the tip vanishes, but the dye emits photons at a constant rate until it suddenly bleaches in a single step. The movie M1 in the supplementary shows this deposition event in detail. The intensity time trace in Fig. 1d clearly shows the deposition of a single-molecule. The finding that this bleaching step size in fluorescence intensity remains the same throughout a large number of experiments together with the clear signature in the single-molecule force scans during deposition unambiguously shows that SMCP allows exquisite control of the deposition of individual fluorophores.

The position of this single-molecule can now be located by fitting Gaussians to the intensity images. The image sequence is collected

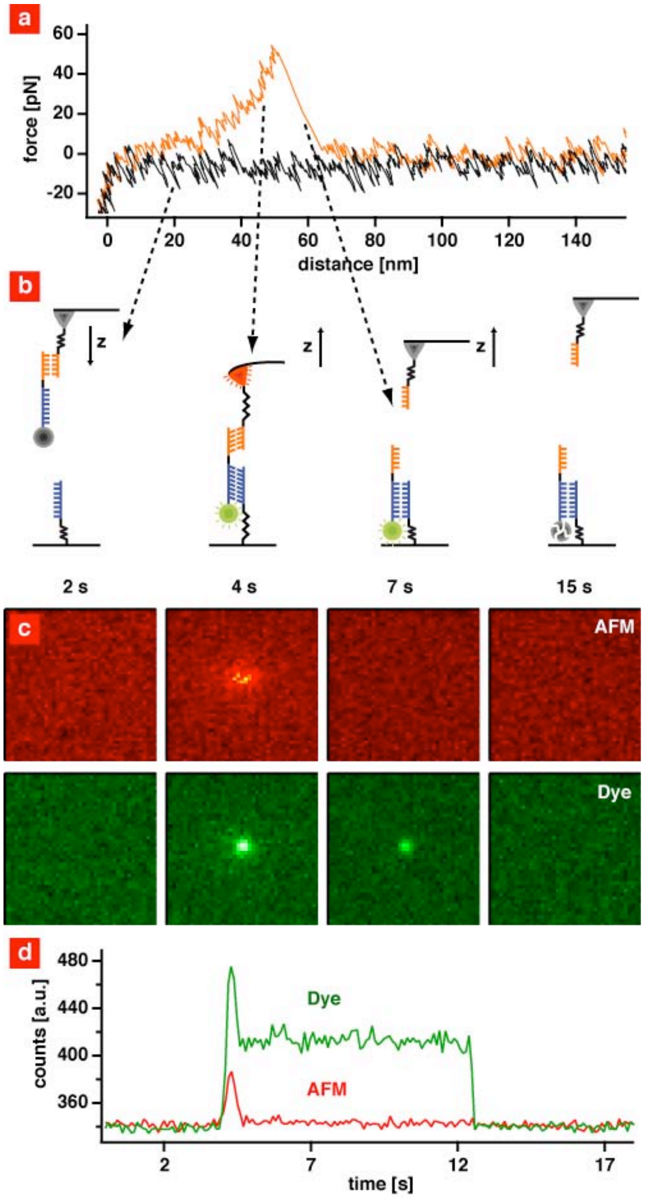

**Figure. 1 Deposition of a single-molecule monitored simultaneously by AFM and TIRF microscopy.** (a) Typical force distance curve of the deposition process. The transfer DNA is picked up from a depot and bound via a 20 bp DNA duplex to the tip. At the deposition site the tip was lowered until it contacts the surface (black curve) and a 30 bp DNA duplex in shear geometry is formed. By retracting the tip from the surface, the force acting on the polyethylene glycol–DNA complex gradually increases until the weakest bond in series ruptures (red curve). (b and c) Since the transfer DNA has a green fluorescence label and the tip inelastically scatters light over a broad range of wavelengths, it is possible to monitor the deposition process also with single-molecule fluorescence microscopy. As long as the tip is far away from the surface (2 s), no fluorescence is detectable in both channels. As soon as the tip penetrates the evanescent excitation field (4 s), a strong signal is detected in both channels. When the cantilever is retracted (7 s), the fluorescence from the tip vanishes whereas the fluorescently labeled transfer DNA remains anchored and emits photons at a constant rate. Finally the fluorophore photobleaches in a single step. (d) Intensity time traces at the deposition site. The red trace results solely from the tip, the green from the deposited fluorophore and inelastically scattered light from the tip. The position of this fluorophore is shown in Fig. 2.

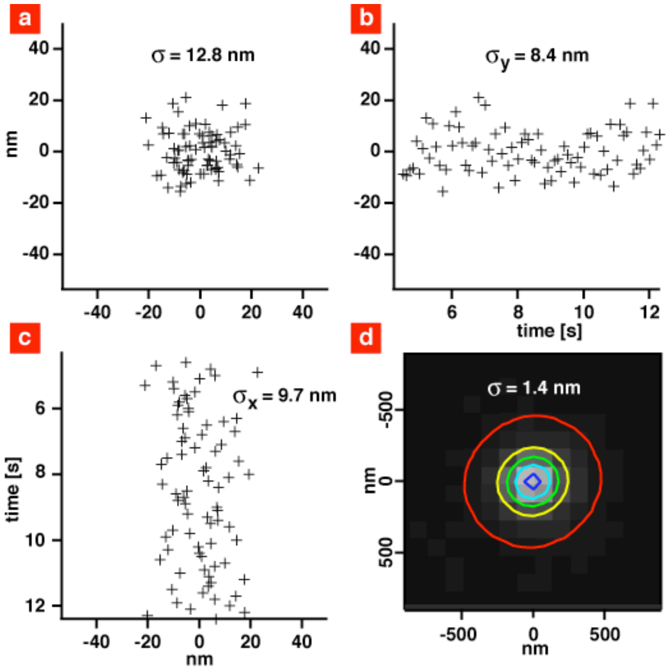

**Figure 2 Nanometer precise localization of single-molecules.** (a) To each frame during the lifetime of the single fluorophore deposited in Fig. 1, two-dimensional Gaussians were fitted. The temporal development of the x- and y-coordinates of the center are shown in (b) and (c). The intensity images were collected at a sampling rate of 10 Hz and the position accuracy of each fit is 13 nm. (d) Since the position of the dye was shown to be free of drift (b and c), an average intensity image of this period was summed and a single Gaussian was fit to it. The position accuracy of the optical part of the combined instrument was in this way determined to be ±1.4 nm.

with a sampling rate of 10 Hz. This means that each frame of the movie is 100 ms long. To evaluate the mechanical stability of our combined instrument, we did not integrate the signal over the lifetime of the fluorophore. Instead for each frame the position of the fluorophore was determined and plotted in Fig. 2a. As can be seen no systematic drift of the molecule is observed and the standard deviation for the 100 ms localization was determined to be ±13 nm. Fig. 2b and c show the temporal development of the x- and y-positions. As drift was negligible, the images were summed, whereby the S/N ratio of this image was roughly improved by a factor √n, where n is the number of images. This means when a single dye remains intact for about 8 s (80 frames) the S/N ratio increases by a factor of 9. Since an increase of the S/N ratio results in an increase of position accuracy, it is possible to improve the localization by calculating an averaged intensity image (Fig 2 d). This molecule that remained active for more then 8 s could thus be located with a precision better than ±1.4 nm. This value is a benchmark for the accuracy with which we can determine the position of a single fluorophore.

Next, the spatial precision of the SMCP process was examined. As was pointed out by Smalley in his dispute with Drexler, "complete" mechanical control over an assembly process on the single-molecule level would hardly be possible because of two intrinsic fundamental limitations commonly referred as the fat and sticky finger problem. SMCP makes use of this seeming limitation in that it employs the selective “stickiness” between the DNA oligomers used for transfer and assembly. However, the spatial precision of the paste process is then limited by the size of the DNA-oligomer, by the functionalization density of the target area and by the rotational mobility of the PEG-spacers used for the covalent attachment of the oligomers to the surfaces. A sketch of this situation is given in Fig. 3a.

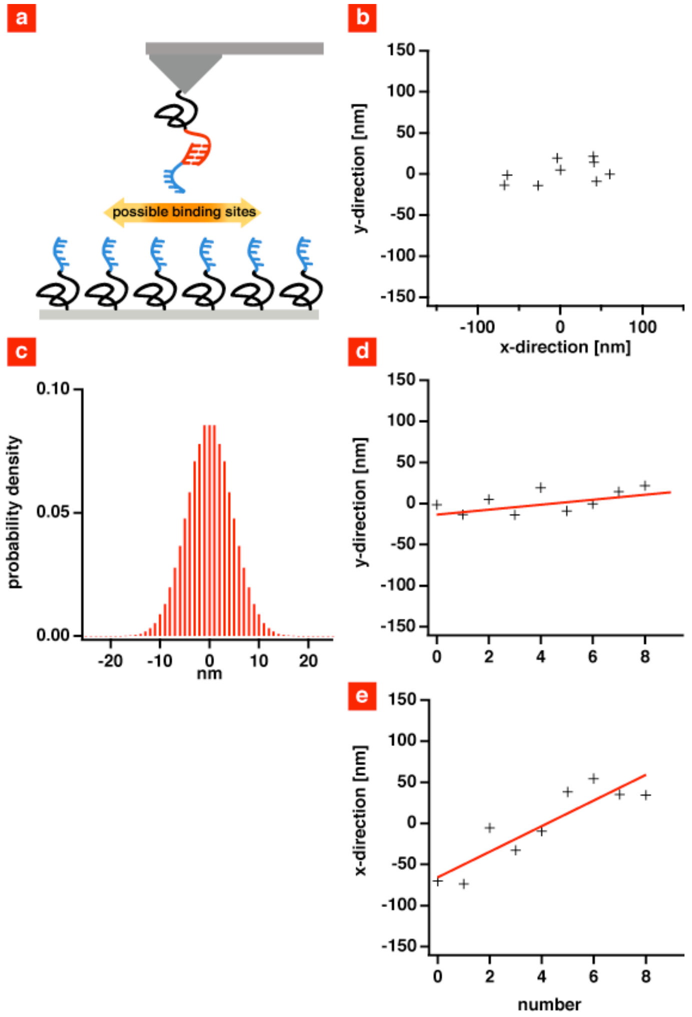

**Figure 3** **Long term drift and position accuracy of the SMCP process.** (a) The tip of an AFM cantilever was covalently modified with a PEG-DNA complex to pick up transfer DNA strands. The substrate was also covalently modified with PEG-DNA complexes. (c) The probability density for the transfer DNA to find a certain anchor DNA is determined by a search process of the partners and could be calculated using a simple theoretical model. (b) To measure the position uncertainty, several single transfer DNA molecules were successively deposited on the same site of an image. The spatial uncertainty of the positions is comprised of both the SMCP process itself and the spatial drift of the setup. (d and e) The x- and y-positions of the deposited molecules are plotted against the number of the deposition event. A movie was recorded after each deposition process. To estimate the long term stability 5 minutes time intervals between subsequent depositions were chosen and the complete experiment lasted for about 45 minutes. During this time the experimental setup drifts laterally in the x- and y-directions. An estimate of the spatial uncertainty of the SMCP process itself can be obtained by subtracting the drift and is given by ±11 nm.

Experimentally, the SMCP precision and the long-term stability of the setup were determined as follows. Several single-molecules were successively deposited at different positions on the target area. However, since only the sample was moved, the position of the deposited molecules relative to the optical axis of the instrument remained constant. For each deposition process a movie was recorded, and the positions of the pasted molecules were determinated as described above. The positions of nine single fluorophores deposited in this way in intervals of five minutes are shown in Fig. 3b. The spatial uncertainty of the experiment presented in Fig. 3b is comprised first of the SMCP process itself but also by spatial drift of the setup. In Fig. 3d and e the x- and y-coordinates are plotted against the number of the deposition event. Both plots clearly show a systematic and correlated drift. The drift in this particular example, which was chosen to highlight the advantage of our procedure to isolate potential artifacts, is mainly caused by temperature drift of the measurement system. An estimate of the SMCP process itself can be given by subtracting the drift (see lines in Fig. 3d and e) resulting in a precision of the y-position of ±11 nm. Under the given conditions of spacer length and anchor density this value can be seen as a benchmark for the deposition precision.

This value agrees well with the predictions of the simple model depicted in Fig 3a and c. Here we assumed the probability for the transfer oligomer to find an anchor oligomer while approaching the surface to be determined by a search process of the partners, both of which are constrained to the surface by PEG spacers. Provided the approach is slow compared to the search process, the area that the oligomers sample prior to finding a partner will depend on the functionalization density, the oligomer length and the end-to-end distance of the spacers. The nearly Gaussian distribution given in Fig 3c is the result of the calculation given in the supplement.

In order to demonstrate the possibility to assemble and resolve pattern comprised of several single fluorophores we pasted six spots with a distance of 1 $\mu$m (Fig. 4a). Each spot was assembled in nine SMCP cycles as sketched in Fig. 4a. However, on average only in every second attempt a fluorophore was deposited. The goal was to identify the location of the pasted molecules by optical means. The intensity time trace of the 16 pixel sized diffraction limited spot #4 is shown in Fig. 4b. The stepwise decay with an exponential envelope is a clear indication for uncorrelated subsequent single fluorophore photobleaching. This stepwise decay of the overall intensity is also seen in the sequence of images in Fig. 4c. This sequence also contains the positional information. We used the sequential photobleaching of the fluorophores to discriminate between them in the following way. The last plateau stems from the last single fluorophore. Therefore the centroid of the corresponding image gives its position. The second to last plateau stems from the last and the second to last fluorophore. We subtracted the image of the last plateau from the image corresponding to the second plateau. The remaining fluorescence distribution must stem from the second to last fluorophore; its centroid was determined. With this iterative analysis we determined the position of the remaining fluorophores (Fig. 4d). As can be seen in Fig. 4e, the measured positions agree well with the expected positions in the assembly pattern. As can also be seen, the size of the error bars increases with decreasing lifetime of the fluorophore. We therefore restricted our quantitative analysis to the last 4 molecules. Nevertheless the precision of the localization of the pasted molecules within the diffraction limited ensemble by means of SRI turned out to be as good as ±12 nm.

In summary, we have demonstrated that SMCP surface assembly combined with SRI allows monitoring of the deposition process of single fluorophores in real time and determination of the position of the deposited molecules with nanometer precision. The precision of the SMCP process was determined to ±11 nm. This value could be improved considerably by using shorter spacers and by an optimized system of unbinding forces, e.g. by employing covalent anchor chemistry in the target area. In doing so, patterns of arbitrary shape and with arbitrary numbers of single-molecules can be created. Such patterns could be used as test systems for novel SRI techniques but could also help to investigate dye-dye interactions in a very controlled manner. While in this study we have not exploited the potential to assemble different fluorophores in well-defined pattern and to analyze their resulting spectral properties, such investigations are feasible and expected to shead new light on the interaction among fluorophores but also between dye molecules and photonic nanostructures or optically active nanoparticles[18].

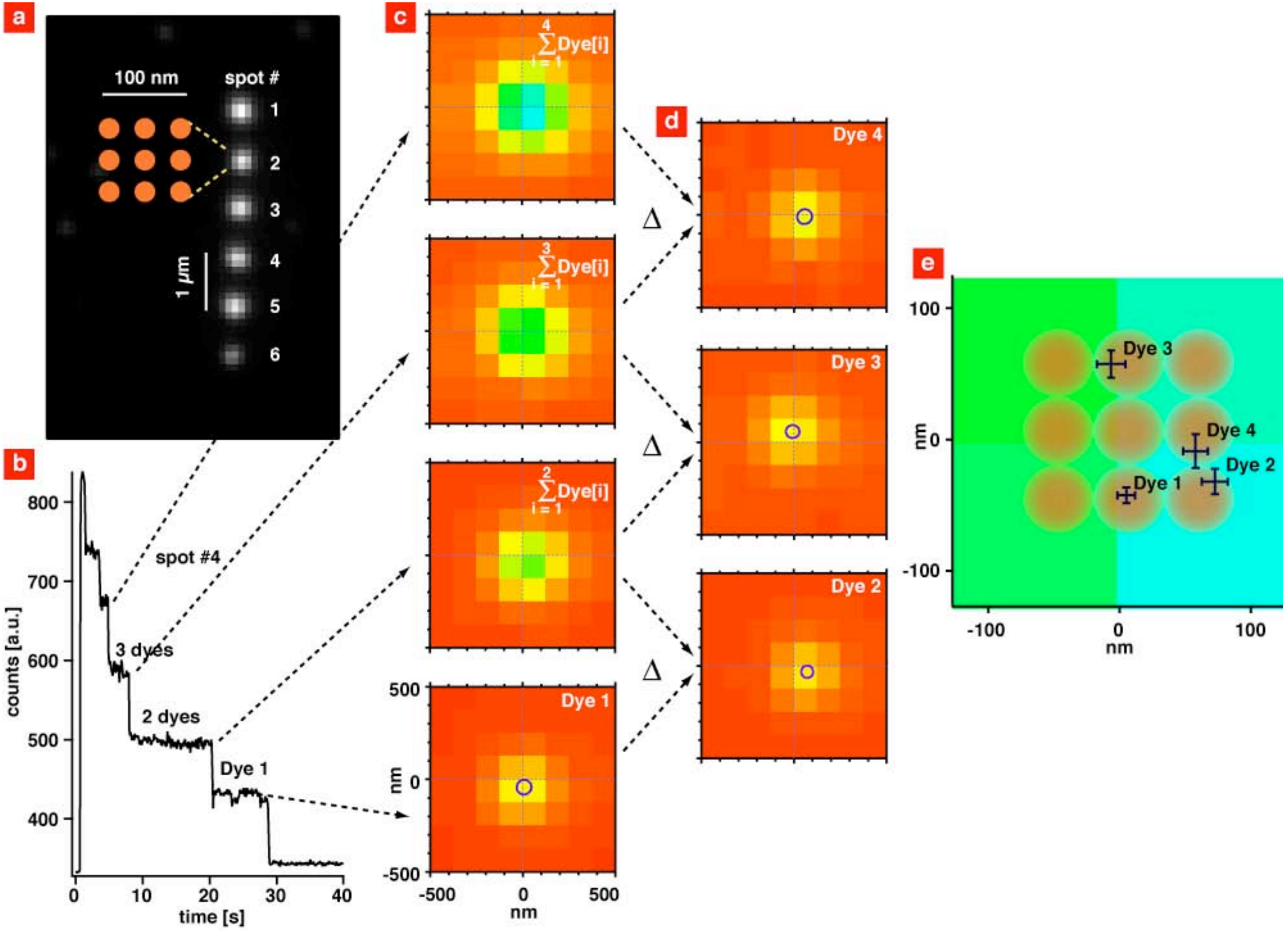

**Figure 4** **Super-resolution imaging with photobleaching.** (a) Fluorescence micrograph of a pattern consisting of six spots with a distance of 1 µm. Each spot was assembled with nine single-molecule cut-and-paste cycles and deposited as sketched in the inset. (b) Intensity time trace of the diffraction limited spot #4. During excitation the Cy3 labels photobleach and show the typical stepwise decay of single fluorophores. After 20 s only one dye is left. (c) Average intensity images were calculated for periods of constant signal. (d) Subsequent images were subtracted to determine the intensity of the photobleached fluorophores, and 2d Gaussians were fit to each image. The positions of the four dyes are shown in (e). The circles indicate the nine single-molecule cut-and-paste deposition sites, and their size indicates the uncertainty of the deposition.

## METHODS

### SAMPLE-PREPARATION

Depot and target areas were prepared on a cover slip as described in[11]. Briefly, cover slips were amino functionalized and covalently modified with NHS-PEG-maleimide (M = 5000 g/mol, Nektar, Huntsville, Alabama, USA). After rinsing with $H_2O$, a PDMS flow chamber with two channels was mounted on one cover slip. Both channels were connected to a peristaltic pump. The anchor oligomers for the depot and target area were reduced using TCEP solution (Pierce, Rockford, Illinois, USA) in order to generate free mercaptans. The left channel (depot area) was rinsed for 1 h with a 10-µM solution of depot anchor oligomers and the right one (target area) with a 10-µM solution of target anchor oligomers. Afterwards both channels were rinsed with $H_2O$ to remove all non-covalently bound oligomers. The left channel (depot area) was rinsed with a 1-µM solution of transfer DNA dissolved in saline sodium citrate (SSC) buffer (150 mM NaCl, 15 mM sodium citrate, pH 7) for 1 h. All oligomers used in this study were synthesized form IBA (IBA GmbH, Göttingen, Germany) and of HPLC-grade. After rinsing the depot channel for 5 min with SSC buffer to remove all non-hybridized transfer DNA, the PDMS flow chamber was removed and the cover slip was dried in a nitrogen stream. Finally the cover slip was mounted to the AFM-TIRF sample holder and immersed in SSC buffer.

### TOTAL INTERNAL REFLECTION FLUORESCENCE (TIRF) MICROSCOPE

Single-molecule fluorescence microscopy was carried out in TIRF excitation. Fluorescence excitation of the Cy3 dyes is performed by a 532 nm, 75 mW DPSS laser (Crystalaser, Nevada, USA) through a 100x/1.49 oil immersion objective lens (Nikon CFI Apochromat TIRF, Japan), where the collimated laser beam is focused in the back focal plane of the objective lens such that the beam is totally reflected at the cover slip. Fluorescence light is split by color with a commercial Dual View (Optical Insights, Arizona, USA) with Brightline HC 582/75 (Semrock, New York, USA) and ET 700/75 (Chroma, Vermont, USA) as emission filters for the green and red channel respectively and a dichroic mirror with a cut-off wavelength of 630 nm (630DCLP). The emitted light is detected by a 512 x 512 pixel back-illuminated EMCCD camera (DU-897, Andor, Belfast, Ireland). Time series where recorded in frame-transfer mode with an integration time of 100 ms per frame. The EMCCD chip was typically operated at a temperature of -75°C and an electron multiplication gain of 300x was used. The magnification was 96, i.e. 125 nm are imaged to one pixel.

## AFM MEASUREMENTS

All SCMP experiments were performed with a custom build AFM[19] at room temperature in SSC buffer. Silicon nitride cantilevers (MLCT-AUHW, Veeco Probes, Camarillo, California, USA) were amino functionalized and covalently modified with NHS-PEG-maleimide (M = 5000 g/mol, Nektar, Huntsville, Alabama, USA) as described in[20]. The spring constant of the DNA modified cantilever was calibrated in solution using the equipartition theorem[21, 22]. This method yielded a spring constant of 12.9 pN/nm and a resonance frequency of 1.24 kHz for the cantilever used in this study. The tip was withdrawn from the surface at a speed of 1500 nm/s until it was 2 µm above the surface. The protocol for the SMCP as well as the data recording was programmed using Igor Pro 5.03 (Wave Metrics, Lake Oswego, Oregon, USA). An Asylum Research controller, which provides ADC and DAC channels as well as a DSP board, was used for setting up feedback loops. Cantilever positioning for pickup and delivery was controlled in closed-loop operation. The precision was set to ±4 nm.

## DATA-ANALYSIS

Fluorescence images were analyzed with Igor Pro 6.01 (Wave Metrics, Lake Oswego, Oregon, USA). Intensity time traces were produced by calculating the average intensity over 4 x 4 pixels in every frame. Centroid localization of a single-molecule was performed by fitting a 2d Gaussian distribution to a 11 x 11 pixel sized diffraction limited image. For localizing the positions of each fluorophore within a cluster, the individual contributions to the intensity images were extracted as follows: An average intensity image was calculated for every period of constant signal. Then subsequent images were subtracted form each other and the differences display the average intensities of the contributing fluorophores. The positions of the fluorophores were again determined by fitting 2d Gaussians.

## REFERENCES

1. Betzig, E. & Trautman, J.K. Near-Field Optics: Microscopy, Spectroscopy, and Surface Modification Beyond the Diffraction Limit. Science 257, 189-195 (1992).
2. Xie, X.S. & Dunn, R.C. Probing Single Molecule Dynamics. Science 265, 361-364 (1994).
3. Hell, S.W. & Wichmann, J. Breaking the diffraction resolution limit by stimulated emission: stimulated-emission-depletion fluorescence microscopy. Opt. Lett. 19, 780 (1994).
4. Lacoste, T.D. et al. Ultrahigh-resolution multicolor colocalization of single fluorescent probes. Proceedings of the National Academy of Sciences 97, 9461-9466 (2000).
5. Dyba, M. & Hell, S.W. Focal Spots of Size lambda /23 Open Up Far-Field Florescence Microscopy at 33 nm Axial Resolution. Physical Review Letters 88, 163901 (2002).
6. Gordon, M.P., Ha, T. & Selvin, P.R. Single-molecule high-resolution imaging with photobleaching. Proceedings of the National Academy of Sciences 101, 6462-6465 (2004).
7. Qu, X., Wu, D., Mets, L. & Scherer, N.F. Nanometer-localized multiple single-molecule fluorescence microscopy. Proceedings of the National Academy of Sciences 101, 11298-11303 (2004).
8. Churchman, L.S., Okten, Z., Rock, R.S., Dawson, J.F. & Spudich, J.A. Single molecule high-resolution colocalization of Cy3 and Cy5 attached to macromolecules measures intramolecular distances through time. Proceedings of the National Academy of Sciences 102, 1419-1423 (2005).
9. Rust, M.J., Bates, M. & Zhuang, X. Sub-diffraction-limit imaging by stochastic optical reconstruction microscopy (STORM). Nat Meth 3, 793-796 (2006).
10. Betzig, E. et al. Imaging Intracellular Fluorescent Proteins at Nanometer Resolution. Science 313, 1642-1645 (2006).
11. Kufer, S.K., Puchner, E.M., Gumpp, H., Liedl, T. & Gaub, H.E. Single-Molecule Cut-and-Paste Surface Assembly. Science 319, 594-596 (2008).
12. Bobroff, N. Position measurement with a resolution and noise-limited instrument. Review of Scientific Instruments 57, 1152-1157 (1986).
13. Thompson, R.E., Larson, D.R. & Webb, W.W. Precise Nanometer Localization Analysis for Individual Fluorescent Probes. Biophys. J. 82, 2775-2783 (2002).
14. Ober, R.J., Ram, S. & Ward, E.S. Localization Accuracy in Single-Molecule Microscopy. Biophys. J. 86, 1185-1200 (2004).
15. Yildiz, A. et al. Myosin V Walks Hand-Over-Hand: Single Fluorophore Imaging with 1.5-nm Localization. Science 300, 2061-2065 (2003).
16. Tinnefeld, P. & Sauer, M. Branching Out of Single-Molecule Fluorescence Spectroscopy: Challenges for Chemistry and Influence on Biology. Angewandte Chemie International Edition 44, 2642-2671 (2005).
17. Gaiduk, A., Kühnemuth, R., Antonik, M. & Seidel, C.A.M. Optical Characteristics of Atomic Force Microscopy Tips for Single-Molecule Fluorescence Applications. ChemPhysChem 6, 976-983 (2005).
18. Bek, A. et al. Fluorescence Enhancement in Hot Spots of AFM-Designed Gold Nanoparticle Sandwiches. Nano Lett. 8, 485-490 (2008).
19. Kühner, F., Lugmaier, R., Mihatsch, S. & Gaub, H.E. Print your atomic force microscope. Rev. Sci. Instrum. 78 (2007).
20. Morfill, J. et al. B-S Transition in Short Oligonucleotides. Biophys. J. (2007).
21. Florin, E.L. et al. Sensing specific molecular interactions with the atomic force microscope. Biosensors and Bioelectronics 10, 895-901 (1995).
22. Butt, H.-J. & Jaschke, M. Calculation of thermal noise in atomic force microscopy. Nanotechnology 6, 1-7 (1995).

## ACKNOWLEDGEMENTS

We thank P. Tinnefeld and A. Fornof for helpful discussions. This work was supported by the German Science Foundation and the Nanosystems Initiative Munich and FuNS.

# Supplementary information

# Optically monitoring the mechanical assembly of single molecules

Stefan K. Kufer[1], Mathias Strackharn[1], Stefan W. Stahl[1], Hermann Gumpp[1], Elias M. Puchner[1,2] and Hermann E. Gaub[1*]

## Hierarchical force system for SMCP:

The probe of an atomic force microscope (AFM) was used to assemble individual single stranded DNA (ssDNA) oligomers carrying dye molecules one by one in aqueous solutions at room temperature. The oligomers were stored on well-defined depot areas, picked up with the tip of an AFM cantilever and reassembled with nanometer precision on a spatial distinct target area. The storage, the pick up and the deposition of the DNA oligomers were realized by using an ordered system of unbinding forces based on DNA interactions.

The dissociation rates of DNA duplexes under load are highly dependent of loading geometries and DNA sequences respectively[1, 2]. When the duplex is stretched along its molecular axis, this means that the DNA duplex is loaded at opposite 5’ ends or 3’ ends, respectively, one speaks of “shear mode”[1] (Fig. S1e). The topological arrangement when double strands are loaded by pulling on the 5’ and 3’ extremities of one end of the duplex is called “unzip mode”[3] (Fig. S1a). These two geometries are well distinguishable concerning their dissociation properties under load.

The rupture forces for DNA duplexes loaded in unzip mode are independent both of the length of the DNA oligomer and the loading rate, but vary for G-C and A-T interactions. G-C pairing results in a dissociation force of roughly 20 pN whereas A-T gives rise to roughly 10 pN[2]. The dissociation forces for DNA duplexes loaded in shear geometry depend both on the length and the loading rate[1].

To connect the transfer DNA to the depot a 30 base pair (bp) long anchor sequence with mixed G-C and A-T is used (Fig. S1a). The transfer DNA has in addition to this 30 bp anchor sequence a 20 bp handle sequence for pick up. The AFM-tip is covalently modified with a ssDNA strand. Since this strand is complementary to the handle sequence a duplex is formed as the tip approaches the depot area (Fig. S1b). Then the tip is retraced from the depot the anchor sequence is loaded in unzip mode whereas the handle sequence in shear mode. Although the 30 bp anchor sequence is longer than the 20 bp handle sequence, its unbinding probability under load is much higher than for the handle sequence and the transfer DNA is picked up (Fig. S1c).

---

[1] Center for Nanoscience & Physics Department, University Munich, Amalienstr. 54, 80799 Munich
[2] Center for Integrated Protein Science Munich
[*] E-mail: Gaub@LMU.de

After translocation of the transfer DNA to its target site the cantilever is lowered towards the surface. Since the target area is covalently modified with ssDNA oligomers that are complementary to the anchor sequence a 30 bp duplex in shear geometry is formed (Fig S1d). As the dissociation force of duplexes in shear geometry depends on the length of the DNA sequence the shorter handle sequence ruptures first and the transfer DNA is attached to the target site (Fig. S1e). It was shown[4] that a length difference of 10 base pairs (bp) is sufficient to make the rupture of the shorter handle duplex more likely by one order of magnitude than the rupture of the longer anchor duplex. The DNA sequences of the oligomers used in this study are shown in Fig. S2. The experimental setup for the SMCP process is shown in Fig. S3.

**Calculation of the SCMP lateral uncertainty:**

For an estimation of lateral uncertainty the total construct consisting of the transfer DNA attached to the cantilever DNA that again is bound to the tip by a PEG spacer was treated in the model of the freely jointed chain (FJC) as one polymer with the effective Kuhn length $b_{eff}$, where $b_{eff}$ was obtained by calculating the weighted average Kuhn length of the three sequences. The weighting coefficients are for each sequence respectively the ratio of sequence contour length to the contour length of the total construct:

$$b_{eff} = \frac{l_{PEG}}{l_{tot}} b_{PEG} + \frac{l_{dsDNA}}{l_{tot}} b_{dsDNA} + \frac{l_{ssDNA}}{l_{tot}} b_{ssDNA},$$

with $l_i$ the contour lengths and $b_i$ the Kuhn lengths. The effective number of Kuhn monomers is then given by $N_{eff} = \frac{l_{tot}}{b_{eff}}$.

The FJC model[5] predicts the distribution of end-to-end distances along each axis as

$$P(x_i) = \sqrt{\frac{3}{2\pi N_{eff} b_{eff}^2}} \exp\left(-\frac{3x_i^2}{2N_{eff} b_{eff}^2}\right).$$

As for the estimation of the binding probability $P_{binding}$ , we assume that the approach of the tip to the surface is faster then the polymer fluctuations. In this case every conformation in the lower half-space contributes to the binding probability, such that the binding probability along the x-axis when the molecule approaches the surface in z-direction corresponds to

$$P_{binding}(x) = \frac{1}{A_{norm}} P(x) \int_{-\infty}^{0} P(z) dz = P(x),$$

where the normalization constant $A_{norm}$ equals the definite integral because of the normalized function $P(x)$. So the binding probability is described by the Gaussian function $P(x)$.

It is worth stressing the fact that if the approach of the tip is slow compared to the polymer fluctuations the binding probability shrinks to a point like distribution. This is because of the fact that if the tip is approached to a distance that is in the range of the contour length of the polymer, it will bind preferred in the projection point of the tip. That means that the calculated distribution above is the worst case that could happen.

We testet that simple model by simulating the polymer as freely jointed chain with the parameters $b_{PEG}$=1.1 nm[5], $N_{PEG}$=27[6], $b_{ssDNA}$=1.5 nm[7] and $N_{DNA}$=8[7], and $N_{dsDNA}$=1 and

$b_{dsDNA}$=6.8 nm[7]. Fig. S4 shows that the simulation and the FJC model do match in a satisfactory manner.

## References:

1. Strunz, T., Oroszlan, K., Schafer, R. & Guntherodt, H.J. Dynamic force spectroscopy of single DNA molecules. *Proceedings of the National Academy of Sciences of the United States of America* **96**, 11277-11282 (1999).
2. Rief, M., Clausen-Schaumann, H. & Gaub, H.E. Sequence-dependent mechanics of single DNA molecules. *Nat Struct Biol* **6**, 346-349 (1999).
3. Levinthal, C. & Crane, H.R. On the Unwinding of DNA. *PNAS* **42**, 436-438 (1956).
4. Albrecht, C. et al. DNA: A Programmable Force Sensor. Science 301, 367-370 (2003).
5. Rubinstein, R.H.C. Polymer Physics. *Oxford University Press* (2005).
6. Oesterhelt, F., Rief, M. & Gaub, H.E. Single molecule force spectroscopy by AFM indicates helical structure of poly(ethylene-glycol) in water. *New Journal of Physics* **1** (1999).
7. Smith, S.B., Cui, Y.J. & Bustamante, C. Overstretching B-DNA: The elastic response of individual double-stranded and single-stranded DNA molecules. *Science* **271**, 795-799 (1996).

**Figures:**

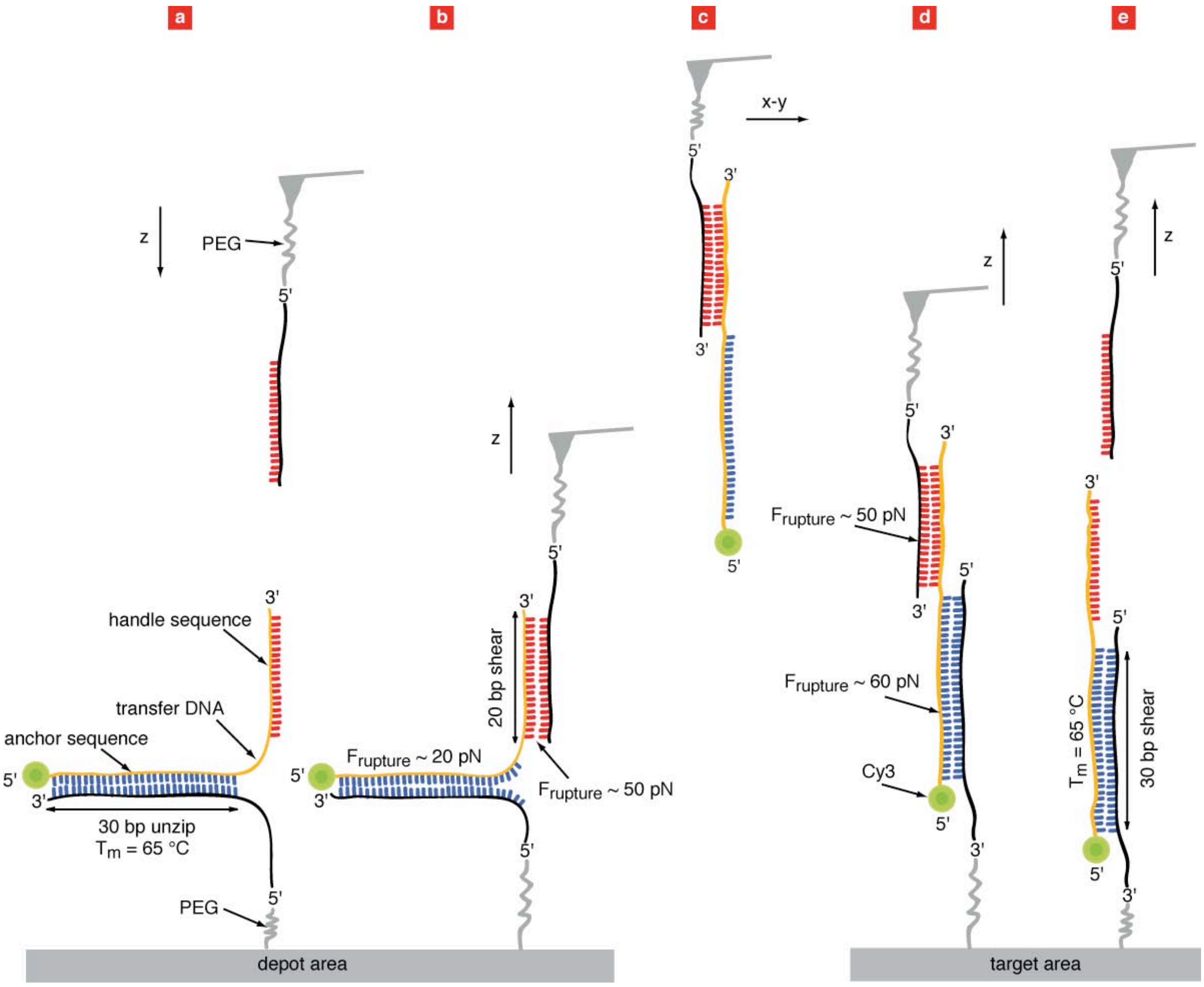
a
b
c
d
e
z
PEG
5'
3'
handle sequence
transfer DNA
anchor sequence
5'
3'
30 bp unzip
$T_m$ = 65 °C
PEG
5'
depot area
z
5'
3'
20 bp shear
5'
$F_{rupture}$ ~ 20 pN
3'
$F_{rupture}$ ~ 50 pN
5'
x-y
5'
3'
3'
5'
z
5'
3'
$F_{rupture}$ ~ 50 pN
3'
5'
$F_{rupture}$ ~ 60 pN
Cy3
5'
3'
target area
z
5'
3'
5'
$T_m$ = 65 °C
30 bp shear
5'
3'

**Fig. S1.** Schematic illustration of the hierarchical force system. (a) To prevent unspecific adsorption, polyethylenglycol (PEG) molecules are covalently attached to the target area. DNA oligomers, complementary to the anchor sequence of the transfer DNA, are covalently bonded with their 5' end to these PEG molecules. Transfer DNA oligomers, which were modified with Cy3 labels on the 5' end, are hybridized to this anchor sequences. The tip of an AFM cantilever is also covalently modified with PEG molecules and a single DNA oligomer, which is complementary to the handle sequence of the transfer DNA, is bonded covalently with its 5' end to a PEG molecule. (b) When the tip is brought into contact with the surface a duplex between the transfer DNA and the cantilever DNA is formed. When the tip is retracted the anchor sequence is loaded in unzip mode and the handle sequence in shear mode. As the unbinding probability for the anchor sequence is higher, the transfer DNA is picked up. (c and d) The target site is also covalently modified with PEG molecules. DNA oligomers, complementary to the anchor sequence of the transfer DNA, are bonded with their 3' end to the PEG molecules. After translocation the tip is moved down and a duplex is formed. When the tip is retracted the handle and the anchor sequences are loaded in shear mode, but this time the shorter handle sequence ruptures first and the transfer DNA is attached to its target site. The tip is now in its initial state and the cycle could be repeated over and over again.

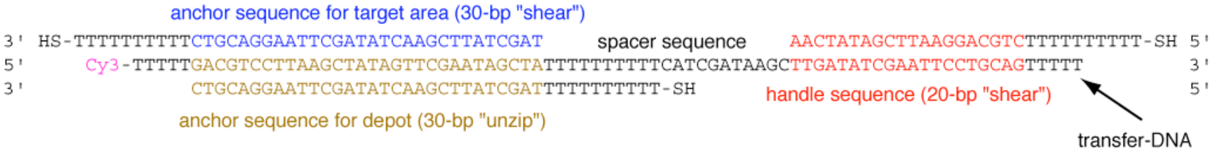
anchor sequence for target area (30-bp "shear")
3' HS-TTTTTTTTTTCTGCAGGAATTCGATATCAAGCTTATCGAT
spacer sequence
AACTATAGCTTAAGGACGTCTTTTTTTTTT-SH 5'
5' Cy3-TTTTTGACGTCCTTAAGCTATAGTTCGAATAGCTATTTTTTTTTTCATCGATAAGCTTGATATCGAATTCCTGCAGTTTTT 3'
3' CTGCAGGAATTCGATATCAAGCTTATCGATTTTTTTTTTT-SH
handle sequence (20-bp "shear")
5'
anchor sequence for depot (30-bp "unzip")
transfer-DNA

**Fig. S2.** Oligomers used in this study. The transfer DNA is 80 bp long and has a Cy3 label on the 5' end. The 30 bp long sequence on the 5' end is used to anchor the transfer DNA both to the depot and to the target site. The 20 bp long sequence on the 3' end is used as a handle for pick up. All oligomers were synthesized and purified (HPLC-grade) form IBA (IBA GmbH, Göttingen, Germany).

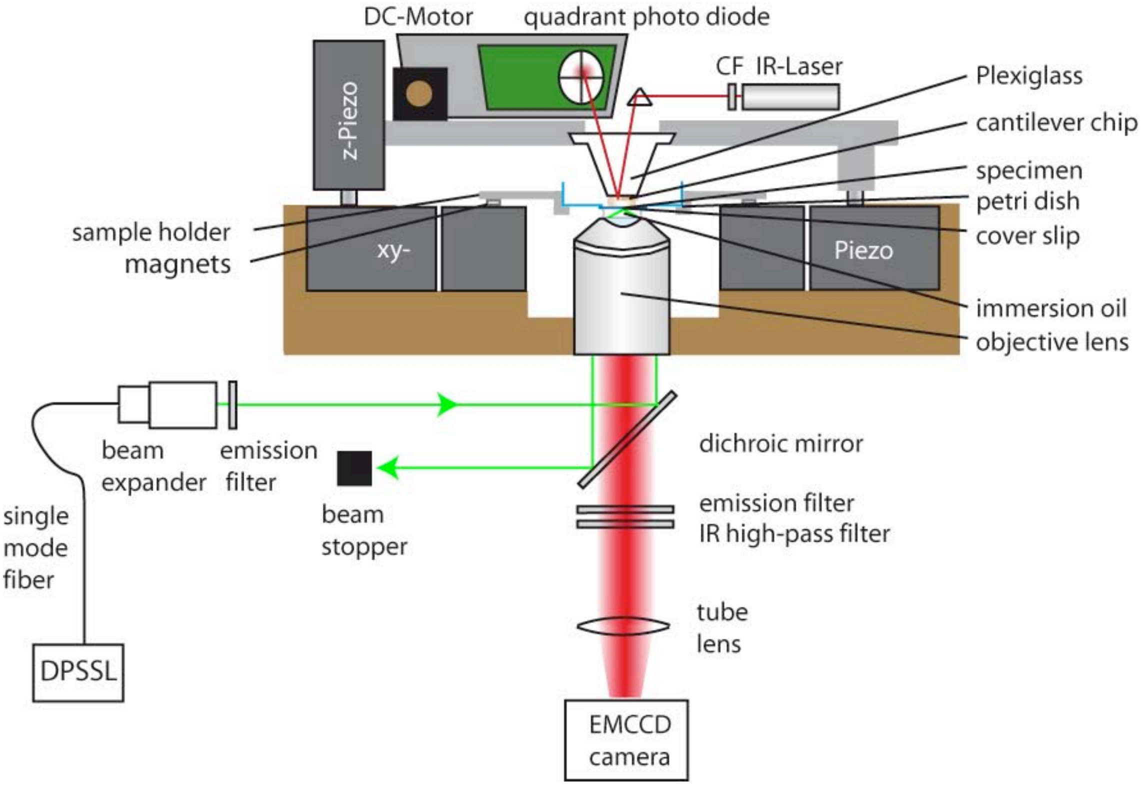
DC-Motor
quadrant photo diode
CF IR-Laser
z-Piezo
Plexiglass
cantilever chip
specimen
petri dish
cover slip
sample holder
magnets
xy-
Piezo
immersion oil
objective lens
beam expander
emission filter
dichroic mirror
beam stopper
emission filter
IR high-pass filter
single mode fiber
tube lens
DPSSL
EMCCD camera

**Fig. S3.** Experimental setup. A custom built AFM head, which is actuated in z direction via a piezo, is combined with an inverted microscope for objective-type wide-field TIRF excitation. The cover slip with the depot- and target areas on top is glued into a bored petri dish. The petri dish is placed in a sample holder, which is fixed through magnets on x-y piezo scanner.

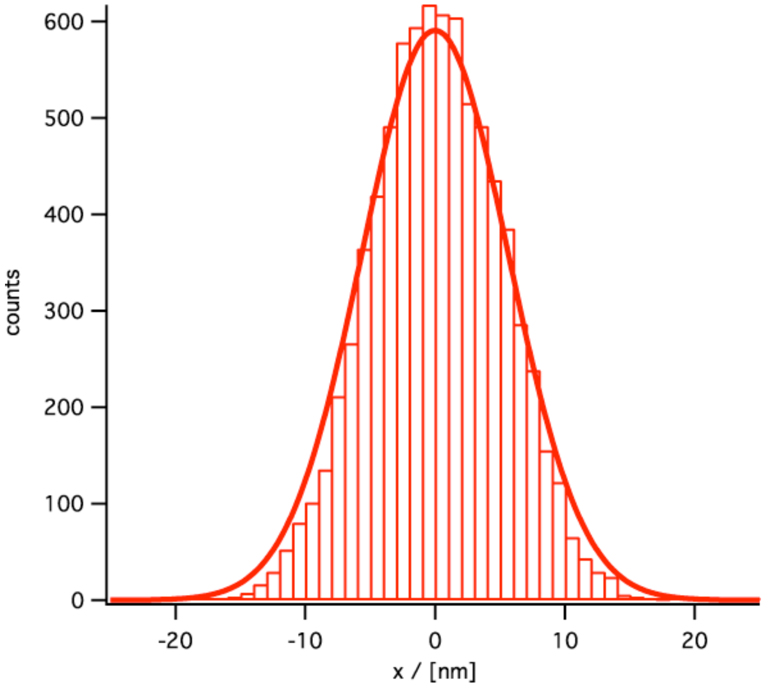

**Fig. S4.** The end position of the end-to-end vector obtained by simulation of the conjugated polymer in FJC model is shown as histogram, the thick line describes shows the distribution according to the FJC model using an effective Kuhn length an effective monomer number.

NANO
LETTERS

XXXX
Vol. xx, No. x
-

# Nanoparticle Self-Assembly on a DNA-Scaffold Written by Single-Molecule Cut-and-Paste

**Elias M. Puchner,[†,‡] Stefan K. Kufer,[†] Mathias Strackharn,[†] Stefan W. Stahl,[†] and Hermann E. Gaub*,[†]**

*Chair for Applied Physics, Center for Nanoscience and Center for Integrated Protein Science Munich, Ludwig-Maximilians-Universität Munich,*
*Amalienstrasse 54, 80799 Munich*

*Received June 27, 2008; Revised Manuscript Received September 16, 2008*

## ABSTRACT

**Self-assembly guided by molecular recognition has in the past been employed to assemble nanoparticle superstructures like hypercrystals or nanoparticle molecules. An alternative approach, the direct molecule-by-molecule assembly of nanoscale superstructures, was demonstrated recently. Here we present a hybrid approach where we first assemble a pattern of binding sites one-by-one at a surface and then allow different nanoparticles to attach by self-assembly. For this approach, biotin bearing DNA oligomers were picked up from a depot using a cDNA strand bound to an AFM tip. These units were deposited in the target area by hybridization, forming a recognition pattern on this surface. Fluorescent semiconductor nanoparticles conjugated with streptavidin were allowed to assemble on this scaffold and to form the final nanoparticle superstructures.**

Two fundamentally different strategies, commonly referred to as top-down or bottom-up, are feasible for the assembly of functional nanosystems. The bottom-up approach has two extremes. In the first, the building blocks are allowed to self-assemble, for example, guided by molecular recognition, much in the way mother nature does in embryogenesis.[1−7] Alternatively, the building blocks are assembled one-by-one, for example, using the tip of a scanning probe microscope, as we have demonstrated recently.[8,9] With the single-molecule cut-and-paste (SMCP) approach, we combine the precision of an AFM[10−12] with the selectivity of the DNA interaction. The units to be assembled, here biotin, are picked up with an AFM tip from a depot, where both the interaction of the unit with the depot surface as well as with the tip are mediated by specific DNA oligomers. Also the target area is covered with DNA oligomers. The interaction forces are chosen by binding geometry and by sequence such that the unit is first transferred from the depot to the tip and then from the tip to the target, allowing for a cyclic operation and thus the assembly of complex patterns of units. In this study, we have merged these two very successful strategies of self- and one-by-one assembly. We combined molecule-by-molecule assembly of patterns of binding sites with the self-assembly of nanoparticles[13] guided by specific molecular interactions to the scaffold.

The surface assembly process of the binding scaffold is schematically depicted in Figure 1. Both depot and target areas were functionalized with DNA anchor oligomers capable of hybridizing with the so-called transfer DNA via a 30 basepair (bp) DNA sequence. In the depot area, the anchor oligomers are covalently attached with the 5′ end and in the target area with the 3′ end. The depot area was then loaded with the transfer DNA, which is used as a carrier for the binding site for the nanoparticles, in this case biotin. The transfer DNA is designed such that it hybridizes at its 5′ end with the anchor sequence and has a 20 bp overhang at the 3′ end. An AFM cantilever was covalently functionalized with a 20 bp DNA oligomer complementary to the overhang sequence. This cantilever was carefully lowered toward the depot surface allowing the tip oligomer to hybridize with the transfer DNA. This approach had been either stopped upon surface contact or alternatively, proximity had been detected by increased viscous damping of the tip vibrations. Typical force extension traces of this contact and noncontact pick up are shown in the Supporting Information (Figure S4).

Upon withdrawing the tip from the surface, the force that is built up in the molecular complex propagates through the two oligomers with the different geometries. Whereas the anchor duplex is loaded in unzip geometry, the tip duplex is loaded in shear geometry. As has been shown, the unbinding forces for these two configurations under load differ signifi-

---

* To whom the correspondence should be addressed. Email: gaub@lmu.de.
[†] Chair for Applied Physics, Munich.
[‡] Center for Integrated Protein Science, Munich.

10.1021/nl8018627 CCC: $40.75 © XXXX American Chemical Society
Published on Web 10/01/2008

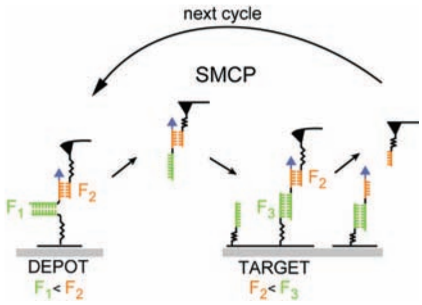

**Figure 1.** Schematics of the SMCP process. The transfer DNA oligomers carry biotin as the functional binding site (blue). They are stored in the depot area through specific DNA hybridization (30 bp, green) to the covalently immobilized depot anchor oligomer in the zipper geometry. The overhanging sequence of the transfer DNA is complementary to a 20 bp sequence, which is covalently attached to a tip of an AFM cantilever. When the cantilever is brought into contact with the surface, a 20 bp duplex (yellow) in shear geometry is formed. Although the binding energy of the transfer DNA to the depot is higher, the unbinding force $F_1$ is lower than the unbinding force $F_2$ between the tip and the transfer DNA due to the different unbinding geometries (zipper vs shear). Therefore, the transfer DNA remains on the tip sequence upon retraction of the cantilever. The tip is then moved to the target area with nm-precision and again brought into contact with the surface. Here the free part of the transfer DNA hybridizes to the 30 bp target sequence in shear mode. Since its rupture force $F_3$ is the highest, the transfer DNA including its functional unit biotin remains on the target site when removing the cantilever. Having transferred one functional unit in this way, the tip sequence is free again for the next cut-and-paste cycle.

cantly.[14,15] The rationale behind this effect is that the mechanical work to overcome the binding energy is performed over paths of different length, resulting in different forces. Despite the higher thermodynamic stability of the 30 bp anchor duplex compared to the 20 bp tip duplex, the rupture probability for the anchor is higher by an order of magnitude than that of the tip duplex. For a quantitative analysis see ref 16. As a result, the transfer DNA with the functional unit biotin is now bound to the tip and may be transferred to the target area.

At the target site the tip is lowered again, allowing the transfer DNA to hybridize at the chosen position with an anchor oligomer. Now, due to the different attachment, both duplexes are loaded in shear geometry when the tip is withdrawn. The longer anchor oligomer keeps the transfer DNA bound, and the tip is free again and ready to pick up the next object. The efficiency of the cut-and-paste process depends both on the density of DNA oligomers and the tip size. It can be adjusted so that rarely more than one oligomer per cycle is picked up.[8] As a consequence of this low functionalization density no pick up occurs in the majority of the attempts. In this study, we have chosen a tip radius of about 20 nm (MLCT lever C, Veeco Instruments GmbH, Mannheim, Germany) and a high functionalization density so that in each cycle at least one molecule, and in most cases more than one molecule, was picked up and delivered. For a detailed description of this ordered system of unbinding forces and the experimental setup see the Supporting Information (Figure S2).

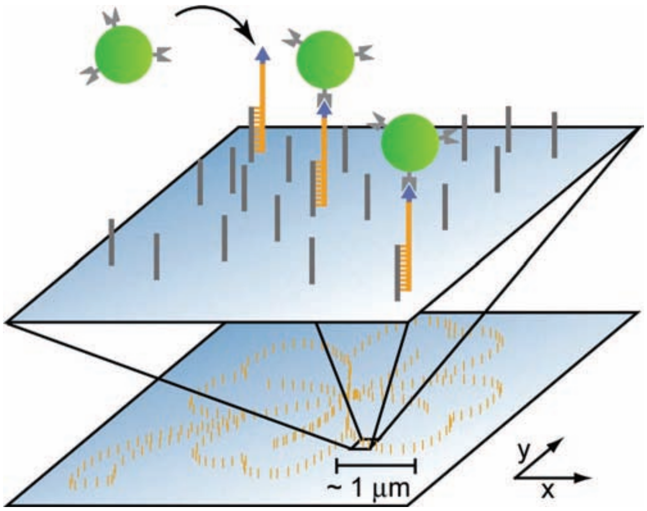

**Figure 2.** Sketch of the self-assembly of nanoparticles to a defined pattern guided by molecular recognition. SMCP allows the creation of DNA scaffolds of arbitrary shape and size. Here, a 5 $\mu$m sized pattern with the shape of a cloverleaf was created by transferring the biotin-modified transfer DNAs one-by-one to the target area. The spacing of binding sites was chosen to be 100 nm. In a second step this DNA scaffold allows for the self-assembly of streptavidin conjugated nanoparticles to form a superstructure.

All transfer steps are monitored online by force extension traces, which have clearly distinguishable fingerprints for each of the unzip or shear processes (see Supporting Information). If needed, each of the individual steps may be corrected or repeated. It should be pointed out here that this hierarchy of binding forces, which is the basis of this single-molecule cut-and-paste surface assembly (SMCP), may be established by a variety of interactions of physical, chemical, or biological nature. We chose DNA here since its properties are conveniently programmed by their sequence and binding geometry. It should also be mentioned that although the AFM potentially has sub-Angström positioning precision, the use of the polymeric spacers that we employ for the attachment of the DNA oligomers to the tip and the surface reduces this precision to the 10 nm range, which for our purposes is easily tolerable.

Following this protocol we now assembled a pattern of attachment points at the target site. We placed biotins 100 nm apart from each other along the outline of a cloverleaf. This is schematically shown in Figure 2. We then incubated the sample with a 500 pM solution of fluorescent nanoparticles (Qdots, streptavidin conjugate starter kit, Invitrogen, California) carrying an average of seven streptavidins, which recognize and selectively bind to biotin.[17] Although some spots of the written pattern may consist of more than one biotin because of the chosen high cut-and-paste efficiency, binding of more than one nanoparticle is unlikely because of their large size (about 20 nm) and their low concentration. We followed the binding process online by fluorescence microscopy in TIRF excitation. As can be seen in the picture series in Figure 3, the nanoparticles gradually assembled on the scaffold and finally decorated the outline of the cloverleaf. We encourage the reader to watch the movie of this nanoparticle attachment to the DNA scaffold published in

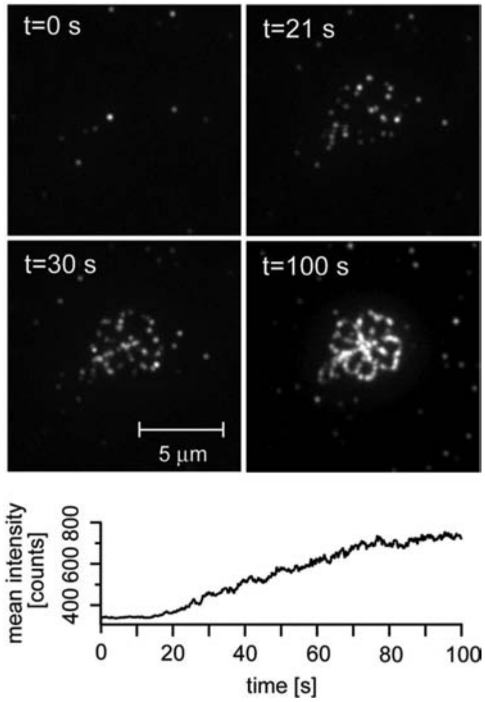

**Figure 3.** Time evolution of the nanoparticle superstructure formation. At time $t = 0$, streptavidin conjugated nanoparticles were incubated on the sample at a concentration of 500 pM. After approximately 20 s, the particles are close to the surface and start to specifically bind to the biotin-DNA scaffold until saturation is reached. The binding kinetics was followed by plotting the mean intensity of the observed area against the time (bottom). After 100 s the formation was completed.

the Supporting Information, as it demonstrates this process in a much clearer way.

This self-assembly process on the predefined scaffold is completed within minutes. Because of the specific binding between biotin and streptavidin and the low concentration of only 500 pM of the nanoparticles, nonspecific adhesion was negligible as can be seen in Figure 3. It is interesting to note that not all of the positions light up, although our transfer protocols corroborate that a biotin was deposited at these optical voids. A comparison of AFM images (not shown here) with the fluorescence images demonstrated that nanoparticles had bound at these positions. Obviously those nanoparticles had been optically inactive, a phenomenon that has been frequently described in the literature.[18,19]

For demonstration purposes, we rewrote the pattern in different sizes and allowed different nanoparticles to assemble on them (see Figure 4). Again a sizable fraction of the nanoparticles was optically inactive. In the assembly of the red pattern, thermal drift caused a slight distortion of the pattern, but even the scale bar could be trustfully assembled. Since for this study we always used the biotin−streptavidin interaction as the coupler, only single component structures were assembled. However, since a multitude of couplers with orthogonal affinities is available, the assembly of multicomponent structures would be straightforward.[20−23]

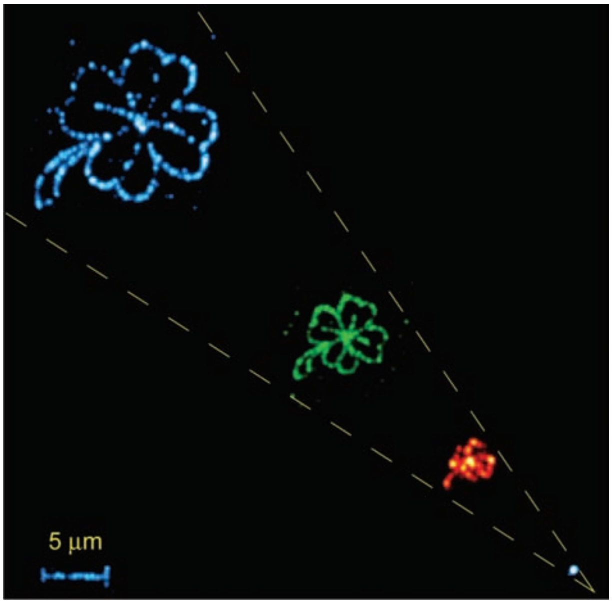

**Figure 4.** Nanoparticle superstructures of different sizes and compounds. To show the possibility to create freely programmable architectures from different compounds, the superstructure was scaled down and built with nanoparticles of different size. For the first cloverleaf (10 $\mu$m, blue), we used nanoparticles emitting at a wavelength of 525 nm, for the second one (5 $\mu$m, green) particles emitting at 565 nm, and for the third one (2.5 $\mu$m, red), already close to the limit of optical resolution, particles emitting at a wavelength of 705 nm. Please note that the 5 $\mu$m scalebar also represents a nanoparticle superstructure. The images are standard deviation maps of the recorded movies.

Nanoparticle self-assembly guided by specific molecular interactions has in the past been very successfully used to design complex structures with novel functions promising a rich field of new applications.[24−29] Here we have expanded this concept by a written scaffold and demonstrated that molecule-by-molecule assembly of a binding pattern combined with the self-assembly of semiconductor nanoparticles guided by molecular interactions is a straightforward and very general means to create nanoparticle superstructures.[30] Whereas the assembly of planar nanoparticle structures of arbitrary design can easily be assembled this way, an expansion into the third dimension appears challenging but achievable. Covalent cross-linking of the DNA oligomers after hybridization can be employed to stabilize the scaffold, and multifunctionality of the nanoparticles attachment sites may be used to build subsequent layers of structures. This could lead to a new dimension of complexity and novel effects.

**Acknowledgment.** We thank A. Fornof, H. Gumpp, H. Clausen-Schaumann, W. Parak, and P. Tinnefeld for helpful discussions. This work was supported by the German Science Foundation, FUNS, and the Nanosystems Initiative Munich (NIM).

**Note Added after ASAP Publication:** This paper was published ASAP on October 1, 2008. Author affiliations and Acknowledgment were updated. The revised paper was reposted on October 8, 2008.

**Supporting Information Available:** This material is available free of charge via the Internet at http://pubs.acs.org.

## References

(1) Park, S. Y.; Lytton-Jean, A. K. R.; Lee, B.; Weigand, S.; Schatz, G. C.; Mirkin, C. A. *Nature* **2008**, *451* (7178), 553–556.
(2) Shevchenko, E. V.; Ringler, M.; Schwemer, A.; Talapin, D. V.; Klar, T. A.; Rogach, A. L.; Feldmann, J.; Alivisatos, A. P. *J. Am. Chem. Soc.* **2008**, *130* (11), 3274.
(3) Nykypanchuk, D.; Maye, M. M.; van der Lelie, D.; Gang, O. *Nature* **2008**, *451* (7178), 549–552.
(4) Mirkin, C. A.; Letsinger, R. L.; Mucic, R. C.; Storhoff, J. J. *Nature* **1996**, *382* (6592), 607–609.
(5) Alivisatos, A. P.; Johnsson, K. P.; Peng, X. G.; Wilson, T. E.; Loweth, C. J.; Bruchez, M. P.; Schultz, P. G. *Nature* **1996**, *382* (6592), 609–611.
(6) Maye, M. M.; Nykypanchuk, D.; van der Lelie, D.; Gang, O. *Small* **2007**, *3* (10), 1678–1682.
(7) Mirkin, C. A. *Inorg. Chem.* **2000**, *39* (11), 2258–2272.
(8) Kufer, S. K.; Puchner, E. M.; Gumpp, H.; Liedl, T.; Gaub, H. E. *Science* **2008**, *319* (5863), 594–596.
(9) Duwez, A. S.; Cuenot, S.; Jerome, C.; Gabriel, S.; Jerome, R.; Rapino, S.; Zerbetto, F. *Nat. Nanotechnol.* **2006**, *1* (2), 122–125.
(10) Binnig, G.; Quate, C. F.; Gerber, C. *Phys. Rev. Lett.* **1986**, *56* (9), 930–933.
(11) Radmacher, M.; Fritz, M.; Hansma, H. G.; Hansma, P. K. *Science* **1994**, *265* (5178), 1577–1579.
(12) Radmacher, M.; Tillmann, R. W.; Fritz, M.; Gaub, H. E. *Science* **1992**, *257* (5078), 1900–1905.
(13) Steigerwald, M. L.; Alivisatos, A. P.; Gibson, J. M.; Harris, T. D.; Kortan, R.; Muller, A. J.; Thayer, A. M.; Duncan, T. M.; Douglass, D. C.; Brus, L. E. *J. Am. Chem. Soc.* **1988**, *110* (10), 3046–3050.
(14) Rief, M.; Clausen-Schaumann, H.; Gaub, H. E. *Nat. Struct. Biol.* **1999**, *6* (4), 346–349.
(15) Strunz, T.; Oroszlan, K.; Schafer, R.; Guntherodt, H. J. *Proc. Natl. Acad. Sci. U.S.A.* **1999**, *96* (20), 11277–11282.
(16) Morfill, J.; Kuhner, F.; Blank, K.; Lugmaier, R. A.; Sedlmair, J.; Gaub, H. E. *Biophys. J.* **2007**, *93* (7), 2400–2409.
(17) Mann, S.; Shenton, W.; Li, M.; Connolly, S.; Fitzmaurice, D. *Adv. Mater.* **2000**, *12* (2), 147–150.
(18) Kuno, M.; Fromm, D. P.; Hamann, H. F.; Gallagher, A.; Nesbitt, D. J. *J. Chem. Phys.* **2000**, *112* (7), 3117–3120.
(19) Kuno, M.; Fromm, D. P.; Johnson, S. T.; Gallagher, A.; Nesbitt, D. J. *Phys. Rev. B* **2003**, *67* (12).
(20) Lacoste, T. D.; Michalet, X.; Pinaud, F.; Chemla, D. S.; Alivisatos, A. P.; Weiss, S. *Proc. Natl. Acad. Sci. U.S.A.* **2000**, *97* (17), 9461–9466.
(21) Gerion, D.; Parak, W. J.; Williams, S. C.; Zanchet, D.; Micheel, C. M.; Alivisatos, A. P. *J. Am. Chem. Soc.* **2002**, *124* (24), 7070–7074.
(22) Sperling, R. A.; Pellegrino, T.; Li, J. K.; Chang, W. H.; Parak, W. J. *Adv. Funct. Mater.* **2006**, *16* (7), 943–948.
(23) Levy, R.; Wang, Z. X.; Duchesne, L.; Doty, R. C.; Cooper, A. I.; Brust, M.; Fernig, D. G. *ChemBioChem* **2006**, *7* (4), 592–594.
(24) Bek, A.; Jansen, R.; Ringler, M.; Mayilo, S.; Klar, T. A.; Feldmann, J. *Nano Lett.* **2008**, *8* (2), 485–490.
(25) Clapp, A. R.; Medintz, I. L.; Uyeda, H. T.; Fisher, B. R.; Goldman, E. R.; Bawendi, M. G.; Mattoussi, H. *J. Am. Chem. Soc.* **2005**, *127* (51), 18212–18221.
(26) Huang, Y.; Duan, X. F.; Cui, Y.; Lauhon, L. J.; Kim, K. H.; Lieber, C. M. *Science* **2001**, *294* (5545), 1313–1317.
(27) Parak, W. J.; Gerion, D.; Pellegrino, T.; Zanchet, D.; Micheel, C.; Williams, S. C.; Boudreau, R.; Le Gros, M. A.; Larabell, C. A.; Alivisatos, A. P. *Nanotechnology* **2003**, *14* (7), R15–R27.
(28) Brennan, J. L.; Hatzakis, N. S.; Tshikhudo, T. R.; Dirvianskyte, N.; Razumas, V.; Patkar, S.; Vind, J.; Svendsen, A.; Nolte, R. J. M.; Rowan, A. E.; Brust, M. *Bioconjugate Chem.* **2006**, *17* (6), 1373–1375.
(29) Zhou, D.; Piper, J. D.; Abell, C.; Klenerman, D.; Kang, D. J.; Ying, L. *Chem. Commun. (Cambridge, U.K.)* **2005**, (38), 4807–9.
(30) Pellegrino, T.; Kudera, S.; Liedl, T.; Munoz Javier, A.; Manna, L.; Parak, W. J. *Small* **2005**, *1* (1), 48–63.

NL8018627

**Supplementary Information**

# Nanoparticle Self-Assembly on a DNA-Scaffold written by Single-Molecule Cut-and-Paste

E.M. Puchner, S.K. Kufer, M. Strackharn, S. Stahl and H.E. Gaub*

Chair for Applied Physics, Center for Nanoscience and Center for Integrated Protein Science Munich,

Ludwig-Maximilians-Universität Munich,

Amalienstr. 54, 80799 Munich

*To whom correspondence should be addressed.
Email: gaub@lmu.de

## Sample Preparation

Depot and target areas were prepared on a cover slip as described in [1]. Briefly, cover slips were amino functionalized and covalently modified with NHS-PEG-maleimide (M = 5000 g/mol, Nektar, Huntsville, Alabama, USA). After rinsing with $H_2O$, a PDMS flow chamber with two channels was mounted on one cover slip. Both channels were connected to a peristaltic pump. The anchor oligomers for the depot and target area were reduced using TCEP solution (Pierce, Rockford, Illinois, USA) in order to generate free mercaptans. The left channel (depot area) was rinsed for 1 h with a 10 µM solution of depot anchor oligomers and the right one (target area) with a 10 µM solution of target anchor oligomers. Afterwards both channels were rinsed with $H_2O$ to remove all non-covalently bound oligomers. The left channel (depot area) was rinsed with a 1 µM solution of transfer DNA dissolved in saline sodium citrate (SSC) buffer (150 mM NaCl, 15 mM sodium citrate, pH 7) for 1 h. All oligomers used in this study were synthesized from IBA (IBA GmbH, Göttingen, Germany) and of HPLC-grade. After rinsing the depot channel for 5 min with SSC buffer to remove all non-hybridized transfer DNA, the PDMS flow chamber was removed and the cover slip was dried in a nitrogen stream. Finally the cover slip was mounted to the AFM-TIRF sample holder and immersed in SSC buffer.

## AFM Measurements

All SCMP experiments were performed with a custom build AFM [2] at room temperature in SSC buffer (Fig. S1). Silicon nitride cantilevers (MLCT-AUHW, Veeco Probes, Camarillo, California, USA) were amino functionalized and covalently modified with NHS-PEG-maleimide (M = 5000 g/mol, Nektar, Huntsville, Alabama, USA) as described in [1]. The spring constant of the DNA modified cantilever was calibrated in solution using the equipartition theorem [3,4]. This method yielded a spring constant of about 15 pN/nm and a resonance frequency of 1.24 kHz for the cantilevers used in this study. The tip was withdrawn from the surface at a speed of 1500 nm/s until it was 2 µm above the surface. The protocol for the SMCP as well as the data recording was programmed using Igor Pro 5.03 (Wave Metrics, Lake Oswego, Oregon, USA). An Asylum Research controller, which provides ADC and DAC channels as well as a DSP board, was used for setting up feedback loops. Cantilever positioning for pickup and delivery was controlled in closed-loop operation. The precision was set to ±4 nm.

## Total Internal Reflection Fluorescence (TIRF) Microscope

Single-molecule fluorescence microscopy was carried out in TIRF excitation (Fig. S1). Fluorescence excitation of nanoparticles was performed by a 532 nm, 75 mW DPSS laser (Crystalaser, Nevada, USA) and by a 473nm, 100 mW DPSS laser (Laser Quantum, UK) through a 100x/1.49 oil immersion objective lens (Nikon CFI Apochromat TIRF, Japan), where the collimated laser beam is focused in the back focal plane of the objective lens such that the beam is totally reflected at the cover slip. Fluorescence light is either split by color with a commercial Dual View (Optical Insights, Arizona, USA) with Brightline HC 582/75 (Semrock, New York, USA) and ET 700/75 (Chroma, Vermont, USA) as emission filters for the green and red channel respectively and a dichroic mirror with a cut-off wavelength of 630 nm (630DCLP) when using 532 nm excitation or filtered by a emission filter HQ 525/50 (Chroma, Vermont, USA) when using 473 nm excitation wavelength. The emitted light is detected by a 512 x 512 pixel back-illuminated EMCCD camera (DU-897, Andor, Belfast, Ireland). Time series where recorded in frame-transfer mode with an integration time of 100 ms per frame. The EMCCD chip was typically operated at a temperature of -75°C and an electron multiplication gain of 300x was used. The magnification was 96, i.e. 125 nm are imaged to one pixel.

**The SMCP force system**

The probe of an atomic force microscope (AFM) was used to assemble individual single stranded DNA (ssDNA) oligomers one by one in aqueous solutions at room temperature. The oligomers were stored on well-defined depot areas, picked up with the tip of an AFM cantilever and reassembled with nanometer precision on a spatial distinct target area. The storage, the pick up and the deposition of the DNA oligomers were realized by using an ordered system of unbinding forces based on DNA interactions.

The dissociation rates of DNA duplexes under load are highly dependent on loading geometries and DNA sequences [5,6]. The geometry, in which the DNA duplex is stretched at opposite 5’ and 3’ ends, is called “shear mode” [5] (Fig. S2e), whereas the arrangement when double strands are loaded by pulling on the 5’ and 3’ extremities of one end of the duplex is called “unzip mode” [7] (Fig. S2a). These two geometries are well distinguishable concerning their dissociation properties under load.

The rupture forces of DNA duplexes loaded in unzip mode are independent both of the length of the DNA sequence and the loading rate, but vary for G-C and A-T interactions. G-C pairing results in a dissociation force of 20 pN whereas A-T gives 10 pN [6]. The dissociation forces for DNA duplexes loaded in shear geometry depend both on the length and sequence of the DNA and the loading rate [5].

To store the transfer DNA in the depot, a 30 base pair (bp) long anchor sequence with mixed G-C and A-T is used (Fig. S2a). The transfer DNA has in addition to this 30 bp anchor sequence a 20 bp handle sequence for pick up. The AFM-tip is covalently modified with a DNA oligomer, which is complementary to the handle sequence and forms a duplex if tip approaches the depot area (Fig. S2b). If the tip is retracted from the depot, the anchor sequence is loaded in unzip mode whereas the handle sequence is loaded in shear mode. Although the 30 bp anchor sequence is longer than the 20 bp handle sequence, its unbinding probability under load is much higher than for the handle sequence so that the transfer DNA is picked up (Fig. S2c, Fig. 4).

After translocation of the transfer DNA to its target site the cantilever is moved down. Since the target area is covalently modified with DNA oligomers that are complementary to the anchor sequence a 30 bp duplex in shear geometry is formed (Fig S2d). As the dissociation force of duplexes in shear geometry depends on the length of the DNA sequence the shorter handle sequence ruptures first and the transfer DNA is attached to the target site (Fig. S2e, Fig. 4). The DNA sequences of the oligomers used in this study are shown in Fig. S3.

**Hybridization of fluorescent nanoparticles to the DNA scaffold**

For the hybridization to the DNA-biotin scaffold, the following fluorescent semiconductor nanoparticles were used:

Invitrogen, Germany, streptavidin conjugate, 1 μM solution, Qdot 525 (colored blue), Qdot 565 (colored green), and Qdot 705 (colored red). The nanoparticles were incubated on the written DNA-biotin pattern at a final concentration of 500 pM in 0.1x SSC buffer. After about one minute, the self assembly process of nanoparticles to the pattern was complete.

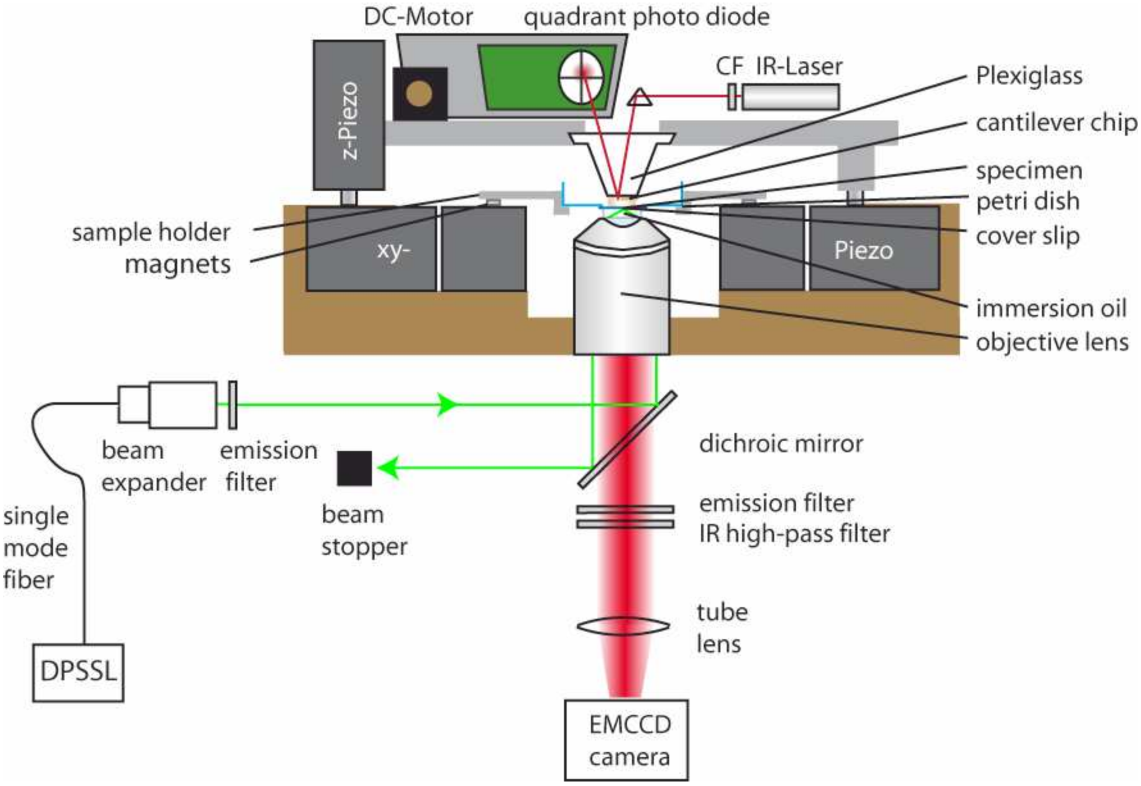
DC-Motor
quadrant photo diode
CF IR-Laser
z-Piezo
Plexiglass
cantilever chip
specimen
petri dish
cover slip
sample holder
magnets
xy-
Piezo
immersion oil
objective lens
beam expander
emission filter
single mode fiber
DPSSL
beam stopper
dichroic mirror
emission filter
IR high-pass filter
tube lens
EMCCD camera

**Fig. S1.** Experimental setup. A custom built AFM, which is moveable in z direction via a piezo, is combined with an inverted microscope for objective-type TIRF excitation. The cover slip with the depot- and target areas on top is glued into a drilled petri dish. The petri dish is placed in a sample holder, which is fixed through magnets on x-y piezo scanner.

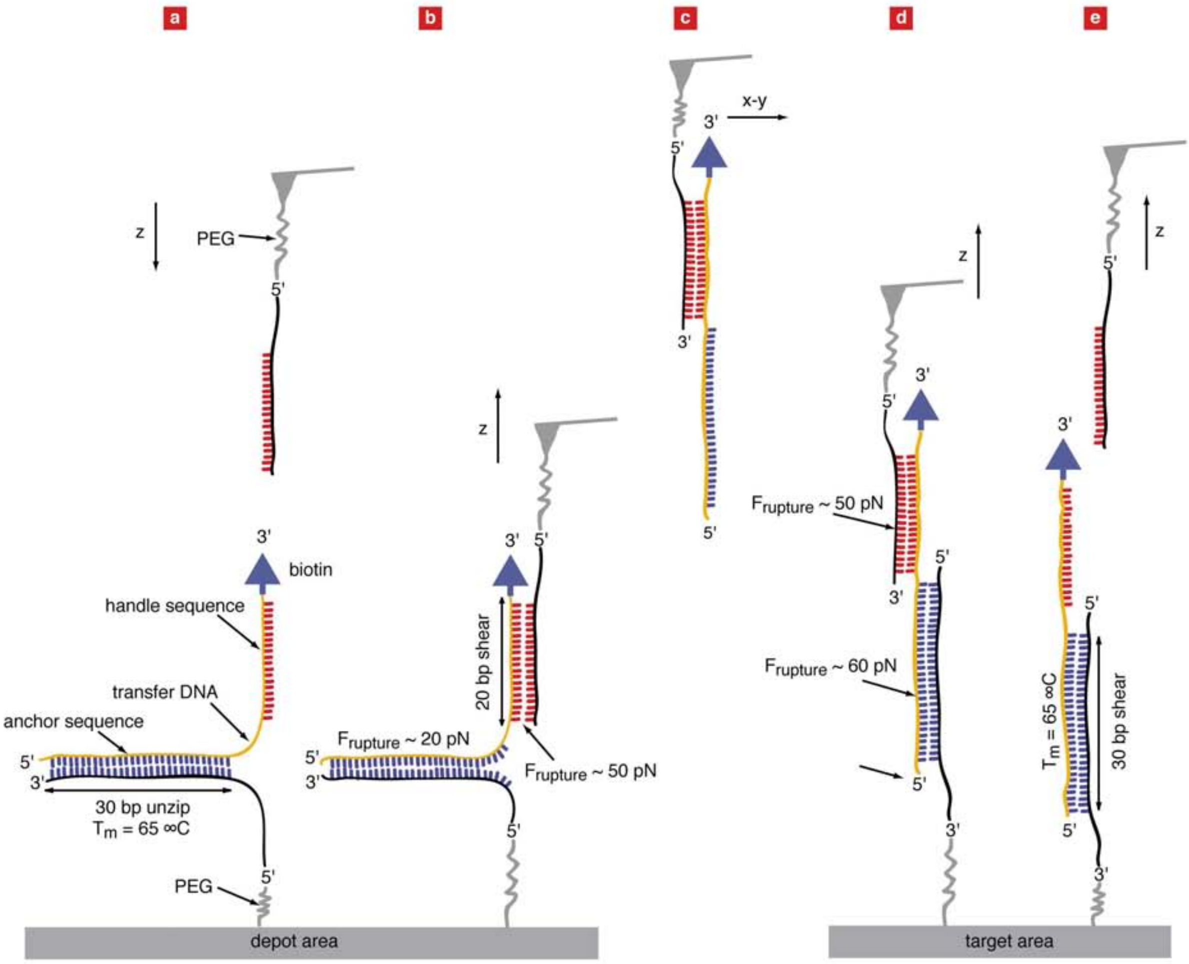
a
b
c
d
e
z
PEG
5'
3'
biotin
handle sequence
transfer DNA
anchor sequence
5'
3'
30 bp unzip
$T_m$ = 65 ∞C
PEG
5'
depot area
z
3'
5'
20 bp shear
$F_{rupture}$ ~ 20 pN
5'
3'
$F_{rupture}$ ~ 50 pN
5'
x-y
3'
5'
3'
5'
z
3'
5'
$F_{rupture}$ ~ 50 pN
5'
3'
$F_{rupture}$ ~ 60 pN
5'
3'
target area
z
5'
3'
5'
$T_m$ = 65 ∞C
30 bp shear
5'
3'

**Fig. S2.** Schematic illustration of the hierarchical force system. (a) To prevent unspecific adsorption, polyethylenglycol (PEG) molecules are covalently attached to the depot area. DNA oligomers, complementary to the anchor sequence of the transfer DNA, are covalently bound with their 5' end to these PEG molecules. Transfer DNA oligomers, which were modified with biotin labels at the 3' end, are hybridized to this anchor sequences. The tip of an AFM cantilever is also covalently modified with PEG molecules and a single DNA oligomer, which is complementary to the handle sequence of the transfer DNA. (b) When the tip is in contact with the surface a duplex between the transfer DNA and the cantilever DNA is formed. When the tip is retracted, the anchor sequence is loaded in unzip mode and the handle sequence in shear mode. As the unbinding probability for the anchor sequence is higher, the transfer DNA is picked up. (c and d) The target site is also covalently modified with PEG molecules. DNA oligomers, complementary to the anchor sequence of the transfer DNA, are bound with their 3' end to the PEG molecules. After translocation, the tip is moved down and a duplex is formed. When the tip is retracted, the handle and the anchor sequences are loaded in shear mode, but this time the shorter handle sequence ruptures first and the transfer DNA is attached to its target site. The tip is now in its initial state and the cycle can be repeated over and over again.

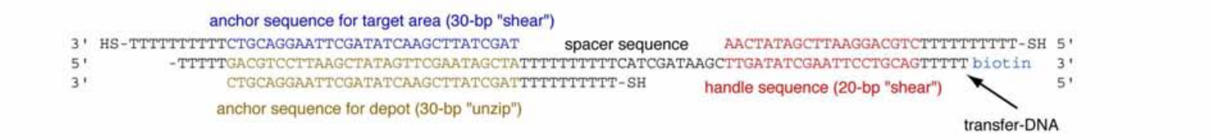
anchor sequence for target area (30-bp "shear")
3' HS-TTTTTTTTTTCTGCAGGAATTCGATATCAAGCTTATCGAT
spacer sequence
AACTATAGCTTAAGGACGTCTTTTTTTTTT-SH 5'
5' -TTTTTGACGTCCTTAAGCTATAGTTCGAATAGCTATTTTTTTTTTCATCGATAAGCTTGATATCGAATTCCTGCAGTTTTT biotin 3'
3' CTGCAGGAATTCGATATCAAGCTTATCGATTTTTTTTTTT-SH
handle sequence (20-bp "shear")
5'
anchor sequence for depot (30-bp "unzip")
transfer-DNA

**Fig. S3.** Oligomers used in this study. The transfer DNA is 80 bp long and has a biotin label at its 3' end. The 30 bp long sequence on the 5' end is used to anchor the transfer DNA both to the depot and to the target site. The 20 bp long sequence on the 3' end is used as a handle for pick up. All oligomers were synthesized and purified (HPLC-grade) form IBA (IBA GmbH, Göttingen, Germany).

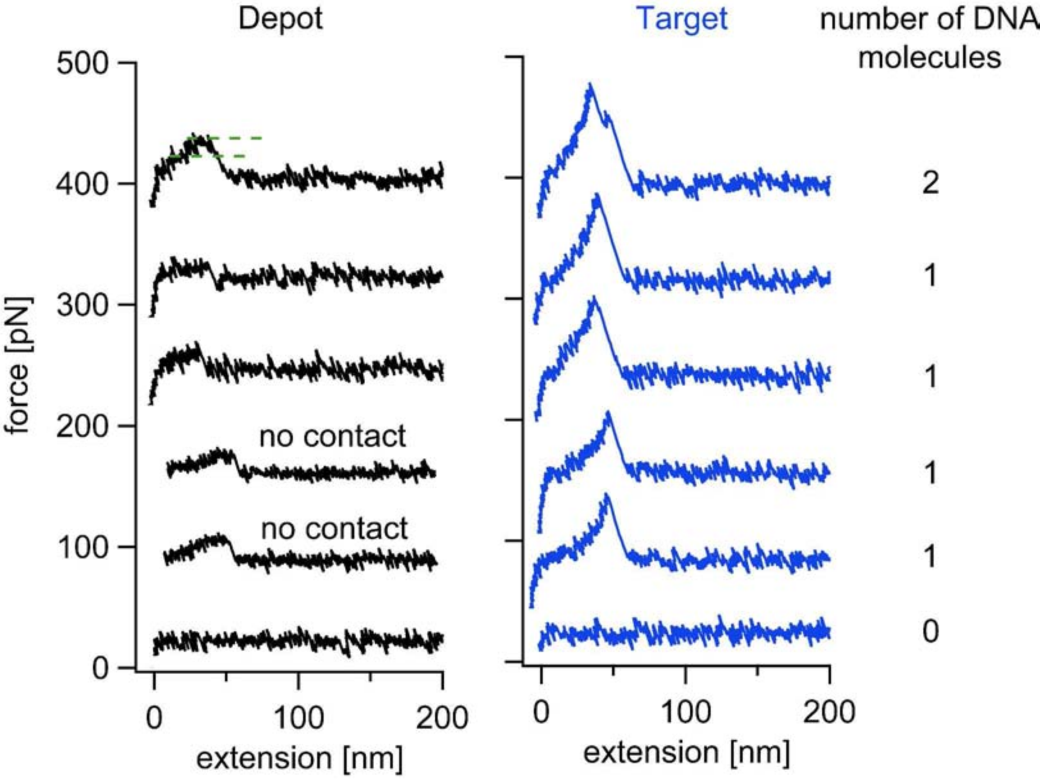

**Fig. S4.** Typical force extension traces of the depot and target region. In the depot region, the transfer DNA oligomer is separated from the depot oligomer in the zipper geometry. This separation process results in a force plateau of about 18 pN. As indicated, the transfer oligomers can also be picked up without contacting the surface. In the target region the transfer oligomer is separated from the tip oligomer in the shear geometry. Here, the force extension traces follows the elasticity of the PEG-spacer and the DNA until they are separated at forces of about 50 pN. For each cut-and-paste cycle, the number DNA oligomers which were picked up and delivered, can be counted. As an example we show traces where two, one and no DNA molecule was detected.

**movie S5.** Hybridization of nanoparticles to the DNA scaffold. (separate download)

## References:

1. Kufer, S.K., Puchner, E.M., Gumpp, H., Liedl, T. & Gaub, H.E. Single-Molecule Cut-and-Paste Surface Assembly. Science 319, 594-596 (2008).

2. Kühner, F., Lugmaier, R., Mihatsch, S. & Gaub, H.E. Print your atomic force microscope. Rev. Sci. Instrum. 78 (2007).

3. Florin, E.L. et al. Sensing specific molecular interactions with the atomic force microscope. Biosensors and Bioelectronics 10, 895-901 (1995).

4. Butt, H.-J. & Jaschke, M. Calculation of thermal noise in atomic force microscopy. Nanotechnology 6, 1-7 (1995).

5. Strunz, T., Oroszlan, K., Schafer, R. & Guntherodt, H.J. Dynamic force spectroscopy of single DNA molecules. Proceedings of the National Academy of Sciences of the United States of America 96, 11277-11282 (1999).

6. Rief, M., Clausen-Schaumann, H. & Gaub, H.E. Sequence-dependent mechanics of single DNA molecules. Nat Struct Biol 6, 346-349 (1999).

7. Levinthal, C. & Crane, H.R. On the Unwinding of DNA. PNAS 42, 436-438 (1956).

4. Rubinstein, R.H.C. Polymer Physics. Oxford University Press (2005).

5. Oesterhelt, F., Rief, M. & Gaub, H.E. Single molecule force spectroscopy by AFM indicates helical structure of poly(ethylene-glycol) in water. New Journal of Physics 1 (1999).

6. Smith, S.B., Cui, Y.J. & Bustamante, C. Overstretching B-DNA: The elastic response of individual double-stranded and single-stranded DNA molecules. Science 271, 795-799 (1996).

## 7.4 Manuskripte

M1:

Hermann Gumpp, Elias M. Puchner, Julia Morfill, Kerstin Blank and Hermann E. Gaub
*Triggering enzymatic activity with force*

M2:

H Gumpp , SW Stahl , M Strackharn , Elias M. Puchner and Hermann E. Gaub
*A combined AFM-TIRF microscope for simultaneous single molecule experiments*

# Triggering enzymatic activity with force

Hermann Gumpp, Elias M. Puchner, Julia Morfill, Kerstin Blank* & Hermann E. Gaub

*Lehrstuhl für Angewandte Physik & Center for Nanoscience, LMU München, Amalienstrasse 54, D-80799 München, Germany*

Present address: Department of Chemistry, Katholieke Universiteit Leuven, Celestijnenlaan 200F, B-3001 Leuven, Belgium

**Enzymes are dynamic entities, which are permanently subjected to thermal fluctuations. They sample a range of different conformations with timescales ranging from picoseconds to milliseconds[1,2]. The interconversion between these different conformations is considered to be directly related to the function of enzymes[1,3-5]. Furthermore, recent studies suggest that different conformations are also involved in the regulation of enzymatic activity[6,7]. Experiments with single enzymes have contributed significantly to our understanding of dynamic contributions to the activity of enzymes[8-12]. However, the investigation of regulatory effects, which requires a defined manipulation of single enzymes during the measurement, is difficult to achieve. Here we present the first example showing the manipulation of single enzymes of *Candida antarctica* lipase B with an externally applied force while monitoring its activity in real time. Using a periodic protocol consisting of a gradually increasing force followed by a sudden release, we show that the enzymatic activity is correlated with this sudden drop of the force. The probability for enzymatic activity is highest approximately 1.7 seconds after this "trigger event". This remarkable finding clearly shows that the relaxation of the enzyme follows a defined pathway even if the enzyme is released in a region of conformational space that is hardly explored by the enzyme by thermal fluctuations. Our results have implications for the current understanding of the *in vivo* process for the conversion of mechanical stimuli into biochemical signals showing that force can directly influence enzymatic activity and, therefore, might be considered to have a similar effect as an allosteric effector.**

In the same way as the energy landscape determines the timescales and the probabilities of certain pathways in protein folding it defines the function of a protein[7,13,14]. Since the first experiments with myoglobin[15] more and more recent studies prove that THE native conformation of a protein does not exist but is instead represented by a dynamic ensemble of different conformations[2,4,6,16,17]. In this ensemble, all functionally relevant conformations might already be present even before the binding of the substrate, an activator or an inhibitor takes place[5-7]. The equilibrium between these conformations is defined by the underlying multidimensional energy landscape. A binding event then modifies the energy landscape and shifts the equilibrium between these conformations thereby enabling a defined series of events[2,6,7,14,16,17].

Among the many influences that can modify the energy landscape of a (bio)molecule the application of an external force is probably the best understood. Theoretical models to describe the effect of forces have been developed[18,19] and a recent example shows that force has the potential to trigger and direct chemical reactions[20]. Furthermore, force has

also been used to study the mechanism of thioredoxin catalysis[21]. In contrast to thioredoxin, where the substrate has been manipulated by the external force, we apply the force to the enzyme and read out its dynamic response in real time. We consider that the external force has a similar effect as an allosteric effector[22] but instead is fully reversible on a faster time scale. There is no need to wait for the effector to dissociate.

In order to follow the enzymatic reaction in real time we make use of the recent advances in single molecule fluorescence spectroscopy (SMFS) that allow the monitoring of catalytic reactions at the single molecule level[23]. SMFS has been applied to a range of different enzymes and has provided additional proof that enzymes exist as an ensemble of different conformers[8-12,24].

For the experiments presented here we have chosen the enzyme lipase B from *Candida antarctica* (CalB)[10,25], which converts the fluorogenic substrate 5-(and-6)-carboxyfluorescein diacetate (CFDA) into the highly fluorescent product 5-(and-6)-carboxyfluorescein. For monitoring the enzymatic turnover events we used a home-built total internal reflection fluorescence (TIRF) microscope (Supplementary Fig. 1). While recording these turnover events, CalB was periodically manipulated with an external force using an atomic force microscope (AFM). Since the direction of the applied force is known to directly influence the pathways on the energy landscape[26,27], the experiment was designed such that the force was applied to the enzyme at two defined positions (Fig. 1). Whereas the bond at one position was covalent, we used a reversible antibody-antigen interaction as the second bond[28]. This allowed stretching of CalB up to a certain threshold force at which the antibody antigen interaction ruptured. Therefore, the antibody antigen interaction was designed to serve as an upper force limit and, in addition, to allow the re-establishment of the interaction once the bond ruptured. Therefore, this reversible interaction is the key element, which allowed reversible stretching and relaxation cycles. Moreover, the bond rupture event (Fig. 2a) can be considered as a trigger, which releases CalB in a higher energy conformation on the energy landscape.

For practical reasons, we did not immobilize the antibody fragment to the cantilever directly but to a bead, which was glued to the cantilever (Supplementary Fig. 2). This strategy increased the number of available antibody fragments for the interaction with CalB and enabled the manipulation of many enzymes in parallel thereby avoiding the need of finding exactly the enzyme, which had been manipulated. The bead consisted of 6 % crosslinked agarose with a size exclusion limit of 4000 kDa and was therefore highly porous allowing the free diffusion of the substrate.

However, whereas the porosity allows for free substrate diffusion it could limit the amount of antibody fragments that was accessible for the interaction with the CalB fusion protein. In order to be able to use the antibody functionalized bead, the density of antibody fragments on the surface of the bead needed to be sufficiently high to provide high interaction frequencies for the force based manipulation with the AFM. To ensure this, we performed force spectroscopy measurements with the antibody-functionalized bead deposited on a glass surface and a peptide functionalized cantilever. We obtained high interaction frequencies and a rupture force for the antibody peptide interaction which was comparable to previous results for this particular interaction[27,28] (Supplementary Fig. 3).

Having characterized the first component of the experimental set-up, namely the antibody-functionalized bead, the functionality of the CalB fusion protein was analyzed with a variety of methods in the next step (see Methods and Supplementary Information for more details). Force spectroscopy measurements were performed with the immobilized CalB fusion protein and an antibody-functionalized cantilever. Fig. 2a shows a characteristic force extension curve. For the most probable rupture force these measurements yielded a value of 57.3 pN (Fig. 2b) and for the most probable rupture length a value of 92.6 nm (fig 2c). The latter value was used to calculate if the CalB fusion protein was unfolded as a result of the force applied to its N- and C-terminus. The length of the unfolded CalB was calculated to be approximately 90 nm (Supplementary Fig. 6). Adding the length of the spacers used in this particular experiment, which was between 80 nm and 100 nm, this would result in a total length of around 180 nm if CalB would be unfolded. However, the measured rupture length is only 92.6 nm, which agrees well with the length of the spacers and the estimated size of the intact CalB fusion protein. Based on this calculation we conclude that CalB is not irreversibly unfolded after stretching it up to a force of around 60 pN. But we also consider that the structure of CalB is disturbed significantly as this force lies in between functionally relevant forces as they can for example be generated by molecular motors that do not normally exceed 15 pN and forces that finally lead to the unfolding of a protein.

The last step before we performed the final experiments to disturb the CalB fusion protein was to prove the possibility of specifically localizing single enzymes with the TIRF microscope. Negative controls without the immobilized CalB fusion protein or without substrate clearly showed that repeated fluorescence emission at certain positions was only detectable on surfaces with the immobilized CalB fusion protein after the addition of substrate. To further confirm that the detected signal originates from immobilized CalB fusion proteins we added a 100x excess of an alternative substrate that does not yield a fluorescent product. Resulting from the expected competition between these two substrates the fluorescent signal originating from the cleavage of CFDA disappeared completely thereby clearly proving that the origin of the fluorescence is the cleavage of CFDA by the immobilized CalB fusion protein (Supplementary Fig. 7). Finally, taking time traces from 11 enzymes (see Full Methods for details) we analyzed the distribution of consecutive turnover events (on-time) and the corresponding off-times[8,10] (Supplementary Fig. 8). The on-time and off-time distributions show that short on-times are followed by off-times that can last up to 2 seconds. As a result, under the conditions of our experiment, the total off-time is much longer than the total on-time suggesting that the inactive conformation has a lower free energy and is therefore more populated. This can easily be imagined considering the artificial nature of our measurement set-up. The size of the CFDA substrate is big compared to the size of the active site pocket and CalB being a lipase normally functions at hydrophobic interfaces. Therefore, we have no reason to assume that CalB shows its maximum activity under the conditions of our experiments.

Having characterized the functionality of the different components of the experimental set-up shown in Fig. 1 we finally set out to manipulate the CalB fusion protein using the periodic protocol shown in Fig. 3a. Cycles of approaching the surface with the bead, waiting for the establishment of the interaction between the antibody fragment and the peptide followed by the retraction of the bead from the surface were repeated with a period of 10 seconds. When retracting the bead from the surface the force on the CalB fusion protein increased gradually until the interaction between the antibody fragment and the peptide finally ruptured. Fig. 3b shows the rupture events, which were recorded with the AFM. Whereas the individual load on each CalB fusion protein is expected to be around 60 pN the measured forces are in the nN range. This clearly shows that many interactions ruptured almost at the same time and that we were able to address and trigger many CalB fusion proteins in parallel. Fig. 3c shows a typical example of the corrected fluorescence time trace of one CalB fusion protein (see Full Methods and Supplementary Fig. 9 for details). The fluorescence intensities clearly show a correlation of the enzymatic activity with the rupture events. This correlation was confirmed after the analysis of 440 cycles (231 with rupture event and 209 without rupture event). The obtained distributions of the fluorescence intensity in Fig. 3d and 3e reveal an increased enzymatic activity after approximately 1.7 seconds following a rupture event. To further corroborate that this increased activity is indeed the result of the applied force we changed the protocol of the bead movement to obtain periods of 5 seconds (Fig. 3f and 3g). The analysis of 720 cycles (216 with rupture event and 504 without rupture event) again revealed an increased activity after 1.7 seconds.

The finding that CalB shows activity after a defined time following the trigger event leads us to propose an underlying simplified sketch of a possible energy landscape as shown in Fig. 4. The observed time of 1.7 seconds is on a time scale that is more representative for protein folding than for a functionally relevant conformational change, which normally occurs on time scales between microseconds and milliseconds. This relatively long time can be explained with the already mentioned disturbance of the protein structure. When looking at the structure it is becoming evident that the applied force is directly transmitted to a long $\alpha$-helix that represents one side of the active site pocket (Supplementary Fig. 10). This $\alpha$-helix has been suggested to adopt different conformations thereby determining the accessibility of the active site[25]. One can easily imagine that the force-induced disturbance relaxes in a way that yields a transient conformation of this $\alpha$-helix that favors the binding of the substrate. The time scale for this relaxation process is very slow but consistent with time scales observed under equilibrium conditions when no force is applied. Following this line of reasoning, our results suggest that the conformations of the enzyme are separated by sizable energy barriers and that the relaxation from the force induced conformation follows a reasonably well defined pathway on the energy landscape.

Even though CalB is only a model system that is not subjected to forces under natural conditions our results shine a new light on the process of mechanosensing, which deals with the conversion of mechanical information into biochemical information. So far, several examples have been shown where the applied force leads to partial unfolding of a protein thereby exposing so-called cryptic sites that might mediate binding or enzymatic activity[29,30]. In contrast, here we show that the force acting on the enzyme can directly influence its activity.

## Methods Summary

The cloning, expression and purification of the CalB fusion protein and the antibody fragment is described in the Methods. The immobilization procedure for the CalB fusion protein to the cover slip and the preparation of the cantilevers with the bead containing the antibody fragment are also described in the Methods. The cover slip and the cantilever were mounted into a home-built AFM-TIRF hybrid instrument (Supplementary Fig. 1). A solution containing 50 mM Na-phosphate pH 7.0, 150 mM NaCl, 5 % DMSO and 1 µM 5-(and-6)-carboxyfluorescein diacetate (CFDA) was pipetted onto the cover slip. While moving the cantilever up and down with the described protocol force time curves were recorded. In parallel, movies (400 seconds) were recorded with an integration time of 20 ms per frame covering an area of 900 $\mu m^2$. Data analysis was performed with a custom written set of procedures. The positions showing enzymatic activity were identified by applying the following criteria: mean fluorescence intensity over all frames above background (> 2x standard deviation) and repeated switching from fluorescent to non-fluorescent states (minimum 3x). The time traces for these positions were used for further analysis to obtain the intensity distributions in Fig. 3.

**Full Methods** and associated references are available in the online version of the paper at www.nature.com/nature.

## References

1. Hammes-Schiffer, S. & Benkovic, S. J. Relating protein motion to catalysis. *Annu. Rev. Biochem.* **75**, 519-541 (2006).
2. Henzler-Wildman, K. & Kern, D. Dynamic personalities of proteins. *Nature* **450**, 964-972 (2007).
3. Eisenmesser, E. Z., Bosco, D. A., Akke, M. & Kern, D. Enzyme dynamics during catalysis. *Science* **295**, 1520-1523 (2002).
4. Eisenmesser, E. Z. et al. Intrinsic dynamics of an enzyme underlies catalysis. *Nature* **438**, 117-121 (2005).
5. Boehr, D. D., McElheny, D., Dyson, H. J. & Wright, P. E. The dynamic energy landscape of dihydrofolate reductase catalysis. *Science* **313**, 1638-1642 (2006).
6. Volkman, B. F., Lipson, D., Wemmer, D. E. & Kern, D. Two-state allosteric behavior in a single-domain signaling protein. *Science* **291**, 2429-2433 (2001).
7. Henzler-Wildman, K. A. et al. Intrinsic motions along an enzymatic reaction trajectory. *Nature* **450**, 838-844 (2007).
8. Lu, H. P., Xun, L. & Xie, X. S. Single-molecule enzymatic dynamics. *Science* **282**, 1877-1882 (1998).
9. Edman, L., Foldes-Papp, Z., Wennmalm, S. & Rigler, R. The fluctuating enzyme: a single molecule approach. *Chem. Phys.* **247**, 11-22 (1999).

10. Velonia, K. et al. Single-enzyme kinetics of CALB-catalyzed hydrolysis. *Angew. Chem. Int. Ed. Engl.* **44**, 560-564 (2005).
11. English, B. P. et al. Ever-fluctuating single enzyme molecules: Michaelis-Menten equation revisited. *Nat. Chem. Biol.* **2**, 87-94 (2006).
12. De Cremer, G. et al. Dynamic disorder and stepwise deactivation in a chymotrypsin catalyzed hydrolysis reaction. *J. Am. Chem. Soc.* **129**, 15458-15459 (2007).
13. Tsai, C. J., Kumar, S., Ma, B. & Nussinov, R. Folding funnels, binding funnels, and protein function. *Protein Sci.* **8**, 1181-1190 (1999).
14. Min, W., Xie, X. S. & Bagchi, B. Two-dimensional reaction free energy surfaces of catalytic reaction: effects of protein conformational dynamics on enzyme catalysis. *J. Phys. Chem. B* **112**, 4544-66 (2008).
15. Frauenfelder, H., Sligar, S. G. & Wolynes, P. G. The energy landscapes and motions of proteins. *Science* **254**, 1598-1603 (1991).
16. Kumar, S., Ma, B., Tsai, C. J., Sinha, N. & Nussinov, R. Folding and binding cascades: dynamic landscapes and population shifts. *Protein Sci.* **9**, 10-19 (2000).
17. Swint-Kruse, L. & Fisher, H. F. Enzymatic reaction sequences as coupled multiple traces on a multidimensional landscape. *Trends Biochem. Sci.* **33**, 104-112 (2008).
18. Bustamante, C., Chemla, Y. R., Forde, N. R. & Izhaky, D. Mechanical processes in biochemistry. *Annu. Rev. Biochem.* **73**, 705-748 (2004).
19. Lomholt, M. A., Urbakh, M., Metzler, R. & Klafter, J. Manipulating single enzymes by an external harmonic force. *Phys. Rev. Lett.* **98**, 168302 (2007).
20. Hickenboth, C. R. et al. Biasing reaction pathways with mechanical force. *Nature* **446**, 423-427 (2007).
21. Wiita, A. P. et al. Probing the chemistry of thioredoxin catalysis with force. *Nature* **450**, 124-7 (2007).
22. Vogel, V. & Sheetz, M. Local force and geometry sensing regulate cell functions. *Nat. Rev. Mol. Cell. Biol.* **7**, 265-275 (2006).
23. Roeffaers, M. B. et al. Single-molecule fluorescence spectroscopy in (bio)catalysis. *Proc. Natl. Acad. Sci. USA* **104**, 12603-12609 (2007).
24. Kuznetsova, S. et al. The enzyme mechanism of nitrite reductase studied at single-molecule level. *Proc. Natl. Acad. Sci. USA* **105**, 3250-3255 (2008).
25. Uppenberg, J., Hansen, M. T., Patkar, S. & Jones, T. A. Sequence, Crystal-Structure Determination And Refinement Of 2 Crystal Forms Of Lipase-B From Candida-Antarctica. *Structure* **2**, 293-308 (1994).
26. Carrion-Vazquez, M. et al. The mechanical stability of ubiquitin is linkage dependent. *Nat. Struct. Biol.* **10**, 738-743 (2003).
27. Morfill, J. et al. Force-Based Analysis of Multidimensional Energy Landscapes: Application of Dynamic Force Spectroscopy and Steered Molecular Dynamics Simulations to an Antibody-Peptide Complex. *J. Mol. Biol.* doi: 10.1016/j.jmb.2008.06.065 (2008).
28. Morfill, J. et al. Affinity-matured recombinant antibody fragments analyzed by single-molecule force spectroscopy. *Biophys. J.* **93**, 3583-3590 (2007).

29. Vogel, V. Mechanotransduction involving multimodular proteins: converting force into biochemical signals. *Annu. Rev. Biophys. Biomol. Struct.* **35**, 459-488 (2006).
30. Puchner, E. M. et al. Mechanically activated ATP binding of the titin kinase domain revealed by single-molecule force spectroscopy. *submitted* (2008).

**Supplementary Information** is linked to the online version of the paper at www.nature.com/nature.

**Acknowledgements** The authors thank Novozymes A/S for the gift of the *calB* gene and Andreas Plückthun for providing the expression vector pAK400 as well as the gene for the scFv fragment. Furthermore, the authors thank Johan Hofkens and Hiroshi Ujii for help in setting up single molecule fluorescence experiments as well as Michael Skjot, Allan Svendsen and Alan E. Rowan for helpful discussions. The work was supported by the European Union, the Deutsche Forschungsgemeinschaft, the Center for Integrative Protein Science Munich and a long-term fellowship from the Human Frontier Science Program (K.B.).

**Author Contributions** K. B. and H. E. G. designed the experiments. H. G. and E. M. P. built up the combined TIRF-AFM instrument. K. B. prepared the molecules. K. B. and J.M. developed the protocols for the immobilization. J. M. and E. M. P. performed single molecule force spectroscopy. H. G. and E. M. P. performed single molecule fluorescence and the combined TIRF-AFM measurements. H. G. and E. M. P. evaluated the data. H. G., K. B. and H. E. G. wrote the paper.

**Author Information** Reprints and permissions information is available at npg.nature.com/reprintsandpermissions. The authors declare no competing financial interests.

Correspondence and requests for materials should be addressed to K. B. (e-mail: kerstin.blank@chem.kuleuven.be)

**Figure 1**

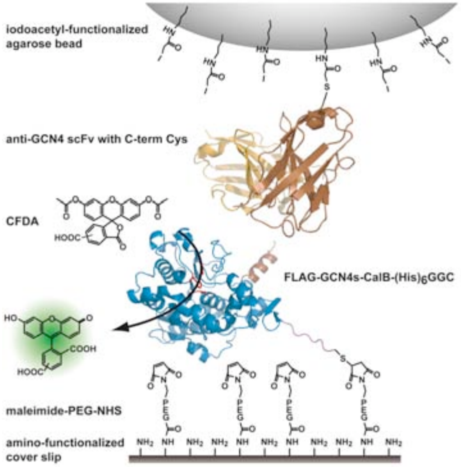
iodoacetyl-functionalized agarose bead
HN
O
S
anti-GCN4 scFv with C-term Cys
CFDA
HOOC
FLAG-GCN4s-CalB-(His)6GGC
HO
COOH
HOOC
N
PEG
maleimide-PEG-NHS
amino-functionalized cover slip
NH2
NH

**Figure 1. Experimental set-up.** The experimental set-up was designed to allow for the application of an external force to the enzyme CalB while monitoring its activity. The force was applied with an AFM and the activity was detected by recording the turnover of the fluorogenic substrate CFDA into the fluorescent product 5-and-6 carboxyfluorescein with a TIRF microscope. In order to apply a force to CalB the enzyme was coupled between two surfaces at specific positions. For this purpose a fusion protein was prepared that provided two site-specific attachment points. The fusion protein was covalently immobilized to a cover slip before the measurement and then connected to the AFM via a reversible antibody antigen interaction during the measurement. For the covalent immobilization, a cysteine was introduced at the C-terminus of CalB. This cysteine allowed the coupling to a cover slip, which was amino-functionalized and subsequently converted into a thiol reactive surface by coupling the hetero-bifunctional poly(ethylene) glycol NHS-PEG-maleimide. To connect CalB to the cantilever a peptide sequence (GCN4s) was fused to the N-terminus of CalB. This peptide sequence was recognized by an antibody fragment (anti-GCN4 scFv). The anti-GCN4 scFv also carried a C-terminal cysteine, which allowed the coupling to an iodoacetly-activated agarose bead glued to the cantilever of the AFM. (The protein structures were prepared with Swiss pdb viewer and Pymol; http://www.pymol.org)

## Figure 2

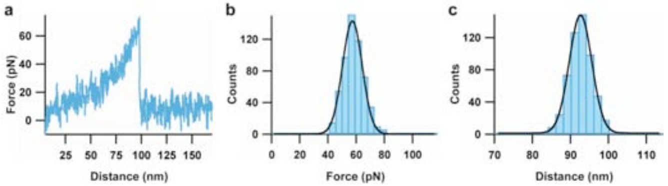

**Figure 2. Characterization of the CalB fusion protein with the AFM. a,** Example of a typical force-extension curve. The curve shows the rupture event of the scFv-peptide complex, experimentally recorded at a retract velocity of 1603 nm/s. **b,** Rupture force distribution. The rupture force histogram contains 560 rupture events and was fitted with a Gaussian curve (black). The most probable rupture force was determined from this fit and equals 57.3 pN. **c,** Rupture length distribution. From the corresponding histogram of the rupture lengths the most probable rupture length was again determined from a Gaussian fit (black curve) and equals 92.6 nm.

## Figure 3

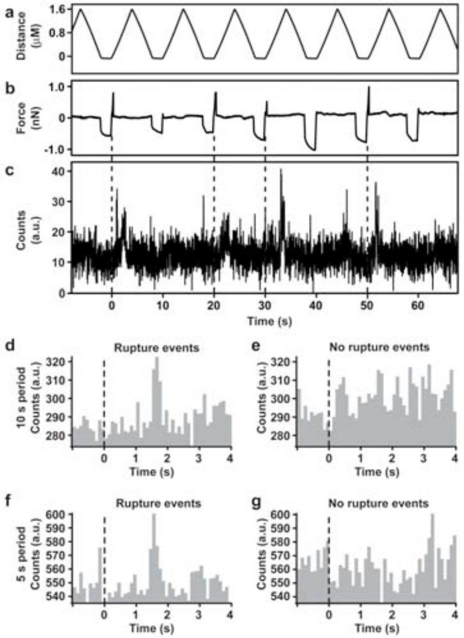

**Figure 3. Triggered CalB activity. a,** Protocol for the movement of the cantilever. Within 4 seconds the bead was moved down onto the surface. The bead was then kept on the surface for 2 seconds to allow the antibody fragment to bind to the peptide at the N-terminus of the CalB fusion protein. Finally, within another 4 seconds the bead was retracted from the surface to a final distance between surface and bead of around 1.6 µm. The whole cycle required 10 seconds and was repeated periodically many times while monitoring enzymatic turnover events with the TIRF microscope. **b,** Force time curve recorded during the periodic movement of the bead. The curve shows that the bead was in contact with the surface in every cycle (negative force values in the 2 second interval). After that, when the bead was retracted from the surface, positive force values in the nN range were detected in some cycles. These force values originate from the rupture of the interactions that have been established between the bead and the surface. **c,** Corrected fluorescence time trace for one enzyme recorded during the periodic movement of the bead. The time trace shows a repeatedly higher fluorescence signal, which can be clearly distinguished from the background noise. This higher signal is correlated with the detected rupture events. **d-g,** Histograms showing the probability to detect a higher fluorescence signal as a result of the rupture event. To generate the histograms the fluorescence time

traces of 11 enzymes were cut in 10 second fragments (setting the start of the retract phase to zero). For the further analysis, fragments where a rupture event took place (231 fragments in total) were treated separately from those fragments where no rupture event was detected (209 fragments in total). In each category, the average intensity for every frame was added up for all enzymes and used to generate histograms with a bin size of 100 ms seconds. As a result, both histograms contain identical enzymes, which had potentially been manipulated with the external force in some fragments (d) and did not experience the force in other fragments (e). In addition, an experiment was performed with a period of 5 seconds (2 seconds approach – 1 second incubation – and 2 seconds retraction; 9 enzymes – 216 fragments with rupture events (f) – 504 fragments without rupture event (g)). For both experiments, the fluorescence intensity is evenly distributed over the whole time of one period when no rupture event took place. In contrast, when a rupture event took place the probability to detect activity is higher after 1.7 seconds.

Figure 4

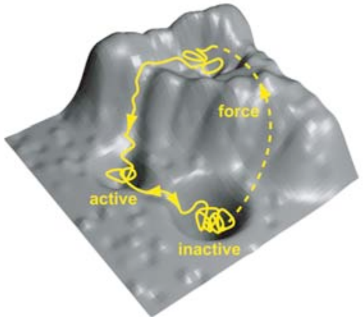

**Figure 4. Model energy landscape.** In equilibrium without an externally applied force CalB constantly interconverts between the active and an inactive conformation since the barrier is sufficiently low that thermal fluctuations provide the required energy. Most likely the inactive conformation has a lower free energy and CalB spends more time in this inactive conformation. The application of an externally applied force brings CalB in a higher energy conformation, which is also considered to be inactive. When the force is released, the system relaxes back to equilibrium following a defined pathway thereby reaching the active conformation after 1.7 seconds. Once in the active conformation, the equilibrium between the active and the inactive conformation establishes again. Alternative pathways that lead to the inactive conformation cannot be ruled out, but only pathways via the active conformation are detectable with the described experimental set-up.

## Supplementary Information

# Triggering enzymatic activity with force

Hermann Gumpp, Elias M. Puchner, Julia Morfill,
Kerstin Blank*, and Hermann E. Gaub

*To whom correspondence should be addressed.

Email: Kerstin.Blank@chem.kuleuven.be

**Cloning, expression and purification of the CalB fusion protein.** In order to be able to purify, detect and immobilize CalB a fusion protein was cloned that added four different functionalities to CalB (FLAG-GCN4s-CalB-$(His)_6$-GGC). At the N-terminus a FLAG tag was fused for detection purposes. The FLAG tag was followed by the GCN4s sequence, which served as the reversible handle providing the attachment of CalB to the AFM cantilever via a recombinant antibody fragment. The GCN4s sequence binds to a series of recombinant antibody fragments (scFv fragments) and the respective interactions have been characterized in detail previously[27,28,31,32]. The peptide antigen is derived from the leucine zipper domain of the yeast transcription factor GCN4. This leucine zipper domain is a homodimer of a 33 amino acid long peptide. From the crystal structure it is known that the antibody binds to a region of 12 amino acids close to the C-terminus of the peptide[32]. For most of the experiments this 12 amino acid long peptide was used. However, for some experiments described below the full length peptide (including the 7P14P mutations[28,31,32]) was used. At the C-terminus the CalB fusion protein contained a his tag for purification purposes. This his tag was followed by two glycines and a cysteine which allowed the site-specific immobilization of the CalB fusion protein.

The plasmid used for the periplasmic expression of this CalB fusion protein was based on the pAK series[33]. Starting point was the plasmid pKB3CalB-$(His)_6$GGC[34,35], which contains the *calB* gene cloned after a *lac* promotor, the strong RBS T7G10 and a pelB signal peptide for periplasmic expression. Furthermore, this plasmid already contains the N-terminal FLAG tag as well as the C-terminal attachments. Using this plasmid as the starting material, the FLAG tag at the N-terminus was replaced by a new tag containing the FLAG sequence followed by the amino acids YHLENEVARLKK using the oligonucleotides FLAG-GCN4s_forw (5’-Pho-CGGCCATGGCGGACTACAAAGA TTATCATCTGGAAAACGA-GGTGGCGCGTCTGAAGAAA-3’) and FLAG-GCN4s_rev (5’-Pho- GATCTTTCTTCAGACGCGCCACCTCGTTTTCCAGATGAT AATCTTTGTAGTCCGCCATGGCCGGCT-3’). These oligonucleotides were hybridized and inserted into the plasmid between the *Nco*I and *Bgl*II sites resulting in the plasmid pKB3-FLAG-GCN4s-CalB-HisGGC. The insertion was verified by sequencing.

For expression in *E. coli* the plasmid was transformed into the *E. coli* K12 strain TB1 (New England Biolabs, Frankfurt, Germany). Expression cultures were grown at 25 °C in 4x 200 ml SB medium (20 g $l^{-1}$ tryptone, 10 g $l^{-1}$ yeast extract, 5 g $l^{-1}$ NaCl, 50 mM $K_2HPO_4$) containing 30 µg $ml^{-1}$ chloramphenicol. The cultures were inoculated from a 20 ml preculture to $OD_{600} = 0.1$. Expression was induced with 1 mM isopropyl-*β*-D-thiogalactopyranosid (IPTG) at an $OD_{600}$ between 1.0 and 1.5. The cells were harvested 3 h after induction by centrifugation at 5000 g and 4° C for 10 min.

The FLAG-GCN4s-CalB-$(His)_6$-GGC fusion protein was purified from periplasmic extracts using immobilized metal ion affinity chromatography (IMAC). The periplasmic extracts were prepared according to a protocol included in the manual for the $Ni^{2+}$-NTA columns (Qiagen, Hilden, Germany). The extracts were dialyzed against loading buffer (50 mM sodium phosphate pH 8.0, 300 mM NaCl, 10 mM imidazole) and loaded onto the column equilibrated with loading buffer. Columns were washed with 20 column volumes of loading buffer, followed by 10 column volumes of loading buffer containing 1 mM Tris(*2*-carboxyethyl)phosphine hydrochloride (TCEP; Perbio Science, Bonn, Germany) and 5 column volumes of a washing buffer (50 mM sodium phosphate pH 8.0, 300 mM NaCl, 30 mM imidazole). Elution was achieved by adding 5 column volumes of elution buffer (50 mM sodium phosphate pH 8.0, 300 mM NaCl, 200 mM imidazole). The eluted fraction was dialyzed against maleimide coupling buffer (50 mM sodium phosphate pH 7.2, 50 mM NaCl, 10 mM EDTA) and concentrated using Centricon YM-10 (Millipore, Schwalbach, Germany). The actual concentration of the purified CalB fusion protein was determined by measuring the absorbance at 280 nm. The extinction coefficient was calculated using the program Vector NTI (Invitrogen). The purified protein was adjusted to a final concentration of 0.8 mg ml$^{-1}$ and stored in aliquots at -80 °C.

For some control experiments FLAG-CalB-(His)$_6$-GGC was required. The purification of this protein followed exactly the same procedure.

**Cloning expression and purification of the recombinant antibody fragment.** The anti-GCN4 scFv fragment binds the GCN4s sequence, which has been described above. Clone C11L34, which in a previous analysis showed the highest binding forces for the full length peptide[28] was chosen as the "force transmitter" between the CalB fusion protein and the AFM cantilever.

As for the CalB fusion protein, the plasmid for the periplasmic expression was based on the pAK series[33] and is very similar to the expression plasmid for the CalB fusion protein. The scFv fragment also carries the N-terminal FLAG tag as well as the C-terminal (His)$_6$-GGC tag. However, in the scFv expression plasmid the gene for coexpression of the periplasmic chaperone Skp was introduced[36].

The expression and purification procedure for the scFv fragment was published previously[27,28]. In short, the bacteria with the transformed plasmid were grown at 25 °C in SB medium (20 g l$^{-1}$ tryptone, 10 g l$^{-1}$ yeast extract, 5 g l$^{-1}$ NaCl, 50 mM K$_2$HPO$_4$) containing 30 μg ml$^{-1}$ chloramphenicol. Expression was induced with 1 mM isopropyl-β-D-thiogalactopyranoside (IPTG) at an OD$_{600}$ between 1.0 and 1.5. The cells were harvested 3 h after induction by centrifugation. Cell disruption was achieved by French Press lysis. Cell lysates were cleared by centrifugation and filtration using a 0.22 μm filter. Cleared lysates were loaded on a Ni$^{2+}$-NTA column. The eluted fraction from the Ni$^{2+}$-NTA column was directly loaded onto an affinity column with immobilized CGGGYHLENEVARLKK peptide. The fractions from the affinity column were dialyzed against maleimide coupling buffer (for the immobilization to a PEG-functionalized cantilever, see below) and concentrated using Centricon YM-10. The actual concentration of the purified scFv fragment was determined by measuring the absorbance at 280 nm. The extinction coefficient was calculated using the program Vector NTI. The concentrations of purified proteins were adjusted to 0.8 mg ml$^{-1}$ and stored in aliquots at -80 °C. Alternatively, for coupling to an iodoacetly-functionalized agarose bead (see below) the eluted fractions were dialyzed against iodoacetyl coupling buffer (50 mM Tris pH 8.5, 5 mM EDTA), concentrated and adjusted to a final concentration of 3 mg ml$^{-1}$. Again, aliquots were stored at -80 °C.

**Immobilization procedures.** In order to be able to observe the force based manipulation of CalB while monitoring enzymatic turnovers the CalB fusion protein had to be immobilized to cover slips and the scFv fragment needed to be immobilized to the activated agarose bead. In addition, to this final, combined TIRF-AFM experiment a variety of control experiments were performed which required the immobilization of different molecules to glass slides and cover slips as well as AFM cantilevers. The different immobilization procedures are described in the following.

The CalB fusion protein was either immobilized onto glass slides or glass cover slips. For experiments where the turnover of CalB was recorded with the TIRF microscope the CalB fusion protein was immobilized onto cover slips. For all other experiments commercially available amino-functionalized glass slides (type A or A+; Schott Nexterion, Mainz, Germany) were used since they are easier to handle. The cover slips were silanized to obtain an amino-functionalized surface. The following procedure was used: the cover slips were sonicated in isopropanol for 10 min. After washing them with isopropanol and ultrapure water they were dried under a stream of N$_2$. Cleaned cover slips were exposed to UV-ozone treatment (FHR, Ottendorf-Okrilla, Germany) for 10 min to bleach potential fluorescent impurities and to activate the surface for the following step. The cover slips were immersed in a solution consisting of 2 % (v/v) 3-aminopropyl dimethyl ethoxysilane (ABCR, Karlsruhe, Germany), 10 % (v/v) ultrapure water and 88 % (v/v) ethanol. After 30 min the cover slips were washed with ethanol abs and ultrapure water and, finally, dried under a stream of N$_2$. In the following steps cover slips prepared in this way and the commercially available amino-functionalized slides were treated exactly the same way as has been described previously[34]. In short, the amino-functionalized surfaces were incubated in 50 mM sodium borate buffer pH 8.5 for 1 h in order to increase the fraction of unprotonated amino groups for coupling to the NHS groups of the NHS-PEG-maleimide used in the next step. To convert the amino surface into a sulfhydryl reactive surface NHS-PEG-maleimide with a molecular weight of 3400 g mol$^{-1}$ (Nektar, Huntsville, Alabama, USA) was used. The PEG was dissolved in the borate buffer in a concentration of 50 mM. For the cover slips a volume of 50 μl of the PEG solution was incubated between two cover slips with the amino-modified surfaces facing each other. When using slides, 200 μl of the PEG solution was incubated on the whole slide covered with a cleaned 24 mm x 60 mm cover slip. After 1 h of incubation in a humid chamber, the surfaces were separated carefully, rinsed with ultrapure water and dried with N$_2$. During the PEG incubation procedure, the CalB fusion protein was reduced using TCEP beads (Perbio Science, Bonn, Germany). This step was carried out to reduce potential disulfide bridges formed between the C-terminal cysteines and to obtain free cysteines for coupling to the maleimide-functionalized surface. For TIRF experiments 15 μl of the reduced protein solution was pipetted on one cover slip. For the control experiments described below a volume between 1 μl and 2 μl was spotted on the surface (either cover slip or slide). The surfaces were incubated in a humid chamber at 4 °C for 1 h. The spots were removed by aspiration and the slide was washed 3x 5 min in the buffer which was required for the following steps.

Control experiments (see below) were performed to characterize the antibody peptide interaction as well as the CalB fusion protein in separate AFM experiments. For this purpose, the scFv fragment and, alternatively, a full-length version of the GCN4 peptide (CGGGRMKQLEPKVEELLPKN**YHLENEVARLKK**LVGER) were immobilized to an

AFM cantilever. (The respective experiments will be described in detail below.) Since the scFv fragment carried a cysteine at its C-terminus and the full length GCN4 peptide carried a cysteine at its N-terminus the immobilization procedure used for the CalB fusion protein could also be applied for this purpose. However, a few modifications were made in the different steps and a more detailed protocol is given in Morfill et al.[28]

The cantilevers (Bio-lever, Olympus, Tokyo, Japan) were activated with a ten-minute UV-ozone treatment and then incubated in concentrated 3-aminopropyl dimethyl ethoxysilane for 60 s. After washing the cantilevers with toluol they were heated to 80 °C for 30 min. Then, the cantilevers were incubated in borate buffer for 1 hour. NHS-PEG-maleimide was dissolved at a concentration of 50 mM in borate buffer and incubated on the surfaces for 1 hour. In parallel, either the peptide or the scFv fragment was reduced using TCEP beads. After washing the cantilevers with ultrapure water, a solution of the peptide (200 µM) or the scFv fragment (0.13 mg ml$^{-1}$), dissolved in maleimide coupling buffer, was incubated on the cantilevers for 1 hour. Finally, the cantilevers were rinsed with PBS (10 mM Na phosphate, pH 7.4, 137 mM NaCl, 2.7 mM KCl) to remove non-covalently bound material and stored in PBS until use.

Finally, for the combined TIRF-AFM measurements the antibody fragment was not immobilized to the cantilever directly but to iodoacetyl-activated agarose beads (Perbio), which were glued to the cantilever. This strategy provided a bigger amount of scFv fragments for interaction with the CalB fusion proteins over a relatively flat surface allowing the simultaneous manipulation of many single enzyme molecules. Furthermore, the bead between the cantilever and the surface reduces the problems with autofluorescence of the cantilever.

The iodoacetyl beads have been dried, picked up with glass needles and put onto cantilevers with removed tips (MLCT-AUHW lever C, Veeco, Camarillo, CA, USA) that were covered with a very small amount of epoxy glue. After hardening of the glue (30 min) the bead modified cantilevers were rinsed with iodoacetyl coupling buffer. When incubating the cantilevers in the buffer the agarose beads swelled to their original size (Supplementary Fig. 2). For the coupling of the scFv fragment the protein was again reduced using TCEP beads. For one cantilever 10 µl of the solution was incubated on the cantilever for 1 hour at 4 °C and at a concentration of 1.5 mg ml$^{-1}$. After removing the solution of the scFv fragment from the bead, the bead was incubated in a solution of 50 mM L-cysteine in iodoacetly coupling buffer for 20 min in order to block the remaining iodoacetyl groups. Finally, the cantilevers were washed and stored in 50 mM sodium phosphate pH 7.0, 150 mM NaCl until use.

**AFM measurements for the characterization of the beads functionalized with the scFv fragment.** In order to test if the immobilization procedure yields beads functionalized with the scFv fragment a fraction of the beads was treated in suspension with the above procedure. Beads prepared in this way were pipetted onto a glass slide and AFM experiments were performed using a cantilever functionalized with the full length GCN4 peptide (prepared as described above). The cantilever was mounted in the AFM part of the AFM-TIRF hybrid instrument and was positioned above a bead. Several hundred force-extension curves were recorded. The extracted rupture forces were plotted and the obtained histogram was fitted with a Gaussian distribution (Supplementary Fig. 3).

**Characterization of the CalB fusion protein.** The purified CalB fusion protein FLAG-GCN4s-CalB-(His)$_6$GGC was characterized with various methods to ensure its functionality and activity. First, measurements were performed to investigate if the attached GCN4s peptide influences the activity of CalB. Second, control experiments were performed to test the activity of surface immobilized CalB as well as the accessibility of the N-terminally fused GCN4s peptide. Third, the accessibility of the GCN4s peptide was verified with AFM measurements using a cantilever containing immobilized scFv fragments. These control experiments will be summarized in detail below.

To compare the activity of FLAG-GCN4s-CalB-(His)$_6$GGC with FLAG-CalB-(His)$_6$GGC measurements in cuvettes were performed with the substrate 5-(and 6-)-carboxyfluorescein diacetate (CFDA; Invitrogen) using the following reaction conditions: 50 mM Na phosphate pH 7.0, 150 mM NaCl, 10 % DMSO, 500 nM enzyme, 50 µM CFDA. The reaction was started by the addition of the substrate, which was dissolved at a concentration of 500 µM in DMSO. Measurements were performed at 25 °C in black 384 well plates with 50 µl reaction volume (triplicates). The excitation wavelength of the microplate reader (SpectraMax M5, Molecular Devices, Wokingham, UK) was set to 495 nm and the emission wavelength to 517 nm. A cut-off filter of 515 nm was used. The fluorescence intensity was measured in intervals of 30 s for a total time of 3 hours. The results of this experiment are summarized in Supplementary Fig. 4 and show that the attached GCN4s peptide does not have a significant influence on the activity of CalB for CFDA.

Having analyzed the activity of CalB in solution, the next step was to characterize the functionality of the surface-immobilized CalB fusion protein. The two main aspects that were analyzed concern the activity of the immobilized CalB fusion protein as well as the accessibility of the N-terminal GCN4s peptide. To prove the mentioned aspects the following experiment was designed: FLAG-GCN4s-CalB-(His)$_6$GGC was immobilized to a functionalized glass slide as described above. FLAG-CalB-(His)$_6$GGC was used as a positive control as the functional and site-specific immobilization of this protein had already been shown before[34]. A GCN4s peptide carrying a C-terminal cysteine (YHLANEVARLKKGGGC) was immobilized as a control to test for the accessibility of the peptide.

For each of the different samples 4 different spotting solutions were prepared: One part of the samples was reduced with TCEP beads as described above. These reduced samples were diluted either in maleimide coupling buffer or maleimide coupling buffer containing free cysteine. In addition non-reduced samples were diluted in both buffers. For this experiment, the final concentration of the samples in the spotting solution was approximately 150 µg ml$^{-1}$ or 4.5 µM. The spotting solutions containing free cysteine exhibit a concentration of cysteine of 45 mM, which represents an excess of 10,000 fold. The solutions were spotted onto two maleimide-functionalized slides using the scheme shown in Supplementary Fig. 4. A volume of 2 µl each was incubated on the slide for 1 hour at 4 °C in a humid chamber. The spots were removed by aspiration and the slide was washed 3x 5 min in TBS (50 mM Tris pH 8.0, 15 mM NaCl, 1 mM $CaCl_2$) + 0.4 % bovine serum albumin (BSA).

One slide was used to obtain information about the density of the immobilized molecules on the surface. For this purpose, the N-terminal FLAG tag was detected using the M1 antibody (Sigma). The antibody was diluted to a final concentration of 4 µg $ml^{-1}$ in TBS+BSA. A volume of 5 ml was incubated on the slide for 1 hour at room temperature. After washing the slide 3x 5 min in TBS+BSA, a secondary rabbit anti-mouse antibody carrying an AlexaFluor 647 label (1 µg $ml^{-1}$ in TBS+BSA; Invitrogen) was incubated on the slide for 30 min. The slide was again washed 3x 5 min in TBS+BSA. The slide was scanned for fluorescence on the spots using a microarray scanner (LS300, Tecan, Crailsheim, Germany).

The second slide was used to determine the accessibility of the GCN4s peptide. For this purpose the anti-GCN4 scFv fragment previously labeled with fluorescein-maleimide at the C-terminal cysteine was added to the above solution to a final concentration of approximately 1 µg $ml^{-1}$. Again the slide was scanned in a micorarray scanner.

Finally, the activity of the immobilized lipases was tested as described previously[34]. In short, one slide containing the immobilized lipases was put up side down on the surface of an agar plate containing Tween 80 and $CaCl_2$. The agar plate was incubated over night at room temperature. Upon cleavage of Tween 80 by the CalB free fatty acids are liberated. These precipitate with the $Ca^{2+}$ ions in the agar plate thereby forming white areas that can be easily detected. The results are summarized in Supplementary Fig. 4.

To further prove the accessibility of the N-terminal GCN4s peptide fused to the CalB fusion protein, single molecule force spectroscopy experiments were performed with the CalB fusion protein immobilized to a glass slide and the scFv fragment immobilized to the cantilever of the AFM. For the exact experimental set-up see Supplementary Fig. 5. The AFM measurements were performed with a MFP-1D atomic force microscope (AFM) (Asylum Research, Santa Barbara, CA, USA) at room temperature in PBS. The cantilever spring constant equaled 7.4 pN/nm (B-Bio-Lever) and was obtained as described previously[37,38]. During the experiments the approach and retract velocity were held constant, whereas the applied force was adjusted by changing the distance between the cantilever tip and the surface to obtain single binding events. To achieve good statistics, several hundred approach-retract cycles were carried out. The obtained data was converted into force-extension curves. From these force-extension curves, the most probable rupture force (the force at which the antibody-antigen complex ruptures) and the rupture length were determined using the program Igor Pro 5.0 (Wavemetrics, Lake Oswego, Oregon, USA) and a custom-written set of procedures. The results are summarized in Supplementary Fig. 5 and in the main text.

**Single enzyme fluorescence experiments.** A series of experiments was performed to prove that the repeated emission of fluorescence on the surface originated from immobilized CalB fusion proteins hydrolyzing the CFDA substrate. For these experiments the CalB fusion protein was immobilized to cover slips as described above. The cover slips were glued into Petri dishes with a drilled hole and mounted onto a steel sample holder on the xy-scanning stage of the home-built TIRF microscope (Supplementary Fig. 1). The fluorogenic substrate CFDA was diluted in activity buffer (50 mM Na-phosphate pH 7.0, 150 mM NaCl) to a concentration of 10 µM and pipetted onto the cover slip immediately before the measurement. For this purpose, first a CFDA stock solution (200 µM) was prepared in DMSO. The stock solution was added to the activity buffer yielding a DMSO concentration of 5 % in the final measurement. After adjusting the focus to be able to detect the turnover events on the surface of the cover slip movies were recorded with the CCD camera. These movies were recorded in frame-transfer mode with an integration time of 20 ms per frame covering an area of 30 µm x 30 µm. Movies consisting of either 10,000 or 20,000 frames were recorded covering a total time of 200 or 400 seconds, respectively. The recorded movies in Andor SIF format were processed with the program Andor Solis (Andor Technology, Belfast, Ireland). For an example see Supplementary Movie 1. They were corrected for the inhomogeneous TIRF field (flat field correction) and the background of the CCD camera was subtracted before they were finally converted into TIFF stacks.

The signal of all frames of the TIFF stacks was integrated for every pixel (Supplementary Fig. 7d left) in order to determine if specific spots occur on the cover slip that might be related to CalB fusion proteins hydrolyzing the fluorogenic CFDA substrate. From the resulting image one position with a high intensity (area of 4 x 4 pixels) was chosen manually to extract the time trace of the fluorescence intensity at this position (Supplementary Fig. 7d right). The time trace shows alterations in fluorescence intensity over time as would be expected for a position where a CalB fusion protein was immobilized. To confirm that this repeated fluorescence emission observed at several positions on the surfaces indeed originated from CalB fusion proteins the following series of control experiments was performed. Movies were recorded from PEG-modified surfaces without immobilized enzymes in the presence and absence of 10 µM CFDA. In addition, movies were recorded from enzyme-containing surfaces but without substrate. Finally, movies were recorded after adding 1 mM para-nitrophenol butyrate (pNPB; Sigma) to the CFDA solution. pNPB is another substrate that is hydrolyzed by CalB[35] but does not yield a fluorescent dye as the product. Therefore, when performing measurements with a 100x excess of pNPB this substrate should reduce the amount of turnovers of CFDA very efficiently. The integrated images and the obtained time traces for the different controls are summarized in Supplementary Fig. 7. They clearly demonstrate that repeated fluorescence emission at defined positions is only detected on surfaces with immobilized enzyme in the presence of CFDA alone.

For further data analysis a more automated procedure for the identification of CalB fusion proteins and the extraction of time traces was employed using the programs Andor Solis, Igor Pro 5.0 and NIH Image (developed at the U.S. National Institutes of Health and available on the Internet at http://rsb.info.nih.gov/nih-image/). First, in addition to the corrections described above, the increasing background signal resulting from the accumulation of product molecules during the measurement was subtracted as a linear ramp. Then, using a custom written set of procedures, time traces of the turnover events of single enzymes were generated from areas where a repeated emission of fluorescence was localized. To identify these areas, the time average of the fluorescence intensity over all frames was calculated for every pixel. Time traces were extracted from areas (4 x 4 pixels) that showed a detectable signal above the background. Then this signal was compared to a reference area (4 x 4 pixels). Areas with a time averaged signal above 2x the standard deviation of the time averaged reference signal were selected as spots of high fluorescence intensity that might represent an immobilized CalB fusion protein. To exclude false positives (i.e. dirt sticking to the surface) only areas showing fluorescence bursts that emerged at least 3 or more times from the respective position within 200 seconds were identified as an enzyme. Having localized the positions of enzymes by applying these criteria, the respective fluorescence time traces showing enzymatic turnover events were used for further processing.

Time traces generated in this way were used to obtain a distribution of the times where the CalB fusion protein is active (on-times) and the duration of inactive phases that separate these on-times (off-times). For this purpose a threshold of 2x the standard deviation of the time-averaged signal was defined. Frames with a value above this threshold were counted as on-events and frames with a value below the threshold were counted as off-events. Consecutive frames showing on-events or off-events were taken together and represent the corresponding on-times or off-times. After converting the number of frames into seconds the on-times determined for 11 enzymes from a 20,000 frame long movie (400 seconds) were plotted in a probability density distribution of the on-times. In the same way a probability density distribution of the off-times was generated. The distributions are shown in Supplementary Fig. 8. We would like to note here, that the obtained distributions do not yield the same quality of information as the distributions obtained from measuring single enzymes with a confocal microscope [10,24] since in our experiment the total measurement time is much shorter. Furthermore, it is not possible to detect single turnover events unambiguously with a time resolution of 20 ms. However, the distributions yield a rough estimate of the timescales which determine the switching between active and inactive phases and as well as the probability to find an enzyme in its active conformation. This probability is 2.7 % and was obtained from relating the integrated on-time to the total time of the measurement.

**Combined AFM-TIRF experiments.** The AFM head was placed on top of the sample and the cantilever was positioned in a way that the bead position matched to field of view of the optical microscope. The AFM was moved by the piezo towards the surface and back while the deflection of the cantilever was determined with a quadrant photo diode, which measured the signal of the IR laser reflected on the cantilever. Two different protocols were employed for the movement of the cantilever. For the “10 second” experiment the cantilever was moved down to the surface within 4 seconds with a speed of 400 nm/s. Then the cantilever was stopped in this position with the bead on the surface for 2 seconds allowing the antibody fragments to bind to the CalB fusion proteins. Finally, the bead was retracted from the surface by 1.6 µm within 4 seconds with a speed of 400 nm/s. This movement of the cantilever was repeated periodically. For the “5 second” experiment the cantilever was moved down within 2 seconds with a speed of 800 nm/s. After incubation of the bead on the surface for 1 second the cantilever was moved away from the surface within 2 seconds with a speed of 800 nm/s. Again this cycle was repeated periodically. While performing these periodic movements, movies were recorded with the CCD camera as described above (20,000 frames; Supplementary Movie 2). In parallel the cantilever deflection was detected.

For the data analysis the AFM deflection curves were converted into force time curves and concatenated in a way that the fluorescence time traces could be correlated with the force time curves. The data analysis of the fluorescence time traces was performed in a similar way as described for the measurements without force-based manipulation. The main differences originate from the alternating background fluorescence that is generated by the periodic movement of the bead (Supplementary Fig. 9). After flat field and background correction the movies were again converted into TIFF stacks. Then the time averaged signal over all frames was calculated to localize areas with a fluorescence intensity above the background. Now, before the above criteria could be employed to identify enzymes the signal generated by the bead had to be subtracted. For this purpose, a reference area where no increased fluorescence was detected was chosen and the signal of this area (4 x 4 pixels) was subtracted from the areas (4 x 4 pixels) that showed increased fluorescence intensity. The corrected time traces generated in this way were now analyzed with the criteria described above: To be identified as an enzyme the time averaged signal had to be higher than 2x the standard deviation of the signal from a reference time trace obtained from an area (4 x 4 pixels) without an enzyme and the signal had to switch between high and low fluorescence for at least 3 times.

Having analyzed 1 movie from both the “10 second” (“5 second”) experiment, 11 (9) enzymes were identified that matched the above criteria. Now, the time traces of these enzymes were synchronized with the movement of the cantilever and cut into 10 second (5 second) fragments. Movies were cut 1 second before the movement of the cantilever away from the surface had been started. This yielded 40 fragments for the “10 second” experiment and 80 fragments of the “5 second” experiment. The fragments of all the time traces were sorted into two categories: The first category contained all fragments where a rupture event was detected with the AFM. The second category contained all fragments where no rupture event occurred. Of the 40 (80) fragments 21 (24) contained a rupture event and 19 (56) contained no rupture event. For every enzyme the fluorescence counts of all the fragments were added up and divided by the number of fragments to obtain the average of the counts for every frame. Now the averaged counts were added for all 11 (9) enzymes. The frames were converted into seconds and histograms with a bin size of 100 ms were generated. For the histograms of the “10 second” experiment in Fig. 3 only the first 5 seconds of each fragment are shown. The complete histograms are shown in Supplementary Fig. 10a. The histograms (each containing at least 200 fragments) show the detected fluorescence at every time after starting the back movement of the bead. Performing the data analysis in this way provides a direct negative control since exactly the same enzymes have been observed with and without the applied force. In this way, artifacts from changes in substrate accessibility, from non-specific interactions with the bead or from background fluorescence of the bead can be directly excluded. To corroborate the results obtained from one movie for each experiment, an additional histogram was generated which contains 2 movies (11 enzymes each) from the “10 second” experiment and 1 movie (9 enzymes each) from the “5 second” experiment (Supplementary Fig. 10b).

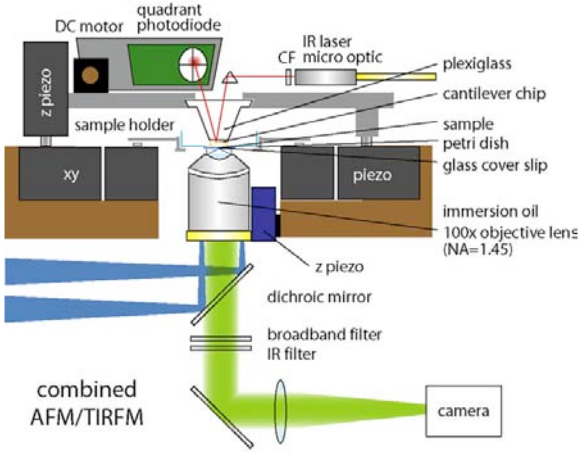
DC motor
quadrant photodiode
IR laser micro optic
CF
plexiglass
cantilever chip
sample
petri dish
glass cover slip
z piezo
sample holder
xy
piezo
immersion oil
100x objective lens (NA=1.45)
z piezo
dichroic mirror
broadband filter
IR filter
combined AFM/TIRFM
camera

**Supplementary Figure 1. Combined AFM-TIRF instrument. The instrument consists of an inverted microscope for objective-type wide-field TIRF excitation and a custom-built AFM head.** TIRF excitation was obtained through a 100x/1.45 oil immersion objective lens (alpha Plan-Fluar, Zeiss, Oberkochen, Germany) using a collimated laser beam focused in the back focal plane of the objective lens such that the beam was totally reflected at the cover slip. In order to excite the carboxyfluorescein dyes a 472 nm, 80 mW DPSS laser (Viasho Technology Co., Ltd., Beijing, China) was used. The focus was controlled using a piezo (Mipos 100, Piezosystemjena, Jena, Germany). Fluorescence imaging was performed using a 128 x 128 pixel back-illuminated EMCCD camera (DU-860, Andor, Belfast, Ireland). The peltier-cooled CCD chip was typically operated at a temperature of -80 °C. An electron multiplication gain of 200x was used. In addition to the appropriate filter set according to the laser and dyes, an IR low-pass filter was built into the detection path in order to block radiation emitted by the AFM's IR laser diode. **The sample was situated on a cover slip glued into a petridish with a hole. This petridish was mounted into a steal vessel that can be moved by the piezo of the TIRF microscope.** In addition the AFM head can be moved relative to the sample.

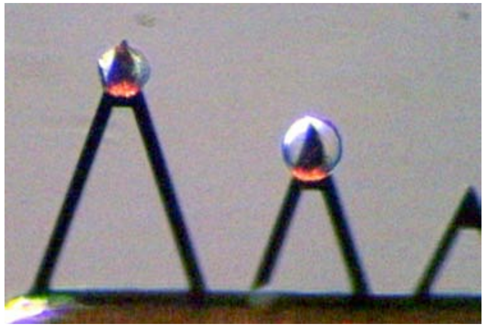

**Supplementary Figure 2. Iodoacetyl-activated beads glued to the cantilever.** After drying, the beads were glued to the cantilevers with glass microneedles and small amounts of epoxy glue. Back in aqueous solution, the beads swell to their original size.

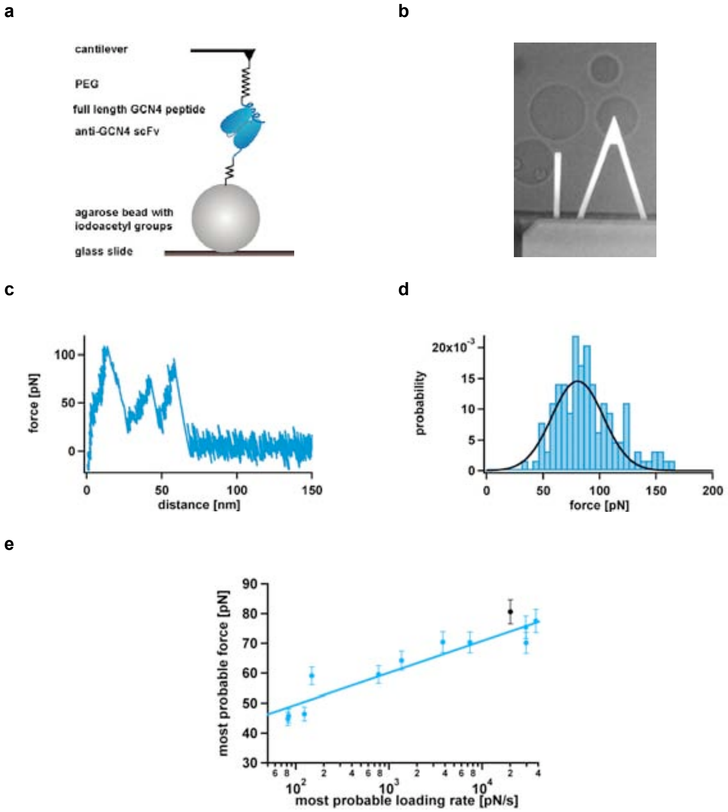

**Supplementary Figure 3. Characterization of the functionality of the antibody functionalized beads. a,** Beads containing the immobilized antibody fragment were deposited on a glass slide. AFM measurements were performed whereby the cantilever containing covalently coupled GCN4 peptide (full length peptide) was brought into contact with one of the beads. During retraction of the cantilever, force extension curves were recorded to characterize the interaction established between the cantilever and the bead. **b,** Image showing the positioning of the cantilever above one of the beads. **c,** Typical force extension curve. During retraction of the cantilever from the bead, the PEG and the agarose spacer flanking the complex of antibody fragment and peptide were stretched and multiple rupture events were observed. **d,** Distribution of rupture forces. The most probable rupture force was determined from a Gaussian fit and equals approximately 80 pN. **e,** Comparison of the obtained rupture force (for a loading rate of 20,000 pN/s) with other values obtained for this interaction. The other data points have been taken from a series of measurements performed to characterize this particular interaction in more detail. In this series of experiments the antibody had been immobilized to the glass slide directly.

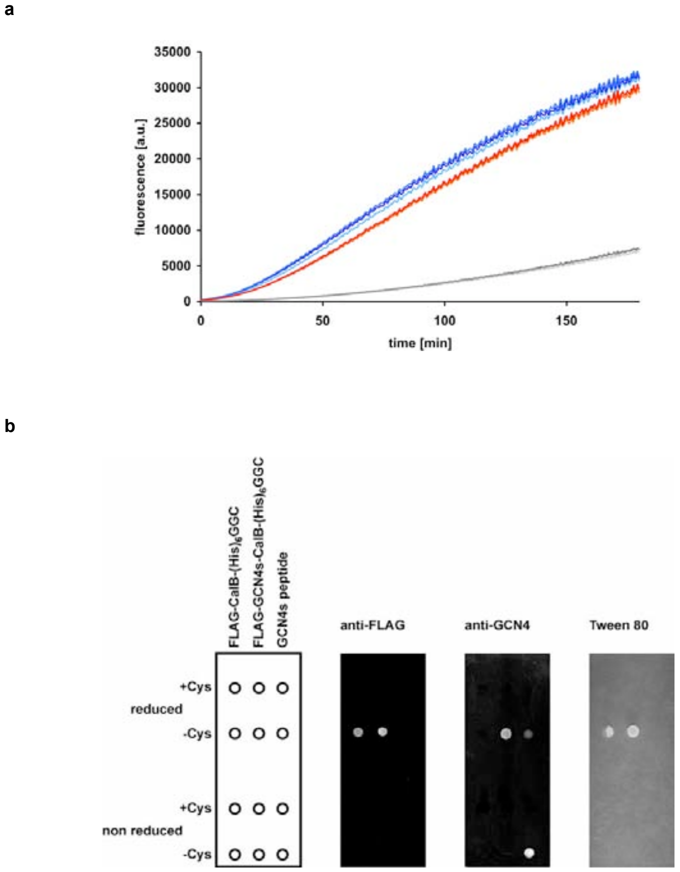

**Supplementary Figure 4. Characterization of the activity of the CalB fusion protein in solution and immobilized onto a surface. a,** Activity measurements in solution. The experiment was carried out to determine the activity of FLAG-GCN4s-CalB-(His)$_6$GGC (red curves) in comparison to FLAG-CalB-(His)$_6$GGC (blue curves). The conversion of the substrate CFDA (50 µM starting concentration) into the fluorescent product carboxyfluoresein was detected as a function of time. The measurements were carried out in triplicate. They yield very similar kinetics for the different fusion proteins clearly showing that the activity of the CalB fusion protein is not influenced by the attached GCN4s peptide. (The grey curves show the autohydrolysis of CFDA in the measurement buffer.) **b,** Characterization of the surface-immobilized CalB fusion protein. The experiment was carried out to determine the activity of surface-immobilized FLAG-GCN4s-CalB-(His)$_6$GGC as well as the accessibility of the N-terminal GCN4s sequence. To test the functional immobilization, FLAG-CalB-(His)$_6$GGC was used as a positive control (since this fusion protein had already been characterized in detail in previous experiments). A chemically synthesized GCN4s peptide (YHLENEVARLKKGGGC) served as the positive control to determine the accessibility of the peptide sequence fused to CalB. For each of the samples (FLAG-GCN4s-CalB-(His)$_6$GGC, FLAG-CalB-(His)$_6$GGC and the GCN4s peptide) different solutions were prepared and spotted onto an maleimide-functionalized glass slide: the samples were spotted on the surface with and without incubating them with the reducing agent (TCEP beads). In addition an excess of free cysteine was added to the reduced and to the non-reduced samples. This was done to investigate the specific binding via the C-terminal cysteines and to detect to what extent non-specific binding to the surface occurs. The samples were spotted on the slide according to the scheme shown on the left side of the figure. The immobilization of the samples to the slide was analyzed with 3 different detection schemes. First, the immobilization of both CalB fusion proteins was proven with an anti-FLAG antibody. The fluorescence scan shows binding of the anti-FLAG antibody to these positions where the reduced fusion proteins have been immobilized. No fluorescence signal is detected at the positions where the non-reduced fusion proteins were immobilized as well as at the positions were the samples with an excess of cysteine were spotted on the surface. This result clearly shows, that the fusion proteins are indeed immobilized via their C-terminal cysteines and that these only become accessible for coupling after treating them with TCEP beads. Second, the slide was incubated in a solution of a fluorescently labeled anti-GCN4 antibody fragment. This antibody fragment only binds to the fusion protein containing the peptide and to the control peptide thereby clearly proving that the peptide sequence attached to the CalB is accessible for the binding of the antibody. (The higher signal for the non-reduced peptide is most likely the result of different concentrations in the spotting solution since the samples are diluted upon incubation with the TCEP beads.) Finally, the activity of the immobilized CalB fusion proteins was detected by incubating the cover slip on agar plates containing Tween 80 and CaCl$_2$. When CalB hydrolyzes the ester bond in Tween 80 the released fatty acid forms a white precipitate with the Ca$^{2+}$ ions. The picture shows this precipitate exactly at those positions where the CalB fusions proteins have been immobilized. In summary, the results of this experiment show that the fusion protein FLAG-GCN4s-CalB-(His)$_6$GGC is immobilized in a site-specific manner and that all the different components are functional.

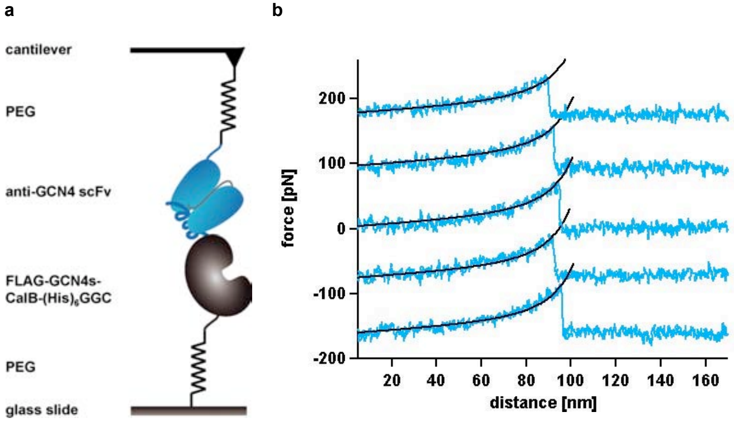

**Supplementary Figure 5. Characterization of the functionality of the CalB fusion protein with the AFM. a,** Experimental set-up. The experiment was performed to prove the accessibility of the GCN4s peptide of the CalB fusion for the recombinant antibody fragment in AFM measurements. This molecular interaction between the antibody fragment and the N-peptide represented the "molecular fuse" which was designed to prevent unfolding of the CalB fusion protein when an external force was applied. The experiment also provides the most probable rupture force and the most probable rupture length which can be used to calculate if the CalB fusion protein is significantly unfolded at the force applied (see Supplementary Figure 6 for more details). The experiment was designed such, that the CalB fusion protein was attached to the glass slide via its C-terminal cysteine using a poly(ethylene glycol) spacer. The antibody fragment was immobilized to the cantilever tip in exactly the same way. **b,** Examples of characteristic force-extension curves. The black lines represent the respective freely jointed chain (FJC) fits for the poly(ethylene glycol) spacer.

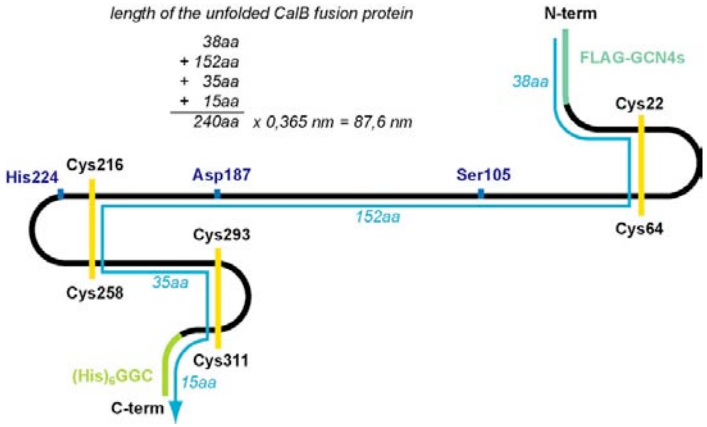

**Supplementary Figure 6. Calculation of the length of the unfolded CalB fusion protein.** If a protein is unfolded as a result of an externally applied force a stretched linear polypeptide chain is obtained. However, when unfolding the CalB fusion protein it has to be considered that CalB contains 3 disulfide bonds (yellow lines). Assuming that the disulfide bonds stay intact when the force is applied, the force in completely unfolded CalB is not entirely transmitted through the polypeptide backbone (black line) but through the disulfide bonds. The path of the force through the unfolded CalB fusion protein is represented by the blue line. The blue values always indicate the number of amino acids up to the next disulfide bond. Adding up these values yields a length of 240 amino acids. In order to obtain the length of the polypeptide in nanometers the number of amino acids needs to be multiplied by the value 0.365 nm, which corresponds to the distance between two adjacent amino acids in a stretched polypeptide chain. Based on this calculation the length of the completely unfolded and stretched CalB fusion protein would equal 87.6 nm. This simplified calculation gives only a rough estimate of the length difference between folded and unfolded CalB. It cannot provide any information if structural disturbations occur in some regions of the protein that might influence the positioning of the amino acids of the catalytic triad (Ser105, Asp187 and His224) or other residues controlling the accessibility of the substrate to the active site.

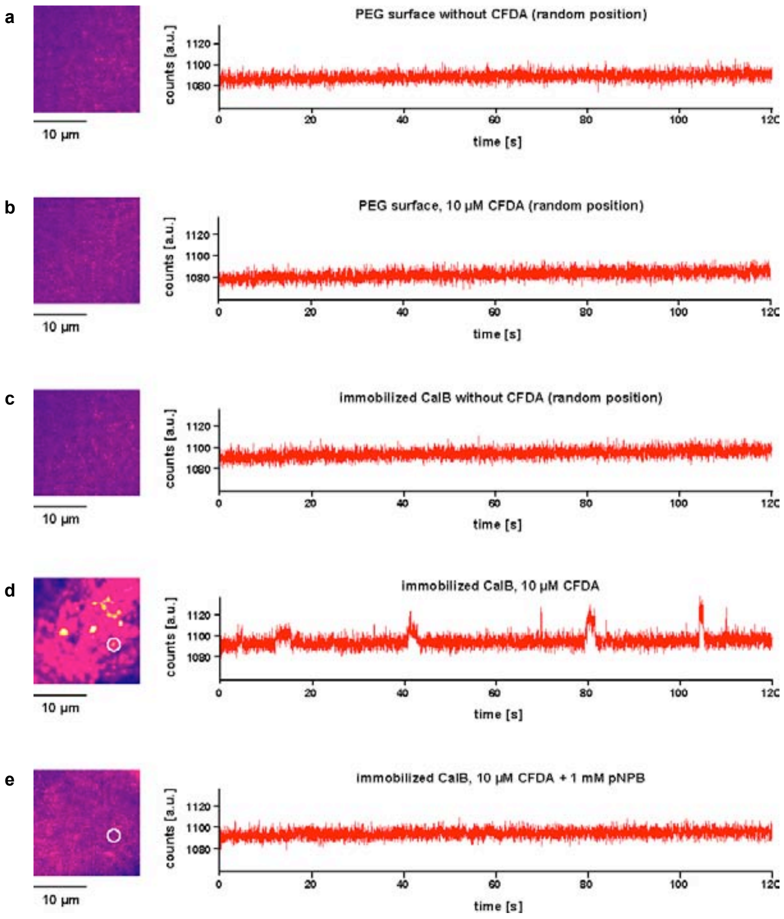

**Supplementary Figure 7. Single enzyme control experiments.** A series of control experiments was performed to relate the detected fluorescence emission at certain positions to the activity of immobilized CalB fusion proteins. **a,** Signal obtained when recording fluorescence emission on a PEG modified surface without immobilized CalB fusion proteins under activity buffer with no CFDA present. A movie was recorded with a frame rate of 50 Hz (integration time 20ms). The signal intensity for each position was integrated over 10,000 frames (left). No specific positions showing fluorescence emission could be

identified Therefore, a random area of 4 x 4 pixels was chosen to generate a time trace of the detected fluorescence intensity (right). **b,** Signal obtained when recording fluorescence emission on a PEG modified surface containing no immobilized CalB fusion proteins under activity buffer with 10 µm CFDA. Again, no specific positions showing fluorescence emission could be identified and a random position was chosen to generate the time trace. **c,** Signal obtained when recording fluorescence emission on a PEG modified surface containing immobilized CalB fusion proteins under activity buffer without substrate. Again, no specific positions showing fluorescence emission could be identified and a random position was chosen to generate the time trace. **d,** Signal obtained when recording fluorescence emission on a PEG modified surface containing immobilized CalB fusion proteins under activity buffer with 10 µm CFDA. After integrating the signal intensity over 10,000 frames several positions become visible on the surface that show a detectably higher fluorescence intensity. Now, an area of 4 x 4 pixels was defined at one of these positions (white circle) and used to generate the time trace. The time trace shows phases with high enzymatic activity separated by phases where no fluorescent product is generated. The switching between these active and inactive phases occurs on a timescale from milliseconds to seconds. **e,** Signal obtained when adding para-nitrophenol butyrate (pNPB) to the experiment. pNPB is a better substrate for CalB than CFDA and was added in 100x excess. The integrated signals as well as the time trace demonstrate that the addition of pNPB reduces the conversion of CFDA and therefore the generation of fluorescent product molecules drastically. The time trace was generated using the same position as for experiment d. In summary these controls show that the emission of fluorescence on the surface originates from the specific hydrolysis of CFDA by the CalB fusion protein.

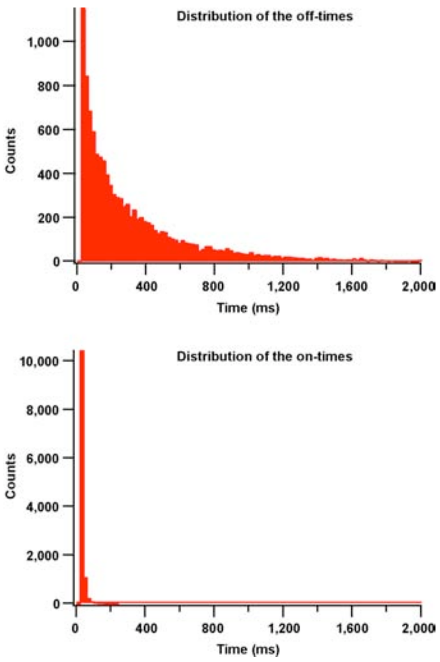

**Supplementary Figure 8. Histograms showing the distribution of the off- and on-times of the CalB fusion protein.** An experiment was performed with a CFDA concentration of 10 µM. Enzymes were identified and time traces were generated from 11 enzymes using an area of 4 x 4 pixels. A threshold (2x standard deviation of the time averaged signal) was defined and values above this threshold were defined as an “on-event” and values below were defined as an “off-event”. The number of frames showing consecutive on- or off-events was counted. The number of frames was converted into milliseconds and the values were plotted into the corresponding on- and off-time histograms, respectively. Because of the relatively short measurement time of 400 seconds (20,000 frames) and the time resolution of 20 ms the data was not fitted with a stretched exponential. However, the distributions clearly show that the probability for an off-state is much higher than for an on-state. The total averaged on-time of these 11 enzymes during the duration of the measurement is only 10.8 seconds or 2.7 % compared to the total time of the measurement. The distributions further show that on-times are relatively short (max. 200 ms) while the off-times can last for up to 2 seconds at the substrate concentration used. Performing the same data analysis on a control area yields a total on-time of 0.3 %. These “on-events” are most likely due to substrate molecules diffusing close to the surface or trace amounts of fluorescent impurities.

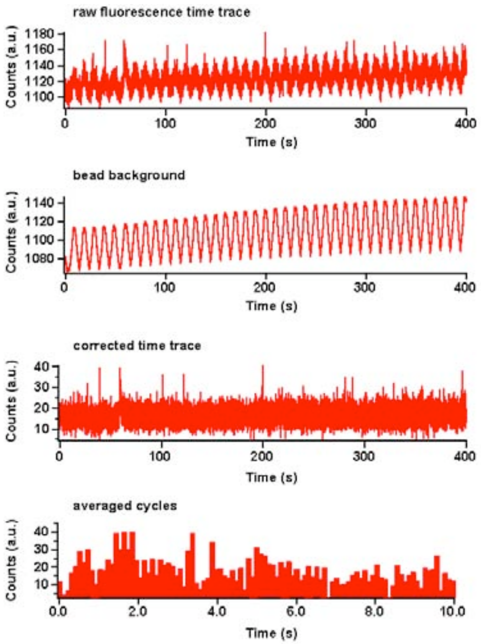

**Supplementary Figure 9. Data evaluation of the fluorescence time traces from the combined AFM-TIRF measurements.** The time traces of the enzymatic turnover events from the combined measurements are overlaid with a periodic alteration of the fluorescence signal originating from the bead. In order to correct for this periodic signal the following procedure was applied: After having identified potential enzymes, an area of 4 x 4 pixels was defined as “enzyme” and a nearby area of the same size showing no enzymatic turnover events was defined as “background”. For each frame the background value was subtracted from the enzyme value yielding the corrected time traces. Now, to ensure that the positions identified indeed represent enzymes, the time average over all frames was calculated for the enzyme and the background. Only time traces where the time average for the “enzyme” was higher than 2x the standard deviation of the “background” were used in the next steps. In addition, the fluorescence intensity had to switch between high fluorescence and low fluorescence at least 3 times within 200 seconds. Based on the periodic movement of the bead these time traces were cut into 10 s fragments using the time at which the bead was moved away from the surfaces as “0”. These fragments were used for further analysis thereby discriminating if a rupture event was recorded with the AFM for the respective fragment. Finally, for all fragments with a rupture event and for all fragments without a rupture event, the fluorescence intensities of all corresponding frames were added and divided by the number of fragments. In this way two histograms were generated with a bin size of 100 ms: one containing all fragments in which no rupture event took place and one which contains the fragments with a rupture event (“averaged cycles” shown above). The histogram shows a slightly higher number of counts after 1.7 seconds, which is becoming more pronounced when adding more time traces from other enzymes.

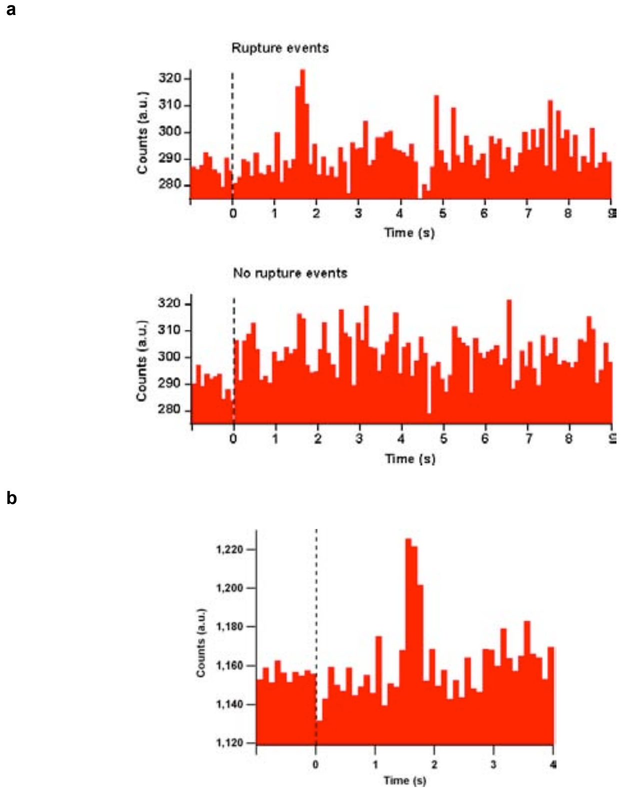

**Supplementary Figure 10. Additional histograms summarizing the results from the combined AFM/TIRF experiments. a,** Histograms summing up the counts obtained for 11 enzymes taken from 1 movie. The total numbers of fragments in the histograms are 231 fragments with a rupture event and 209 fragments without a rupture event, respectively. The data is identical with the data used for Figure 3 but shows the whole time of one manipulation cycle, which is 10 seconds in this case. **b,** Histogram summing up the counts obtained from 3 movies in total (2 movies with a 10 second manipulation cylce – 11 enzymes each; 1 movie with 5 second manipulation cycle – 9 enzymes). This histogram confirms the higher amount of counts after 1.7 seconds while the counts at other times are homogenously distributed during the manipulation cycle.

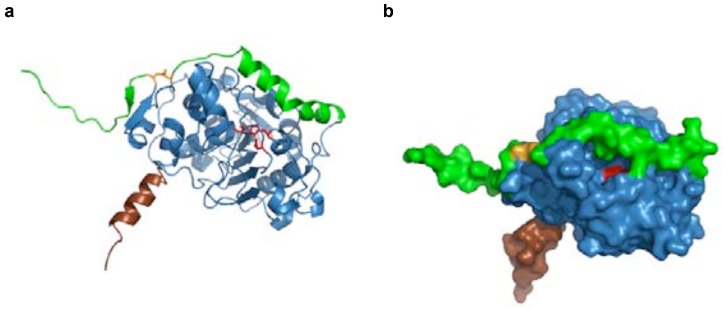

**Supplementary Figure 11. Possible influence of the applied force on CalB activity.** In contrast to other lipases CalB is not interfacially activated and a lid structure has not been clearly identified. However, concluding from the crystal structure, two $\alpha$-helices, which are close to the active site, might be able to undergo conformational changes thereby defining the access of substrate to the active site. The shown structure (PDB code 1TCA; N-terminal and C-terminal tags attached with Swiss pdb viewer and figure prepared with Pymol) is considered to represent CalB in the "open conformation". **a,** One of the relevant $\alpha$-helices is shown in green. This $\alpha$-helix is directly connected to the C-terminus of the CalB fusion protein via a disulfide bond (shown in yellow). Therefore, a force, which is applied at the C-terminus, is directly transmitted to the active site (residues labeled in red). **b,** Since the active site is relatively narrow and this $\alpha$-helix lines one side of the active site pocket a disturbed $\alpha$-helix might give more access to the active site especially for bulky substrates such as CFDA. Based on this picture the increased activity after 1.7 seconds might indeed originate from a significant perturbation of the CalB structure. After the release of the force the molecule rearranges thereby generating a different conformation of the relevant $\alpha$-helix. This conformation determining a different shape of the active site then further rearranges thereby again restricting the access of CFDA to the active site.

# A combined AFM-TIRF microscope for simultaneous single molecule experiments

H Gumpp[1], SW Stahl[1], M Strackharn[1], EM Puchner[1,2] and HE Gaub[1]
[1] Chair for Applied Physics and Center for NanoScience
Ludwig-Maximilians-University Munich, Germany
[2] Center for Integrated Protein Science Munich

October 28, 2008

**The Atomic Force Microscope (AFM) has revolutionized nano science in many ways and today is also widely used in biophysics as a tool to image nanoscale structures, as well as to measure and apply forces (*2, 17, 18*). While AFM techniques are very precise in terms of spatial and force resolution, even the fastest AFMs currently are orders of magnitude slower in terms of imaging compared to optical methods (*7*). On the other hand traditional optical microscopy provides fast readout, but is limited by diffraction. Therefore it is obvious that AFM and single molecule fluorescence microscopy are complementing each other very well (*8*). As the AFM is a tool to operate on surfaces, the choice of Total Internal Fluorescence as illumination source for single molecule microscopy is convenient. However vibrations of the sample that could have been neglected in sole single molecules TIRF microscope setups become an issue, because they are prohibiting high-precision AFM measurements. Here, we present a very compact microscope setup featuring a solid connection between an immersion objective lens, AFM and sample. By mechanically decoupling the focus mechanism from the sample and the AFM-head, vibrations limiting the force resolution can be eliminated virtually completely.**

## 1 Objective-type TIRF microscopy

There are different methods commonly used for coupling light into a glass cover slip in order to obtain an evanescent field for TIRF illumination (*1*). Whereas prism-based systems allow for use of variety of glass substrates and incident angles, and are not limited by the numerical aperture of the objective lens, combining them with an AFM is difficult. An objective-type TIRF setup installed at an inverted microscope has the advantage of using a objective lens with high numerical aperture for excitation as well as for collection of emission, therefore leaving the upper half space above the sample free. A scanning probe microscope, like the AFM can then be placed above the sample for simultaneous imaging, force measurements and manipulating the sample.

Since high NA-objective lenses have very short working distances, objective-type TIRF can only be performed on thin cover slips, with a thickness of up to 0.15mm. These thin glass substrates are prone to deformation and vibrations, coupling through the system mechanically and the air. This makes it hard to do high-resolution AFM measurements since noise is typically very high. While sound coupling into the system can be damped effectively by putting the whole setup into a soundproof box, mechanical vibrations are still hard to handle. Oscillations below 100Hz, as arising from the building, can be effectively damped by active tables, but higher frequencies and especially noise sources inside the microscope itself still have to be eliminated.

A high numerical aperture objective lens needs immersion oil to be operated to match the refractive index of the glass substrate. When using the objective lens for adjusting the focus, as it is done with virtually all commercially available objective-type TIRF setups so far, additional vibrations from e.g. a focussing piezo are coupled into the glass cover slip. For TIRF illumination the focus has to be adjusted very precisely, because the evanescent field is only a few hundred nm. During long measurements temperature changes as well as puffer evaporation may cause the surface to drift out of focus. Hence when operating commercially available focus piezo stages of the objective lens in a closed loop in order to correct for this focus drift, strong vibrations couple into the sample through the immersion oil, thereby making high resolution AFM experiments virtually impossible. Figure 2 shows the spectral distribution of noise, i.e. vibrations of the cover slip, comparing a traditional setup with focus-piezo and our new setup with fixed objective lens. Measurements have been accomplished by putting the AFM cantilever on the surface and taking thermal noise spectra.

## 2 Experimental setup

Whereas in most microscopes an objective lens is mounted on a revolver and/or focus piezo, our setup contains a high NA objective lens which is rigidly mounted at a big aluminum block on which the AFM head stands on as Fig. 1 shows. Focussing is facilitated by moving the tube lens via a linear motor (High-Accuracy Linear Translation Stage M-605, Physik Instrumente, Karlsruhe, Germany) which focuses the fluorescence light from the sample on the chip of the EMCCD camera (Andor iXon DU-888, Andor Technology, Belfast, Ireland) . This motor is completely mechanically decoupled from the rest of the instrument and does not need to stand on the vibration insulation table. In order to build a most compact instrument, for the excitation path, the light of a solid state diode pulsed laser (532nm DPSS Laser, CrystaLaser, Reno, NV, USA) is coupled into a single-mode optical fiber and used for fluorescence excitation via a compact slider unit consisting of, a collimator lens, a clean-up filter, a lens for focussing the beam into the back focal plane of the objective lens and an adjustable dichroic mirror that directs the light to the sample. This unit can be replaced easily with another one containing another filterset, when working with a different laser. In total internal reflection the back-reflected beam hits a quadrant photo diode afterwards, which measures its position. This way a change in angle of the reflected beam and hence a change in distance between the objective lens and the cover slip can be determined. Finally this information can be used for correction of focus via the tube lens.

Modern objective lenses with high numerical aperture, like the Nikon 100x lens (CFI Apo TIRF 100x, N.A. 1.49, Nikon Inc., Tokyo, Japan) we used here, allow for varying the penetration depth of

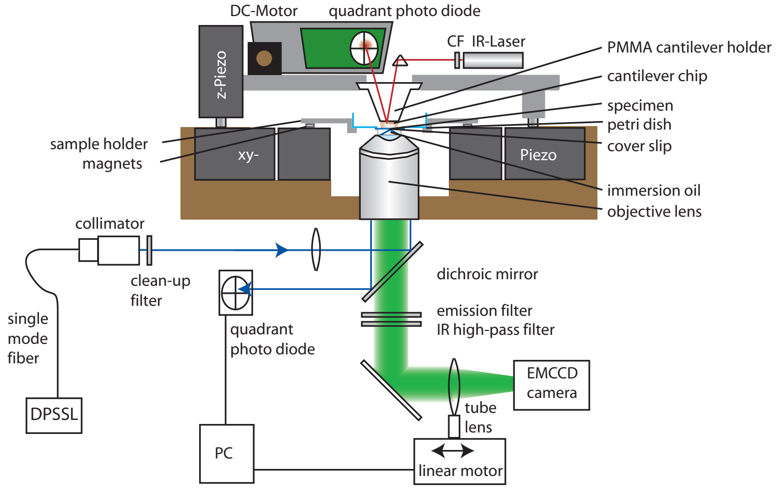
DC-Motor
quadrant photo diode
CF
IR-Laser
z-Piezo
PMMA cantilever holder
cantilever chip
specimen
petri dish
cover slip
sample holder
magnets
xy-
Piezo
immersion oil
objective lens
collimator
clean-up
filter
dichroic mirror
emission filter
IR high-pass filter
single
mode
fiber
quadrant
photo diode
EMCCD
camera
DPSSL
tube
lens
PC
linear motor

Figure 1: Schematic drawing of the combined AFM/TIRF microscope. TIRF excitation is performed by a diode pulsed solid-state laser coupled to a single-mode fiber. Using a collimator lens and a biconcave lens for focussing the beam on the back focal plane of the objective lens, wide-field TIRF illumination is achieved. Fluorescence emission passes through an appropriate filter-set and is collected by the EMCCD camera. The tube lens is used for focussing and therefore mounted on a linear motor controlled by a PC that reads the position of the back-reflected beam from a quadrant photo diode. This feedback ensures a constantly sharp image.

the evanescent field, depending on the distance of the beam from the rim of the objective lens. This is achieved by shifting laser orthogonally to the optical axis of the objective lens. Like this the penetration depth can be varied between approx. 200-500 nm.

## 3 Experimental Results

In order to compare the new setup with conventional combined AFM-TIRF hybrids we measured the vibrations of the sample, noise spectra were taken with an AFM cantilever contacting the surface. Measurements were performed using a Veeco MLCT-C Cantilever at a contact force of 1nN. The sample is clamped tightly to the xy-piezo scanner by small magnets. It can be adjusted using micrometer screws for coarse alignment, since the objective lens is fixed rigidly attached to the aluminum block that incorporates the piezo table. As the noise spectra show, cover slip vibrations are one or two magnitudes higher when operating the focus piezo in closed loop and even with the piezo switched off there are still some noise peaks visible. In contrast, even when operating the new setup with fixed objective but moveable tube lens in closed loop, cover slip vibrations are reduced to a minimum.

When the z-piezo is operated in closed loop, simultanteous AFM measurement become very noisy. Vibrations in the frequency of the electricity carrier frequency of 50Hz (and multiples) as well as the resonance frequency of the cover slip at about 300 Hz become clearly visible.

This combined AFM-TIRF instrument was used for simultaneous single molecule experiments like the single molecule cut and paste technique as described in (*9*) . Using hierarchical forces fluorescently labelled biomolecules were picked up from a depot, transported and deposited with nm precision to a target area. The above described setup made it possible to obtain sharp images at all time while allowing for high resolution force curves for many hours.

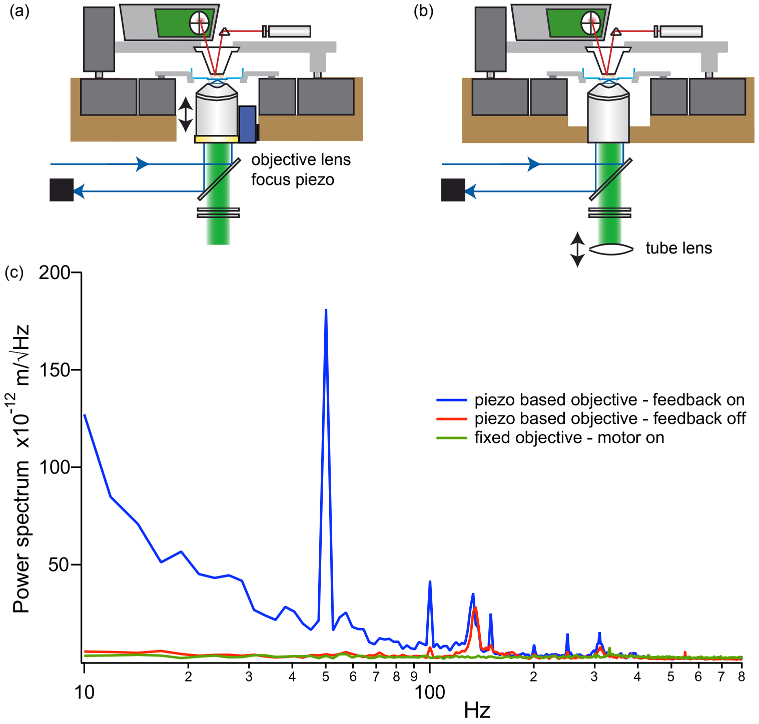

Figure 2: Comparison of noise spectra taken by contacting the surface of the cover slip with the AFM cantilever tip. (a) shows the old setup with objective lens focus piezo and (b) the new setup with moveable tube lens for focussing. The corresponding noise spectra are plotted in (c).

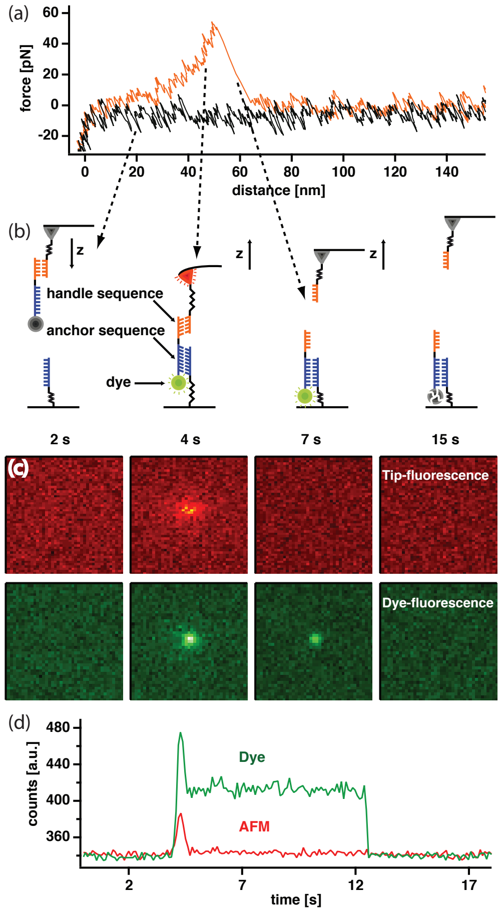

Figure 3: Single molecule cut-and-paste experiment performed using the combined TIRF-AFM microscope. Flourescently labelled DNA strands are transported by the AFM using a specific handle sequence on the tip and an anchor sequence on the cover slip surface. High-resolution force spectra and single molecule fluorescence time traces are recorded simultaneously for many hours.

## 4 Concluding Remarks

During day-to-day use, this combined TIRF-AFM instrument proved to be a versatile instrument for many kinds of single molecule experiments. The compact design with decoupled focussing succeeded in reaching a maximum of force resolution on the AFM side, while at the same time assuring a constantly sharp image for state-of-the-art single molecule microscopy.

## 5 Acknowledgements

(*1, 3–6, 8, 10–16, 19–23*)

## References

1. D Axelrod, N L Thompson, and T P Burghardt. Total internal inflection fluorescent microscopy. *Journal of microscopy*, 129(Pt 1):19–28, Jan 1983.

2. Andreas Engel and Hermann E Gaub. Structure and mechanics of membrane proteins. *Annu Rev Biochem*, 77:127–48, Jan 2008.

3. R Fiolka, Y Belyaev, H Ewers, and A Stemmer. Even illumination in total internal reflection fluorescence microscopy using laser light. *Microsc Res Tech*, 71(1):45–50, Jan 2008.

4. T Funatsu, Y Harada, H Higuchi, M Tokunaga, K Saito, Y Ishii, R D Vale, and T Yanagida. Imaging and nano-manipulation of single biomolecules. *Biophys Chem*, 68(1-3):63–72, Oct 1997.

5. T Funatsu, Y Harada, M Tokunaga, K Saito, and T Yanagida. Imaging of single fluorescent molecules and individual atp turnovers by single myosin molecules in aqueous solution. *Nature*, 374(6522):555–9, Apr 1995.

6. Alexander Gaiduk, Ralf Kühnemuth, Matthew Antonik, and Claus A M Seidel. Optical characteristics of atomic force microscopy tips for single-molecule fluorescence applications. *Chemphyschem : a European journal of chemical physics and physical chemistry*, 6(5):976–83, May 2005.

7. Paul K Hansma, Georg Schitter, Georg E Fantner, and Craig Prater. Applied physics. high-speed atomic force microscopy. *Science*, 314(5799):601–2, Oct 2006.

8. Andrew Hards, Chunqing Zhou, Markus Seitz, Christoph Bräuchle, and Andreas Zumbusch. Simultaneous afm manipulation and fluorescence imaging of single dna strands. *Chemphyschem : a European journal of chemical physics and physical chemistry*, 6(3):534–40, Mar 2005.

9. S K Kufer, E M Puchner, H Gumpp, T Liedl, and H E Gaub. Single-molecule cut-and-paste surface assembly. *Science*, 319(5863):594–6, Feb 2008.

10. E Lang, J Baier, and J Köhler. Epifluorescence, confocal and total internal reflection microscopy for single-molecule experiments: a quantitative comparison. *Journal of microscopy*, 222(Pt 2):118–23, May 2006.

11. Robert A Lugmaier, Thorsten Hugel, Martin Benoit, and Hermann E Gaub. Phase contrast and dic illumination for afm hybrids. *Ultramicroscopy*, 104(3-4):255–60, Oct 2005.

12. A B Mathur, G A Truskey, and W M Reichert. Atomic force and total internal reflection fluorescence microscopy for the study of force transmission in endothelial cells. *Biophys J*, 78(4):1725–35, Apr 2000.

13. C G Morgan and A C Mitchell. Total internal reflection fluorescence imaging using an upconverting cover slip for multicolour evanescent excitation. *Journal of microscopy*, 222(Pt 1):48–57, Apr 2006.

14. Shuhei Nishida, Yutaka Funabashi, and Atsushi Ikai. Combination of afm with an objective-type total internal reflection fluorescence microscope (tirfm) for nanomanipulation of single cells. *Ultramicroscopy*, 91(1-4):269–74, May 2002.

15. So Nishikawa. [basics of tirfm]. *Nippon Rinsho*, 65(2):263–9, Feb 2007.

16. Lu Peng, Bryan J Stephens, Keith Bonin, Roger Cubicciotti, and Martin Guthold. A combined atomic force/fluorescence microscopy technique to select aptamers in a single cycle from a small pool of random oligonucleotides. *Microsc Res Tech*, 70(4):372–81, Apr 2007.

17. Elias M Puchner, Alexander Alexandrovich, Ay Lin Kho, Ulf Hensen, Lars V Schäfer, Birgit Brandmeier, Frauke Gräter, Helmut Grubmüller, Hermann E Gaub, and Mathias Gautel. Mechanoenzymatics of titin kinase. *Proc Natl Acad Sci USA*, 105(36):13385–90, Sep 2008.

18. M Rief, M Gautel, and H E Gaub. Unfolding forces of titin and fibronectin domains directly measured by afm. *Adv Exp Med Biol*, 481:129–36; discussion 137–41, Jan 2000.

19. Herbert Schneckenburger. Total internal reflection fluorescence microscopy: technical innovations and novel applications. *Curr Opin Biotechnol*, 16(1):13–8, Feb 2005.

20. Andreea Trache and Gerald A Meininger. Atomic force-multi-optical imaging integrated microscope for monitoring molecular dynamics in live cells. *Journal of biomedical optics*, 10(6):064023, Jan 2005.

21. Alejandro Valbuena, Javier Oroz, Andrés Manuel Vera, Alejandro Gimeno, Julio Gómez-Herrero, and Mariano Carrión-Vázquez. Quasi-simultaneous imaging/pulling analysis of single polyprotein molecules by atomic force microscopy. *The Review of scientific instruments*, 78(11):113707, Nov 2007.

22. Tetsuichi Wazawa and Masahiro Ueda. Total internal reflection fluorescence microscopy in single molecule nanobioscience. *Adv Biochem Eng Biotechnol*, 95:77–106, Jan 2005.

23. Takafumi Yamada, Rehana Afrin, Hideo Arakawa, and Atsushi Ikai. High sensitivity detection of protein molecules picked up on a probe of atomic force microscope based on the fluorescence

detection by a total internal reflection fluorescence microscope. *FEBS Lett*, 569(1-3):59–64, Jul 2004.

# 8. Referenzen

1. Morfill, J., et al., *B-S transition in short oligonucleotides.* Biophys J, 2007. 93(7): p. 2400-9.
2. Lange, S., et al., *The kinase domain of titin controls muscle gene expression and protein turnover.* Science, 2005. 308(5728): p. 1599-603.
3. Kersey, P.J., et al., *The International Protein Index: An integrated database for proteomics experiments.* Proteomics, 2004. 4(7): p. 1985-1988.
4. Davison, D.B., *The number of human genes and proteins.* 2006 International Conference on Computational Nanoscience and Nanotechnology - ICCN 2002 - AN INTERDISCIPLINARY INTEGRATIVE FORUM ON NANOTECHNOLOGY COMPUTATIONAL EFFORTS IN THE BIOLOGY, CHEMISTRY, PHYSICS AND MATERIALS FIELDS, 2002: p. 6-9.
5. Debrunner, P.G. and H. Frauenfelder, *Dynamics of Proteins.* Annual Review of Physical Chemistry, 1982. 33: p. 283-299.
6. Frauenfelder, H., F. Parak, and R.D. Young, *Conformational Substates in Proteins.* Annual Review of Biophysics and Biophysical Chemistry, 1988. 17: p. 451-479.
7. Frauenfelder, H., S.G. Sligar, and P.G. Wolynes, *The Energy Landscapes and Motions of Proteins.* Science, 1991. 254(5038): p. 1598-1603.
8. Eisenmesser, E.Z., et al., *Enzyme dynamics during catalysis.* Science, 2002. 295(5559): p. 1520-3.
9. Eisenmesser, E.Z., et al., *Intrinsic dynamics of an enzyme underlies catalysis.* Nature, 2005. 438(7064): p. 117-21.
10. Edman, L., et al., *The fluctuating enzyme: a single molecule approach.* Chemical Physics, 1999. 247(1): p. 11-22.
11. Lu, H.P., L. Xun, and X.S. Xie, *Single-molecule enzymatic dynamics.* Science, 1998. 282(5395): p. 1877-82.
12. English, B.P., et al., *Ever-fluctuating single enzyme molecules: Michaelis-Menten equation revisited.* Nat. Chem. Biol., 2006. 2(2): p. 87-94.
13. Bell, G.I., *Models for the specific adhesion of cells to cells.* Science, 1978. 200(4342): p. 618-27.
14. Evans, E. and K. Ritchie, *Dynamic strength of molecular adhesion bonds.* Biophys J, 1997. 72(4): p. 1541-55.
15. Evans, E. and K. Ritchie, *Strength of a weak bond connecting flexible polymer chains.* Biophys J, 1999. 76(5): p. 2439-47.
16. Dudko, O.K., et al., *Beyond the conventional description of dynamic force spectroscopy of adhesion bonds.* Proc Natl Acad Sci U S A, 2003. 100(20): p. 11378-81.
17. Sarkar, A., S. Caamano, and J.M. Fernandez, *The elasticity of individual titin PEVK exons measured by single molecule atomic force microscopy.* J Biol Chem, 2005. 280(8): p. 6261-4.
18. Li, H., et al., *Multiple conformations of PEVK proteins detected by single-molecule techniques.* Proc Natl Acad Sci U S A, 2001. 98(19): p. 10682-6.
19. Linke, W.A., et al., *PEVK domain of titin: an entropic spring with actin-binding properties.* J Struct Biol, 2002. 137(1-2): p. 194-205.
20. Rief, M., et al., *Reversible unfolding of individual titin immunoglobulin domains by AFM.* Science, 1997. 276(5315): p. 1109-12.
21. Kellermayer, M.S., et al., *Folding-unfolding transitions in single titin molecules characterized with laser tweezers.* Science, 1997. 276(5315): p. 1112-6.
22. Rief, M., et al., *The mechanical stability of immunoglobulin and fibronectin III domains in the muscle protein titin measured by atomic force microscopy.* Biophys J, 1998. 75(6): p. 3008-14.
23. Li, H., et al., *Reverse engineering of the giant muscle protein titin.* Nature, 2002. 418(6901): p. 998-1002.

24. Li, H., et al., *Point mutations alter the mechanical stability of immunoglobulin modules.* Nat Struct Biol, 2000. 7(12): p. 1117-20.
25. Lange, S., et al., *Dimerisation of myomesin: Implications for the structure of the sarcomeric M-band.* Journal of Molecular Biology, 2005. 345(2): p. 289-298.
26. Fukuzawa, A., et al., *Interactions with titin and myomesin target obscurin and obscurin-like 1 to the M-band: implications for hereditary myopathies.* J Cell Sci, 2008. 121(Pt 11): p. 1841-51.
27. Mayans, O., et al., *Structural basis for activation of the titin kinase domain during myofibrillogenesis.* Nature, 1998. 395: p. 863-869.
28. Nicolao, P., et al., *Autosomal dominant myopathy with proximal weakness and early respiratory muscle involvement maps to chromosome 2q.* Am J Hum Genet, 1999. 64(3): p. 788-92.
29. Edstrom, L., et al., *Myopathy with respiratory failure and typical myofibrillar lesions.* J Neurol Sci, 1990. 96(2-3): p. 211-28.
30. Peng, J., et al., *Cardiac hypertrophy and reduced contractility in hearts deficient in the titin kinase region.* Circulation, 2007. 115(6): p. 743-51.
31. Volkman, B.F., et al., *Two-state allosteric behavior in a single-domain signaling protein.* Science, 2001. 291(5512): p. 2429-33.
32. Henzler-Wildman, K. and D. Kern, *Dynamic personalities of proteins.* Nature, 2007. 450: p. 964-972.
33. Boehr, D.D., et al., *The dynamic energy landscape of dihydrofolate reductase catalysis.* Science, 2006. 313(5793): p. 1638-42.
34. Hammes-Schiffer, S. and S.J. Benkovic, *Relating protein motion to catalysis.* Annu. Rev. Biochem., 2006. 75: p. 519-41.
35. Xie, X.S. and H.P. Lu, *Single-molecule enzymology.* Journal of Biological Chemistry, 1999. 274(23): p. 15967-15970.
36. Edman, L. and R. Rigler, *Memory landscapes of single-enzyme molecules.* Proceedings of the National Academy of Sciences of the United States of America, 2000. 97(15): p. 8266-8271.
37. Sarda, L. and P. Desnuelle, *Action De La Lipase Pancreatique Sur Les Esters En Emulsion.* Biochimica Et Biophysica Acta, 1958. 30(3): p. 513-521.
38. Yuan, Z., J. Zhao, and Z.X. Wang, *Flexibility analysis of enzyme active sites by crystallographic temperature factors.* Protein Engineering, 2003. 16(2): p. 109-114.
39. Uppenberg, J., et al., *Sequence, Crystal-Structure Determination and Refinement of 2 Crystal Forms of Lipase-B from Candida-Antarctica.* Structure, 1994. 2(4): p. 293-308.
40. Velonia, K., et al., *Single-enzyme kinetics of CALB-catalyzed hydrolysis.* Angew Chem Int Ed Engl, 2005. 44(4): p. 560-4.
41. Engelkamp, H., et al., *Do enzymes sleep and work?* Chem Commun (Camb), 2006(9): p. 935-40.
42. Flomenbom, O., et al., *Stretched exponential decay and correlations in the catalytic activity of fluctuating single lipase molecules.* Proc Natl Acad Sci U S A, 2005. 102(7): p. 2368-72.
43. De Cremer, G., et al., *Dynamic disorder and stepwise deactivation in a chymotrypsin catalyzed hydrolysis reaction.* J. Am. Chem. Soc., 2007. 129(50): p. 15458-9.
44. Luo, G., et al., *Dynamic distance disorder in proteins is caused by trapping.* J. Phys. Chem. B, 2006. 110(19): p. 9363-7.
45. Pluckthun, A., *Antibody Engineering.* Current Opinion in Biotechnology, 1991. 2(2): p. 238-246.
46. Hanes, J. and A. Pluckthun, *In vitro selection and evolution of functional proteins by using ribosome display.* Proceedings of the National Academy of Sciences of the United States of America, 1997. 94(10): p. 4937-4942.
47. Zahnd, C., et al., *Directed in vitro evolution and crystallographic analysis of a peptide-binding single chain antibody fragment (scFv) with low picomolar affinity.* Journal of Biological Chemistry, 2004. 279(18): p. 18870-18877.

48. Binnig, G., C.F. Quate, and C. Gerber, *Atomic Force Microscope.* Physical Review Letters, 1986. 56(9): p. 930-933.
49. Watson, J.D. and F.H.C. Crick, *Molecular Structure of Nucleic Acids - a Structure for Deoxyribose Nucleic Acid.* Nature, 1953. 171(4356): p. 737-738.
50. Chen, J.H. and N.C. Seeman, *Synthesis from DNA of a molecule with the connectivity of a cube.* Nature, 1991. 350(6319): p. 631-3.
51. Shih, W.M., J.D. Quispe, and G.F. Joyce, *A 1.7-kilobase single-stranded DNA that folds into a nanoscale octahedron.* Nature, 2004. 427(6975): p. 618-21.
52. Rothemund, P.W., et al., *Design and characterization of programmable DNA nanotubes.* J Am Chem Soc, 2004. 126(50): p. 16344-52.
53. Winfree, E., et al., *Design and self-assembly of two-dimensional DNA crystals.* Nature, 1998. 394(6693): p. 539-44.
54. Rothemund, P.W., *Folding DNA to create nanoscale shapes and patterns.* Nature, 2006. 440(7082): p. 297-302.
55. Pellegrino, T., et al., *On the development of colloidal nanoparticles towards multifunctional structures and their possible use for biological applications.* Small, 2005. 1(1): p. 48-63.
56. Mirkin, C.A., et al., *A DNA-based method for rationally assembling nanoparticles into macroscopic materials.* Nature, 1996. 382(6592): p. 607-9.
57. Nykypanchuk, D., et al., *DNA-guided crystallization of colloidal nanoparticles.* Nature, 2008. 451(7178): p. 549-52.
58. Alivisatos, A.P., et al., *Organization of 'nanocrystal molecules' using DNA.* Nature, 1996. 382(6592): p. 609-11.
59. Strunz, T., et al., *Dynamic force spectroscopy of single DNA molecules.* Proc Natl Acad Sci U S A, 1999. 96(20): p. 11277-82.
60. EssevazRoulet, B., U. Bockelmann, and F. Heslot, *Mechanical separation of the complementary strands of DNA.* Proceedings of the National Academy of Sciences of the United States of America, 1997. 94(22): p. 11935-11940.
61. Rief, M., H. Clausen-Schaumann, and H.E. Gaub, *Sequence-dependent mechanics of single DNA molecules.* Nat Struct Biol, 1999. 6(4): p. 346-9.
62. Krautbauer, R., M. Rief, and H.E. Gaub, *Unzipping DNA oligomers.* Nano Letters, 2003. 3(4): p. 493-496.
63. Finer, J.T., R.M. Simmons, and J.A. Spudich, *Single Myosin Molecule Mechanics - Piconewton Forces and Nanometer Steps.* Nature, 1994. 368(6467): p. 113-119.
64. Molloy, J.E., et al., *Single-Molecule Mechanics of Heavy-Meromyosin and S1 Interacting with Rabbit or Drosophila Actins Using Optical Tweezers.* Biophysical Journal, 1995. 68(4): p. S298-S305.
65. Tskhovrebova, L. and J. Trinick, *Titin: Properties and family relationships.* Nature Reviews Molecular Cell Biology, 2003. 4(9): p. 679-689.
66. Huxley, H.E., et al., *Time-Resolved X-Ray-Diffraction Studies of the Myosin Layer-Line Reflections During Muscle-Contraction.* Journal of Molecular Biology, 1982. 158(4): p. 637-684.
67. Linari, M., et al., *Interference fine structure and sarcomere length dependence of the axial x-ray pattern from active single muscle fibers.* Proceedings of the National Academy of Sciences of the United States of America, 2000. 97(13): p. 7226-7231.
68. Minajeva, A., et al., *Unfolding of titin domains explains the viscoelastic behavior of skeletal myofibrils.* Biophysical Journal, 2001. 80(3): p. 1442-1451.
69. Blank, K., J. Morfill, and H.E. Gaub, *Site-specific immobilization of genetically engineered variants of Candida antarctica lipase B.* Chembiochem, 2006. 7(9): p. 1349-1351.
70. Blank, K., et al., *Functional expression of Candida antarctica lipase B in Eschericha coli.* Journal of Biotechnology, 2006. 125(4): p. 474-483.
71. Morfill, J., et al., *Force-based analysis of multidimensional energy landscapes: Application of dynamic force spectroscopy and steered molecular dynamics simulations to an antibody fragment-peptide complex.* Journal of Molecular Biology, 2008. 381(5): p. 1253-1266.

72. Levene, M.J., et al., *Zero-mode waveguides for single-molecule analysis at high concentrations.* Science, 2003. 299(5607): p. 682-6.
73. Ashkin, A., *Applications of Laser Radiation Pressure.* Science, 1980. 210(4474): p. 1081-1088.
74. Ashkin, A., *Optical trapping and manipulation of neutral particles using lasers.* Proc Natl Acad Sci U S A, 1997. 94(10): p. 4853-60.
75. Dumont, S., et al., *RNA translocation and unwinding mechanism of HCVNS3 helicase and its coordination by ATP.* Nature, 2006. 439(7072): p. 105-108.
76. Maier, B., D. Bensimon, and V. Croquette, *Replication by a single DNA polymerase of a stretched single-stranded DNA.* Proceedings of the National Academy of Sciences of the United States of America, 2000. 97(22): p. 12002-12007.
77. Smith, D.E., et al., *The bacteriophage phi 29 portal motor can package DNA against a large internal force.* Nature, 2001. 413(6857): p. 748-752.
78. Rock, R.S., et al., *In vitro assays of processive myosin motors.* Methods-a Companion to Methods in Enzymology, 2000. 22(4): p. 373-381.
79. Bockelmann, U., et al., *Unzipping DNA with optical tweezers: high sequence sensitivity and force flips.* Biophysical Journal, 2002. 82(3): p. 1537-1553.
80. Visscher, K., M.J. Schnitzer, and S.M. Block, *Single kinesin molecules studied with a molecular force clamp.* Nature, 1999. 400(6740): p. 184-189.
81. Mehta, A.D., et al., *Myosin-V is a processive actin-based motor.* Nature, 1999. 400(6744): p. 590-593.
82. Smith, S.B., L. Finzi, and C. Bustamante, *Direct Mechanical Measurements of the Elasticity of Single DNA-Molecules by Using Magnetic Beads.* Science, 1992. 258(5085): p. 1122-1126.
83. Strick, T.R., V. Croquette, and D. Bensimon, *Single-molecule analysis of DNA uncoiling by a type II topoisomerase.* Nature, 2000. 404(6780): p. 901-904.
84. Merkel, R., et al., *Energy landscapes of receptor-ligand bonds explored with dynamic force spectroscopy.* Nature, 1999. 397(6714): p. 50-3.
85. Lindsay, S.M., et al., *Stm and Afm Images of Nucleosome DNA under Water.* Journal of Biomolecular Structure & Dynamics, 1989. 7(2): p. 279-287.
86. Weisenhorn, A.L., et al., *Molecular-Resolution Images of Langmuir-Blodgett-Films and DNA by Atomic Force Microscopy.* Langmuir, 1991. 7(1): p. 8-12.
87. Radmacher, M., et al., *From Molecules to Cells - Imaging Soft Samples with the Atomic Force Microscope.* Science, 1992. 257(5078): p. 1900-1905.
88. Radmacher, M., et al., *DIRECT OBSERVATION OF ENZYME-ACTIVITY WITH THE ATOMIC-FORCE MICROSCOPE.* SCIENCE, 1994. 265(ISI:A1994PF33600034).
89. Butt, H.J. and J. M., *CALCULATION OF THERMAL NOISE IN ATOMIC-FORCE MICROSCOPY.* Nanotechnology, 1995. 6(1): p. 1-7.
90. Walters, D.A., et al., *Short cantilevers for atomic force microscopy.* Review of Scientific Instruments, 1996. 67(10): p. 3583-3590.
91. Viani, M.B., et al., *Small cantilevers for force spectroscopy of single molecules.* Journal of Applied Physics, 1999. 86(4): p. 2258-2262.
92. Beyder, A. and F. Sachs, *Microfabricated torsion levers optimized for low force and high-frequency operation in fluids.* Ultramicroscopy, 2006. 106(8-9): p. 838-46.
93. Schlierf, M. and M. Rief, *Temperature softening of a protein in single-molecule experiments.* J Mol Biol, 2005. 354(2): p. 497-503.
94. Janovjak, H., et al., *Unfolding pathways of native bacteriorhodopsin depend on temperature.* Embo J, 2003. 22(19): p. 5220-9.
95. Bustamante, C., et al., *Entropic elasticity of lambda-phage DNA.* Science, 1994. 265(5178): p. 1599-600.
96. Marko, J.F. and E.D. Siggia, *Stretching DNA.* Macromolecules, 1995. 28(26): p. 8759-8770.
97. Hugel, T., et al., *Highly stretched single polymers: atomic-force-microscope experiments versus ab-initio theory.* Phys Rev Lett, 2005. 94(4): p. 048301.

98. Verdier, P.H., *Relaxation Behavior of Freely Jointed Chain.* Journal of Chemical Physics, 1970. 52(11): p. 5512-&.
99. Perico, A., S. Bisio, and C. Cuniberti, *Polymer Dynamics in Dilute-Solutions - the Freely Rotating Chain.* Macromolecules, 1984. 17(12): p. 2686-2689.
100. Livadaru, L., R.R. Netz, and H.J. Kreuzer, *Stretching Response of Discrete Semiflexible Polymers.* Macromolecules, 2003. 36(10): p. 3732-14.
101. Axelrod, D., *Total internal reflection fluorescence microscopy in cell biology.* Traffic, 2001. 2(11): p. 764-774.
102. Funatsu, T., et al., *Imaging of Single Fluorescent Molecules and Individual Atp Turnovers by Single Myosin Molecules in Aqueous-Solution.* Nature, 1995. 374(6522): p. 555-559.
103. Tokunaga, M., et al., *Single molecule imaging of fluorophores and enzymatic reactions achieved by objective-type total internal reflection fluorescence microscopy.* Biochemical and Biophysical Research Communications, 1997. 235(1): p. 47-53.
104. Axelrod, D., *Selective imaging of surface fluorescence with very high aperture microscope objectives.* Journal of Biomedical Optics, 2001. 6(1): p. 6-13.
105. Ober, R.J., S. Ram, and E.S. Ward, *Localization accuracy in single-molecule microscopy.* Biophysical Journal, 2004. 86(2): p. 1185.
106. Yildiz, A., et al., *Myosin V walks hand-over-hand: Single fluorophore imaging with 1.5-nm localization.* Science, 2003. 300(5628): p. 2061-2065.
107. Bobroff, N., *Position Measurement with a Resolution and Noise-Limited Instrument.* Review of Scientific Instruments, 1986. 57(6): p. 1152-1157.
108. Lacoste, T.D., et al., *Ultrahigh-resolution multicolor colocalization of single fluorescent probes.* Proceedings of the National Academy of Sciences of the United States of America, 2000. 97(17): p. 9461-9466.
109. Qu, X.H., et al., *Nanometer-localized multiple single-molecule fluorescence microscopy.* Proceedings of the National Academy of Sciences of the United States of America, 2004. 101(31): p. 11298-11303.
110. Rust, M.J., M. Bates, and X.W. Zhuang, *Sub-diffraction-limit imaging by stochastic optical reconstruction microscopy (STORM).* Nature Methods, 2006. 3(10): p. 793-795.
111. Huang, B., et al., *Three-dimensional super-resolution imaging by stochastic optical reconstruction microscopy.* Science, 2008. 319(5864): p. 810-813.
112. Bates, M., et al., *Multicolor super-resolution imaging with photo-switchable fluorescent probes.* Science, 2007. 317(5845): p. 1749-1753.
113. Heilemann, M., et al., *Subdiffraction-resolution fluorescence imaging with conventional fluorescent probes.* Angewandte Chemie-International Edition, 2008. 47(33): p. 6172-6176.
114. Betzig, E., et al., *Imaging intracellular fluorescent proteins at nanometer resolution.* Science, 2006. 313(5793): p. 1642-1645.
115. Gordon, M.P., T. Ha, and P.R. Selvin, *Single-molecule high-resolution imaging with photobleaching.* Proceedings of the National Academy of Sciences of the United States of America, 2004. 101(17): p. 6462-6465.

# 9. Lebenslauf

## Persönliche Daten

Dipl. Phys. Elias Puchner
Horemansstr. 23
80636 München
Geboren am 18.01.1981 in Nürnberg.
Familienstand: ledig

## Bildung

| | |
|---|---|
| 1988-2000 | Abitur an der Rudolf-Steiner Schule Nürnberg |
| 1998 | "Summer-Term" an der Harvard University, Cambridge, MA, USA, "Fundamentals of Contemporary Astronomy" |
| 2000-2006 | Studium der Physik an der Ludwig-Maximilians-Universität München mit Schwerpunkt Biophysik und Nebenfach Biochemie<br>Diplomarbeit am Lehrstuhl für Angewandte Physik bei Prof. Hermann E. Gaub: "Enzymmechanik - Einzelmolekülexperimente mit einem AFM-TIRF Hybrid" |
| 2006 | Beginn der Promotion an der Ludwig-Maximilians-Universität München am Lehrstuhl für Angewandte Physik bei Prof. Hermann E. Gaub: „Einzelmolekül-Mechanoenzymatik“ |
| seit 2007 | Mitglied im "International Doctorate Program NanoBioTechnology" |

## Praktika

| | |
|---|---|
| 2003 | Werkstudent bei Dr. Parak, Lehrstuhl für Angewandte Physik<br>"Synthesis of highly fluorescing CdSe/ZnS nanocrystals" |
| 3/04 - 4/04 | Biochemisches Praktikum bei Prof. Beyer am Lehrstuhl für Stoffwechselbiochemie, LMU München: "Untersuchung von Lipidmembranen mit NMR" |
| 4/04 – 6/04 | Forschungsaufenthalt bei Prof. Fernandez, Dept. of Biological Sciences, Columbia University, New York, NY, USA: "Construction of a combined magnetic tweezers - TIRF-hybrid and its application to protein unfolding" |

## Vorträge und Konferenzbeiträge

| | |
|---|---|
| 2003 | Nanoparticle Symposium, IPHT Jena, Poster: "Synthesis of highly fluorescing CdSe/ZnS nanocrystals" |
| 2007 | European Biophysics Congress, London,<br>Poster: "Single Molecule Studies on the Mechanical Activation of the Molecular Force Sensor Titin Kinase" |
| | Euro AFM Forum, Münster. Eingeladener Vortrag: “Single Molecule Studies on the Mechanical Avtivation of the Molecular Force Sensor Titin Kinase” |

| | |
|---|---|
| 2008 | X. Linz Winter Workshop "Advances in Single-Molecule Research for Biology & Nanoscience. Poster: "Comparing Proteins by their Unfolding Pattern" |

## Patente

"Anordnung zum Untersuchen und/oder Manipulieren von Proben" DE 10 2007 010 890.0

„Method for Data analysis“, Prüfung vom Europäischen Patentamt

## Stipendien/Preise

| | |
|---|---|
| 2007 | Posterpreis der European Biophysical Society in London |
| seit 2007 | Mitglied „International Doctorate Program NanoBioTechnology“ |

# 10. Danksagung

An dieser Stelle möchte ich ganz herzlich bei allen Bedanken, die mich während meiner Doktorarbeit begleitet und unterstütz haben.

Größter Dank gilt meinem Doktorvater Hermann Gaub, der mich in jeder Hinsicht gefördert hat. Er stand mir jederzeit auf herzliche Art mit Rat, Inspiration und Zuspruch zur Seite und hat mir äußerst spannende und lehrreiche Projekte ermöglicht. Überdies sollte sein Lehrstuhl im Michelin-Führer Erwähnung finden.

Meinem IDK-Mentor Joachim Rädler möchte ich für Unterstützung und Rat danken, wie auch dem IDK und seinen Mitarbeitern für das vielseitige und interdisziplinäre Forschungs- und Bildungsprogramm.

Der ganzen Gambicrew möchte ich für die unvergleichlich angenehme, abwechslungsreiche und inspirierende Zeit Dank sagen. Besonders:

Stefan Kufer für seine Kontinuität, den durchhaltenden Ehrgeiz und die angenehme Experimentieratmosphäre. Hätten wir nur „a bissi" früher gewusst wie toll das alles wird, dann wär's noch schöner gewesen!

Stefan Stahl für die gute Zusammenarbeit und Unterstützung bei vielen Projekten, sowie für das Aufbauen des besten New-Gereration-AFM mit opto-thermischer Cantileverregelung. May the force be with you!

Hermann Gumpp für die lange und gute Zusammenarbeit bei vielen Projekten.

Kerstin Blank für die gute Zusammenarbeit bei fluktuierenden Enzymen und anderen Projekten, wie auch bei Ralf David, Mathias Strackharn, und Julia Zimmermann, der besten Banknachbarin überhaupt.

Kay Gottschalk, Julia Schmitz für die Zell-Experimente, bei denen ich seit langer Zeit wieder etwas Größeres als einzelne Moleküle gesehen habe.

Philip Tinnefeld, Jan Vogelsang und Thorben Cordes für die neuen SMCP-Versuche auf dem besten Mikroskop überhaupt.

Ann Fornof for correcting my papers and our interesting discussions.

Angelika Kardinal und Thomas Nicolaus für die chemische Unterstützung und Vorbereitung.

Dominik Ho, Philip Severin und allen Stemplern für die geselligen Grill-Zeiten und Diskussionen.

Prof. Mathias Gautel vom King`s College London möchte ich für die sehr spannende Kollaboration bezüglich der Titinkinase danken, das Projekt hat mir spannende medizinisch relevante Forschung ermöglicht und er fand immer für lehrreiche Diskussionen Zeit. Auch den Mitgliedern seiner Gruppe, Birgit Brandmeier, Alexander Alexandrovich, Gereon Franzen und Ay Lin Kho, sei für die gute Zusammenarbeit gedankt.

Prof. Helmut Grubmüller vom Max-Planck Institut Göttingen danke ich ganz herzlich für die tolle Zusammenarbeit bei unserem Titinkinase-Projekt. Auch er stand mir immer mit wertvollem Rat zur Seite. Besonderer Dank auch an seine Gruppe, Frauke Gräter, Ulf Hensen und Lars Schäfer.

Stephan von Cölln aus Prof. Mandfred Radmachers Gruppe für die Kollaboration mit der alkalischen Phosphatase.

Prof. Hans Heuss, Njimegen, für die Zusammenarbeit mit RNA-Riboswitches und die interessanten und lehrreichen Gespräche.

Den Korrekturlesern meiner Arbeit möchte ich für die Unterstützung im Endspurt danken: Stefan Kufer, Stefan Stahl, Philip Severin, Mathias Strackharn, Hermann Gumpp, Ralf David, Britta Person und Stephan Puchner.

Zuletzt möchte ich mich bei meiner Familie bedanken, die mich immer auf meinem Weg unterstützt und motiviert hat. Meiner Mutter vor allem für ihre Fürsorge und Unterstützung, meinen Brüdern Martin und Stephan für ihre hilfreichen Ratschläge, anspornende Diskussionen und unseren Humor.